Lattice Boltzmann Methods for Turbulent Flows

Application to Coriolis Mass Flowmeter

zur Erlangung des akademischen Grades eines
DOKTORS DER INGENIEURWISSENSCHAFTEN (DR.-ING.)

von der KIT-Fakultät für Chemieingenieurwesen und Verfahrenstechnik des
Karlsruher Instituts für Technologie (KIT)
genehmigte

DISSERTATION

von
M. Sc. Marc Haussmann
aus Frankenthal (Pfalz)

Tag der mündlichen Prüfung: 30.09.2020

Referent: Prof. Dr.-Ing. habil. Hermann Nirschl
Erste Korreferentin: PD Dr. Gudrun Thäter
Zweiter Korreferent: Dr. Mathias J. Krause

Abstract

Complex flow phenomena make it difficult to simulate engineering applications at a level of detail and accuracy that allows a characterization and improvement of their working principle. This thesis shows that the lattice Boltzmann method (LBM) is very well suited for this purpose. The focus is on the simulation and modeling of turbulent flows. Due to the excellent parallelizability of the LBM, turbulent flows are calculated with large-eddy simulations instead of Reynolds-averaged Navier–Stokes models, which are common for industrial applications. Thus, transient complex turbulent flows can be investigated simulatively. The knowledge gained from these simulations is particularly useful for the design and optimization of devices and processes.

All described LBM simulations are performed with the open source software OpenLB. For this purpose, OpenLB is extended to allow a validation of implemented turbulence models by means of canonical flow types. Furthermore, a framework for the simulation of fluid-structure interaction (FSI) is created.

Initially, the collision operators Bhatnagar–Gross–Krook (BGK), entropic lattice Boltzmann (ELB), two-relaxation-time (TRT), regularized lattice Boltzann (RLB) and multiple-relaxation-time (MRT) are investigated in the Taylor-Green vortex flow, a paragon of decaying homogeneous isotropic turbulence (DHIT). The focus is on stability, consistency and accuracy of the used schemes. The study includes the comparison of the turbulent kinetic energy, the energy dissipation rate and the energy spectrum to a reference solution. Three different Reynolds numbers $\mathrm{Re} = 800$, $\mathrm{Re} = 1600$ and $\mathrm{Re} = 3000$ are considered using both acoustic and diffusive scaling to characterize the influence of the lattice Mach number. In highly underresolved grid configurations the BGK scheme shows unstable behaviour. Diverging simulations using the MRT scheme are due to a strong dependence on the lattice Mach number. Although ELB changes the viscosity, no behaviour corresponding to a eddy viscosity model can be found. At low lattice Mach numbers, the RLB scheme shows very low energy levels at high wave numbers. The "magic parameter" of the TRT scheme is determined in terms of energy contribution. Nevertheless, no increased stability compared to the BGK scheme is found. Overall, the lattice Mach number should be chosen with respect to the collision scheme to ensure stability and improve accuracy.

For the realization of a near-wall-modeled large-eddy simulation (NWM-LES) approach the BGK collision operator is selected. The Smagorinsky eddy viscosity model with the van Driest damping function is used in the turbulent boundary layer. The influence of different velocity boundary implementations and wall functions is investigated in a bi-periodic, fully developed turbulent channel flow for friction Reynolds numbers of $\mathrm{Re}_\tau = 1000$, $\mathrm{Re}_\tau = 2000$ and $\mathrm{Re}_\tau = 5200$. The validation is carried out using direct numerical simulation (DNS) data for first and second order turbulence statistics. Applying this approach to a Coriolis mass flowmeter (CMF) shows that the pressure drop can be described up to a Reynolds number of $\mathrm{Re} = 127\,800$.

Furthermore, the developed NWM-LES LBM approach is compared with OpenFOAM, an open source implementation of the finite volume method (FVM), for complex turbulent flows relevant for internal combustion engines. The previously developed and validated LBM approach is extended with a curved boundary scheme for set velocity. The results of both flow solvers are compared with data from a particle image velocimetry (PIV) experiment. The validation includes both time-averaged and root mean square (RMS) velocity fields. In addition, both the run-time of the simulation and the duration of the different grid generation processes are determined. The performance analysis shows that OpenLB is 32 times faster than OpenFOAM for the tested configuration. Consequently, the developed NWM-LES LBM approach is able to describe complex turbulent flows in an engineering application accurately while simultaneously reducing the required computational effort.

Vortex induced vibrations (VIV) also play an important role in many engineering applications. For the investigation of these, different fluid structure approaches for LBM are implemented, compared and evaluated. The two investigated classes are the moving boundary methods (MBM) and the partially saturated methods (PSM). First, the Galilean invariance of aerodynamic coefficients for the individual schemes is investigated. The BGK scheme is used to simulate an eccentrically positioned cylinder in a Couette flow. Furthermore, different volume approximation methods for PSM and refill algorithms for MBM are compared. Both, the grid convergence and the Galilean invariance convergence, are considered. The study of VIV phenomena includes a transversely oscillating cylinder in a free stream at a Reynolds number of $Re = 100$. Free and forced oscillation are examined to investigate known phenomena such as lock-in and lock-out zones. The results show that both, MBM and PSM, are in good agreement with literature data, which confirms their suitability for VIV simulations.

Finally, a fluid-structure interaction approach is realized using an MBM approach for the simulation of a CMF. Here, OpenLB is coupled with Elmer, an open source implementation of the finite element method, to describe the structural dynamics. A staggered coupling approach between the two software packages is presented. The finite element mesh is created by the grid generation tool Gmsh to ensure a complete open source workflow. First, the Eigenmodes of the CMF are calculated and compared with measurement data. The resulting excitation frequency is used to determine the phase shift in a partitioned fully coupled FSI simulation. The calculated phase shift is in good agreement with measured data

and confirms that this model is able to describe the working principle of a CMF.

The conducted studies demonstrate the great potential of the LBM for the simulation of engineering applications, especially when turbulent flows are considered.

Zusammenfassung

Komplexe Strömungsphänomene machen es schwierig Ingenieursanwendungen so detailliert und genau zu simulieren, dass eine Charakterisierung und Verbesserung ihres Funktionsprinzips möglich ist. Diese Arbeit zeigt, dass die Lattice-Boltzmann-Methode (LBM) sehr gut für diesen Zweck geeignet ist. Im Vordergrund stehen hierbei die Simulation und Modellierung von turbulenten Strömungen. Diese lassen sich auf Grund der hervorragenden Parallelisierbarkeit der LBM mit Large-eddy Simulationen an Stelle von Reynolds-gemittelten Navier–Stokes Modellen, die im industriellen Umfeld üblich sind, berechnen. Somit können komplexe transiente turbulente Strömungen simulativ untersucht werden. Die daraus gewonnenen Erkenntnisse dienen insbesondere der Auslegung und Optimierung von Bauteilen und Prozessen.

Alle beschriebenen LBM Simulationen werden mit der Open Source Software OpenLB durchgeführt. Dazu wird OpenLB erweitert, um eine Validierung von implementierten Turbulenzmodellen mittels kanonischer Strömungsformen zu ermöglichen. Des Weiteren wird ein Framework für die Simulation von Fluid-Struktur Interaktion (FSI) geschaffen.

Anfangs werden die Kollisionsoperatoren Bhatnagar–Gross–Krook (BGK), Entropic Lattice Boltzmann (ELB), Two-Relaxation-Time (TRT), Regularized Lattice

Boltzmann (RLB) und Multiple-Relaxation-Time (MRT) in der Taylor-Green Vortex Strömung, einem klassischen Beispiel für abklingende homogene isotrope Turbulenz (DHIT), untersucht. Hierbei liegt der Fokus auf Stabilität, Konsistenz und Genauigkeit der verwendeten Schemata. Die Studie beinhaltet den Vergleich der turbulenten kinetischen Energie, der Dissipationsrate der Energie und dem Energiespektrum zu einer Referenzlösung. Drei unterschiedliche Reynoldszahlen, $\mathrm{Re} = 800$, $\mathrm{Re} = 1600$ und $\mathrm{Re} = 3000$, werden sowohl unter Verwendung einer akustischen als auch einer diffusiven Skalierung betrachtet, um den Einfluss der Lattice Machzahl zu charakterisieren. In stark unteraufgelösten Gitterkonfigurationen zeigt das BGK Schema ein instabiles Verhalten. Divergierende Simulationen unter der Verwendung des MRT Schemas sind auf eine starke Abhängigkeit von der Lattice Machzahl zurückzuführen. Obwohl ELB die Viskosität verändert, kann kein Verhalten, das einem Wirbelviskositätsmodell entspricht, gefunden werden. Bei geringen Lattice Machzahlen zeigt das RLB Schema sehr geringe Energielevel bei hohen Wellenzahlen. Der „magic parameter” des TRT Schemas wird bestimmt im Hinblick auf den Energieeintrag. Trotzdem wird keine erhöhte Stabilität im Vergleich zum BGK Schema festgestellt. Insgesamt sollte die Lattice Machzahl bezüglich des verwendeten Kollisonsschemas gewählt werden, um die Stabilität zu gewährleisten und die Genauigkeit zu verbessern.

Für die Realisierung eines wandmodellierten Large-Eddy Simulation (NWM-LES) Ansatzes wird der BGK Kollisionsoperator ausgewählt. Das Smagorinsky Wirbelviskositätsmodell kommt hierbei zum Einsatz und wird in der turbulenten Grenzschicht mit der van Driest'schen Dämpfungsfunktion verwendet. Der Einfluss verschiedener Implementierungen von Geschwindigkeitsrandbedingungen und Wandfunktionen wird in einer biperiodischen, voll ausgebildeten turbulenten Kanalströmung für Schubspannungs-Reynoldszahlen von $\mathrm{Re}_\tau = 1000$, $\mathrm{Re}_\tau = 2000$ und $\mathrm{Re}_\tau = 5200$ untersucht. Die Validierung erfolgt mittels Daten einer direkten numerischen Simulation (DNS) für Turbulenzstatistiken erster und zweiter Ordnung. Die Anwendung dieses Ansatzes auf einen Coriolis Massendurchflussmesser (CMF) zeigt, dass der Druckverlust bis zu einer Reynoldszahl $\mathrm{Re} = 127\,800$ beschrieben werden kann.

Des Weiteren wird der entwickelte NWM-LES LBM Ansatz mit OpenFOAM, einer Open Source Implementierung der finititen Volumen Methode (FVM) für komplexe turbulente Strömungen, die relevant für Verbrennungsmotoren sind, verglichen. Der zuvor entwickelte und validierte LBM Ansatz wird mit einer Geschwindigkeitsrandbedingung für gekrümmte Ränder erweitert. Die Ergebnisse beider Strömungslöser werden mit Daten eines Particle Image Velocimetry (PIV) Experiments verglichen. Die Validierung umfasst sowohl die zeitgemittelten als auch die quadratisch gemittelten (RMS) Geschwindigkeitsfelder. Zusätzlich wird sowohl die Laufzeit der Simulation als auch die Dauer der unterschiedlichen Gittergenerierungsprozesse bestimmt. Die Performanceanalyse der getesteten Konfiguration zeigt, dass OpenLB 32-mal schneller ist als OpenFOAM. Folglich ist der entwickelte NWM-LES LBM Ansatz dazu in der Lage, komplexe turbulente Strömungen in einer Ingenieursanwendung akkurat und mit einem verringerten Rechenaufwand zu beschreiben.

Wirbel induzierte Vibrationen (VIV) sind ein weiterer wichtiger Anwendungsfall für Ingenieursapplikationen. Für die Untersuchung dieser werden verschiedene Fluid-Struktur Ansätze für LBM implementiert, verglichen und evaluiert. Die zwei untersuchten Klassen sind die Moving Boundary Methods (MBM) und die Partially Saturated Methods (PSM). Als erstes wird die Galiläische Invarianz von aerodynamischen Koeffizienten für die einzelnen Schemata untersucht. Dazu wird das BGK Schema verwendet, um einen exzentrisch positionierten Zylinder in einer Couette Strömung zu simulieren. Überdies werden verschiedene Volumenapproximationsmethoden für PSM und Auffüllmechanismen für MBM verglichen. Sowohl die Gitterkonvergenz als auch die Konvergenz der Galiläischen Invarianz werden betrachtet. Die Studie der VIV-Phänomene umfasst einen transvers oszillierenden Zylinder in einem Freistrom bei einer Reynoldszahl von $\mathrm{Re} = 100$. Dabei werden freie und erzwungene Oszillation betrachtet, um bekannte Phänomene, wie Lock-in und Lock-out Zonen, zu untersuchen. Die Ergebnisse zeigen, dass sowohl MBM als auch PSM eine gute Übereinstimmung zu Literaturdaten aufweisen, womit die Eignung für VIV-Simulationen bestätigt werden kann.

Schließlich wird ein Fluid-Struktur Interaktionsansatz unter der Verwendung eines MBM Ansatzes für die Simulation eines CMFs realisiert. Hierbei wird OpenLB mit Elmer, einer Open Source Implementierung der Finite-Elemente-Methode, gekoppelt, um auch die Strukturdynamik zu beschreiben. Ein gestaffelter Kopplungsansatz zwischen den beiden Softwarepaketen wird präsentiert. Das Finite-Elemente-Gitter wird durch das Gittergenerierungstool Gmsh erstellt, um einen kompletten Open Source Workflow zu garantieren. Zunächst werden die Eigenmoden des CMFs berechnet und mit Messdaten verglichen. Die daraus bestimmte Anregungsfrequenz wird zur Bestimmung des Phasenshifts in einer partitionierten voll gekoppelten FSI Simulation verwendet. Der berechnete Phasenshift zeigt eine gute Übereinstimmung mit den Messdaten und bestätigt, dass dieses Modell in der Lage ist, das Funktionsprinzip eines CMFs zu beschreiben.

Die durchgeführten Studien zeigen das große Potential der LBM für die Simulation von Ingenieursapplikationen, insbesondere wenn turbulente Strömungen betrachtet werden.

Contents

1

Introduction

In many engineering applications numerical simulations are essential to govern and manage their product life cycles. This becomes particularly evident when looking at the following selection, which intends to illustrate the importance of numerical simulations in engineering. Firstly, it is generally understood that the operating costs of pumps in pipeline systems are mainly influenced by the pressure drop [19]. Numerical simulations enable the fast and precise calculation of arbitrarily shaped pipeline elements, and thus help to substantially minimize their operating cost. Another prominent example is the construction of bridges [31]. Here, vortex-induced vibrations (VIV) have to be taken into account carefully. Otherwise this phenomenon can have disastrous consequences as could be seen from the collapse of the Tacoma Narrows Bridge [9]. In this regard, numerical simulations help to understand and predict VIV phenomena, thus improving durability, efficiency and safety during a bridge's life cycle. Also, numerical simulations represent an essential tool for the analysis of internal combustion (IC) engines, where they help to understand the complex processes in turbulent intake flows of IC engines, resulting in improved engine efficiency and reduced pollutant emissions [89]. Lastly, the Coriolis mass flowmeter (CMF), which is a highly accurate instrument for mass flow measurements, can benefit from numerical simulations as its design can be improved for extended range of use by simulating its working principle [105].

Unfortunately, precise numerical simulations of engineering applications are complex and time-consuming, even if many cores and a large amount of memory is used [26]. This is often related to the interconnection of various multiphysical phenomena and the turbulent flow regime of fluids [79]. The three-dimensional, unsteady and irregular nature of turbulence is the reason why the simulation of turbulent flows is challenging [77]. In this respect, three approaches have emerged prominently to model turbulent flows, namely direct numerical simulation (DNS), large-eddy simulation (LES) and Reynolds-averaged Navier–Stokes equations (RANS) [104]. The idea behind the direct numerical simulation is to solve the Navier–Stokes equations. Here, no turbulence modeling is used, but all time and length scales of the flow have to be resolved. LES, in contrast, simulates the large energy-containing scales and models the small scales based on the universal character hypothesis. The RANS approach can be seen as a statistical approach that describes the mean motion of the flow field. This approach is especially common to describe industry applications due to its fast solution procedure for statistically stationary flows and its reduced requirements on the spatial resolution of numerical grids [29].

Nevertheless, RANS describes the entire energy spectrum by a few turbulence quantities and the high level of modeling can lead to inaccurate and non physical results, if complex turbulent flows are considered [29]. The use of LES can avoid this problem but goes hand in hand with a significantly increased computing effort [77]. The higher computational demand can be compensated by a highly parallel and fast algorithm [97]. The lattice Boltzmann method (LBM), which has gained interest over the last decades [7, 17, 1], demonstrates this advantage [48, 47] and is therefore an alternative to traditional discretization methods such as the finite volume method (FVM) or the finite difference method

(FDM).

The main aim of this work is to show that LBM is an excellent choice for the simulation of engineering applications, especially if turbulent flows are considered. This thesis contributes to the four main areas of numerical simulation: method development, implementation, validation and application.

A novel LBM near-wall modeled large eddy simulation (NWM-LES) method is proposed to accurately simulate engineering applications at high Reynolds numbers. A particular challenge is the correct estimation of turbulence statistics when a coarse mesh is used.

Based on the methodological development, a highly modular and fast NWM-LES algorithm is implemented in the LBM framework OpenLB. Thanks to the modular structure also curved boundaries can be handled. Furthermore, various fluid-solid interfaces for moving boundaries are implemented in a new framework for OpenLB. Additionally, a complete open source coupling workflow between OpenLB and the structural solver Elmer [24] is developed to simulate fluid-structure interaction (FSI).

Rigorous validation is carried out to analyze and compare commonly used collision operators for decaying homogeneous isotropic turbulence in terms of accuracy, consistency and stability. The implemented NWM-LES approach is validated in a fully developed bi-periodic channel flow. Moreover, the distinct fluid-solid interfaces are compared in a Couette flow using a Galilean invariance analysis.

The implemented and validated approaches are used to address various engineering applications. The simulation of a CMF at high Reynolds numbers with LBM is enabled for the first time by using the NWM-LES approach and compared to measurement data. A further application case of the NWM-LES approach is the in-cylinder flow in an IC-engine, thus demonstrating the broad field of application. The analysis of VIV phenomena as an important engineering relevant challenge in a free stream shows the suitability of the fluid-solid interface approaches. The implemented FSI workflow makes it possible for the first time to simulate the working principle of a CMF with LBM.

This thesis is structured as follows: Chapter 2 introduces the DNS, LES and RANS approach for the simulation of turbulent flows, while focusing on the implementation in the LBM framework. The subsequent Chapters 3-7 represent published articles. A DNS for different collision operators is obtained in Chapter 3 to analyze the properties of each collision operator in terms of lattice Mach number, Reynolds number and grid resolution dependency. In Chapter 4, the BGK collision operator is selected to implement a NWM-LES, enabling the simulation of the pressure drop in a CMF geometry. An extension of this approach for curved boundaries to address IC-engine flows is depicted in Chapter 5. Next, the evaluation of various fluid-solid interfaces in the context of VIV is presented in Chapter 6. On this basis, Chapter 7 shows a complete open source FSI workflow to simulate the working principle of a CMF. Finally, Chapter 8 summarizes the results and provides an outlook about future research topics.

2

Modeling and Simulation Approaches for Turbulent Flows

The complexity of turbulence modeling originates from its multiscale character. Turbulence motion appears on a broad range of time and length scales. Turbulence is still a not fully understood physical phenomenon, and the existing theories are based on simplifications that lead to limitations of applicability for complex turbulent flows [38]. It is worth noting that turbulence theory is based on working hypotheses. The behavior of turbulence in the limit of very high Reynolds numbers has not been experimentally tested and therefore the validation of turbulence theories is based on a limited database. This fact leads to a field of tension between distinct theories that propagate a certain view on turbulence.

Nevertheless, for a better understanding of the different approaches to turbulence modeling, established concepts are introduced which – strictly speaking – only apply to homogeneous isotropic turbulence at high Reynolds numbers.

Homogeneous turbulence means that all statistical properties are invariant by spatial translation. If the statistical properties are also invariant to any axial rotation, the flow is called homogeneous and isotropic [5].

The concepts are explained with the help of Figure 2.1, which displays a model spectrum of the kinetic energy E as a function of the wave number κ. Hereby, the wave number and the corresponding length scale l are connected by $\kappa = 2\pi/l$. Important turbulent quantities are the turbulent kinetic energy k and the dissipation rate of the turbulent kinetic energy ε. The turbulent kinetic energy k is defined as

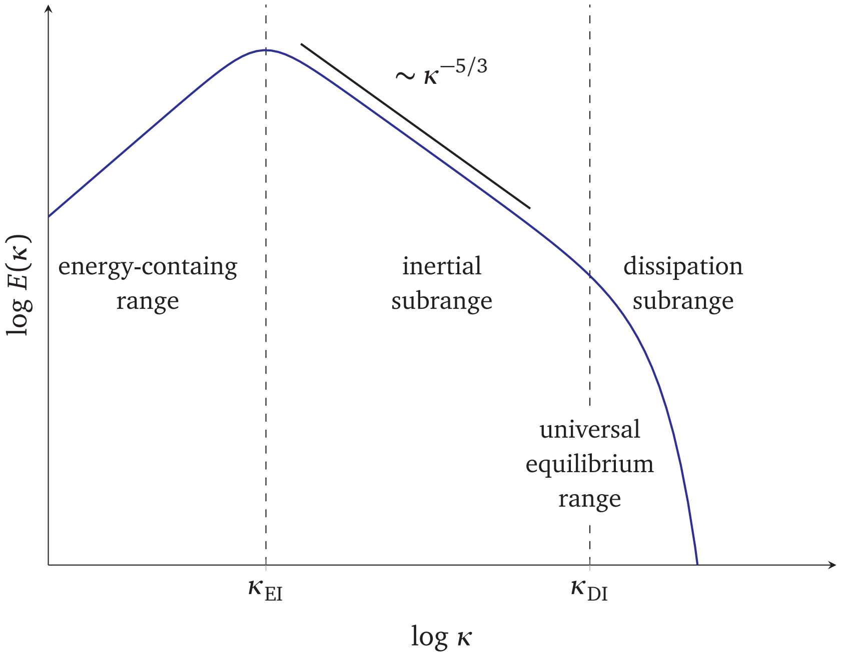

Figure 2.1: *Characteristic ranges in the model spectrum of the turbulent kinetic energy*

$$k = \frac{1}{2}\langle u'_\alpha u'_\alpha \rangle, \tag{2.1}$$

where Greek indices obey the Einstein notation, u'_α is the fluctuation component of the velocity field $\boldsymbol{u}$ and $\langle\cdot\rangle$ denotes a time-averaged quantity. The dissipation rate of the turbulent kinetic energy ε reads

$$\varepsilon = \nu \left\langle \frac{\partial u'_\alpha}{\partial x^\beta} \frac{\partial u'_\alpha}{\partial x^\beta} \right\rangle, \tag{2.2}$$

where x_β is the position.

In 1922, Richardson [83] introduced the concept of the energy cascade, which is still an important qualitative model to understand the energy transfer from large scales to small scales. The largest occurring eddies are usually in the order of the characteristic length scale of the flow. They are located at small wave numbers $\kappa < \kappa_{\mathrm{EI}}$ in the energy containing range. These energy containing large scales are unstable and break up into smaller eddies. The process can be seen as a cascading waterfall from pool to pool, which means that energy can only be transferred between scales that are similar in size and no long-range energy transfer takes place. The break-up process, where the eddies become smaller and smaller, takes place in the inertial subrange $\kappa_{\mathrm{EI}} < \kappa < \kappa_{\mathrm{DI}}$. The process lasts until the eddy motion is stable at high wave numbers $\kappa > \kappa_{\mathrm{DI}}$ in the dissipation subrange. Here, the kinetic energy is dissipated by the effect of molecular viscosity.

Further questions concerning the scales of the energy cascade can be answered with the K41 theory proposed by Kolmogorov [52] and restated by Pope [77]. The theory is that the small scales of turbulence $\kappa > \kappa_{\mathrm{EI}}$ are statistically isotropic at high Reynolds numbers Re, which is known as Kolmogorov's hypothesis of local isotropy [77]. Hence, the large energy containing scales are characterized as anisotropic and the small scales can be seen as statistically isotropic. Additionally, small scales in the universal equilibrium range $\kappa > \kappa_{\mathrm{EI}}$ can be unambiguously determined by the viscosity ν and the turbulent kinetic energy dissipation ε. This dependency is known as the first similarity hypothesis. The dependency of ν and ε is used to describe the smallest occurring dissipative scales in the flow, namely the Kolmogorov scales. The Kolmogorov length scale η, velocity scale

u_η and time scale τ_η are respectively defined by

$$\eta = \left(\frac{\nu^3}{\varepsilon}\right)^{1/4}, \tag{2.3}$$

$$u_\eta = (\varepsilon\,\nu)^{1/4}, \tag{2.4}$$

$$\tau_\eta = \left(\frac{\nu}{\varepsilon}\right)^{1/2}. \tag{2.5}$$

The second similarity hypothesis states that the small scales in the inertial subrange $\kappa_{\mathrm{EI}} < \kappa < \kappa_{\mathrm{DI}}$ are only determined by the turbulent kinetic energy dissipation ε. This implies that viscous effects are negligible in the inertial subrange and only motions in the dissipation range are affected by the viscosity. The decrease of energy according to the energy cascade in the inertial subrange scales with $\sim \kappa^{-5/3}$.

The following sections introduce the three basic approaches to turbulence modeling, namely the direct numerical simulation (DNS), the large-eddy simulation (LES) and the Reynolds-averaged Navier–Stokes (RANS) approach. Hereby, the focus is set on the implementation in the LBM, which is illustrated by an exemplary selection of models.

2.1 Direct Numerical Simulation

DNS is the most accurate and conceptually the simplest approach to simulate turbulent flows, because no additional turbulence modeling is involved. Therefore, the Navier–Stokes equations are approximated and the occurring errors are solely due to discretization. The basic idea is to resolve all scales of motion using suitable fine discretization, initial and boundary conditions. The obtained flow field is equivalent to a single realization of a flow or a short term laboratory experiment [25]. Nevertheless, the computational demand rapidly increases with the Reynolds number. Hence, the application of DNS is restricted to low and moderate Reynolds numbers, which excludes most large-scale industrial applications.

Assuming homogeneous isotropic turbulence, the high computational effort can be estimated, which was shown by Pope [77]. Firstly, a turbulence Reynolds number Re_L is defined as

$$\mathrm{Re}_L = \frac{k^{\frac{1}{2}} L}{\nu} = \frac{k^2}{\varepsilon \nu}, \tag{2.6}$$

where k is the turbulent kinetic energy and $L = k^{3/2}/\varepsilon$ the characteristic length scale of the flow. The domain size $\mathscr{L}$ must be large enough to capture the largest appearing energy-containing motions. A reasonable choice to capture the large scale energy-containing motions is that the domain size $\mathscr{L}$ is eight times the longitudinal integral length scale L_{11}, which is defined by

$$L_{11}(t) = \int_0^\infty = \frac{\langle u_1'(\boldsymbol{x} + \boldsymbol{e}_1 r, t) u_1'(\boldsymbol{x}, t)\rangle}{\langle (u_1')^2 \rangle} \mathrm{d}r, \tag{2.7}$$

where $\boldsymbol{e}_1$ is the unit vector in direction 1. Furthermore, the grid spacing Δx must be smaller than the Kolmogorov length scale η or at least in the same order of magnitude. Consequently, the resolution N with respect to the Kolmogorov length scale $\eta = 1.5/(\pi \Delta x)$ [109] assuming high Reynolds numbers ($L_{11}/L = 0.43$) [77] is given by

$$N = \frac{\mathscr{L}}{\Delta x} = 8\frac{L_{11}}{\Delta x} \approx 3.8\frac{L_{11}}{\eta} \approx 1.6\frac{L}{\eta} = 1.6\mathrm{Re}_L^{\frac{3}{4}}. \tag{2.8}$$

The number of time steps M supposes a simulation duration of four times the turbulence time scale $\tau_s = k/\varepsilon$ and a Courant–Friedrichs–Lewy number of $\mathrm{CFL} = k^{1/2}\Delta t/\Delta x = 0.05$ [77]. Hence, the number of time steps is estimated by

$$M = \frac{4}{\tau_s} = 80\frac{L}{\Delta x} \approx 38.2\frac{L}{\eta} = 38.2\mathrm{Re}_L^{\frac{3}{4}}. \tag{2.9}$$

Finally, the number of mode-steps $N^3 M$ [77] yields

$$N^3 M = 160\mathrm{Re}_L^3. \tag{2.10}$$

This result underlines the high computational effort that is necessary to address transient high Reynolds number flows with DNS.

In this section, the Navier–Stokes equations that must be solved for DNS are introduced. Afterwards the Boltzmann equation and its discretization, the lattice Boltzmann equation, is described. The focus is on different LBM collision operators that are commonly used to recover the Navier–Stokes equations.

2.1.1 Navier–Stokes Equations

The Navier–Stokes equations are a fundamental set of partial differential equations to describe a fluid as a continuum. They are based on the conservation principles for mass, momentum and energy. The corresponding continuity and momentum equations are introduced in the following.

2.1.1.1 Continuity Equation

The continuity equation describes the conservation of mass, i.e. the sum of the masses flowing in and out of a unit volume per unit time is equal to the mass change per unit time due to density changes. This implies that the fluid mass can neither be created nor destroyed. The continuity equation reads

$$\frac{\partial \rho}{\partial t} + u_\alpha \frac{\partial \rho}{\partial x_\alpha} + \rho \frac{\partial u_\alpha}{\partial x_\alpha} = 0, \tag{2.11}$$

where ρ is the fluid density and t is the time. The first two terms of Eq. (2.11) represent the material derivative of the density. If the fluid is assumed to be incompressible, the material derivative equals zero. The fluid velocity is therefore divergence-free or solenoidal and the incompressible continuity equation is written as

$$\frac{\partial u_\alpha}{\partial x_\alpha} = 0. \tag{2.12}$$

It is worth noting that a constant density is not a necessary condition for incompressible flows, an example of which are density layers in oceans [75, 110]. The incompressibility assumption of the flow is justified for low Mach numbers ($\mathrm{Ma} < 0.3$) [2].

2.1.1.2 Momentum Equation

The momentum equation is based on Newton's second law of motion. It postulates that the fluid acceleration equals the sum of surface and body forces experienced by the fluid. Hence, the momentum equation in convective form reads

$$\rho\left(\frac{\partial u_\alpha}{\partial t}+u_\beta\frac{\partial u_\alpha}{\partial x_\beta}\right)=\frac{\partial T_{\alpha\beta}}{\partial x_\beta}-\frac{\partial p}{\partial x_\alpha}+\rho g_\alpha, \tag{2.13}$$

where p is the pressure field, g_α is the body acceleration and $T^f_{\alpha\beta}$ is the fluid stress tensor. Assuming an incompressible Newtonian fluid, the fluid stress tensor is given by

$$T_{\alpha\beta}=\mu\left(\frac{\partial u_\alpha}{\partial x_\beta}+\frac{\partial u_\beta}{\partial x_\alpha}\right), \tag{2.14}$$

where μ is the dynamic viscosity.

2.1.2 Boltzmann Equation

A fluid can be statistically described by a particle distribution function f, which depends on position $\boldsymbol{x}$, particle velocity $\boldsymbol{\xi}$ and time t. The transport process of f is described by the Boltzmann equation, which reads

$$\frac{\partial f}{\partial t}+\xi_\alpha\frac{\partial f}{\partial x_\alpha}+\frac{F_\alpha}{\rho}\frac{\partial f}{\partial \xi_\alpha}=\Omega(f). \tag{2.15}$$

This equation can be interpreted as an advection equation [54]. The first two terms are the material derivative of f and therefore describe the advection with velocity ξ. The third term is related to the acting forces. The source term on the right hand side is the collision operator $\Omega(f)$. It can be simplified by the Bhatnagar-Gross-Krook (BGK) [8] collision operator, which is commonly used to derive LBM collision operators. The BGK-Boltzmann equation reads

$$\frac{\partial f}{\partial t} + \xi_\alpha \frac{\partial f}{\partial x_\alpha} + \frac{F_\alpha}{\rho} \frac{\partial f}{\partial \xi_\alpha} = -\frac{1}{\tau}(f - f^{eq}), \tag{2.16}$$

where τ is the relaxation time and f^{eq} a distribution function at equilibrium state. Assuming a three dimensional velocity space and an ideal gas, f^{eq} is defined by the Maxwell-Boltzmann distribution

$$f^{eq} = \rho \left(\frac{m}{2\pi k_B T} \right)^{\frac{3}{2}} \exp\left(\frac{m\left(\xi - \boldsymbol{u}\right)^2}{2k_B T} \right), \tag{2.17}$$

where m is the particle mass and k_B the Boltzmann constant, $\boldsymbol{u}$ the local mean velocity and T the temperature. The macroscopic quantities of the fluid such as mass density ρ, momentum density $\rho\boldsymbol{u}$, total energy density ρE and internal energy density ρe are defined by the moments of the particle distribution function, respectively

$$\rho(\boldsymbol{x}, t) = \int f(\boldsymbol{x}, \xi, t) \mathrm{d}\xi, \tag{2.18}$$

$$\rho(\boldsymbol{x}, t)\boldsymbol{u}(\boldsymbol{x}, t) = \int \xi f(\boldsymbol{x}, \xi, t) \mathrm{d}\xi, \tag{2.19}$$

$$\rho(\boldsymbol{x}, t)E(\boldsymbol{x}, t) = \frac{1}{2} \int |\xi|^2 f(\boldsymbol{x}, \xi, t) \mathrm{d}\xi, \tag{2.20}$$

$$\rho(\boldsymbol{x}, t)e(\boldsymbol{x}, t) = \frac{1}{2} \int |\xi - \boldsymbol{u}|^2 f(\boldsymbol{x}, \xi, t) \mathrm{d}\xi. \tag{2.21}$$

In the hydrodynamic limit, the incompressible Navier-Stokes equations can be derived from the BGK-Boltzmann equation (2.16) [91].

2.1.3 Lattice Boltzmann Method

The discretization of the BGK-Boltzmann equation (2.16) in the hydrodynamic regime [53] on an equidistant Cartesian grid yields a finite number of particle distribution functions f_i. The resulting lattice is defined by d dimensions and q lattice velocities $\boldsymbol{c}_i$, $i = 0, 1, \ldots, q-1$. A commonly used descriptor set in three dimensions is $D3Q19$, where the lattice velocities $\boldsymbol{c}_i$ are defined as

$$\boldsymbol{c}_i = \begin{cases} (0,0,0) & i = 0, \\ (\pm1,0,0),\ (0,\pm1,0),\ (0,0,\pm1) & i = 1,2,\ldots,6, \\ (\pm1,\pm1,0),\ (\pm1,0,\pm1),\ (0,\pm1,\pm1) & i = 7,8,\ldots,18. \end{cases} \tag{2.22}$$

The lattice Boltzmann equation (LBE) without external forces is given by

$$f_i\left(\boldsymbol{x}^{\mathrm{LB}} + \boldsymbol{c}_i, t^{\mathrm{LB}} + 1\right) = f_i\left(\boldsymbol{x}^{\mathrm{LB}}, t^{\mathrm{LB}}\right) + \Omega_i, \tag{2.23}$$

where f_i is the particle distribution function at discrete lattice position $\boldsymbol{x}^{\mathrm{LB}}$ and time step t^{LB}. On the right hand side of Eq. (2.23) Ω_i represents the lattice collision operator, which relaxes the particle distribution functions f_i towards their corresponding discretised equilibria f_i^{eq}, under the conservation constraints for mass and momentum.

For an isothermal, weakly compressible flow, the particle distribution function at equilibrium state f_i^{eq} is described by a low Mach number truncation of the Maxwell-Boltzmann distribution (see Eq. (2.17)). It reads

$$f_i^{eq}\left(\rho^{\mathrm{LB}}, \boldsymbol{u}^{\mathrm{LB}}\right) = \rho^{\mathrm{LB}} w_i \left[1 + \frac{c_{i\alpha} u_\alpha^{\mathrm{LB}}}{c_s^2} + \frac{u_\alpha^{\mathrm{LB}} u_\beta^{\mathrm{LB}} (c_{i\alpha} c_{i\beta} - c_s^2 \delta_{\alpha\beta})}{2 c_s^4}\right], \tag{2.24}$$

where w_i are the lattice weights obtained by the Gauss-Hermite quadrature [45, 95], $c_s = 1/\sqrt{3}$ is the speed of sound of the lattice and $\delta_{\alpha\beta}$ is the Kronecker delta.

Similar to Eqs. (2.18) and (2.19), the moments of the discrete particle distribution functions f_i are used to calculate macroscopic flow quantities. The zeroth, first and second moment of f_i yield the density ρ^{LB}, momentum $\rho^{\mathrm{LB}}\boldsymbol{u}^{\mathrm{LB}}$, and momentum flux $\mathbf{\Pi}$, respectively. These discrete moments of f_i are obtained by

$$\rho^{\mathrm{LB}} = \sum_{i=0}^{q-1} f_i \,, \tag{2.25}$$

$$\rho^{\mathrm{LB}}\boldsymbol{u}^{\mathrm{LB}} = \sum_{i=0}^{q-1} \boldsymbol{c}_i f_i, \tag{2.26}$$

$$\mathbf{\Pi}_{\alpha\beta} = \sum_{i=0}^{q-1} c_{i\alpha} c_{i\beta} f_i \,. \tag{2.27}$$

A simplifed isothermal equation of state relates the pressure p^{LB} to the density ρ^{LB} through

$$p^{\mathrm{LB}} = c_s^2 \rho^{\mathrm{LB}}. \tag{2.28}$$

The lattice Mach number $\mathrm{Ma}^{\mathrm{LB}}$ is written as

$$\mathrm{Ma}^{\mathrm{LB}} = \frac{u_{char}^{\mathrm{LB}}}{c_s}, \tag{2.29}$$

where u_{char}^{LB} is the characteristic lattice velocity. In the incompressible limit ($\mathrm{Ma}^{\mathrm{LB}} \rightarrow 0$), the incompressible Navier–Stokes equations (see Eqs. (2.12) and (2.80)) are recovered.

Finally, the lattice Boltzmann algorithm is divided in 2 steps: the local collision step and the streaming step. The local collision step is described by the right-hand side of Eq. (2.23) and the subsequent streaming step is represented by the left-hand side of Eq. (2.23).

2.1.4 Collision Operators

Various collision operators for LBM have been proposed over the last decades to improve certain properties such as stability, consistency or accuracy. The following sections introduce commonly used collision operators to approximate the incompressible Navier–Stokes equations. A more detailed comparison and discussion of these collision operators for homogeneous isotropic turbulence can be found in Haussmann et al. [44].

2.1.4.1 Bhatnagar–Gross–Krook Collision Scheme

One of the oldest single relaxation time (SRT) collision operators is the Bhatnagar, Gross and Krook (BGK) [8] operator. It describes the linear relaxation towards a particle distribution function at equilibrium state. The discretization of the continuous form in Eq. (2.16) yields

$$\Omega_i = -\frac{1}{\tau}\left(f_i\left(\boldsymbol{x}^{\mathrm{LB}}, t^{\mathrm{LB}}\right) - f_i^{\mathrm{eq}}\left(\rho^{\mathrm{LB}}, \boldsymbol{u}^{\mathrm{LB}}\right)\right). \tag{2.30}$$

If Eq. (2.30) is inserted in Eq. (2.23), we obtain the BGK scheme as

$$f_i\left(\boldsymbol{x}^{\mathrm{LB}} + \boldsymbol{c}_i, t^{\mathrm{LB}} + 1\right) = f_i\left(\boldsymbol{x}^{\mathrm{LB}}, t^{\mathrm{LB}}\right) - \frac{1}{\tau}\left(f_i\left(\boldsymbol{x}^{\mathrm{LB}}, t^{\mathrm{LB}}\right) - f_i^{\mathrm{eq}}\left(\rho^{\mathrm{LB}}, \boldsymbol{u}^{\mathrm{LB}}\right)\right). \tag{2.31}$$

Within the incompressible limit, the relaxation time τ is connected to the kinematic viscosity ν^{LB} of the fluid by

$$\nu^{\mathrm{LB}} = c_s^2\left(\tau - \frac{1}{2}\right). \tag{2.32}$$

This represents an interconnection of viscosity and stability. It is well-known that the BGK operator suffers from instability at coarse grid resolutions and small viscosities, see e.g. Yasduda et al. [108] or Chen and Doolen [17]. Nathen et al. [71] showed that the instabilities originate from an increased energy at high wave numbers. In the case of fully developed turbulent channel flows, Lammers et al. [57] found a stability criterion at $y^+ < 2.5$ (see Eq. (2.67)) using an equidistant grid and a bounce back formulation for the walls.

2.1.4.2 Multiple-Relaxation-Time Collision Scheme

The lattice BGK equation can be interpreted as a special case of an LBE with multiple relaxation times (MRT) [22, 54]. Therefore, τ is replaced by a $q \times q$ matrix $\boldsymbol{S}$.

The moment vector $\boldsymbol{m}$ with q entries is calculated by multiplying the particle distribution functions $\boldsymbol{f} = \left(f_0, \ldots, f_{q-1}\right)^{\mathrm{T}}$ with the rows $\boldsymbol{M}_j$ of a regular $q \times q$ matrix $\boldsymbol{M}$. To be precise, for $j = 0, \ldots, q-1$

$$m_j = \boldsymbol{M}_j \boldsymbol{f}. \tag{2.33}$$

The vectors $\boldsymbol{M}_j^{\mathrm{T}}$ can be obtained by a Gram-Schmidt orthogonalization procedure or Hermite polynomials [54, 22, 55]. Furthermore, it can be represented as a linear combination of Hermite vectors, which allows to construct equilibrium moments for an arbitrary matrix $\boldsymbol{M}$ [54]. It is noteworthy that the column-wise arrangement of $\boldsymbol{M}$ follows the order of the velocity set [88, 22].

The equilibrium moments m_j^{eq} are similarly expressed by

$$m_j^{\mathrm{eq}} = \boldsymbol{M}_j \boldsymbol{f}^{\mathrm{eq}}. \tag{2.34}$$

Consequently, the MRT scheme [22, 54, 55] is written as

$$\boldsymbol{f}\left(\boldsymbol{x}^{\mathrm{LB}} + \mathbf{c}_i, t^{\mathrm{LB}} + 1\right) = \boldsymbol{f}\left(\boldsymbol{x}^{\mathrm{LB}}, t^{\mathrm{LB}}\right) - \boldsymbol{M}^{-1}\boldsymbol{S}\left[\boldsymbol{m}\left(\boldsymbol{x}^{\mathrm{LB}}, t^{\mathrm{LB}}\right) - \boldsymbol{m}^{\mathrm{eq}}\left(\boldsymbol{x}^{\mathrm{LB}}, t^{\mathrm{LB}}\right)\right]. \tag{2.35}$$

Applying a $D3Q19$ velocity set, d'Humières et al. [22] proposed a moment vector

$$\boldsymbol{m} = \left(\rho^{\mathrm{LB}}, e, e^2, j_x, q_x, j_y, q_y, j_z, q_z, 3\sigma_{xx}, 3\pi_{xx}, \sigma_{ww}, \pi_{ww}, \sigma_{xy}, \sigma_{yz}, \sigma_{xz}, n_x, n_y, n_z\right)^{\mathrm{T}}, \tag{2.36}$$

where m_0, m_3, m_5 and m_7 represent the density and the momentum flux. The moments $m_1 = e$ and $m_2 = e^2$ are internal energy, respectively the squared internal energy, whereas $m_4 = q_x$, $m_6 = q_y$ and $m_8 = q_z$ are heat flux components. The symmetric traceless viscous stress tensor is given by $m_9 = 3\sigma_{xx}$, $m_{11} = \sigma_{ww} = \sigma_{yy} - \sigma_{zz}$, $m_{13} = \sigma_{xy}$, $m_{14} = \sigma_{yz}$ and $m_{15} = \sigma_{xz}$. The remaining five moments of higher polynomial order, $m_{10} = 3\pi_{xx}$, $m_{12} = \pi_{ww}$, $m_{16} = n_x$, $m_{17} = n_y$ and $m_{18} = n_z$, can be symmetrically traced back to parts of tensors corresponding to products of the previously mentioned moments [22].

The according diagonal collision matrix is defined as

$$\boldsymbol{S} = \mathrm{diag}\left(0, \omega_1, \omega_2, 0, \omega_4, 0, \omega_4, 0, \omega_4, \omega_9, \omega_{10}, \omega_9, \omega_{10}, \omega_{13}, \omega_{13}, \omega_{13}, \omega_{16}, \omega_{16}, \omega_{16}\right), \quad (2.37)$$

where the relaxation frequencies of the conserved moments ρ^{LB} and $\boldsymbol{j} = \rho^{\mathrm{LB}}\boldsymbol{u}^{\mathrm{LB}}$ yields $S_0 = S_3 = S_5 = S_7 = 0$. The relaxation frequencies ω_1, ω_9 and ω_{13} corresponding to the relaxation of e, diagonal and off-diagonal entries of $\boldsymbol{\sigma}$, are connected to kinematic and bulk viscosity via

$$\nu^{\mathrm{LB}} = c_s^2\left(\frac{1}{\omega_9} - \frac{1}{2}\right) = c_s^2\left(\frac{1}{\omega_{13}} - \frac{1}{2}\right), \quad \nu_{\mathrm{B}}^{\mathrm{LB}} = \frac{2}{3}c_s^2\left(\frac{1}{\omega_1} - \frac{1}{2}\right). \quad (2.38)$$

The relaxation frequency according the kinemtic viscosity is given by $\omega_9 = \omega_{13} = \frac{1}{\tau}$. The remaining adjustable parameters have been optimized with local analysis in Fourier space with respect to the tested Reynolds numbers: $\omega_1 = 1.19$, $\omega_2 = \omega_{10} = 1.4$, $\omega_4 = 1.2$ and $\omega_{16} = 1.98$ [22, 56].

The major advantage of MRT is the maximum number of tunable relaxation times and equilibrium populations [22]. Thus, multiple possibilities exist to influence the stability and the physical behavior. The MRT scheme claimed to avoid the upcoming instabilities as they occur for BGK at low resolutions [55, 22]. Nevertheless, disadvantages were identified by Nathen et al. [71], who showed that instabilities appear at high Reynolds numbers and fine grids.

2.1.4.3 Two-Relaxation-Time Collision Scheme

The two-relaxation-time (TRT) scheme was proposed by Ginzburg et al. [41] to circumvent the complexity of optimizing several relaxation rates. The basic idea is to relax the moments in $\boldsymbol{m}$ either with the lattice relaxation time $\omega^+ = \frac{1}{\tau^+} = \frac{1}{\tau}$ or with a second relaxation time $\omega^- = \frac{1}{\tau^-}$, depending on the underlying polynomial degree. Moments with an even order are relaxed with ω^+ and moments with an odd order are relaxed with ω^-.

The equilibrium distribution is parted into a symmetric and an antisymmetric contribution

$$f_i^{\text{eq}+} = \frac{1}{2}\left(f_i^{\text{eq}} + f_{\bar{i}}^{\text{eq}}\right), \tag{2.39}$$

$$f_i^{\text{eq}-} = \frac{1}{2}\left(f_i^{\text{eq}} - f_{\bar{i}}^{\text{eq}}\right), \tag{2.40}$$

where the index $\bar{i}$ denotes the opposite direction $\mathbf{c}_{\bar{i}} = -\mathbf{c}_i$ in the lattice. Similarly, the decomposition of the particle distributions is

$$f_i^+ = \frac{1}{2}\left(f_i + f_{\bar{i}}\right), \tag{2.41}$$

$$f_i^- = \frac{1}{2}\left(f_i - f_{\bar{i}}\right). \tag{2.42}$$

The TRT scheme describes the relaxation to the antisymmetric and symmetric non-equilibrium populations separately with relaxation rates ω^- and ω^+. It is written as

$$f_i\left(\boldsymbol{x}^{\text{LB}} + \mathbf{c}_i, t^{\text{LB}} + 1\right) = f_i - \omega^+\left(f_i^+ - f_i^{\text{eq}+}\right) - \omega^-\left(f_i^- - f_i^{\text{eq}-}\right). \tag{2.43}$$

The decoupling of stability from viscosity is obtained through the individual relaxation of even and odd order moments. This leads to larger stability regions of TRT in comparsion to BGK [40].

Ginzburg et al. [40, 41] summarized the stability increasing properties of the

TRT scheme based on the so-called “magic parameter”,

$$\Lambda = \left(\frac{1}{\omega^+} - \frac{1}{2}\right)\left(\frac{1}{\omega^-} - \frac{1}{2}\right). \tag{2.44}$$

Krüger et al. [54] recommended to keep the value for Λ constant, when the viscosity is changed through $\tau^+ = \tau$ in Eq. (2.32). Consequently, the magnitude ratio of τ^- to τ^+ is calculated according to Eq. (2.44) and should maintain the desired TRT solution behavior throughout the choices of ν^{LB}. A “magic parameter” of $\Lambda = 0.25$ is recommended because of its stability properties [40].

2.1.4.4 Regularized Lattice Boltzmann Collision Scheme

Another attempt to increase the stability of the BGK scheme is the regularized lattice Boltzmann (RLB) scheme proposed by Latt et al. [58].

Hereby, the non-equilibrium part f_i^{neq} of the particle distribution function $f_i = f_i^{\mathrm{eq}} + f_i^{\mathrm{neq}}$ is regularized according to

$$f_i^{\mathrm{neq}} \approx f_i^{(1)} = \frac{w_i}{2c_s^4}\left(c_{i\alpha}c_{i\beta} - c_s^2\delta_{\alpha\beta}\right)\sum_{j=0}^{q} c_{j\alpha}c_{j\beta}f_j^{\mathrm{neq}}. \tag{2.45}$$

Hence, the regularization of Eq. (2.31) is written as

$$f_i\left(\boldsymbol{x}^{\mathrm{LB}} + \mathbf{c}_i, t^{\mathrm{LB}} + 1\right) = f_i^{\mathrm{eq}}\left(\boldsymbol{x}^{\mathrm{LB}}, t^{\mathrm{LB}}\right) + \left(1 - \frac{1}{\tau}\right) f_i^{(1)}\left(\boldsymbol{x}^{\mathrm{LB}}, t^{\mathrm{LB}}\right). \tag{2.46}$$

It is worth mentioning that Eq. (2.45) can be calculated purely locally and therefore maintains computational efficiency.

Moreover, Latt et al. [58] showed the equivalence of Eq. (2.46) to an MRT formulation, where the hydrodynamic moments for density ρ^{LB}, momentum $\rho^{\mathrm{LB}}\boldsymbol{u}^{\mathrm{LB}}$ and momentum flux $\mathbf{\Pi}$ are relaxed with $\frac{1}{\tau}$, whereas the kinetic moments are relaxed with a relaxation time of one. As a result, the RLB scheme has an increased stability in case of large pressure gradient problems and turbulent flows.

2.1.4.5 Entropic Lattice Boltzmann Collision Scheme

The Maxwell–Boltzmann equilibrium distribution approximation in Eq. (2.24) violates Boltzmann's $\mathscr{H}$-theorem. [4]

Nevertheless, the $\mathscr{H}$-functional has a convex-composed, discrete velocity counterpart

$$H(\boldsymbol{f}) = \sum_{i=0}^{q-1} f_i \ln\left(\frac{f_i}{w_i}\right), \tag{2.47}$$

upholding the second law of thermodynamics [10]. $H(\boldsymbol{f})$ is minimized with respect to the conservation constraints for mass and momentum by [10, 3]

$$\check{f}_i^{\mathrm{eq}} := \operatorname{argmin}_{\boldsymbol{f}} H(\boldsymbol{f}) = \rho^{\mathrm{LB}} w_i \prod_{\alpha=1}^{d} \left(2 - \sqrt{1 + 2(u_\alpha^{\mathrm{LB}})^2}\right) \left(\frac{2u_\alpha^{\mathrm{LB}} + \sqrt{1 + 3(u_\alpha^{\mathrm{LB}})^2}}{1 - u_\alpha^{\mathrm{LB}}}\right)^{c_{i\alpha}}. \tag{2.48}$$

Additionaly, a viscosity related parameter b [18] is calculated as

$$b = \frac{1}{6\nu^{\mathrm{LB}} + 1} = \frac{1}{2\tau} \in (0, 1]. \tag{2.49}$$

Hence, the entropic lattice Boltzmann (ELB) scheme is written as

$$f_i\left(\boldsymbol{x}^{\mathrm{LB}} + \mathbf{c}_i, t^{\mathrm{LB}} + 1\right) = f_i\left(\boldsymbol{x}^{\mathrm{LB}}, t^{\mathrm{LB}}\right) + ab\left(\check{f}_i^{\mathrm{eq}}\left(\boldsymbol{x}^{\mathrm{LB}}, t^{\mathrm{LB}}\right) - f_i\left(\boldsymbol{x}^{\mathrm{LB}}, t^{\mathrm{LB}}\right)\right). \tag{2.50}$$

The over-relaxation parameter $a > 0$ is defined as the non-trivial root of the isentropic condition [10]

$$H\left(f_i + a\left(\check{f}_i^{\mathrm{eq}} - f_i\right)\right) = H(f_i). \tag{2.51}$$

Eqs. (2.48) and (2.51) have to be estimated in every time step. The latter is nonlinear and typically solved iteratively using the Newton–Raphson method [18]. The ELB scheme can be interpreted as an SGS model and an according turbulent viscosity expression was derived by Malaspinas et al. [64]. If a is chosen to $a = 2$, the ELB scheme is equivalent to the BGK scheme [18].

2.2 Large-Eddy Simulation

As already mentioned at the beginning of this chapter, the small scales of turbulence can be seen as homogeneous, isotropic and universal. In contrast, the large scales are anistropic and inhomogeneous. The idea of LES is to differentiate between these large and small scales by simulating the large eddies and modeling the small scales. For better comprehension, Figure 2.2 shows a model DNS and LES energy spectrum. The small wave numbers $\kappa < \kappa_{\text{cut-off}}$ describe the resolved scales that are simulated and the high wave numbers $\kappa > \kappa_{\text{cut-off}}$ are the unresolved small scales that have to be modeled. The separation of the resolved and unresolved scales should take place in the inertial subrange, so that the eddies in the energy-containing range are simulated and only the dissipative motion needs to be modeled. Hence, the main function of the LES modeling terms is the description of the dissipation of the turbulent kinetic energy. Especially the

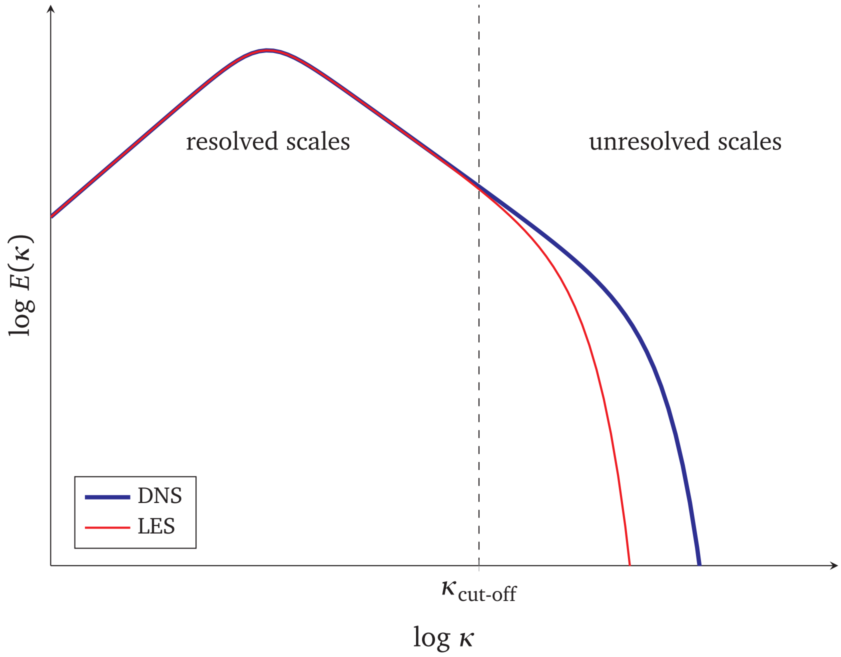

Figure 2.2: *DNS and LES model spectrum of the turbulent kinetic energy*

fact that energy is transported on average from the large to the small scales and the universal character of the small scales is used.

First, this section introduces the filtered Navier–Stokes equations that have to be solved for LES. Next, the filtered lattice Boltzmann equation is described. Afterwards, LBM implementations of distinct SGS approaches are shown. Finally, the concept of near-wall modeled (NWM) and near-wall resolved (NWR) approaches in LBM for addressing wall-bounded turbulence is discussed.

2.2.1 Filtered Navier–Stokes Equations

The velocity field is decomposed into a filtered part $\overline{\boldsymbol{u}}$ and an SGS part $\boldsymbol{u}^{\mathrm{SGS}}$. This decomposition reads

$$\boldsymbol{u}(\boldsymbol{x},t)=\overline{\boldsymbol{u}}(\boldsymbol{x},t)+\boldsymbol{u}^{\mathrm{SGS}}(\boldsymbol{x},t). \tag{2.52}$$

Analogously, the pressure field is parted in a filtered contribution $\overline{p}$ and an SGS part p^{SGS}. A general filtering operation can be written as

$$\overline{\boldsymbol{u}}(\boldsymbol{x},t)=\int G(\boldsymbol{r},\boldsymbol{x})\boldsymbol{u}(\boldsymbol{x}-\boldsymbol{r},t)\mathrm{d}\boldsymbol{r}, \tag{2.53}$$

where G is the filter operation and $\boldsymbol{r}$ the radial coordinate. Common filter operations are box filter, Gausian filter, or the spectral cut-off filter. If no explicit filter is applied, the discretization itself can be seen as an implicit filter operation with constant filter width Δx. Hereby, the filter operation G is not known and additionally the filter is time dependent [29]. Using the decomposition Eq. (2.52) to Eq. (2.12), the filtered incompressible Navier–Stokes continuity equation reads

$$\frac{\partial \overline{u}_\alpha}{\partial x_\alpha}=0, \tag{2.54}$$

and the momentum equation without body force according Leonard's decomposition [60] is given by

$$\frac{\partial \overline{u}_\alpha}{\partial t} + \frac{\partial \overline{u}_\alpha \overline{u}_\beta}{\partial x_\beta} = \nu \frac{\partial}{\partial x_\beta} \left(\frac{\partial \overline{u}_\alpha}{\partial x_\beta} + \frac{\partial \overline{u}_\beta}{\partial x_\alpha} \right) - \frac{\partial T^{\mathrm{SGS}}_{\alpha\beta}}{\partial x_\beta} - \frac{1}{\rho} \frac{\partial \overline{p}}{\partial x_\alpha}, \tag{2.55}$$

where $T^{\mathrm{SGS}}_{\alpha\beta}$ is the SGS stress tensor. The tensor $T^{\mathrm{SGS}}_{\alpha\beta}$ is expressed as

$$T^{\mathrm{SGS}}_{\alpha\beta} = \overline{u_\alpha u_\beta} - \overline{u}_\alpha \overline{u}_\beta \tag{2.56}$$

Therefore, it can be interpreted as the effect of unresolved fluctuations on the resolved motion. This SGS stress tensor is not known and must be modeled to close the set of filtered incompressible Navier–Stokes equations.

2.2.1.1 Filtered Lattice Boltzmann Method

Applying the filtering operation to the Boltzmann equation (2.15) and subsequent discretization, the filtered lattice Boltzmann equation without external forces [50] is given by

$$\overline{f}_i \left(\boldsymbol{x}^{\mathrm{LB}} + \boldsymbol{c}_i, t^{\mathrm{LB}} + 1 \right) = \overline{f}_i \left(\boldsymbol{x}^{\mathrm{LB}}, t^{\mathrm{LB}} \right) + \overline{\Omega}_i, \tag{2.57}$$

where $\overline{f}_i$ is the filtered particle distribution function. The filtered collision operator $\overline{\Omega}_i$ can be implemented by a single-relaxation time model proposed by the BGK collision operator (see Section 2.1.4.1). It reads

$$\overline{\Omega}_i = -\frac{1}{\tau^{eff}} \left(\overline{f}_i(\boldsymbol{x}^{\mathrm{LB}}, t^{\mathrm{LB}}) - \overline{f}^{eq}_i(\overline{\rho}^{\mathrm{LB}}, \overline{\boldsymbol{u}}^{\mathrm{LB}}) \right), \tag{2.58}$$

where τ^{eff} is the effective relaxation time towards the filtered discrete particle distribution function at equilibrium state $\overline{f}^{eq}_i$, $\overline{\rho}^{\mathrm{LB}}$ is the filtered lattice density and $\overline{\boldsymbol{u}}^{\mathrm{LB}}$ the filtered lattice velocity field. The equilibrium distribution function $\overline{f}^{eq}_i$ and the moments of $\overline{f}_i$, the density $\overline{\rho}^{\mathrm{LB}}$, the momentum $\overline{\rho}^{\mathrm{LB}} \overline{\boldsymbol{u}}^{\mathrm{LB}}$ and the momentum flux $\overline{\boldsymbol{\Pi}}$ are calculated according to Eqs. (2.25), (2.26) and (2.27) by replacing f_i by $\overline{f}_i$.

2.2.2 Subgrid-Scale Models

The main idea of an SGS model is to describe the interaction of the unresolved flow patterns with the resolved ones. It is therefore necessary to introduce a certain amount of dissipation to dissipate as much energy as a DNS of the same configuration. The influence of an SGS model is visible in spectral space, as depicted in Figure 2.2. Beyond the cut-off wave number $\kappa_{\text{cut-off}}$, which means on smaller scales, the SGS model in a LES causes a much faster energy dissipation compared to a DNS. A reliable SGS model should then provide accurate statistics of the resolved energy-containing scales of motion. The choice of a suitable LES depends largely on the filter width and the flow type. This is often a compromise between accuracy and computational demand.

2.2.2.1 Eddy Viscosity Models

In order to close Eq. (2.55), the SGS stress tensor is described using the linear eddy viscosity hypothesis [12]. Hence, the SGS stress tensor reads

$$T_{\alpha\beta}^{\text{SGS}} = -\nu^{\text{SGS}} \left(\frac{\partial \overline{u}_\alpha}{\partial x_\beta} + \frac{\partial \overline{u}_\beta}{\partial x_\alpha} \right), \tag{2.59}$$

where ν^{SGS} is the SGS viscosity.

Eddy viscosity models are often introduced in LBM by adding the turbulent viscosity to the molecular viscosity [50], which results in an effective viscosity

$$\nu^{\text{LB},eff} = \nu^{\text{LB}} + \nu^{\text{LB,SGS}}. \tag{2.60}$$

A consistent approach to implement eddy viscosity models in LBM was derived by Malaspinas and Sagaut [66]. They presented that due to the connection between lattice viscosity and lattice relaxation time (see Eq. (2.32)), the relaxation time is also divided in a molecular and an SGS contribution

$$\tau^{eff} = \tau + \tau^{\text{SGS}}, \tag{2.61}$$

where $\tau^{\mathrm{SGS}} = \frac{\nu^{\mathrm{LB,SGS}}}{c_s^2}$ is the eddy contribution. The eddy viscosity ν^{SGS} in Eq. (2.60) is evaluated by an SGS viscosity model, which can be generally written in lattice units as

$$\nu^{\mathrm{LB,SGS}} = (C_M \Delta_{grid}^{\mathrm{LB}})^2 D_M, \tag{2.62}$$

where C_M is a model coefficient, $\Delta_{grid}^{\mathrm{LB}}$ is the lattice grid filter and D_M a model-related operator.

Smagorinsky Model The probably most popular SGS viscosity models is the Smagorinsky model [98]. The according model operator is defined as

$$D_M = \sqrt{2\overline{S}_{\alpha\beta}^{\mathrm{LB}}\overline{S}_{\alpha\beta}^{\mathrm{LB}}}, \tag{2.63}$$

where $\overline{S}_{\alpha\beta}$ is the filtered strain rate. The literature values for the Smagorinsky-Lilly model constant C_M are in the range of $0.065 \leq C_M \leq 0.24$ [67, 87]. For a complex turbulent flow, a Smagorinsky-Lilly constant of $C_M = 0.1$ is a common choice [29]. There are several possibilities in the LBM framework to estimate the filtered strain rate $\overline{S}_{\alpha\beta}^{\mathrm{LB}}$. The first one is the approximation of the velocity gradient by a finite difference scheme. Another approach is the local estimation of the filtered strain rate by

$$\overline{S}_{\alpha\beta}^{\mathrm{LB}} = -\frac{\overline{\Pi}_{\alpha\beta}^{neq}}{2\overline{\rho}^{\mathrm{LB}}\tau^{eff}c_s^2}, \tag{2.64}$$

where $\overline{\Pi}_{\alpha\beta}^{neq}$ is the second moment of the non-equilibrium parts of the particle distribution function, which can be calculated according to Eq. (2.27) by replacing $\overline{f}_i$ with $\overline{f}_i^{neq} = (\overline{f}_i - \overline{f}_i^{eq})$. This leads to an implicit relation of the effective relaxation time τ^{eff} and the filtered strain rate $\overline{S}_{\alpha\beta}^{\mathrm{LB}}$. Therefore, Malaspinas and Sagaut [66] proposed an explicit expression for the Bhatnagar–Gross–Krook (BGK) collision operator. This explicit expression for determining the effective relaxation time τ^{eff} is calculated by

$$\tau^{eff} = \sqrt{\tau^2 + \frac{2(C_M\Delta_{grid}^{\mathrm{LB}})^2}{\overline{\rho}^{\mathrm{LB}}c_s^4}\sqrt{2\overline{\Pi}_{\alpha\beta}^{neq}\overline{\Pi}_{\alpha\beta}^{neq}}} + \frac{\tau}{2}, \tag{2.65}$$

where the lattice grid filter $\Delta^{\mathrm{LB}}_{grid}$ corresponds to the lattice grid spacing Δx^{LB}, i.e. $\Delta^{\mathrm{LB}}_{grid} = 1$.

Smagorinsky Model with Van Driest Damping It is well known that the Smagorinsky model suffers from a too dissipative behavior in the near-wall region [72, 39, 85]. One possibility to circumvent this drawback is the introduction of a damping function that reduces the SGS viscosity depending on the wall distance. The van Driest damping function [23] can be incorporated in the grid filter $\Delta^{\mathrm{LB}}_{grid}$ by

$$\Delta^{\mathrm{LB}}_{grid} = \min\left[1,\ \frac{\kappa y^{\mathrm{LB}}}{C_\Delta}\left(1 - e^{(-\frac{y^+}{A^+})}\right)\right], \tag{2.66}$$

where y^{LB} is the lattice wall distance, $A^+ = 26$ is the van Driest parameter, $C_\Delta = 0.158$ is a model constant and $\kappa = 0.41$ is the von Kármán constant [69]. The dimensionless wall distance y^+ in Eq. (2.66) is defined as

$$y^+ = \frac{u^{\mathrm{LB}}_\tau y^{\mathrm{LB}}}{\nu^{\mathrm{LB}}}, \tag{2.67}$$

where $u^{\mathrm{LB}}_\tau = \sqrt{\frac{T^{\mathrm{LB}}_w}{\rho^{\mathrm{LB}}}}$ is the friction velocity and T^{LB}_w the wall shear stress.

Further examples of Smagorinsky based SGS models are the dynamic Smagorinsky model [39] implemented by Premnath et al. [80] and the shear-improved Smagorinsky model realized by Leveque et al. [61].

Wall-Adapting Local Eddy-Viscosity Model The wall-adapting local eddy-viscosity (WALE) model [72] is able to adapt the dissipation near the wall without using a wall-damping function. The model is based on the calculation of the resolved velocity gradient tensor $\partial \overline{u}^{\mathrm{LB}}_\alpha / \partial x^{\mathrm{LB}}_\beta$. The model parameter D_M is written as

$$D_M = \frac{\left(G^{\mathrm{LB}}_{\alpha,\beta} G^{\mathrm{LB}}_{\alpha,\beta}\right)^{1.5}}{\left(\overline{S}^{\mathrm{LB}}_{\alpha\beta} \overline{S}^{\mathrm{LB}}_{\alpha\beta}\right)^{2.5} + \left(G^{\mathrm{LB}}_{\alpha,\beta} G^{\mathrm{LB}}_{\alpha,\beta}\right)^{1.25}}. \tag{2.68}$$

Hereby, $G^{\mathrm{LB}}_{\alpha,\beta}$ is the traceless symmetric part of the squared resolved velocity gradient, which is given by

$$G^{\mathrm{LB}}_{\alpha,\beta} = \frac{1}{2}\left[\left(\frac{\partial \overline{u}^{\mathrm{LB}}_{\alpha}}{\partial x^{\mathrm{LB}}_{\beta}}\right)^2 + \left(\frac{\partial \overline{u}^{\mathrm{LB}}_{\beta}}{\partial x^{\mathrm{LB}}_{\alpha}}\right)^2\right] - \frac{1}{3}\delta_{\alpha\beta}\left(\frac{\partial \overline{u}^{\mathrm{LB}}_{\gamma}}{\partial x^{\mathrm{LB}}_{\gamma}}\right)^2 . \tag{2.69}$$

Weickert et al. [106] use a central finite difference scheme to explicitly obtain the filtered strain rate $\overline{S}^{\mathrm{LB}}_{\alpha\beta}$ and $G^{\mathrm{LB}}_{\alpha,\beta}$. The model constant in the range of $0.45 \leq C_M \leq 0.5$ are recommended for homogeneous isotropic turbulence.

There are several advantages of the WALE model. Firstly, it is able to predict correctly the behavior near the wall, $\nu^{\mathrm{LB,SGS}} \propto (y^+)^3$. Furthermore, no additional explicit filtering procedure is required compared to the dynamic Smagorinsky models [39]. In a laminar shear flow the turbulent viscosity is correctly reduced to zero. Hence, the model can be used to describe relaminarization or transition to turbulence [86].

2.2.2.2 Approximate Deconvolution Model

The main idea of the approximate deconvolution model (ADM) [99] is the reconstruction of sub-grid quantities by using the filtered resolved quantities. Therefore, an inverse filtering operation (deconvolution) is used. Since the deconvolution requires information of the sub-grid scales, the reconstruction is only approximate. Sagaut [90] and Malsapinas and Sagaut [65] introduced the ADM to the LBM framework. In the following an ADM-LBM approach using viscosity filters [102, 84, 65], which was proposed by Nathen et al. [70], is presented. The ADM-LBM algorithm consists of three steps: a standard BGK collsion step (right hand side of Eq. (2.23)), a subsequent streaming step (left hand side of Eq. (2.23)) and an explicit filter operation. This explicit filter operation is calculated by

$$\mathcal{Q} * \mathcal{G} * \hat{f}_i = -\sigma(\boldsymbol{x}^{\mathrm{LB}}, t^{\mathrm{LB}}) \sum_{j=1}^{D} \sum_{m=-M}^{M} d_m \hat{f}_i(\boldsymbol{x}^{\mathrm{LB}} + m\boldsymbol{e}_j, t^{\mathrm{LB}}), \tag{2.70}$$

where $\mathcal{Q} * \mathcal{G} * \hat{f}_i$ is the inverse filter operation, $\boldsymbol{e}$ the Cartesian basis vectors and M the filter stencil size. The filter weighting coefficients d_m for the selective viscosity filter of order $M = 2$ are $d_0 = 6/16$, $d_1 = -4/16$ and $d_2 = 1/16$. The coefficents for other orders can be found by Malaspinas and Sagaut [65]. The filter strength is estimated by

$$\sigma(\boldsymbol{x}^{\mathrm{LB}}, t^{\mathrm{LB}}) = \left(|S_{\alpha\beta}^{\mathrm{LB}}(\boldsymbol{x}^{\mathrm{LB}}, t^{\mathrm{LB}}) - \langle S_{\alpha\beta}^{\mathrm{LB}}(\boldsymbol{x}^{\mathrm{LB}}, \tilde{t}^{\mathrm{LB}}) \rangle | \right) \sqrt{\left(\frac{2\rho^{\mathrm{LB}} c_s^2}{|\Pi_{\alpha\beta}^{neq}|} \right)}, \tag{2.71}$$

where $\langle S_{\alpha\beta}^{\mathrm{LB}}(\boldsymbol{x}^{\mathrm{LB}}, \tilde{t}^{\mathrm{LB}}) \rangle$ is the phase averaged strain rate. The filter strength is estimated locally without using finite differences.

In comparison to an eddy viscosity model no additional model parameters are introduced that depend on the flow configuration and the mesh size. Furthermore, ADM is able to take backscatter into account in a physical way [86].

2.2.3 Wall Bounded Turbulence

In the case of wall-bounded turbulence the size of the energy-containing eddies is drastically reduced. However, the emerging coherent structures influence the behavior of the flow in the vicinity of the wall. The two different approaches to deal with the phenomena of wall-bounded turbulence are described in the following.

2.2.3.1 Near-Wall Resolved Large-Eddy Simulation

In a near-wall resolved large-eddy simulation (NWR-LES) all energy containg scales near to the walls are resolved, which means that the grid and the filter are fine enough to resolve 80% of the energy everywhere [77]. The chosen SGS model for NWR-LES should be able to describe the wall-near behavior. If the scaling laws of the turbulent boundary layer are taken into account, the amount of grid points is in $\mathcal{O}(\mathrm{Re}_L^{1.8})$ in the wall-near region, while it is only in $\mathcal{O}(\mathrm{Re}_L^{0.4})$ in the outer region [15]. Considering the time step scaling, the neceassary runtime $t_{calc,\text{NWR-LES}}$ [29] is given by

$$t_{calc,\text{NWR-LES}} \sim \mathrm{Re}_L^{2.7}. \tag{2.72}$$

A recommendation for the grid spacing in the wall-near region is $\Delta y^+ \leq 2$ [15, 76].

2.2.3.2 Near-Wall Modeled Large-Eddy Simulation

The near-wall modeled large-eddy simulation (NWM-LES) approach circumvents the high computational demand for higher Reynolds numbers (see Eq. (2.72)) by modeling the effects of the turbulent boundary layer. As a consequence, the energy-containing scales are only resolved remote from the wall. The required calculation runtime $t_{calc,\text{NWM-LES}}$ [29] is therefore drastically reduced to

$$t_{calc,\text{NWM-LES}} \sim \mathrm{Re}_L^{0.53}. \tag{2.73}$$

The grid spacing is usually chosen, so that the first grid point is located in the logarithmic layer $30 \leq \Delta y^+ \leq 150$ [76]. NWM-LES is commonly based on an empirical wall function [59, 107, 93] to describe the velocity profile in the turbulent boundary layer. This wall function is needed to correctly describe the otherwise strongly underestimated high velocity gradient near the wall.

In LBM, wall models for turbulent flows were initially investigated in the context of a two-equation RANS model [103, 28]. NWM-LES was introduced into the LBM framework by Malaspinas and Sagaut [62]. They used the MRT collision operator for the wall function model. Schneider [94] used the MRT-LES approach coupled with a three equations model based on the Werner and Wengle function [107]. A cumulant LBM [34] approach was proposed by Pasquali et al. [74] to obtain the required velocity information in a local manner suitable for GPUs.

Haussmann et al. [42] adapted the approach of Malaspinas and Sagaut [62] to the BGK collision operator and evaluated different boundary schemes and wall functions. Furthermore, they incorporate an curved boundary formulation in the wall model approach [43]. The following listing summarizes and unifies the proposed algorithms.

1. The velocity of the first cell in discrete normal direction $\overline{\boldsymbol{u}}_n^{\mathrm{LB}}$ that is not part of the boundary scheme is calculated according to Eq. (2.27).

2. The distance to the boundary y_{bc}^{LB} is defined in the discrete normal direction $\boldsymbol{c}_n$. It is worth mentioning that in common wet-node approaches the physical boundary and the simulation domain are the same. In the case of a wall function the distance of the boundary cell to the physical boundary y_{bc}^{LB} is changed. The choice of $y_{bc} = 0.5\Delta x^{\mathrm{LB}}|\boldsymbol{n}|$ leads to accurate results [42]. Accordingly, the distance from the neighbor fluid node at position $\boldsymbol{x}_n^{\mathrm{LB}}$ to the boundary is given by

$$y_n^{\mathrm{LB}} = y_{bc}^{\mathrm{LB}} + |\boldsymbol{c}_n|. \tag{2.74}$$

3. The applied wall profile uses only the stream-wise velocity component, a local stream-wise unit vector $\mathbf{e}_s$ is obtained by

$$\boldsymbol{e}_s = \frac{\overline{\boldsymbol{u}}_n^{\mathrm{LB}} - (\overline{\boldsymbol{u}}_n^{\mathrm{LB}} \cdot \boldsymbol{c}_n)\boldsymbol{c}_n}{|\overline{\boldsymbol{u}}_n^{\mathrm{LB}} - (\overline{\boldsymbol{u}}_n^{\mathrm{LB}} \cdot \boldsymbol{c}_n)\boldsymbol{c}_n|}. \tag{2.75}$$

4. Hence, the stream-wise component $\overline{u}_{n,\parallel}^{\mathrm{LB}}$ of $\overline{\mathbf{u}}_{n}^{\mathrm{LB}}$ can be calculated by
$$\overline{u}_{n,\parallel}^{\mathrm{LB}} = \overline{\boldsymbol{u}}_{n}^{\mathrm{LB}} \cdot \mathbf{e}_s. \tag{2.76}$$

5. The boundary distance y_n^{LB} and the stream-wise velocity component $\overline{u}_{n,\parallel}^{\mathrm{LB}}$ are used to obtain the averaged wall shear stress $\tilde{T}_w^{\mathrm{LB}}$. Hereby, different wall function formulations can be used. According to the work of Haussmann et al. [42], the use of the Musker profile [68] or a three layer model proposed by Schmitt [93] leads to accurate results. Subsequently, the stream-wise component $\tilde{u}_{bc,\parallel}^{\mathrm{LB}}$ of $\tilde{\boldsymbol{u}}_f^{\mathrm{LB}}$ is calculated by the chosen wall function using the boundary distance y_{bc}^{LB} and the averaged wall shear stress $\tilde{T}_w^{\mathrm{LB}}$.

6. Then, the velocity $\tilde{\boldsymbol{u}}_{bc}^{\mathrm{LB}}$ of the boundary node is computed by
$$\tilde{\boldsymbol{u}}_{bc}^{\mathrm{LB}} = \mathbf{e}_s \tilde{u}_{bc,\parallel}^{\mathrm{LB}}. \tag{2.77}$$

7. Next, a velocity boundary scheme is used to reconstruct the particle distribution function at node position $\boldsymbol{x}_{bc}^{\mathrm{LB}}$. In the case of a straight boundary orientation the wet node scheme proposed by Guo et al. [112] can be used to impose $\tilde{\boldsymbol{u}}_{bc}^{\mathrm{LB}}$. A curved boundary formulation can be obtained by the scheme of Bouzidi et al. [13]. Thereby a velocity correction step is required instead of an additional velocity term in the boundary scheme, because the velocity $\tilde{\boldsymbol{u}}_{bc}^{\mathrm{LB}}$ should be set on the position of $\boldsymbol{x}_{bc}^{\mathrm{LB}}$ and not on the physical wall.

8. The effective relaxation time τ^{eff} is calculated according a suitable SGS model, see Section 2.2.2.

9. Finally, the stream and collide algorithm is applied according Eq. (2.57).

This algorithm is expandable to further collision operators, SGS models, velocity boundary formulations and wall functions by altering the corresponding steps.

2.3 Reynolds-Averaged Navier–Stokes

In RANS models, the entire turbulence spectrum is described by a few quantities [29]. As a result, a high degree of modeling is taken into account. In contrast to LES and DNS, the flow quantities are time averaged. If statistically stationary flows are addressed with RANS, the reduction of the dimensions is possible for symmetric flow problems. RANS is known to be a grid independent physical system, which means that the spatial discretization has only a low influence on the solution. The main advantage of RANS is the faster computation time due to its used assumptions. Especially the time-averaging process in DNS and LES requires an averaging procedure over a long time span. RANS avoids this problem by swapping the order of averaging and simulation. Due to the complexity of turbulent phenomena, a single RANS model may not be able to describe all canonical flow types with sufficient precision. Therefore, turbulence models using RANS should be seen as an engineering approximation instead of a scientific law [27].

This section starts with an introduction of the Reynolds-averaged Navier–Stokes equations. Then, the group of turbulent viscosity models are described. As an example, the two-equation k-ε model and its corresponding implementation for LBM are outlined.

2.3.1 Reynolds-Averaged Navier–Stokes Equations

The Reynolds decomposition [82] for the velocity $\boldsymbol{u}$ reads

$$\boldsymbol{u}(\boldsymbol{x},t) = \langle \boldsymbol{u} \rangle(\boldsymbol{x}) + \boldsymbol{u}'(\boldsymbol{x},t), \tag{2.78}$$

where $\langle \boldsymbol{u} \rangle$ is the time-averaged contribution and $\boldsymbol{u}'$ the fluctuation component. In the same way, the pressure field is decomposed in a time-averaged contribution $\langle p \rangle$ and a fluctuation part p'.

By applying the Reynolds decomposition Eq. (2.78) to Eq. (2.12), the Reynolds-averaged incompressible Navier–Stokes continuity equation [82] reads

$$\frac{\partial \langle u_\alpha \rangle}{\partial x_\alpha} = 0, \tag{2.79}$$

and the according momentum equation without body force is given by

$$\frac{\partial \langle u_\alpha \rangle}{\partial t} + \frac{\partial \langle u_\alpha \rangle \langle u_\beta \rangle}{\partial x_\beta} = \nu \frac{\partial}{\partial x_\beta} \left(\frac{\partial \langle u_\alpha \rangle}{\partial x_\beta} + \frac{\partial \langle u_\beta \rangle}{\partial x_\alpha} \right) - \frac{\partial \langle u'_\alpha u'_\beta \rangle}{\partial x_\beta} - \frac{1}{\rho} \frac{\partial \langle p \rangle}{\partial x_\alpha}, \tag{2.80}$$

where $\langle u'_\alpha u'_\beta \rangle$ is the Reynolds stress tensor.

2.3.2 Turbulent Viscosity Models

The Reynolds stresses can be modeled using the turbulent viscosity hypothesis to close the RANS equations. Taking the hypothesis into account the Reynolds stresses are written as

$$\langle u'_\alpha u'_\beta \rangle = \frac{2}{3} k \delta_{\alpha\beta} - \nu^{turb} \left(\frac{\partial \langle u_\alpha \rangle}{\partial x_\beta} + \frac{\partial \langle u_\beta \rangle}{\partial x_\alpha} \right), \tag{2.81}$$

where ν^{turb} is the turbulent kinematic viscosity.

2.3.2.1 k-ε model

The k-ε model proposed by Launder and Spalding [59] is a commonly used two-equation turbulent viscosity model. The two turbulence quantities, namely the turbulent kinetic energy k and the turbulent kinetic energy dissipation ε are described by two additional transport equations. The empirical model transport equation for k reads

$$\begin{aligned} \frac{\partial k}{\partial t} + \langle u_\beta \rangle \frac{\partial k}{\partial x_\beta} = & \frac{\partial}{\partial x_\beta} \left[\frac{\nu^{turb}}{\sigma_k} \frac{\partial k}{\partial x_\beta} \right] + \\ & \nu^{turb} \left(\frac{\partial \langle u_\alpha \rangle}{\partial x_\beta} + \frac{\partial \langle u_\beta \rangle}{\partial x_\alpha} \right) \frac{\partial \langle u_\alpha \rangle}{\partial x_\beta} - \varepsilon, \end{aligned} \tag{2.82}$$

and the second model transport equation for ε is given by

$$\begin{aligned}\frac{\partial \varepsilon}{\partial t}+\langle u_\beta\rangle\frac{\partial \varepsilon}{\partial x_\beta}=&\frac{\partial}{\partial x_\beta}\left[\frac{\nu^{turb}}{\sigma_\varepsilon}\frac{\partial \varepsilon}{\partial x_\beta}\right]+\\ &C_1\frac{\nu^{turb}\varepsilon}{k}\left(\frac{\partial\langle u_\alpha\rangle}{\partial x_\beta}+\frac{\partial\langle u_\beta\rangle}{\partial x_\alpha}\right)\frac{\partial\langle u_\alpha\rangle}{\partial x_\beta}-C_2\frac{\varepsilon^2}{k}.\end{aligned} \tag{2.83}$$

By solving the two transport equations, the turbulent viscosity ν^{turb} is written as

$$\nu^{turb}=C_\mu\frac{k^2}{\varepsilon}. \tag{2.84}$$

The occurring model constants can be chosen according to the work of Laudner et al. [59] to

$$C_\mu=0.09,\quad \sigma_k=1.00,\quad \sigma_\epsilon=1.30,\quad C_1=1.44,\quad C_2=1.92. \tag{2.85}$$

The first attempt to implement a k-ε model into the LBM framework was made by Succi et al. [100]. They deploy two additional particle distribution functions to approximate the solution of the transport equations. Another possibility to discretize the transport equations is the use of a Lax–Wendroff scheme [101, 103]. In the following the method of Sajjadi et al. [92] is presented, which follows the idea of Succi et al. [100]. The zeroth order moment of the distribution functions g_i and h_i are defined as

$$k^{\mathrm{LB}}=\sum_{i=0}^{q-1}g_i, \tag{2.86}$$

$$\varepsilon^{\mathrm{LB}}=\sum_{i=0}^{q-1}h_i. \tag{2.87}$$

Both transport equations are given by

$$g_i(\boldsymbol{x}^{\mathrm{LB}}+\boldsymbol{c}_i,t^{\mathrm{LB}}+1)=g_i(\boldsymbol{x}^{\mathrm{LB}},t^{\mathrm{LB}})-\frac{1}{\tau^k}\left[g_i(\boldsymbol{x}^{\mathrm{LB}},t^{\mathrm{LB}})-g_i^{\mathrm{eq}}(\boldsymbol{x}^{\mathrm{LB}},t^{\mathrm{LB}})\right]+F_i^k, \tag{2.88}$$

$$h_i(\boldsymbol{x}^{\mathrm{LB}}+\boldsymbol{c}_i,t^{\mathrm{LB}}+1)=h_i(\boldsymbol{x}^{\mathrm{LB}},t^{\mathrm{LB}})-\frac{1}{\tau^\varepsilon}\left[h_i(\boldsymbol{x}^{\mathrm{LB}},t^{\mathrm{LB}})-h_i^{\mathrm{eq}}(\boldsymbol{x}^{\mathrm{LB}},t^{\mathrm{LB}})\right]+F_i^\varepsilon, \tag{2.89}$$

where F_i^k and F_i^ε are defined as

$$F_i^k = \omega_i \left(\nu^{\mathrm{LB},turb} |S_{\alpha\beta}^{\mathrm{LB}}|^2 - \varepsilon^{\mathrm{LB}} \right) \left(1 + \frac{c_{i\alpha} u_\alpha^{\mathrm{LB}} (\tau^k - 0.5)}{c_s^2 \tau^k} \right), \tag{2.90}$$

$$F_i^\varepsilon = \omega_i \left(C_1 \frac{\varepsilon^{\mathrm{LB}}}{k^{\mathrm{LB}}} \left(\nu^{\mathrm{LB},turb} |S_{\alpha\beta}^{\mathrm{LB}}|^2 \right) - C_2 \frac{(\varepsilon^{\mathrm{LB}})^2}{k^{\mathrm{LB}}} \right) \left(1 + \frac{c_{i\alpha} u_\alpha^{\mathrm{LB}} (\tau^\varepsilon - 0.5)}{c_s^2 \tau^\varepsilon} \right). \tag{2.91}$$

The according equilibrium distribution functions g_i^{eq} and h_i^{eq} are respectively written as

$$g_i^{\mathrm{eq}} \left(k^{\mathrm{LB}}, \boldsymbol{u}^{\mathrm{LB}} \right) = \omega_i k^{\mathrm{LB}} \left[1 + \frac{c_{i\alpha} u_\alpha^{\mathrm{LB}}}{c_s^2} + \frac{u_\alpha^{\mathrm{LB}} u_\beta^{\mathrm{LB}} \left(c_{i\alpha} c_{i\beta} - c_s^2 \delta_{\alpha\beta} \right)}{2 c_s^4} \right], \tag{2.92}$$

$$h_i^{\mathrm{eq}} \left(\varepsilon^{\mathrm{LB}}, \boldsymbol{u}^{\mathrm{LB}} \right) = \omega_i \varepsilon^{\mathrm{LB}} \left[1 + \frac{c_{i\alpha} u_\alpha^{\mathrm{LB}}}{c_s^2} + \frac{u_\alpha^{\mathrm{LB}} u_\beta^{\mathrm{LB}} \left(c_{i\alpha} c_{i\beta} - c_s^2 \delta_{\alpha\beta} \right)}{2 c_s^4} \right]. \tag{2.93}$$

The relaxation times τ^k and τ^ε are obtained by

$$\tau^k = \tau + \frac{\sigma_k \nu^{\mathrm{LB},turb}}{c_s^2}, \tag{2.94}$$

$$\tau^\varepsilon = \tau + \frac{\sigma_\varepsilon \nu^{\mathrm{LB},turb}}{c_s^2}. \tag{2.95}$$

Finally, the lattice turbulent viscosity $\nu^{\mathrm{LB},turb}$ is calculated similarly to Eq. (2.84) by

$$\nu^{\mathrm{LB},turb} = C_\mu \frac{(k^{\mathrm{LB}})^2}{\varepsilon^{\mathrm{LB}}}. \tag{2.96}$$

3

Comparison of Distinct Collision Operators for Direct Numerical Simulation

This chapter was published in the following article:

M. Haussmann, S. Simonis, H. Nirschl and M. J. Krause
Direct numerical simulation of decaying homogeneous isotropic turbulence – numerical experiments on stability, consistency and accuracy of distinct lattice Boltzmann methods
International Journal of Modern Physics C (IJMPC), 30.09 (2019)
https://doi.org/10.1142/S0129183119500748

My contribution according to the contributor role taxonomy system [14] included conceptualization, methodology, software, validation, formal analysis, investigation, data curation, writing – original draft, visualization and project administration.

International Journal of Modern Physics C
Vol. 30, No. 9 (2019) 1950074 (29 pages)

DOI: 10.1142/S0129183119500748

Direct numerical simulation of decaying homogeneous isotropic turbulence — numerical experiments on stability, consistency and accuracy of distinct lattice Boltzmann methods

Marc Haussmann* and Stephan Simonis†
Lattice Boltzmann Research Group, Karlsruhe Institute of Technology
Karlsruhe 76131, Germany
**marc.haussmann@kit.edu*
†stephan.simonis@kit.edu

Hermann Nirschl
Institute for Mechanical Process Engineering and Mechanics
Karlsruhe Institute of Technology
Karlsruhe 76131, Germany
hermann.nirschl@kit.edu

Mathias J. Krause
Lattice Boltzmann Research Group, Karlsruhe Institute of Technology
Karlsruhe 76131, Germany
mathias.krause@kit.edu

Received 8 November 2018
Accepted 26 June 2019
Published 19 August 2019

Stability, consistency and accuracy of various lattice Boltzmann schemes are investigated by means of numerical experiments on decaying homogeneous isotropic turbulence (DHIT). Therefore, the Bhatnagar–Gross–Krook (BGK), the entropic lattice Boltzmann (ELB), the two-relaxation-time (TRT), the regularized lattice Boltzann (RLB) and the multiple-relaxation-time (MRT) collision schemes are applied to the three-dimensional Taylor–Green vortex, which represents a benchmark case for DHIT. The obtained turbulent kinetic energy, the energy dissipation rate and the energy spectrum are compared to reference data. Acoustic and diffusive scaling is taken into account to determine the impact of the lattice Mach number. Furthermore, three different Reynolds numbers $\mathrm{Re} = 800$, $\mathrm{Re} = 1600$ and $\mathrm{Re} = 3000$ are considered. BGK shows instabilities, when the mesh is highly underresolved. The diverging simulations for MRT are ascribed to a strong lattice Mach number dependency. Despite the fact that the ELB modifies the bulk viscosity, it does not mimic a turbulence model. Therefore, no significant increase of stability in comparison to BGK is observed. The TRT "magic parameter" for DHIT at moderate Reynolds numbers is estimated with respect to the energy contribution. Stability and accuracy of the TRT scheme is found to be similar to BGK. For small lattice Mach numbers, the RLB scheme exhibits lowered energy contribution in the dissipation range

---

*Corresponding author.

compared to an analytical model spectrum. Overall, to enhance stability and accuracy, the lattice Mach number should be chosen with respect to the applied collision scheme.

Keywords: Decaying homogeneous isotropic turbulence; Taylor–Green vortex; lattice Boltzmann methods; OpenLB; direct numerical simulation.

PACS Nos.: 47.11.–j, 47.27.Gs, 02.60.Cb.

1. Introduction

In addition to conventional approaches to numerically solving the Navier–Stokes equations, e.g. finite volume methods or finite element methods, the lattice Boltzmann methods (LBM) have gained in importance in recent decades. Based on kinetic gas theory, the LBM evolved from the lattice gas cellular automata.[46] Due to the highly parallelizable algorithm[22,23] and the associated increase in performance, the LBM has proven broad applicability, for example in particle flows[26,44] or flows in complex geometries.[3,21] Despite its multiple uses, especially turbulent flow simulations with the LBM require further validation and important developments of established Navier–Stokes solvers have to be caught up. The simplest canonical flow for the validation of turbulence quantities is homogeneous isotropic turbulence (HIT). Regardless of the academic character of this type of flow, fundamental statements can be made about the numerical method itself and the development of turbulence models.

One of the first decaying homogeneous isotropic turbulence (DHIT) simulations with LBM was performed in 1992 by Chen *et al.*[10] They used 128^3 grid points for Reynolds numbers $\mathrm{Re} = 200$ and $\mathrm{Re} = 300$ and observed good agreement with spectral methods for time-dependent energy and enstrophy decay as well as spatial evolution of vortices. Ten years later, Luo *et al.*[34] discovered similar results to pseudo-spectral methods revealing an increase of dissipation at high wave numbers. The work of Yu *et al.*[49] comprises a DNS study at $\mathrm{Re} = 600$ and reproduces two power-law scalings of the low wavenumber energy spectrum with different initial conditions. Furthermore, the power-law decay of the kinetic energy and the suppression of the spectral cascade by rotation were examined. The influence of temperature fluctuations on DHIT were investigated by Lee *et al.*[31] The results confirm the applicability of LBM for compressible turbulence with a thermal field. In 2009, the first forced HIT simulation for two lattice velocity sets $D3Q15$ and $D3Q19$ were obtained by Kareem *et al.*[24] The study concluded that an increase in resolution reduces the influence of the underlying velocity set. Peng *et al.*[40] compared LBM with pseudo-spectral methods for DHIT and found that LBM requires double resolution to accurately capture pressure fluctuations. Nathen *et al.*[38] were the first to examine differences of various collision schemes in DHIT. They applied three distinct collision schemes on the three-dimensional Taylor–Green vortex (TGV) flow to compare accuracy and stability. Notwithstanding the numerous findings of this study, some influencing factors, e.g. the lattice Mach number, have been disregarded. In this work, we aim to extend the TGV study in Ref. 38 with additional collision schemes and complete the statements that have been made.

In this paper, we present a detailed analysis of five commonly used collision schemes on turbulent flows. The work covers the advantages and drawbacks of each scheme concerning accuracy, consistency and stability. We set the focus on DHIT, due to the absence of boundaries and forcing schemes, which interfere with the applied collision scheme. Solely direct numerical simulations (DNS) are performed to determine the viscous effects caused by the collision scheme itself, and not by a turbulence model. The TGV is chosen to evaluate the kinetic energy and the energy dissipation rate. Furthermore, a spectral analysis is performed. Subsequent error calculations are conducted to quantitatively assess each collision scheme with respect to a reference solution. This reference solution is computed on a grid that resolves the Kolmogorov scales, and is validated with previously published pseudo-spectral DNS results. For the first time, we cross-compare the Bhatnagar–Gross–Krook (BGK),[4] the entropic lattice Boltzmann (ELB),[2] the two-relaxation-time (TRT),[18] the regularized lattice Boltzann (RLB),[30] and the multiple-relaxation-time (MRT)[14] collision scheme in terms of solution dependencies on the lattice Mach number, the Reynolds number and the grid resolution. In particular, the TRT scheme is presented for the first time in a three-dimensional DHIT setting, where the effect of the “magic parameter”[18] on turbulence quantities is scrutinized.

The paper is organized as follows. Section 2 gives a brief introduction to the LBM, and specifies the used collision schemes. In Sec. 3, the TGV benchmark case for DHIT, and the turbulence quantities examined therein, are described. Section 4 validates a high resolution LBM DNS against pseudo-spectral methods. Section 5 studies the TRT scheme’s second relaxation parameter with respect to the energy dissipation rate and the energy spectrum. Section 6.1 determines the stability and accuracy in underresolved DNS for the different collision schemes. Based on two common scaling approaches, we further examine the lattice Mach number influence in Sec. 6.2. The grid convergence with respect to the calculated turbulence quantities is analyzed in Sec. 6.3. Finally, we conclude the paper with continuative remarks in Sec. 7.

2. LBM

Discretizing the kinetic Boltzmann equation on a Cartesian grid leads to a finite number of particle distribution functions f_i. The topology of the lattice is defined by d dimensions and q lattice velocities $\mathbf{c}_i$, $i = 0, 1, \ldots, q-1$. In this work, the velocity set $D3Q19$ is utilized to discretize the velocity space. This choice is justified by the absence of transformations as well as lower memory costs for computations. The following section is formulated in lattice units with the common choice of $\delta x = \delta t = 1$, for the node distance δx and the lattice time step δt. The lattice velocities $\mathbf{c}_i$ in $D3Q19$ are given by

$$\mathbf{c}_i = \begin{cases} (0,0,0), & i = 0, \\ (\pm 1,0,0),(0,\pm 1,0),(0,0,\pm 1), & i = 1,2,\ldots,6, \\ (\pm 1,\pm 1,0),(\pm 1,0,\pm 1),(0,\pm 1,\pm 1), & i = 7,8,\ldots,18. \end{cases} \tag{1}$$

The lattice Boltzmann equation reads

$$f_i(\mathbf{x}+\mathbf{c}_i, t+1) = f_i(\mathbf{x},t) + \Omega_i, \tag{2}$$

where $\mathbf{x}$ specifies the lattice location. Furthermore, the relaxation of the populations f_i towards their respective equilibria f_i^{eq}, under the conservation constraints for mass and momentum, is manifested in the collision operator Ω_i.

For an isothermal, weakly compressible flow, a truncated Maxwell–Boltzmann equilibrium distribution f_i^{eq} is given by[35]

$$f_i^{\mathrm{eq}}(\rho,\mathbf{u}) = \rho w_i \left[1 + \frac{c_{i\alpha}u_\alpha}{c_s^2} + \frac{u_\alpha u_\beta (c_{i\alpha}c_{i\beta} - c_s^2\delta_{\alpha\beta})}{2c_s^4}\right], \tag{3}$$

where Greek indices obey the Einstein notation, $\delta_{\alpha\beta}$ denotes the Kronecker delta, ω_i are lattice weights obtained from the Gauss–Hermite quadrature,[20,42] and $c_s = \frac{1}{\sqrt{3}}$ represents the speed of sound within the lattice.

Macroscopic flow quantities such as density ρ, momentum $\rho\mathbf{u}$, and momentum flux $\mathbf{\Pi}$ are obtained from the moments of f_i, respectively

$$\rho = \sum_{i=0}^{q-1} f_i, \tag{4}$$

$$\rho\mathbf{u} = \sum_{i=0}^{q-1} \mathbf{c}_i f_i, \tag{5}$$

$$\Pi_{\alpha\beta} = \sum_{i=0}^{q-1} c_{i\alpha}c_{i\beta} f_i. \tag{6}$$

A simplified isothermal equation of state relates the pressure p to the density through

$$p = c_s^2 \rho. \tag{7}$$

The lattice Mach number Ma is defined as

$$\mathrm{Ma} = \frac{u^{\mathrm{L}}}{c_s}, \tag{8}$$

where u^{L} denotes the lattice velocity. Hence, the incompressible Navier–Stokes equations are recovered for $\mathrm{Ma} \to 0$.

Finally, the lattice Boltzmann algorithm is conceptually parted in a local collision step, associated to the right-hand side of Eq. (2), and subsequent streaming, executed according to the left-hand side of Eq. (2).

2.1. ***BGK collision scheme***

Bhatnagar, Gross and Krook[4] proposed a collision operator with a single relaxation time. Discretization yields

$$\Omega_i = -\frac{1}{\tau}(f_i(\mathbf{x}, t) - f_i^{\mathrm{eq}}(\rho, \mathbf{u})), \tag{9}$$

and with Eq. (2), we obtain the BGK scheme as

$$f_i(\mathbf{x} + \mathbf{c}_i, t+1) = f_i(\mathbf{x}, t) - \frac{1}{\tau}(f_i(\mathbf{x}, t) - f_i^{\mathrm{eq}}(\rho, \mathbf{u})). \tag{10}$$

In the incompressible limit, the relaxation time τ is coupled with the kinematic viscosity ν of the fluid through

$$\nu = c_s^2\left(\tau - \frac{1}{2}\right), \tag{11}$$

which results in an interconnection of viscosity and stability. Stability deficiencies for small viscosities and low resolutions are well-known and have already been observed among others by Yasduda *et al.*,[48] Nathen *et al.*[38]

2.2. ***MRT collision scheme***

As a generalization of the BGK scheme, τ is replaced by a $q \times q$ matrix $\mathbf{S}$ comprising several relaxation times.[14,27]

The particle distributions $\mathbf{f} = (f_0, \dots, f_{q-1})^{\mathrm{T}}$ are multiplied with the rows $\mathbf{M}_j$ of a regular $q \times q$ matrix $\mathbf{M}$, constructed from velocity components,[14] to obtain a moment vector $\mathbf{m}$ with q entries

$$m_j = \mathbf{M}_j \mathbf{f}. \tag{12}$$

The equilibrium moments m_j^{eq} are similarly revealed by

$$m_j^{\mathrm{eq}} = \mathbf{M}_j \mathbf{f}^{\mathrm{eq}}. \tag{13}$$

The MRT scheme[14,27,29] then reads

$$\mathbf{f}(\mathbf{x} + \mathbf{c}_i, t+1) = \mathbf{f}(\mathbf{x}, t) - \mathbf{M}^{-1}\mathbf{S}[\mathbf{m}(\mathbf{x}, t) - \mathbf{m}^{\mathrm{eq}}(\mathbf{x}, t)]. \tag{14}$$

For the $D3Q19$ lattice, d'Humières *et al.*[14] proposed a moment vector

$$\mathbf{m} = (\rho, e, e^2, j_x, q_x, j_y, q_y, j_z, q_z, 3\sigma_{xx}, 3\pi_{xx}, \sigma_{ww}, \pi_{ww}, \sigma_{xy}, \sigma_{yz}, \sigma_{xz}, n_x, n_y, n_z)^{\mathrm{T}}, \tag{15}$$

where the corresponding diagonal collision matrix is defined as[14]

$$\mathbf{S} = \mathrm{diag}(0, \omega_1, \omega_2, 0, \omega_4, 0, \omega_4, 0, \omega_4, \omega_9, \omega_{10}, \omega_9, \omega_{10}, \omega_{13}, \omega_{13}, \omega_{13}, \omega_{16}, \omega_{16}, \omega_{16}). \tag{16}$$

The relaxation of the conserved moments ρ and $\mathbf{j} = \rho\mathbf{u}$ yields zero. Hence, the associated relaxation frequencies in $\mathbf{S}$ are negligible and nulled out. Further, $\omega_{1,9,13}$ for the relaxation of e, diagonal and off-diagonal entries of, are connected to kinematic and bulk viscosity via

$$\nu = c_s^2\left(\frac{1}{\omega_9} - \frac{1}{2}\right) = c_s^2\left(\frac{1}{\omega_{13}} - \frac{1}{2}\right), \quad \nu_\mathrm{B} = \frac{2}{3}c_s^2\left(\frac{1}{\omega_1} - \frac{1}{2}\right). \tag{17}$$

The remaining free parameters $w_{2,4,10,16}$ are respectively related to kinetic moments for the components of $e^2, \mathbf{q}, \boldsymbol{\pi}, \mathbf{n}$, and have been optimized by d'Humières *et al.*[14] with local analysis in Fourier space as suggested by Lallemand *et al.*[28]

Offering advanced possibilities to influence stability and physical behavior, the maximum number of tunable relaxation rates and equilibrium populations, resembles the main advantage of the MRT.[14]

2.3. *TRT collision scheme*

To counteract the complexity of tuning individual relaxation rates, a simplification of the MRT scheme was introduced by Ginzburg *et al.*[18] It is accomplished by relaxing the subset of even order moments in $\mathbf{m}$ with $\omega^+ = \frac{1}{\tau^+} = \frac{1}{\tau}$ and the complement with $\omega^- = \frac{1}{\tau^-}$.

The equilibrium distribution is split into a symmetric and an antisymmetric contribution

$$f_i^{\mathrm{eq}+} = \frac{1}{2}(f_i^{\mathrm{eq}} + f_{\bar{i}}^{\mathrm{eq}}), \tag{18}$$

$$f_i^{\mathrm{eq}-} = \frac{1}{2}(f_i^{\mathrm{eq}} - f_{\bar{i}}^{\mathrm{eq}}), \tag{19}$$

where the index $\bar{i}$ denotes the opposite direction $\mathbf{c}_{\bar{i}} = -\mathbf{c}_i$ in the lattice. Analogously, the decomposition of the particle distributions is

$$f_i^+ = \frac{1}{2}(f_i + f_{\bar{i}}), \tag{20}$$

$$f_i^- = \frac{1}{2}(f_i - f_{\bar{i}}). \tag{21}$$

The relaxation to the antisymmetric and symmetric nonequilibrium populations, separately with relaxation rates ω^- and ω^+, yields the TRT scheme

$$f_i(\mathbf{x} + \mathbf{c}_i, t + 1) = f_i - \omega^+(f_i^+ - f_i^{\mathrm{eq}+}) - \omega^-(f_i^- - f_i^{\mathrm{eq}-}). \tag{22}$$

Resulting in larger stability regions of TRT compared to BGK,[17] a decoupling of stability from viscosity, is obtained through the individual relaxation of even and odd order moments.

Ginzburg *et al.*[17,18] summarized the stability enhancing attributes of the TRT scheme, based on the so-called "magic parameter",

$$\Lambda = \left(\frac{1}{\omega^+} - \frac{1}{2}\right)\left(\frac{1}{\omega^-} - \frac{1}{2}\right). \tag{23}$$

When changing the viscosity through $\tau^+ = \tau$ in Eq. (11), Λ should be kept constant according to Krüger *et al.*[27] Hence, the magnitude ratio of τ^- to τ^+ obeys Eq. (23) and should ensure the desired TRT solution behavior throughout the choices of ν.

2.4. *RLB collision scheme*

Latt *et al.*[30] presented a possible regularization of the nonequilibrium part f_i^{neq} of the particle distribution function $f_i = f_i^{\mathrm{eq}} + f_i^{\mathrm{neq}}$ via

$$f_i^{\mathrm{neq}} \approx f_i^{(1)} = \frac{w_i}{2c_s^4}(c_{i\alpha}c_{i\beta} - c_s^2\delta_{\alpha\beta})\sum_{j=0}^{q} c_{j\alpha}c_{j\beta}f_j^{\mathrm{neq}}. \tag{24}$$

Hence, the regularization of Eq. (10) yields

$$f_i(\mathbf{x}+\mathbf{c}_i, t+1) = f_i^{\mathrm{eq}}(\mathbf{x}, t) + \left(1 - \frac{1}{\tau}\right) f_i^{(1)}(\mathbf{x}, t). \tag{25}$$

Equation (24) acts as a purely local variation and maintains computational efficiency.

Further, Latt *et al.*[30] established the equivalence of Eq. (25) to an MRT formulation, where the hydrodynamic moments for density ρ, momentum $\rho\mathbf{u}$ and momentum flux $\mathbf{\Pi}$ are relaxed with $\frac{1}{\tau}$, whereas the kinetic moments are prescribed with a unity relaxation time. As a consequence, the RLB scheme exhibits increased stability for large pressure gradient problems and turbulent flows.

2.5. *ELB collision scheme*

The Maxwell–Boltzmann equilibrium distribution approximation in Eq. (3) does not agree with Boltzmann's $\mathcal{H}$-theorem.[2]

Nevertheless, the $\mathcal{H}$-functional has a convex-composed, discrete velocity counterpart

$$H(\mathbf{f}) = \sum_{i=0}^{q-1} f_i \ln\left(\frac{f_i}{w_i}\right), \tag{26}$$

upholding the second law of thermodynamics.[6] Further, $H(\mathbf{f})$ is minimized with respect to the conservation constraints for mass and momentum by[6,1]

$$\check{f}_i^{\mathrm{eq}} := \mathrm{argmin}_{\mathbf{f}} H(\mathbf{f}) = \rho w_i \prod_{\alpha=1}^{d} \left(2 - \sqrt{1 + 2u_\alpha^2}\right)\left(\frac{2u_\alpha + \sqrt{1+3u_\alpha^2}}{1-u_\alpha}\right)^{c_{i\alpha}}. \tag{27}$$

With a viscosity related parameter[11]

$$b = \frac{1}{6\nu + 1} = \frac{1}{2\tau} \in (0, 1], \tag{28}$$

the ELB scheme then reads

$$f_i(\mathbf{x}+\mathbf{c}_i, t+1) = f_i(\mathbf{x}, t) + ab(\check{f}_i^{\mathrm{eq}}(\mathbf{x}, t) - f_i(\mathbf{x}, t)). \tag{29}$$

The over-relaxation parameter $a > 0$ is defined as the nontrivial root of the isentropic condition[6]

$$H(f_i + a(\check{f}_i^{\text{eq}} - f_i)) = H(f_i). \tag{30}$$

Equations (27) and (30) have to be solved in every time step. The latter is nonlinear and typically executed iteratively with the Newton–Raphson method.[11] Prescribing a tolerance, at which the solution to Eq. (30) is analytically computed by asymptotically expanding a, helps to cut back the ELB scheme's increased computational effort. Setting $a = 2$ generates equivalence to the BGK scheme.[11]

2.6. *Initialization*

In addition to the initial velocity field $\mathbf{u}_0 = \mathbf{u}(\mathbf{x}, t_0)$ at $t_0 = 0$, the initial pressure $p_0 = p(\mathbf{x}, t_0)$ is required to guarantee a divergence free initial solution for the incompressible NSE. Based on the absence of a given p_0, the naive approach, initializing the populations via Eq. (3) with

$$f_i(\mathbf{x}, t_0) = f_i^{\text{eq}}(\rho_0, \mathbf{u}_0), \tag{31}$$

where ρ_0 is set to a constant value, violates the Poisson equation for the initial pressure field.[37,27] In case p_0 is available, the initialization of f_i through Eq. (31) with $\rho_0 = \frac{p_0}{c_s^2}$ instead, still neglects the influence of f_i^{neq}. An initial state, additionally taking nonequilibrium contributions for $f_i = f_i^{\text{eq}} + f_i^{\text{neq}}$ into account, is given in Ref. 27 as

$$f_i^{\text{neq}}(\rho_0, \mathbf{u}_0) \approx -\frac{w_i \rho_0 \tau}{c_s^2}(c_{i\alpha} c_{i\beta} - c_s^2 \delta_{\alpha\beta})\partial_\alpha u_{0\beta}. \tag{32}$$

3. The TGV Benchmark

The partly universal character of turbulent scales, gave rise to the investigation of DHIT in simplified geometries in the first place. Typically, an initial velocity field solution to the incompressible Navier–Stokes equations is subscribed to a periodic flow domain and subsequently evolves in time. The obtained results give insight to characteristic attributes of more complex turbulent flows.[41] Pseudo-spectral DNS methods are the preferred tool for DHIT and were frequently used in the past, see Refs. 5, 8 and 9. The highly simplified setting and fairly accurate DNS reference solutions turned DHIT flows such as the TGV into common benchmark problems for the validation of numerical methods. Whereas the present work focuses on the three-dimensional TGV, a detailed comparison of pseudo-spectral DNS to BGK LBM with respect to turbulence quantities for the two-dimensional TGV is provided by Tauzin *et al.*[43]

For this section, we assume a physical unit system if not stated otherwise, and set the domain to a fully periodic cube of volume $\Omega = (2\pi l_c)^3$. Characteristic length, velocity and density are denoted as l_c, U_c and ρ_c, respectively. According to the work of Brachet *et al.*,[9] the initial velocity field for the TGV flow at $t_0 = 0$ is defined as

$$\mathbf{u}(\mathbf{x}, t_0) = \begin{pmatrix} U_c \sin\left(\frac{x}{l_c}\right) \cos\left(\frac{y}{l_c}\right) \cos\left(\frac{z}{l_c}\right) \\ -U_c \cos\left(\frac{x}{l_c}\right) \sin\left(\frac{y}{l_c}\right) \cos\left(\frac{z}{l_c}\right) 0 \end{pmatrix}. \tag{33}$$

Further, the initial pressure profile is given by

$$p(\mathbf{x}, t_0) = p_\infty + \frac{\rho_c U_c^2}{16} \left(\cos\left(\frac{2x}{l_c}\right) + \cos\left(\frac{2y}{l_c}\right) \right) \left(\cos\left(\frac{2z}{l_c}\right) + 2 \right), \tag{34}$$

where p_∞ is a reference pressure. To achieve a physical solution for the incompressible NSE, a consistent initialization for the LBM with Eq. (32) is obtained via analytically calculating the velocity gradient from Eq. (33).

3.1. *Turbulence quantities*

As a first step to analyze the simulation results, time-dependent global quantities are evaluated. Starting with the Reynolds decomposition, a flow variable φ can be split into mean $\bar{\varphi}$ and fluctuation φ'. Assuming DHIT the mean velocity of the flow is zero, $\bar{\varphi} = 0$. Moreover, we may approximately replace spatial averages, denoted by $\langle \cdot \rangle$, with spatial integrals.[16] Consequently, the turbulent kinetic energy is written as

$$k(t) = \frac{1}{2} \langle u'_\alpha u'_\alpha \rangle = \frac{1}{2|\Omega|} \int_\Omega u_\alpha u_\alpha \mathrm{d}\mathbf{x}. \tag{35}$$

Under these assumptions, the energy dissipation rate can be similarly calculated from

$$\epsilon(t) = 2\nu \langle s'_{\alpha\beta} s'_{\alpha\beta} \rangle = \nu \left\langle \frac{\partial u'_\alpha}{\partial x_\beta} \frac{\partial u'_\alpha}{\partial x_\beta} \right\rangle = \nu \frac{1}{|\Omega|} \int_\Omega \frac{\partial u_\alpha}{\partial x_\beta} \frac{\partial u_\alpha}{\partial x_\beta} \mathrm{d}\mathbf{x}, \tag{36}$$

where $s'_{\alpha\beta}$ is the fluctuating part of the strain rate tensor

$$s_{\alpha\beta} = \frac{1}{2} \left(\frac{\partial u_\alpha}{\partial x_\beta} + \frac{\partial u_\beta}{\partial x_\alpha} \right). \tag{37}$$

Secondly, the accuracy in terms of a quantity $\chi \in \{\epsilon, k\}$ with respect to its reference solution χ^{ref}, is measured by evaluating $\chi(t_m)$ at a total number of 10^3 time steps $t_m \in [t_0, t_M]$, where $t_M = 10$. Subsequently, the relative L^2-error norm is defined as

$$\text{err}_{L^2}(\chi) := \sqrt{\frac{\sum_{m=0}^{M} [\chi^{\text{ref}}(t_m) - \chi(t_m)]^2}{\sum_{m=0}^{M} [\chi^{\text{ref}}(t_m)]^2}}. \tag{38}$$

The global error out of ϵ and k is then computed as the mean

$$\text{gerr}_{L^2}(\epsilon, k) := \frac{1}{2} [\text{err}_{L^2}(\epsilon) + \text{err}_{L^2}(k)]. \tag{39}$$

As a third evaluation quantity, the band averaged three-dimensional energy spectrum

$$E(\xi, t) = \frac{1}{2} \sum_{\xi} |\hat{\mathbf{u}}(\boldsymbol{\xi}, t)|^2, \tag{40}$$

is calculated at fixed instants of time. In Eq. (40), $\hat{\mathbf{u}}$ denotes the complex Fourier transform of the velocity field, $\boldsymbol{\xi}$ the wavenumber vector and $\xi = |\boldsymbol{\xi}|$ its absolute value. Kolmogorov's theory of HIT postulates that small scales exist down to a length of

$$\eta(\nu, \epsilon) = \left(\frac{\nu^3}{\epsilon}\right)^{\frac{1}{4}}. \tag{41}$$

In contrast to that, the largest scales are limited by the domain size $L \leq 2\pi$.[40] To create a visual reference, as suggested by Pope,[41] a model spectrum, suitable for high enough Reynolds numbers, is generated from

$$E^{\star}(\xi) = C\epsilon^{\frac{2}{3}}\xi^{-\frac{5}{3}} f_L(L\xi) f_\eta(\eta\xi). \tag{42}$$

The inertial range prediction is given through

$$f_L(L\xi) = \left(\frac{L\xi}{\sqrt{(L\xi)^2 + c_L}}\right)^{\frac{5}{3}+p_0}, \tag{43}$$

and the exponential decay rate within the dissipation range is obtained with

$$f_\eta(\eta\xi) = \exp(-\beta\{[(\eta\xi)^4 + c_\eta^4]^{\frac{1}{4}} - c_\eta\}). \tag{44}$$

According to Pope,[41] parameters, aligned with experimental data, read $C = 1.5$, $c_L = 6.78$, $c_\eta = 0.4$, $\beta = 5.2$, and the van Kármán inertial spectrum is employed with $p_0 = 4$. Subscribing ν, ϵ, L, and η with Eq. (41), completes the model.

4. Reference Solution

Due to the absence of extensive databases for TGV solutions at various Reynolds numbers, including turbulence quantities at exact instants of time, an LBM reference solution is computed with the BGK scheme. For the sake of error minimization, the following contributions are taken into account.

With $l_c = 1[\mathrm{m}]$ and $U_c = 1[\frac{\mathrm{m}}{\mathrm{s}}]$ we define the Reynolds number as $\mathrm{Re} = \frac{U_c l_c}{\nu} = \frac{1}{\nu}$. Observations in previous publications confirm that fully developed turbulence behavior occurs after the dissipation rate peak $\epsilon = \epsilon_{\max}$.[5,8,9] We conclude that the smallest appearing length scales can be approximated from Eq. (41) to $\eta(\nu, \epsilon_{\max})$. In the following, the resolution N is related to the edge length of the cube $2\pi l_c$. Hence, with a reference dissipation rate from pseudo-spectral DNS results published by Brachet *et al.*,[9] for $\mathrm{Re} = 800, 1600, 3000$ the required resolutions capturing any appearing scales, can be approximated to $N \gtrsim \frac{2\pi l_c}{\eta} = 313, 537, 896$, respectively.

By Chapman–Enskog analysis, the compressibility error is found to be of order $\mathcal{O}(Ma^2)$.[27] A resolution of $N = 1024$, with $\Delta t \sim \Delta x^2$, decreases the compressibility error to $\mathcal{O}(10^{-4})$ and exceeds the Kolmogorov scale bound for $\mathrm{Re} = 800, 1600, 3000$. The thus obtained solution is hereafter referred to as LBM-DNS$_{1024}$. The calculation required ca. 15.2 hours using 55 nodes, where each node consists of two Intel Xeon E5-2660 v3 deca cores. The performance is estimated to 5.149 giga lattice cell updates per second.

In Fig. 1 and Table 2, the resulting values for dissipation rate and kinetic energy at $\mathrm{Re} = 1600$ are compared to pseudo-spectral reference data from Refs. 9, 45 and 12. The difference to latter reference data is estimated according to Eq. (38). Simulation parameters are summarized in Table 1.

Figure 1(b) shows that the LBM-DNS$_{1024}$ solution is very close to the pseudo-spectral results from Van Rees *et al.*[45] and DeBonis[12] ($\mathrm{err}_{L^2}(\epsilon) < 0.005$). The higher deviation to the results of Brachet[9] is justified by the lower resolution of 256, which is still remarkable considering the computational resources more than 30 years ago. Taking the pseudo-spectral results with a resolution of 512 into account, the error of the LBM-DNS$_{1024}$ solution reduces to approximately 0.5%, see Table 2. Assuming that a Reynolds number $\mathrm{Re} \leq 3000$ does not have a large influence on the accuracy at a resolution of $N = 1024$, further LBM-DNS$_{1024}$ reference solutions for $\mathrm{Re} = 800$ and $\mathrm{Re} = 3000$, with a hypothetical error bound $g\mathrm{err}_{L^2}(\epsilon, k) \leq 0.01$, are obtained. To enable a quantitative error estimation, the following studies utilize the LBM-DNS$_{1024}$ as a reference.

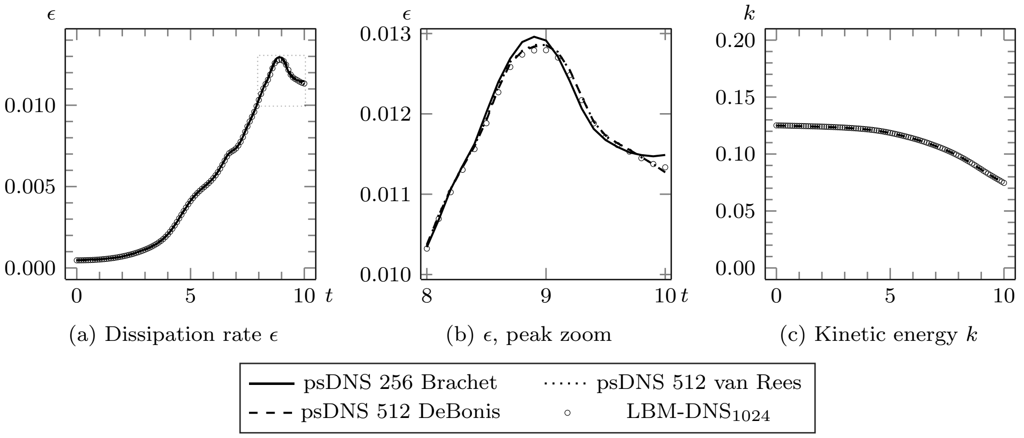

(a) Dissipation rate ϵ (b) ϵ, peak zoom (c) Kinetic energy k

Fig. 1. Dissipation rate $\epsilon(t)$ and kinetic energy $k(t)$ of the TGV flow at $\mathrm{Re} = 1600$. Present LBM-DNS$_{1024}$ solution in comparison to pseudo-spectral DNS (psDNS) reference results from Brachet,[9] van Rees,[45] DeBonis.[12]

Table 1. Methodology and discretization summary of numerical solutions for the TGV flow at Re = 1600. Present LBM-DNS$_{1024}$ solution in comparison to pseudo-spectral DNS (psDNS) results from Brachet *et al.*,[9] van Rees *et al.*,[45] DeBonis.[12]

Method	Equation	Timestepping	N	Δt
psDNS Brachet *et al.*[9]	NSE	leapfrog, Crank–Nicolson	256	0.005
psDNS van Rees *et al.*[45]	NSE vorticity form	Runge–Kutta	512	0.0092
psDNS DeBonis[12]	NSE	Runge–Kutta	512	0.001
present BGK LBM DNS	LBGK	explicit Euler	1024	0.00004

Table 2. Global error of LBM-DNS$_{1024}$ for the TGV flow at Re = 1600 with dissipation rate and kinetic energy error contributions against pseudo-spectral DNS (psDNS) reference solutions from Brachet *et al.*,[9] van Rees *et al.*,[45] DeBonis.[12]

Reference	$\mathrm{err}_{L^2}(\epsilon)$	$\mathrm{err}_{L^2}(k)$	$g\mathrm{err}_{L^2}(\epsilon, k)$
psDNS 256 Brachet *et al.*[9]	0.00675	—	—
psDNS 512 van Rees *et al.*[45]	0.00460	—	—
psDNS 512 DeBonis[12]	0.00358	0.00161	0.00260

5. Parameter Tests for the TRT Collision Scheme

The influence of the "magic parameter" Λ on the dissipation rate ϵ was investigated for Re = 800, by varying $\Lambda \in [0.25, \hat{\Lambda}]$, where $\hat{\Lambda} = (\tau_+ - 0.5)^2$ implies equivalence to the BGK scheme, via $\tau_- = \tau_+$. The viscosity connected relaxation time was set to $\tau_+ = 0.50375$ and the lattice velocity was chosen to $u_L = 0.1$ within the weakly compressible regime.

Figure 2 visualizes how the definition-wise decoupling of odd and even order moments in the TRT scheme influences the magnitude of the dissipation rate. The often proposed value[17,18] $\Lambda = 0.25$ overestimates the dissipation rate and finally results in a diverging simulation for $N = 64$ and $N = 128$. Lowering the "magic parameter", decreases the dissipation rate until a maximum of the damping effect is reached for $\Lambda = 0.002$. A higher grid resolution N broadens the possible Λ range for stable results but likewise reduces the influence of the "magic parameter" on the dissipation rate. The choice of $\Lambda = 0.002$ leads to a lower dissipation rate than $\tau_+ = \tau_-$. Figure 2(c) depicts the energy spectrum at $t = 9$ for each tested Λ. In case of $\Lambda = 0.002$ the decrease in $E(\xi)$ for increasing ξ is sustained, whereas other "magic parameter" choices lead to an unphysical growth of energy contained in the wavenumber regime around $\xi > 10$.

For $\tau_- < \tau_+ = 0.50375$, neither the dissipation rate, nor the energy spectrum features notable differences to $\tau_- = \tau_+$. A further decrease of Λ, i.e. $\tau_- - 0.5 \ll 0.00375$, eventually results in diverging simulations as $\tau_- \to 0.5$. In this study, the specific values of τ_- and Λ inducing these instabilities, seem nondeterministic and varied for each resolution. For the sake of simplicity, these parameter choices are excluded from Fig. 2.

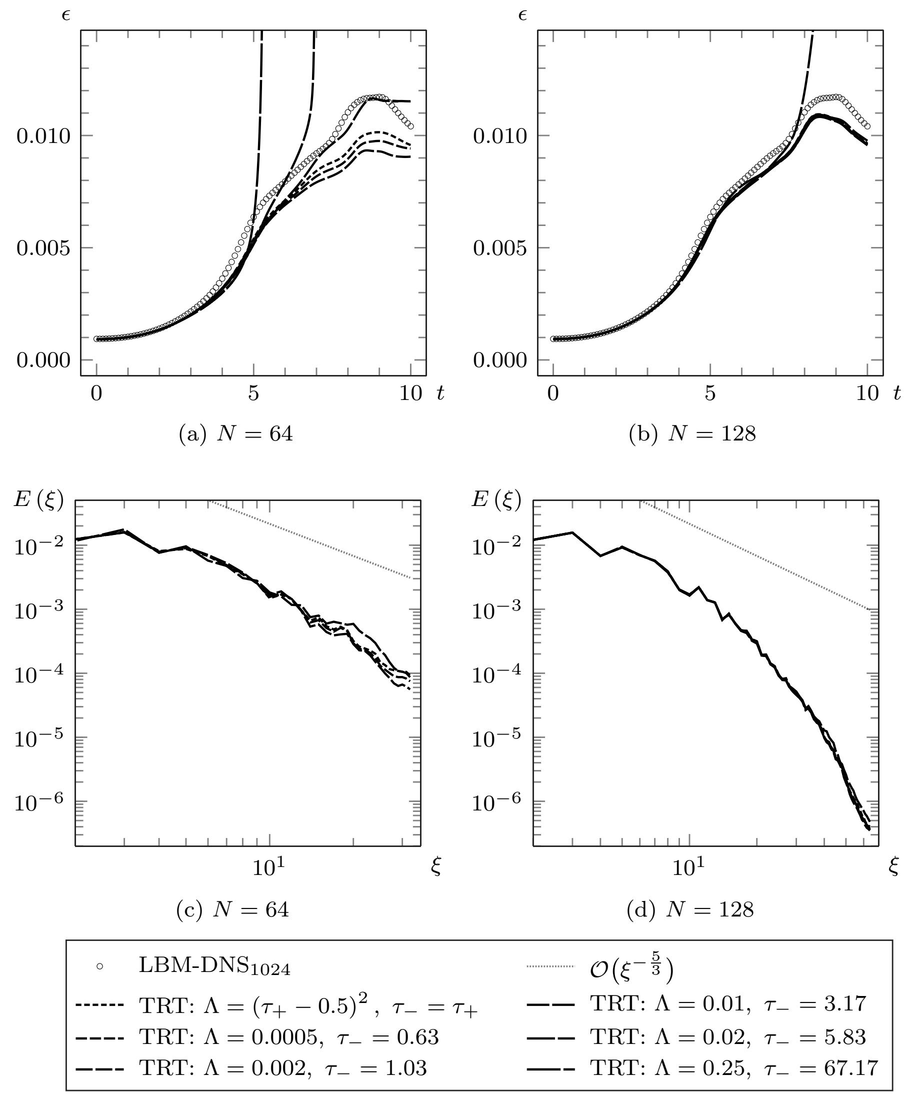

(a) $N = 64$ (b) $N = 128$

(c) $N = 64$ (d) $N = 128$

Fig. 2. Dissipation rate $\epsilon(t)$ and energy spectrum $E(\xi) = E(\xi, t = 9)$ of the TGV flow at Re = 800. TRT results with various "magic parameters", where $\tau_+ = \tau = 0.50375$, for $N = 64$ (left column) and $N = 128$ (right column), are compared to the present LBM-DNS$_{1024}$ solution and Kolmogorov's power-law for the inertial subrange.[41]

Comparing the ϵ-slope with $E(\xi)$ for $\Lambda = 0.01$, we deduce that the added amount of energy artificially increases the dissipation rate. Thus, to enhance stability through a lowered dissipation, avoiding unphysical energy allocation, $\Lambda = 0.002$ is used for all following computations.

6. Collision Scheme Comparison

Nathen *et al.*[38] provided a comparison of MRT, BGK, and RLB collision schemes and investigated mesh convergence abilities with a resolution sequence $N = 64$,

Table 3. Summary of LBM discretization parameters. Diffusive scaling (DS) and acoustic scaling (AS) for resolutions $N = 64, 128, 256, 512$ and Reynolds numbers $\mathrm{Re} = 800, 1600, 3000$.

N	u^{L}	Ma	Δx	Δt	$\mathrm{Re} = 800$	$\mathrm{Re} = 1600$	$\mathrm{Re} = 3000$
		DS			τ	τ	τ
64	0.1	0.17321	0.1	0.01	0.50375	0.50188	0.501
128	0.04952	0.08578	0.04947	0.00245	0.50375	0.50188	0.501
256	0.02476	0.04288	0.02464	0.00061	0.50375	0.50188	0.501
512	0.01219	0.02112	0.0123	0.00015	0.50375	0.50188	0.501
		AS			τ	τ	τ
64	0.1	0.17321	0.1	0.01	0.50375	0.50188	0.501
128	0.1	0.17321	0.04947	0.00495	0.50758	0.50379	0.50202
256	0.1	0.17321	0.02464	0.00246	0.51522	0.50761	0.50406
512	0.1	0.17321	0.0123	0.00123	0.53049	0.51525	0.50813

$128, 256, 512$ for Reynolds numbers $\mathrm{Re} = 800$, 1600 and 3000. Furthermore, using spectral analysis, they described the appearance of spurious oscillations for the MRT at high Reynolds numbers, which prevents the scheme from reaching second-order accuracy in the incompressible limit.[38] To continue the work in Ref. 38, we analyze the influence of diffusive scaling on the results for the BGK, TRT, MRT, RLB and the ELB scheme, using the dissipation rate to quantify the point in time where instability occurs. Additionally, acoustic scaling (AS) was tested as well, fixing the lattice Mach number for any Reynolds number and resolution. Finally, an error computation for each scaling is obtained with the help of the definitions in Eqs. (38) and (39). The dependency on the grid resolution, the Reynolds number and the lattice Mach number is used to determine and quantify accuracy, stability and consistency of each collision scheme. The discretization parameters for both approaches with a starting point at $N = 64$ are listed in Table 3.

6.1. *On the stability, highly underresolved DNS*

If the grid spacing Δx is greater than the occurring Kolmogorov length scales η, defined by Eq. (41), the simulation is termed as underresolved. The consequent effects for the each collision scheme become visible in Fig. 3. The grid resolution is set constant to $N = 64$ and three Reynolds numbers are applied to analyze the instability issues in highly underresolved meshes.

The BGK, MRT and RLB dissipation rate results in Fig. 3 agree with Ref. 38. For $\mathrm{Re} = 800$, BGK and ELB with $N = 64$ already predict ϵ quite well with respect to magnitude and slope shape. The increased numerical dissipation with a subsequent damping effect[38] of the RLB are present. A similar observation can be made for the TRT with $\Lambda = 0.002$ compared to the BGK scheme.

If the Reynolds number is increased to $\mathrm{Re} = 1600$, the BGK, ELB and TRT scheme become unstable. Although the dissipation rate is slightly diminished by

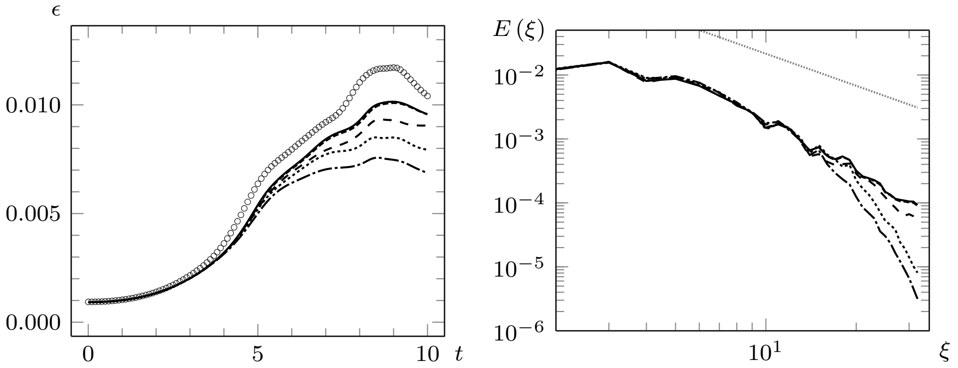

(a) Re = 800 (b) Re = 800

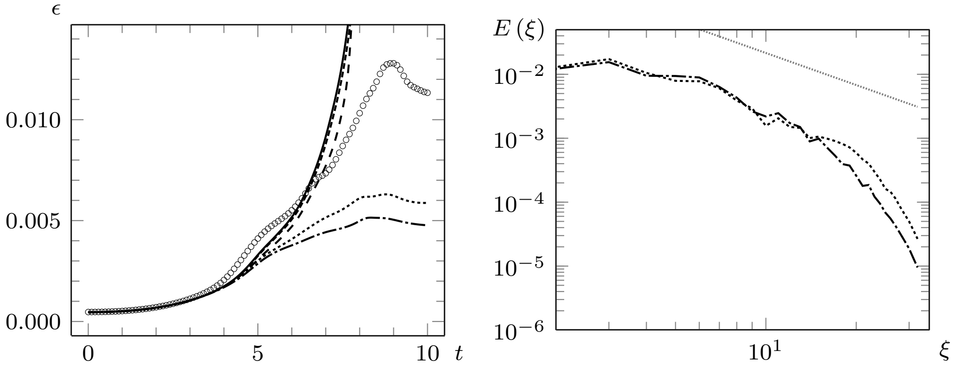

(c) Re = 1600 (d) Re = 1600

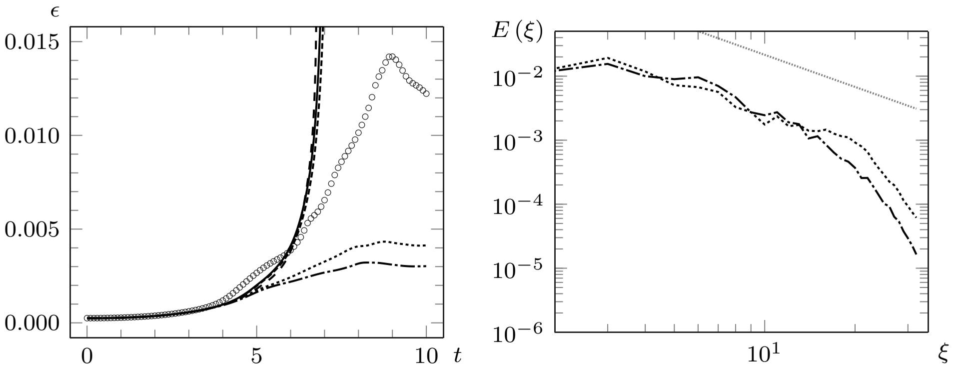

(e) Re = 3000 (f) Re = 3000

Fig. 3. Dissipation rate $\epsilon(t)$ and energy spectrum $E(\xi) = E(\xi, t = 9)$ of the TGV flow at Re $= 800, 1600, 3000$. BGK, TRT, MRT, RLB, ELB results for $N = 64$ in comparison to the present LBM-DNS$_{1024}$ solution and Kolmogorov's power-law for the inertial subrange.[41]

TRT, the instabilities still occur. The MRT and RLB scheme are able to stabilize the simulation but underestimate the course of the dissipation rate. The results for $\mathrm{Re} = 3000$ show that the behavior is amplified by increasing the Reynolds number. The BKG, ELB and TRT schemes exhibit an onset of instabilities earlier in time. Similarly, the damping of the dissipation rate for MRT and RLB is more pronounced.

Further observations can be made with the three-dimensional energy spectra for each Reynolds number at $t = 9$, presented in Fig. 3. At $\mathrm{Re} = 800$, the BGK scheme shows a nonphysical high energy level at wavenumbers $\xi \gg 10$, as already observed in Ref. 38. The excessive amount of energy contained in the small scales is also visible for the ELB and slightly reduced for the TRT scheme as a consequence of the choice for Λ. This higher energy contribution is responsible for the diverging simulations for TRT, ELB and BGK at $\mathrm{Re} = 1600$ and $\mathrm{Re} = 3000$ in the underresolved grid. However, the MRT and RLB scheme exhibit the characteristic strong decrease of energy in the dissipative range. Considering solely the inertial subrange, both schemes describe the expected power-law slope of the energy cascade. In the dissipative range, the MRT scheme contains more energy in comparison to the RLB scheme. Although stability is preserved, the MRT scheme's unphysical energy contributions at $\xi > 10$ as a consequence of the low resolution, increase with the Reynolds number, similar to those observed for BGK, ELB and TRT.

Yu *et al.*[49] studied the energy spectrum for DNS and large eddy simulation (LES) with the BGK scheme on DHIT. Compared to the DNS results, the added artificial viscosity in LES led to lowered energy levels at high wavenumbers.[49] Hence, in the case of an underresolved DNS, a turbulence model should be applied to model the unresolved scales, consequently preventing instabilities for the BGK scheme and unphysical results with the MRT scheme.

6.2. *Acoustic and diffusive scaling*

DS and AS is tested for three different grid resolutions $N = 128$, $N = 256$ and $N = 512$ and three Reynolds numbers $\mathrm{Re} = 800$, $\mathrm{Re} = 1600$ and $\mathrm{Re} = 3000$. The dissipation rate for DS and AS at $\mathrm{Re} = 800$ is depicted in Fig. 4. All tested schemes are stable in this case, regardless of the applied lattice Mach number. Minor differences between the collision schemes are visible at a grid resolution $N = 128$. The courses of the dissipation rate for TRT, ELB and BGK are very close to each other, whereas MRT lies slightly above them, and RLB is located below. This behavior is more pronounced by DS.

If the Reynolds number is increased to $\mathrm{Re} = 1600$, a difference between DS and AS can be observed. At a grid resolution of $N = 128$ all collision operators are stable. Again, the RLB underestimates the dissipation rate, but meets the course of the reference solution. However, MRT is not able to follow the reference course in the peak region. Figures 5(c) and 5(d) show that further decreasing Ma in the case of DS leads to an instability of MRT. On the other hand, a constant Mach number effects a good approximation of the reference solution. The damping of the

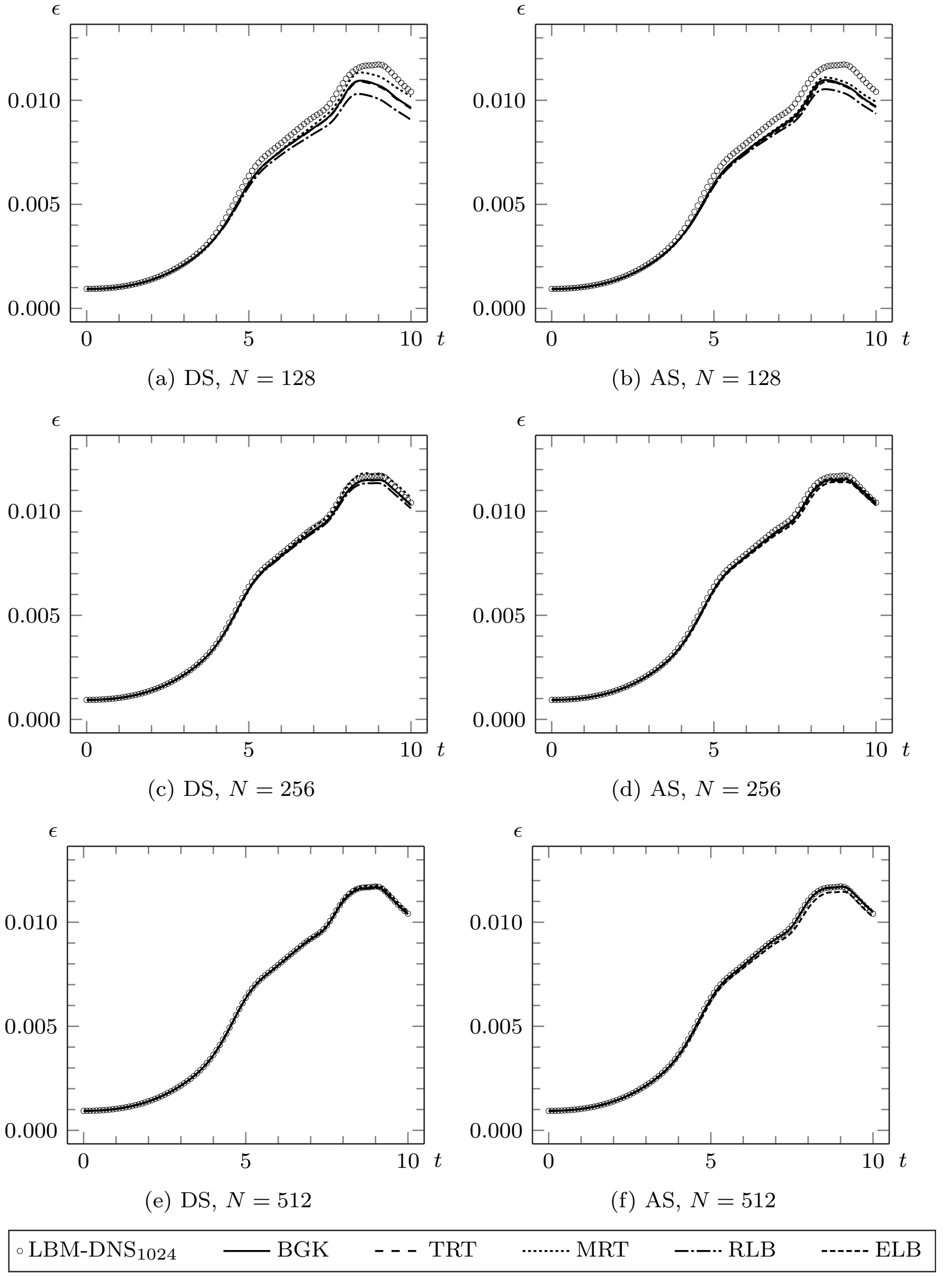

(a) DS, $N = 128$

(b) AS, $N = 128$

(c) DS, $N = 256$

(d) AS, $N = 256$

(e) DS, $N = 512$

(f) AS, $N = 512$

Fig. 4. Dissipation rate $\epsilon(t)$ of the TGV flow at $\mathrm{Re} = 800$. BGK, TRT, MRT, RLB, ELB results for $N = 128, 256, 512$ with parameters obtained from DS (left column) and AS (right column) are compared to the present LBM-DNS$_{1024}$ solution.

dissipation rate in the case of ELB is greater by AS. A higher grid resolution of $N = 512$ amplifies the unstable behavior of MRT on account of the Mach number, such that instabilities occur earlier, result in a diverging simulation and hence, violate the consistency.

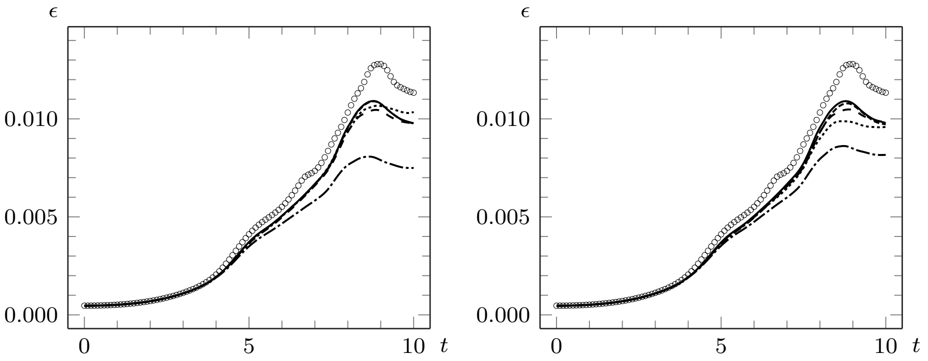

(a) DS, $N = 128$ (b) AS, $N = 128$

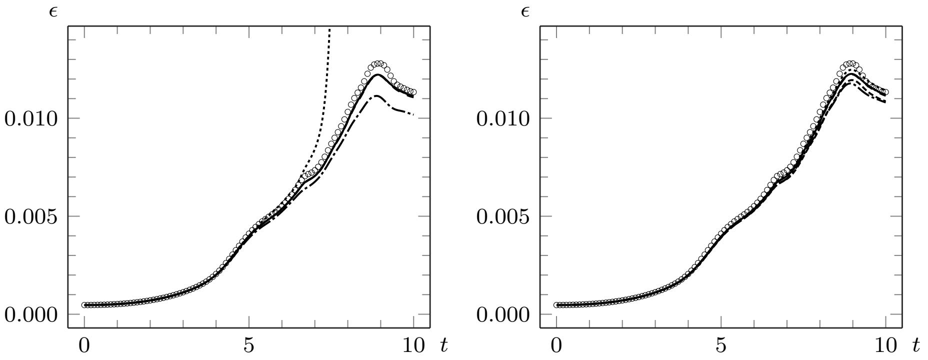

(c) DS, $N = 256$ (d) AS, $N = 256$

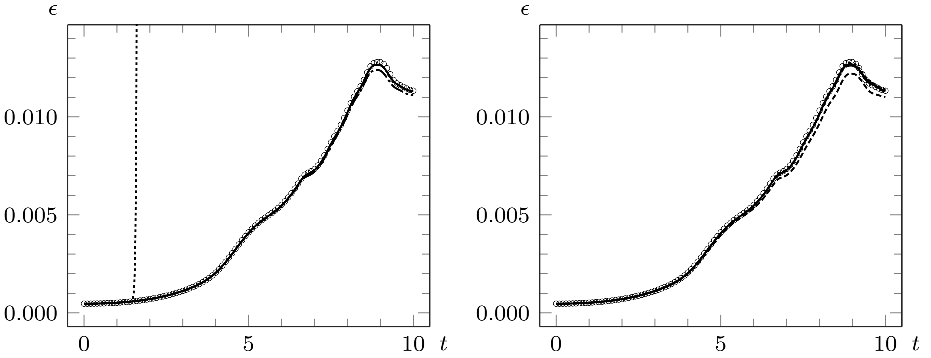

(e) DS, $N = 512$ (f) AS, $N = 512$

○ LBM-DNS$_{1024}$ —— BGK - - - TRT ········ MRT —·— RLB ------ ELB

Fig. 5. Dissipation rate $\epsilon(t)$ of the TGV flow at $\mathrm{Re} = 1600$. BGK, TRT, MRT, RLB, ELB results for $N = 128, 256, 512$ with parameters obtained from DS (left column) and AS (right column) are compared to the present LBM-DNS$_{1024}$ solution.

The dissipation rate for the highest considered Reynolds number $\mathrm{Re} = 3000$ is shown in Fig. 6. Independent of the scaling, BGK, ELB and TRT are not stable for $N = 128$. The instability of TRT develops earlier in comparison to BGK. However, ELB is slightly longer stable than BGK. The results of MRT are

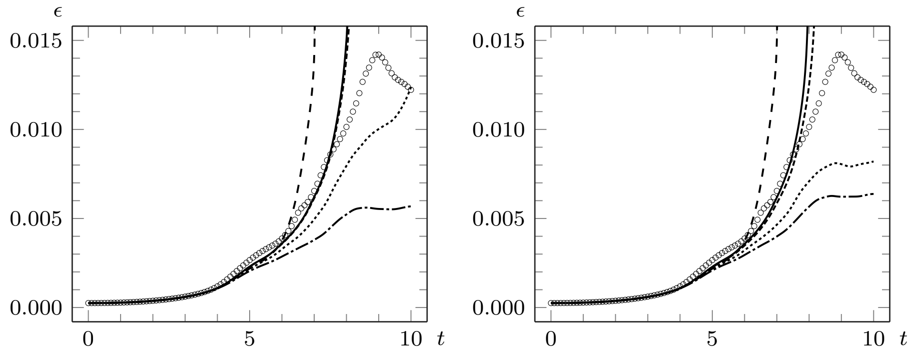

(a) DS, $N = 128$ (b) AS, $N = 128$

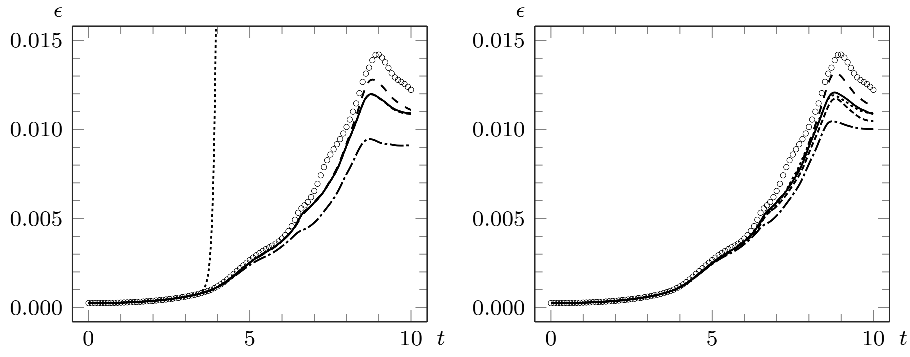

(c) DS, $N = 256$ (d) AS, $N = 256$

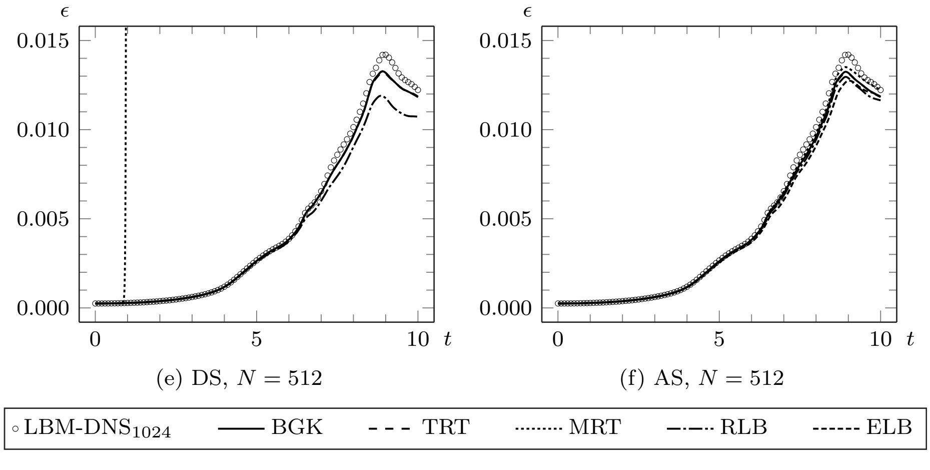

(e) DS, $N = 512$ (f) AS, $N = 512$

Fig. 6. Dissipation rate $\epsilon(t)$ of the TGV flow at $\mathrm{Re} = 3000$. BGK, TRT, MRT, RLB, ELB results for $N = 128, 256, 512$ with parameters obtained from DS (left column) and AS (right column) are compared to the present LBM-DNS$_{1024}$ solution.

again related to the lattice Mach number. A smaller Ma affects the stability and causes a diverging simulation. If the fraction $\frac{\mathrm{Ma}_{\mathrm{DS}}}{\mathrm{Ma}_{\mathrm{AS}}}$ is diminished, i.e. the grid resolution is increased, the instability sets in earlier. The underestimation of the dissipation rate by RLB is more pronounced by DS. Nevertheless, solely the RLB scheme is stable throughout all tested Re numbers.

Additionally, a spectral analysis of the energy is considered for a further investigation of the observed phenomena. The three dimensional energy spectra for Re $=$ 3000 at $t = 9$ with DS and AS are depicted in Fig. 7. To visualize the model spectrum, defined in Eq. (42), the dissipation rate maximum was calculated from the LBM-DNS$_{1024}$ reference solution for each Reynolds number, with a subsequent definition of η. In the case of the MRT scheme a lowered Mach number effects an overestimated energy at the end of the inertial subrange in comparison to the model spectrum, see Figs. 7(a) and 7(d). This nonphysical overestimation of the energy leads to a diverging simulation, for increasing Ma. The RLB scheme also displays a high Ma-dependency. If AS is applied, the course of the energy spectrum converges to the model spectrum. However, DS induces an underestimation of the energy in the

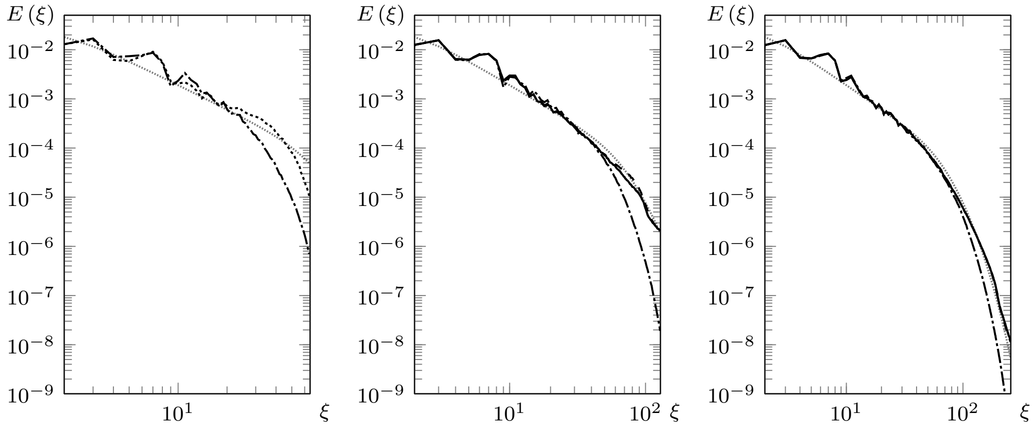

(a) DS, $N = 128$ (b) DS, $N = 256$ (c) DS, $N = 512$

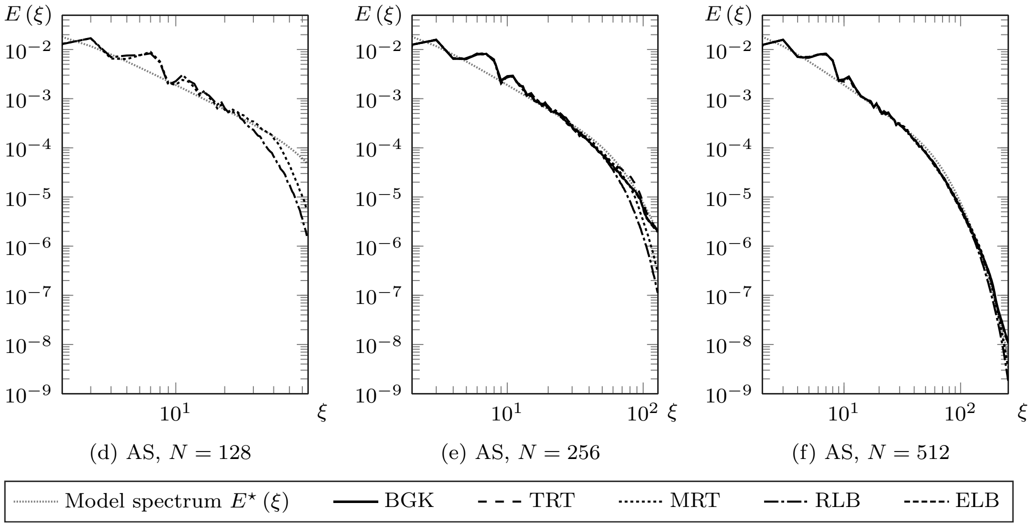

(d) AS, $N = 128$ (e) AS, $N = 256$ (f) AS, $N = 512$

Fig. 7. Energy spectrum $E(\xi) = E(\xi, t = 9)$ of the TGV flow at Re $= 3000$. BGK, TRT, MRT, RLB, ELB results with parameters from DS (top row) and AS (bottom row) for $N = 128, 256, 512$ in comparison to the analytical model spectrum $E^{\star}(\xi)$ derived from Kolmogorov's theory for HIT.[41]

dissipation range. Compared to MRT and RLB, which show a strong dependence on the Mach number, TRT, BGK and ELB are not sensitive to the used scaling. The latter schemes exhibit a good agreement to the model spectra for the grid resolutions $N = 256$ and $N = 512$.

The observed behavior for each collision operator can be summarized as follows.

- **BGK**: The BGK scheme is able to obtain accurate results, if the grid resolution is chosen with respect to the Kolmogorov length. Otherwise, the higher energy budget in the dissipation range leads to instabilities.
- **TRT**: The proposed “magic parameter” of $\Lambda = 0.25$ is magnitudes too large for turbulence simulation, where τ_+ is usually close to 0.5. The choice of the Λ should be done carefully, due to the observed dependency on the Reynolds number, the Mach number and the grid resolution. The stability issues of BGK are still present in the TRT and are only slightly affected by the choice of Λ.
- **ELB**: Although the entropic scheme is a viscosity controlling scheme it is not able to mimic a turbulence model or to stabilize the simulation. Furthermore, an increased accuracy is not observed in comparison to BGK.
- **MRT**: The accuracy and the stability of MRT strongly depends on the Mach number. If the Mach number is decreased, instabilities arising from the overestimated energy level at the end of the inertial subrange. On the other hand, MRT is able to avoid the stability issues of BGK in underresolved grids.
- **RLB**: The increase of stability based on the regularization guarantees stable simulations for any herein applied grid resolutions, Reynolds numbers and Mach numbers. However, the dissipation rates are strongly damped, which limits the accuracy at low resolutions. In addition, a small Mach number decreases the energy in the dissipation range.

6.3. *On the accuracy and consistency*

The error contributions from dissipation rate and kinetic energy for DS and AS are calculated according to Eq. (38), and summarized in Tables 5–8. Every diverging simulation is indicated by the term “not a number” (nan). The postpositioned value in parenthesis indicates the approximate point in time at which the instabilities occur in the simulation. The $g\mathrm{err}_{L^2}(\epsilon, k)$ error takes the error of the dissipation rate and the turbulent kinetic energy into account to provide an accuracy benchmark value. The validity of this error corresponds to the accuracy of the reference solution LBM-DNS$_{1024}$ that is estimated to 0.01 in Sec. 4. In Fig. 8 the $g\mathrm{err}_{L^2}(\epsilon, k)$ error is calculated for the DS and AS. Moreover, the averaged experimental order of convergence $\overline{EOC}$ was computed as the arithmetic mean of the convergence speeds

$$EOC_{N_i,N_j} = \frac{\ln\left(\frac{g\mathrm{err}^{N_i}_{L^2}(\epsilon,k)}{g\mathrm{err}^{N_j}_{L^2}(\epsilon,k)}\right)}{\ln\left(\frac{N_j}{N_i}\right)}, \tag{45}$$

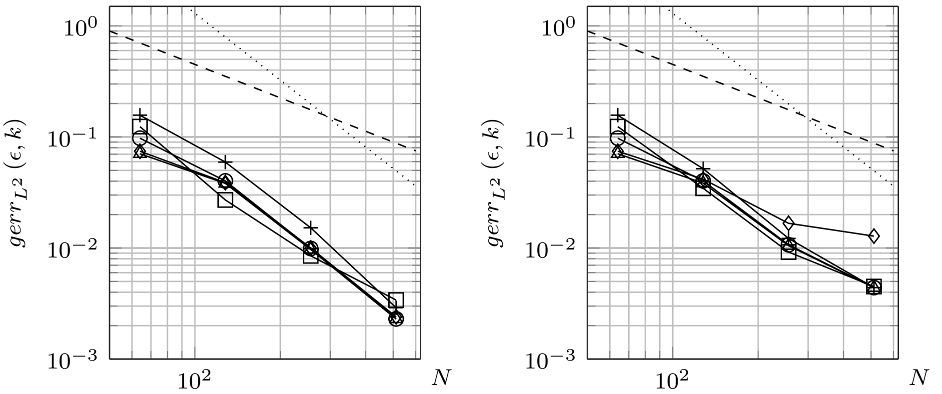

(a) DS, $Re = 800$ (b) AS, $Re = 800$

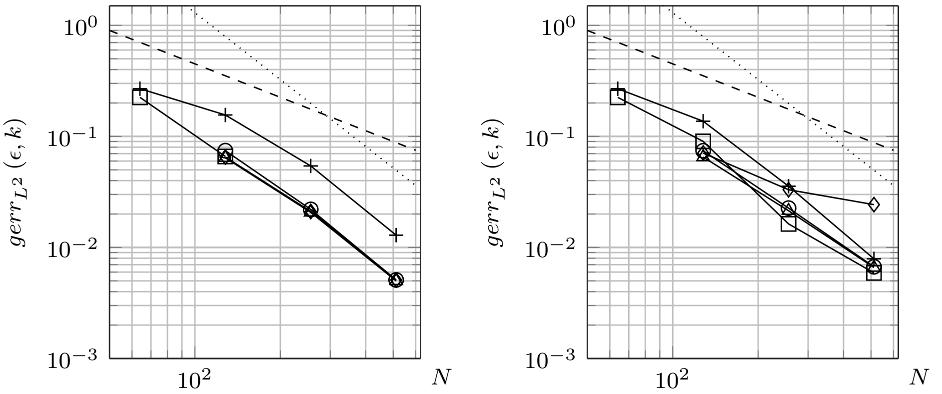

(c) DS, $Re = 1600$ (d) AS, $Re = 1600$

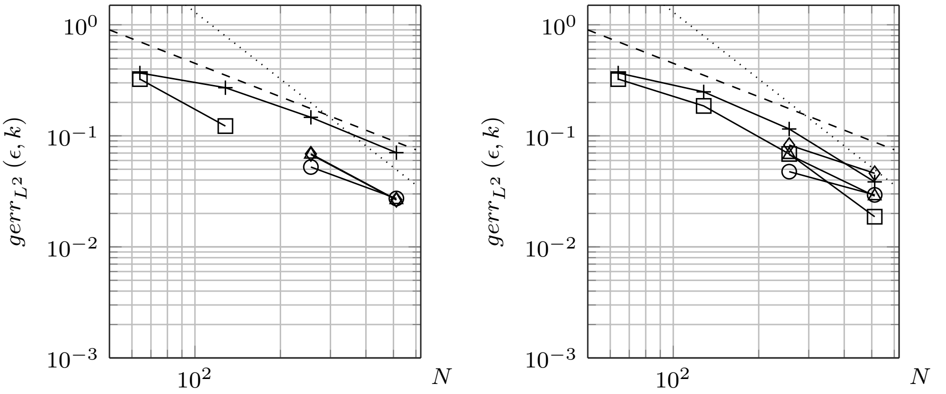

(e) DS, $Re = 3000$ (f) AS, $Re = 3000$

- - - $\mathcal{O}(\Delta x)$ ······· $\mathcal{O}(\Delta x^2)$ △ BGK ○ TRT □ MRT + RLB ◇ ELB

Fig. 8. Global error $\text{gerr}_{L^2}(\epsilon, k)$ for $t \in [0, 10]$ of stable DS (left column) and AS (right column) computations with BGK, TRT, MRT, RLB, ELB at $N = 64, 128, 256, 512$ against the present LBM-DNS$_{1024}$ solution for the TGV flow at Re $= 800, 1600, 3000$.

where $N_i < N_j$ denote two subsequent resolutions. Table 4 provides the convergence order calculations for both scalings.

The results for $\mathrm{Re} = 800$ in Figs. 8(b) and 8(a) underline the significant differences between AS and DS for each collision operator. If the grid resolutions are highly underresolved, the convergence order of BGK, TRT and ELB is $EOC_{64,128} \approx 1$ independent of the applied scaling. However, the convergence speeds for higher grid resolutions are of second order for DS and superlinear for AS. This reduction of the convergence order is related to the Mach number-dependent truncation error, which is strongly pronounced at low Reynolds numbers. Furthermore, the decreasing convergence order for AS leads to inconsistency for higher grid resolutions caused by the constant truncation error. The ELB scheme shows the strongest Mach number dependency, resulting in a drastically reduced convergence speed of $EOC_{256,512} = 0.38$. MRT and RLB exhibit a higher convergence order for smaller grid resolutions, which is induced by the larger error at $N = 64$.

In the case of $\mathrm{Re} = 1600$, the $EOC_{256,512}$ for ELB, TRT and BGK is second order for DS. The corresponding AS value is smaller for BGK and TRT $EOC_{256,512} \approx 1.7$, but strongly decreased for ELB. This indicates that the influence of the truncation error is still present at higher grid resolution but reduced in comparison to $\mathrm{Re} = 800$. In contrast, the convergence speed of RLB is increased for AS, irrespective of the resolution. The $EOC_{64,128}$ for MRT suggests an increased convergence order for DS.

The DS applied at $\mathrm{Re} = 3000$ leads to an $EOC_{256,512} = 1.06$ for RLB. The AS however, increases the $EOC_{256,512}$ to 1.58. For the ELB, the decrease in convergence order from DS to AS is less pronounced for $\mathrm{Re} = 3000$ than for $\mathrm{Re} = 1600$. Similarly,

Table 4. Experimental order of convergence $\overline{EOC}$ for BGK, TRT, MRT, RLB, ELB with parameters from DS and AS. Convergence speeds for subsequent grid resolutions are computed from $\mathrm{gerr}_{L^2}(\epsilon, k)$ for $t \in [0, 10]$ against the present LBM-DNS$_{1024}$ solution for the TGV flow at $\mathrm{Re} = 800, 1600, 3000$.

Re		BGK		TRT		MRT		RLB		ELB	
		DS	AS	DS	AS	DS	AS	DS	AS	DS	AS
800	$EOC_{64,128}$	0.89	0.88	1.28	1.28	2.19	1.85	1.40	1.60	0.94	0.84
	$EOC_{128,256}$	1.98	1.87	2.02	1.91	1.67	1.91	1.97	2.09	1.96	1.32
	$EOC_{256,512}$	2.08	1.25	2.11	1.28	1.32	1.03	2.39	1.47	2.06	0.38
	$\overline{EOC}$	1.65	1.33	1.80	1.49	1.73	1.59	1.92	1.72	1.65	0.85
1600	$EOC_{64,128}$	—	—	—	—	1.77	1.32	0.79	0.97	—	—
	$EOC_{128,256}$	1.63	1.61	1.76	1.72	—	2.47	1.52	1.94	1.63	1.10
	$EOC_{256,512}$	2.05	1.70	2.11	1.75	—	1.47	2.07	2.17	2.05	0.45
	$\overline{EOC}$	1.84	1.65	1.93	1.73	1.77	1.75	1.46	1.70	1.84	0.77
3000	$EOC_{64,128}$	—	—	—	—	1.41	0.80	0.44	0.57	—	—
	$EOC_{128,256}$	—	—	—	—	—	1.44	0.89	1.11	—	—
	$EOC_{256,512}$	1.36	1.23	0.94	0.70	—	1.88	1.06	1.58	1.37	0.84
	$\overline{EOC}$	1.36	1.23	0.94	0.70	1.41	1.37	0.79	1.09	1.37	0.84

Table 5. Dissipation rate error $\mathrm{err}_{L^2}(\epsilon)$ for $t \in [0, 10]$ of DS computations with BGK, TRT, MRT, RLB, ELB at $N = 64, 128, 256, 512$ against the present LBM-DNS$_{1024}$ solution for the TGV flow at $\mathrm{Re} = 800, 1600, 3000$. The approximate instability onset at time $t \approx \tilde{t}$ is denoted as "nan ($\tilde{t}$)".

DS		$\mathrm{err}_{L^2}(\epsilon)$				
Re	N	BGK	TRT	MRT	RLB	ELB
800	64	0.1227	0.1764	0.2271	0.2997	0.1297
	128	0.0657	0.0695	0.0416	0.1090	0.0667
	256	0.0146	0.0150	0.0116	0.0255	0.0149
	512	0.0030	0.0030	0.0050	0.0042	0.0031
1600	64	nan (7.5)	nan (7.6)	0.4352	0.5255	nan (7.5)
	128	0.1201	0.1404	0.1209	0.3043	0.1220
	256	0.0372	0.0399	nan (7.3)	0.1046	0.0380
	512	0.0084	0.0087	nan (1.5)	0.0244	0.0086
3000	64	nan (6.9)	nan (6.7)	0.6366	0.7214	nan (6.9)
	128	nan (7.6)	nan (6.8)	0.2340	0.5355	nan (7.6)
	256	0.1310	0.1000	nan (4.5)	0.2890	0.1327
	512	0.0505	0.0518	nan (0.9)	0.1378	0.0506

the $\overline{EOC}$ reduction for BGK and TRT from DS to AS lessens with the decreasing influence of Ma at this Reynolds number.

Moreover, the change in stability from DS to AS can be evaluated from Tables 5 and 6. The coarse grid induced instabilities for BGK, TRT and ELB set in at similar points in time for both scalings. A coarse grid leads to earlier occurring instabilities when the Reynolds number is increased. Similarly, low Mach number instabilities of

Table 6. Dissipation rate error $\mathrm{err}_{L^2}(\epsilon)$ for $t \in [0, 10]$ of AS computations with BGK, TRT, MRT, RLB, ELB at $N = 64, 128, 256, 512$ against the present LBM-DNS$_{1024}$ solution for the TGV flow at $\mathrm{Re} = 800, 1600, 3000$. The approximate instability onset at time $t \approx \tilde{t}$ is denoted as "nan ($\tilde{t}$)".

AS		$\mathrm{err}_{L^2}(\epsilon)$				
Re	N	BGK	TRT	MRT	RLB	ELB
800	64	0.1227	0.1764	0.2271	0.2997	0.1297
	128	0.0642	0.0680	0.0557	0.0918	0.0706
	256	0.0140	0.0143	0.0112	0.0174	0.0266
	512	0.0048	0.0048	0.0049	0.0048	0.0235
1600	64	nan (7.5)	nan (7.6)	0.4352	0.5254	nan (7.5)
	128	0.1206	0.1385	0.1693	0.2646	0.1316
	256	0.0367	0.0391	0.0263	0.0650	0.0609
	512	0.0094	0.0096	0.0079	0.0119	0.0470
3000	64	nan (6.9)	nan (6.7)	0.6366	0.7213	nan (6.9)
	128	nan (7.6)	nan (6.8)	0.3622	0.4894	nan (7.6)
	256	0.1279	0.0884	0.1307	0.2227	0.1592
	512	0.0521	0.0534	0.0325	0.0716	0.0894

Table 7. Turbulent kinetic energy error $\mathrm{err}_{L^2}(k)$ for $t \in [0, 10]$ of DS computations with BGK, TRT, MRT, RLB, ELB at $N = 64, 128, 256, 512$ against the present LBM-DNS$_{1024}$ solution for the TGV flow at Re $= 800, 1600, 3000$. The approximate instability onset at time $t \approx \tilde{t}$ is denoted as "nan ($\tilde{t}$)".

DS		$\mathrm{err}_{L^2}(k)$				
Re	N	BGK	TRT	MRT	RLB	ELB
800	64	0.0184	0.0186	0.0209	0.0148	0.0191
	128	0.0108	0.0108	0.0125	0.0098	0.0110
	256	0.0049	0.0049	0.0055	0.0048	0.0050
	512	0.0017	0.0017	0.0018	0.0017	0.0017
1600	64	nan (7.5)	nan (7.6)	0.0142	0.0127	nan (7.5)
	128	0.0084	0.0084	0.0111	0.0076	0.0085
	256	0.0041	0.0041	nan (7.3)	0.0038	0.0042
	512	0.0015	0.0015	nan (1.5)	0.0014	0.0015
3000	64	nan (6.9)	nan (6.7)	0.0124	0.0154	nan (6.9)
	128	nan (7.6)	nan (6.8)	0.0110	0.0073	nan (7.6)
	256	0.0049	0.0047	nan (4.5)	0.0046	0.0050
	512	0.0026	0.0027	nan (0.9)	0.0035	0.0026

the MRT set in earlier with increasing Re. This reveals that the stability of the MRT scheme depends on the Re and Ma. Comparable observations are found by Dellar,[13] who proved that MRT diverged in the order of $\mathcal{O}(\mathrm{Ma}^{-1})$ for an inclined jet test case.

Additionally, the costs for diffusive scaling can be estimated. The number of arithmetic operations doubles for $N = 128$, quadruples for $N = 256$ and increases

Table 8. Turbulent kinetic energy error $\mathrm{err}_{L^2}(k)$ for $t \in [0, 10]$ of AS computations with BGK, TRT, MRT, RLB, ELB at $N = 64, 128, 256, 512$ against the present LBM-DNS$_{1024}$ solution for the TGV flow at Re $= 800, 1600, 3000$. The approximate instability onset at time $t \approx \tilde{t}$ is denoted as "nan ($\tilde{t}$)".

AS		$\mathrm{err}_{L^2}(k)$				
Re	N	BGK	TRT	MRT	RLB	ELB
800	64	0.0185	0.0186	0.0209	0.0148	0.0191
	128	0.0125	0.0125	0.0133	0.0119	0.0129
	256	0.0071	0.0071	0.0072	0.0070	0.0067
	512	0.0040	0.0040	0.0040	0.0040	0.0022
1600	64	nan (7.5)	nan (7.6)	0.0143	0.0127	nan (7.5)
	128	0.0099	0.0100	0.0111	0.0095	0.0099
	256	0.0062	0.0062	0.0063	0.0061	0.0053
	512	0.0038	0.0038	0.0039	0.0038	0.0017
3000	64	nan (6.9)	nan (6.7)	0.0124	0.0153	nan (6.9)
	128	nan (7.6)	nan (6.8)	0.0098	0.0085	nan (7.6)
	256	0.0071	0.0068	0.0067	0.0078	0.0060
	512	0.0053	0.0054	0.0049	0.0054	0.0026

eightfold for $N = 512$. Therefore, a fundamental recommendation of the scaling can be made for RLB and MRT, where the AS significantly improves the accuracy for the RLB at higher Reynolds numbers and leads to a stable simulation if MRT is applied. For ELB, the error displays a strong Ma-dependency. Therefore, DS is preferable. In the case of BGK and TRT no uniform recommendation can be given and should be decided on a case-by-case basis.

7. Conclusion

The collision schemes BGK, TRT, MRT, RLB and ELB for LBM DNS calculations of DHIT were presented and discussed concerning stability, accuracy and consistency. The three-dimensional energy spectrum, integral quantities and resulting global error measurements with respect to a priorly validated high resolution LBM-DNS$_{1024}$ reference, were investigated. Subsequently, lattice Mach number, Reynolds number and resolution dependencies of the solution for the individual collision schemes were quantified and visualized. A comparison of AS and DS was executed and results were analyzed in detail.

The present DS observations for BGK agree with previous test cases[38] and theoretical predictions,[27] approving the suitability for accurate, DHIT DNS computations in the incompressible limit.

The BGK and TRT results for AS only slightly differed from the ones obtained with DS at high Reynolds numbers. However, at the lowest Reynolds number $\mathrm{Re} = 800$ the constant truncation error of AS is more pronounced, which leads to a diminished convergence speed. Additionally, the tests proved that with the AS approach, the $\overline{EOC}$ for the RLB scheme is increased at $\mathrm{Re} = 1600$ and $\mathrm{Re} = 3000$. The absence of instabilities, using AS for the MRT scheme, is a clear advantage over DS at high Reynolds numbers, which resulted in instabilities induced by decreasing Ma and amplified with increasing Re. When comparing the results with the ELB scheme to the ones obtained with BGK, neither could instabilities for low resolutions be prevented with the additional entropy correction, nor was an increased accuracy noted. This absence of higher accuracy and stability was also observed by Luo *et al.*[32] for a single relaxation-time entropic LBM scheme without a bulk viscosity modification. Besides, the AS results with the ELB scheme exhibited strongly reduced accuracy as opposed to the DS parameter setting.

We draw the conclusion that, when executing LBM DNS DHIT computations with the MRT, and RLB for high Reynolds numbers as defined here, reduced runtime along with increased stability for the MRT scheme and an increased $\overline{EOC}$ for the RLB scheme, approve that it suffices to lower the lattice Mach number to the weakly compressible regime and retain a ratio of $\Delta t \sim \Delta x$. In case of the ELB scheme, decreasing Ma is still advisable, due to the strong decrease in accuracy observed with AS. In contrast to that, a universal recommendation cannot be made for the BGK and the TRT scheme, because the influence of the Mach number truncation error corresponds to the Reynolds number. AS leads per definition to a constant truncation error resulting in inconsistency, if the resolution goes to infinity. Despite these effects, the increased effort of DS and the decreasing influence of the truncation error at larger Reynolds numbers, justify a lattice velocity of $u_L = 0.1$ for high Reynolds number flows.

Since we ascertained a stability dependency on Re, Ma and N for the MRT, it is believed that future studies on relaxation time optimization for kinetic moments, connecting the present work with results from different test cases (see Refs. 13, 33, 47), should lead to more satisfying simulations in the incompressible limit. The fact that the consistently stable RLB scheme constitutes a subclass of MRT,[30] underlines the possibility of stabilizing MRT computations in the incompressible limit for DHIT with non-hydrodynamic relaxation times as functions of Re, Ma and N. Furthermore, recent developments such as the cumulant lattice Boltzmann[15] model provide another approach to circumvent the Mach number-dependent stability issues of the MRT.

In addition, the observed close interaction of τ_- with the solution behavior for the TRT, also motivates the possible necessity of relaxation time scaling. We found that the value of the "magic parameter", which was suggested in previous literature,[17,18] required further scaling to yield stable results at all. Moreover, a constant Λ for TRT, did, against expectations,[27] not lead to stability enhancing features throughout every tested parameter combination. Although dissipative effects were partly controllable, low resolution induced instabilities could not be avoided. Hence, an advisable "magic parameter" handling for three-dimensional DHIT computations with the TRT scheme is yet to be investigated and optimized, for example by extending the theory-based work of Ginzburg *et al.*,[17,18] combined with a similar analysis as proposed above.

The computationally demanding, though, in terms of solution quality unsatisfying features of the ELB, underline the requisiteness of studying more advanced entropy consistent schemes such as the Karlin–Bösch–Chikatamarla (KBC) model.[25] One advantage of the Karlin–Chikatamarla–Bösch model in comparison to ELB is the reduced artificial energy injection in high wavenumbers at low resolutions and the consequential stability enhancement.[7]

Finally, testing subsequent versions of each collision scheme, comprising deficiency compensating features or consistently incorporated turbulence models,[35] should be of major concern to achieve stable and sufficiently accurate LBM results for turbulent flows in general. As an example of analyzing a more complex canonical flow, a comparison of RLB, MRT, and BGK for wall-bounded turbulence can be found in Ref. 38. At higher Reynolds numbers, where the turbulent boundary is difficult to resolve due to the large number of required grid points, wall-modeled approaches are advantageous. So far, wall models for BGK,[19] MRT[36] and cumulant LBM[39] have been successfully implemented.

Acknowledgments

This work was performed on the computational resource ForHLR II funded by the Ministry of Science, Research and the Arts Baden-Württemberg and DFG ("Deutsche Forschungsgemeinschaft").

References

1. S. Ansumali, I. Karlin, C. E. Frouzakis and K. Boulouchos, *Phys. A, Stat. Mech. Appl.* **359**, 289 (2006).
2. S. Ansumali and I. V. Karlin, *Phys. Rev. E* **65**, 056312 (2002).
3. L. d. L. X. Augusto, J. Ross-Jones, G. C. Lopes, P. Tronville, J. A. S. Gonçalves, M. Rädle and M. J. Krause, *Commun. Comput. Phys.* **23**, 910 (2018).
4. P. L. Bhatnagar, E. P. Gross and M. Krook, *Phys. Rev.* **94**, 511 (1954).
5. O. N. Boratav and R. B. Pelz, *Phys. Fluids* **6**, 2757 (1994).
6. F. Bösch, *Entropic lattice Boltzmann models for fluid dynamics*, PhD thesis, ETH Zurich (2017).
7. F. Bösch, S. S. Chikatamarla and I. V. Karlin, *Phys. Rev. E* **92**, 043309 (2015).
8. M. E. Brachet, *Fluid Dynamics Res.* **8**, 1 (1991).
9. M. E. Brachet, D. I. Meiron, S. A. Orszag, B. Nickel, R. H. Morf and U. Frisch, *J. Fluid Mech.* **130**, 411 (1983).
10. S. Chen, Z. Wang, X. Shan and G. D. Doolen, *J. Stat. Phys.* **68**, 379 (1992).
11. S. Chikatamarla, S. Ansumali and I. Karlin, *Phys. Rev. Lett.* **97**, 010201 (2006).
12. J. DeBonis, Solutions of the Taylor–Green vortex problem using high-resolution explicit finite difference methods, in *51st AIAA Aerospace Sciences Meeting including the New Horizons Forum and Aerospace Exposition*, p. 382 (2013).
13. P. J. Dellar, *J. Comput. Phys.* **190**, 351 (2003).
14. D. d'Humières, *Philos. Trans. Roy. Soc. London A: Math. Phys. Eng. Sci.* **360**, 437 (2002).
15. M. Geier, M. Schönherr, A. Pasquali and M. Krafczyk, *Comput. Math. Appl.* **70**, 507 (2015).
16. W. K. George, *Lectures in Turbulence for The 21st Century* (Chalmers University of Technology, 2013).
17. I. Ginzburg, D. d'Humières and A. Kuzmin, *J. Stat. Phys.* **139**, 1090 (2010).
18. I. Ginzburg, F. Verhaeghe and D. d'Humieres, *Commun. Comput. Phys.* **3**, 427 (2008).
19. M. Haussmann, A. C. Barreto, G. L. Kouyi, N. Rivière, H. Nirschl and M. J. Krause, *Comput. Math. Appl.* (2019) (in press).
20. X. He and L.-S. Luo, *Phys. Rev. E* **56**, 6811 (1997).
21. T. Henn, V. Heuveline, M. J. Krause and S. Ritterbusch, Aortic coarctation simulation based on the lattice Boltzmann method: Benchmark results, in *Statistical Atlases and Computational Models of the Heart, Imaging and Modelling Challenges*, eds. O. Camara, T. Mansi, M. Pop, K. Rhode, M. Sermesant, and A. Young, (Springer, Berlin, 2013), pp. 34–43.
22. V. Heuveline and M. J. Krause, OpenLB: towards an efficient parallel open source library for lattice Boltzmann fluid flow simulations, in *Int. Workshop on State-of-the-Art in Scientific and Parallel Computing. PARA*, Vol. **9** (2010).
23. V. Heuveline, M. J. Krause and J. Latt, *Comput. Math. Appl.* **58**, 1071 (2009).
24. W. A. Kareem, S. Izawa, A.-K. Xiong and Y. Fukunishi, *Comput. Math. Appl.* **58**, 1055 (2009).
25. I. V. Karlin, F. Bösch, and S. Chikatamarla, *Phys. Rev. E* **90**, 031302 (2014).

26. M. J. Krause, F. Klemens, T. Henn, R. Trunk and H. Nirschl, *Particuology* **34**, 1 (2017).
27. T. Krüger, H. Kusumaatmaja, A. Kuzmin, O. Shardt, G. Silva and E. M. Viggen, *The Lattice Boltzmann Method*, Vol. **10** (Springer, 2017).
28. P. Lallemand and L.-S. Luo, *Phys. Rev. E* **61**, 6546 (2000).
29. P. Lallemand and L.-S. Luo, *Phys. Rev. E* **68**, 036706 (2003).
30. J. Latt and B. Chopard, *Math. Comput. Simul.* **72**, 165 (2006).
31. K. Lee, D. Yu and S. S. Girimaji, *Int. J. Comput. Fluid Dyn.* **20**, 401 (2006).
32. L.-S. Luo, W. Liao, X. Chen, Y. Peng, W. Zhang *et al.*, *Phys. Rev. E* **83**, 056710 (2011).
33. L.-S. Luo, W. Liao, X. Chen, Y. Peng, W. Zhang *et al.*, *Phys. Rev. E* **83**, 056710 (2011).
34. L.-S. Luo, D. Qi and L.-P. Wang, in *High Performance Scientific and Engineering Computing* (Springer, 2002), pp. 123–130.
35. O. Malaspinas and P. Sagaut, *J. Fluid Mech.* **700**, 514 (2012).
36. O. Malaspinas and P. Sagaut, *J. Comput. Phys.* **275**, 25 (2014).
37. R. Mei, L.-S. Luo, P. Lallemand and D. d'Humières, *Comput. Fluids* **35**, 855 (2006).
38. P. Nathen, D. Gaudlitz, M. J. Krause and N. A. Adams, *J. Commun. Comput. Phys.* **23**, 846 (2017).
39. A. Pasquali, M. Geier and M. Krafczyk, *Comput. Math. Appl.* (2017) (in press).
40. Y. Peng, W. Liao, L.-S. Luo, and L.-P. Wang, *Comput. Fluids* **39**, 568 (2010).
41. S. B. Pope, *Turbulent Flows* (Cambridge University Press, New York, USA, 2001).
42. X. Shan, X.-F. Yuan and H. Chen, *J. Fluid Mech.* **550**, 413 (2006).
43. G. Tauzin, L. Biferale, M. Sbragaglia, A. Gupta, F. Toschi, A. Bartel and M. Ehrhardt, *Comput. Fluids* **172**, 241 (2018).
44. R. Trunk, T. Henn, W. Dörfler, H. Nirschl and M. J. Krause, *J. Comput. Sci.* **17**, 438 (2016).
45. W. M. Van Rees, A. Leonard, D. Pullin and P. Koumoutsakos, *J. Comput. Phys.* **230**, 2794 (2011).
46. D. A. Wolf-Gladrow. *Lattice-gas Cellular Automata and Lattice Boltzmann Models: An Introduction* (Springer, 2004).
47. H. Xu, O. Malaspinas and P. Sagaut, *J. Comput. Phys.* **231**, 7335 (2012).
48. T. Yasduda, T. Hashimoto, H. Minagawa, K. Morinishi and N. Satofuka, *Proc. Eng.* **61**, 173 (2013).
49. H. Yu, S. S. Girimaji and L.-S. Luo, *J. Comput. Phys.* **209**, 599 (2005).

4

Near-Wall-Modeled Large-Eddy Simulation of a Coriolis Mass Flowmeter

This chapter was published in the following article:

M. Haussmann, A. Claro Barreto, G. Lipeme Kouyi, N. Rivière, H. Nirschl and M. J. Krause
Large-eddy simulation coupled with wall models for turbulent channel flows at high Reynolds numbers with a lattice Boltzmann method – Application to Coriolis mass flowmeter
Computers & Mathematics with Applications, 78.10 (2019)
https://doi.org/10.1016/j.camwa.2019.04.033

My contribution according to the contributor role taxonomy system [14] included conceptualization, methodology, software, validation, formal analysis, investigation, data curation, writing – original draft, visualization and project administration.

Computers and Mathematics with Applications 78 (2019) 3285–3302

Contents lists available at ScienceDirect

Computers and Mathematics with Applications

journal homepage: www.elsevier.com/locate/camwa

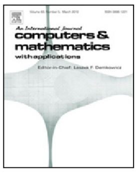

Large-eddy simulation coupled with wall models for turbulent channel flows at high Reynolds numbers with a lattice Boltzmann method — Application to Coriolis mass flowmeter[☆]

Marc Haussmann[a,*], Alejandro CLARO BARRETO[b], Gislain LIPEME KOUYI[b], Nicolas Rivière[d], Hermann Nirschl[c], Mathias J. Krause[a]

[a] *Lattice Boltzmann Research Group, Karlsruhe Institute of Technology, Germany*
[b] *University of Lyon, National Institute of Applied Sciences of Lyon - INSA Lyon, Laboratory Wastes Water Environment Pollutions (DEEP), France*
[c] *Institute for Mechanical Process Engineering and Mechanics, Karlsruhe Institute of Technology, Germany*
[d] *University of Lyon, INSA Lyon, Laboratory of Fluid Mechanics and Acoustics (LMFA), France*

ARTICLE INFO

Article history:
Received 17 October 2018
Received in revised form 15 February 2019
Accepted 27 April 2019
Available online 20 May 2019

Keywords:
Turbulent flow
Large-eddy simulation
BGK
OpenLB
Wall function
Coriolis mass flowmeter

ABSTRACT

The numerical prediction of pressure drop within wall-bounded flow domains at high Reynolds numbers (Re) using a large-eddy simulation (LES) approach is a challenging task for industrial applications because the fluid domain is usually underresolved. A lattice Boltzmann method (LBM) with Bhatnagar, Gross and Krook (BGK) collision operator coupled with the Smagorinsky–Lilly turbulence model is used to model these wall-bounded turbulent flows. The near wall region is modelled using wall functions to decrease the required mesh resolution for high Re. The influence of different velocity boundary approaches and wall functions is investigated for the benchmark bi-periodic fully developed turbulent channel flow for friction Reynolds numbers (Re_τ) of 1000, 2000 and 5200. This benchmark case is validated against direct numerical simulation (DNS) results for turbulent statistics of 1st and 2nd order. Based on this validation, the pressure drop of an industrial Coriolis mass flowmeter is compared to experimental data for Re up to 127 800. The error of the pressure drop calculation in underresolved grids is reduced by two orders of magnitude in comparison to a no-slip approach for curved boundaries.

1. Introduction

The pressure drop in a pipeline system of a plant is a key parameter to scale the size of pumps and the associated investment and operating costs [1]. Common pipeline elements, e.g. pipe bends or flow dividers, are described by well examined empirical correlations. However, manufacturer-specific designs of special elements, as flow meters, are either not covered by these correlations or they suffer from a lack of accuracy. The numerical prediction of pressure drops is an alternative to expensive experiments or to the development of new empirical correlations, which are still dedicated

---

[☆] This document is a collaborative effort.

[*] Corresponding author.

E-mail addresses: marc.haussmann@kit.edu (M. Haussmann), alejandro.claro-barreto@insa-lyon.fr (A.C. BARRETO), gislain.lipeme-kouyi@insa-lyon.fr (G.L. KOUYI), nicolas.riviere@insa-lyon.fr (N. Rivière), hermann.nirschl@kit.edu (H. Nirschl), mathias.krause@kit.edu (M.J. Krause).

https://doi.org/10.1016/j.camwa.2019.04.033

to a certain flow regime. The numerical prediction within turbulent flows at high Reynolds numbers (Re) is challenging because of the three-dimensional, unsteady and irregular nature of turbulence [2]. Besides, wall-bounded turbulent flows add a degree of complexity due to the wall-near region treatment.

The computational cost of wall-resolving approaches is $\mathcal{O}(\mathrm{Re}^{1.8})$ in the wall-near region, while it is only $\mathcal{O}(\mathrm{Re}^{0.4})$ in the outer region [3]. This fact leads to a tremendous increase of computation time due to the higher mesh resolution required. Therefore, different approaches have been proposed to model the effects that rise in the turbulent boundary layer. The wall model approaches [4–6] are usually based on an empirical function. They cover the course of the velocity in the wall-near region due to the high velocity gradient in vicinity of the wall that is otherwise highly underpredicted.

Wall function modelling was first accessed by the Reynolds averaged Navier–Stokes (RANS) approaches to allow higher grid spacing for the wall region [4]. The RANS approaches require extra boundary conditions for each turbulent quantity, e.g. the k-epsilon model demands two additional conditions. Moreover, the position of the first grid point is generally restricted to the logarithmic layer of the time-averaged stream-wise velocity to ensure the taken hypothesizes [7]. These functions can be implemented on the large-eddy simulation (LES) models by applying the same assumptions as for RANS approaches, e.g. the numerical estimation of the time-averaged wall shear stress. The main objective is thereby that turbulence quantities in the bulk domain can be addressed with a higher accuracy.

The wall function approach within an LES framework was introduced by Deardoff [8] in 1970 with a logarithmic average velocity profile to model implicitly the near-wall region. Laudner and Spalding [4] proposed to calculate the mean wall shear stress and the turbulent viscosity from the logarithmic velocity profile. This wall function was applied to a RANS k-epsilon model. Based on this idea, other researches proposed different wall functions within an LES framework. Schumann [9] proposed a two layer equations model under the assumption of the so called subgrid scale (SGS) motion model. This model was extended by Schmitt [6] to three layers in order to approximate the buffer layer with a higher accuracy. Furthermore, Werner and Wengle [5] postulated an approach to circumvent iterative schemes to estimate the wall shear stress and calculate it directly using a power-law profile. A special formulation for curved boundaries was given by Shih et al. [10] that takes into account encountered adverse and favourable pressure gradients.

In the lattice Boltzmann (LB) community wall models for turbulent flows were initially investigated in the context of a k-epsilon RANS model [11,12]. Wall functions coupled with LES models were first proposed by Malaspinas and Sagaut [13]. They modelled the near wall region with the Musker profile and the bulk domain with a multi-relaxation time (MRT) LB scheme. Their numerical results were in good agreement against DNS data [14,15]. Schneider [16] used the MRT-LES approach coupled with a three equations model based on the Werner and Wengle function [5]. In 2017 Pasquali et al. [17] proposed an approach based on the cumulant LB method to obtain the needed velocity information in a local manner which is suitable for graphic processing units.

The previous works simulated mainly benchmark cases of simple geometry, e.g. the bi-periodic turbulent channel, even if the LB method is suitable for complex geometries [18–20] thanks to its highly parallel algorithm [21,22]. Also, they used only the MRT LB approach even though Nathen et al. [23] have shown the suitability of a single relaxation time (SRT) model for wall-bounded turbulent flows. Therefore, the applicability of the SRT model proposed by Bhatnagar, Gross and Krook (BGK) [24] to mimic turbulent industrial cases still needs to be investigated. Also no quantitative error analysis of the Reynolds stresses has been considered so far.

The main aim of this paper is to demonstrate that an SRT-LBM coupled to a wall function is able to predict the turbulent statistics of 1st and 2nd order in highly underresolved grids with sufficient accuracy and therefore suitable for industrial and engineering field applications.

In this work, we propose the adaption of the Malaspinas and Sagaut approach to a SRT-LBM. In addition, we evaluated several velocity boundary schemes and wall function approaches according to different grid resolutions and friction Reynolds numbers (Re_τ). We performed detailed error calculations and convergence speed analyses for the Reynolds stresses, which had never before been demonstrated for an LBM wall function approach. This scheme is applied, for the first time, to an industrial Coriolis mass flowmeter (CMF) to predict the pressure drop at high Re numbers.

The paper is organized in the following way: Section 2 gives a brief introduction to the SRT-LBM coupled to the LES model. Furthermore, the used wall function equations are described in detail. The results of the validation case, the bi-periodic turbulent channel flow, are pointed out in Section 3. Based on this validation, the pressure drop study for the application case, the CMF, is presented in Section 4. Finally, Section 5 summarizes the results and focuses on future research topics.

2. Theoretical background and modelling

2.1. Lattice Boltzmann method

An LBM simplifies the kinetic Boltzmann equation to a discrete set of particle distribution functions f_i, $i = 0, 1, \ldots, q-1$, i.e. the movement of particles is restricted to a finite number of directions. In the case of a three dimensional lattice $D3Q15$, $D3Q19$ and $D3Q27$ are the most popular descriptor sets employed to solve e.g. the Navier–Stokes equation. The LB equation with external body force proposed by Guo et al. [25] is given by

$$f_i(t + \Delta t, \mathbf{x} + \mathbf{c}_i \Delta t) = f_i(t, \mathbf{x}) + \Omega_i + \Delta t\, F_i(\rho, \mathbf{u}^*)\,, \tag{1}$$

where $\mathbf{x}$ is the position vector in the discrete lattice; Δt is the discrete time step; $\mathbf{c}_i$ is the discrete velocity; Ω_i is the collision operator; and $F_i(\rho, \mathbf{u}^*)$ is the external body force. The discrete velocities in $D3Q19$ are given by

$$c_i = \begin{cases} (0,0,0) & i = 0 \\ (\pm 1,0,0),\ (0,\pm 1,0),\ (0,0,\pm 1) & i = 1,2,\ldots,6 \\ (\pm 1,\pm 1,0),\ (\pm 1,0,\pm 1),\ (0,\pm 1,\pm 1) & i = 7,8,\ldots,18 \end{cases} \tag{2}$$

The collision operator is approximated with the SRT model proposed by Bhatnagar, Gross and Krook [24], written as

$$\Omega_i = -\frac{1}{\tau}(f_i(t,\mathbf{x}) - f_i^{eq}(\rho,\mathbf{u}^*)), \tag{3}$$

where f_i^{eq} is the discrete Maxwell–Boltzmann equilibrium distribution function; and τ is the relaxation time towards this equilibrium. The collision operator Ω_i relaxes the particle distribution f_i towards the equilibrium f_i^{eq} while conserving mass and momentum. The particle distribution function at equilibrium f_i^{eq} and the external body force $F_i\,(\rho,\mathbf{u}^*)$ are given by

$$f_i^{eq}\left(\rho,\mathbf{u}^*\right) = \rho\omega_i[1 + \frac{\mathbf{c}_i\cdot\mathbf{u}^*}{c_s^2} + \frac{(\mathbf{c}_i\mathbf{c}_i - c_s^2\mathbf{I}) : \mathbf{u}^*\mathbf{u}^*}{2c_s^4}], \tag{4}$$

$$F_i\left(\rho,\mathbf{u}^*\right) = \rho\omega_i\left(1 - \frac{1}{2\tau}\right)[\frac{\mathbf{c}_i - \mathbf{u}^*}{c_s^2} + \frac{\mathbf{c}_i(\mathbf{c}_i\cdot\mathbf{u}^*)}{2c_s^4}]\cdot\mathbf{g}, \tag{5}$$

where ω_i are the lattice weights obtained by the Gauss–Hermite quadrature [26,27]; $c_s = 1/\sqrt{3}$ is the speed of sound of the lattice; $\delta_{\alpha\beta}$ is the Kronecker operator; $\mathbf{g}$ is the external body acceleration.

The zeroth to second moments of f_i give the macroscopic density ρ, momentum $\rho\mathbf{u}^*$, and momentum flux $\mathbf{\Pi}$, respectively. These discrete moments of f_i are given by

$$\rho = \sum_{i=0}^{q-1} f_i\,, \tag{6}$$

$$\rho\mathbf{u}^* = \sum_{i=0}^{q-1}(\mathbf{c}_i f_i) + \frac{1}{2}\mathbf{F}\,, \tag{7}$$

$$\prod\nolimits_{\alpha\beta} = \sum_{i=0}^{q-1} c_{i\alpha}c_{i\beta}f_i. \tag{8}$$

Besides, the kinematic viscosity of the fluid ν is related to the relaxation time τ as follows

$$\nu = c_s^2\,(\tau - 0.5)\,. \tag{9}$$

The momentum equation (7) contains the term $\frac{1}{2}\mathbf{F}$ to correct the momentum calculation due to the body force. A multi-scale Chapman–Enskog expansion of the lattice Boltzmann equation (1) allows to recover the Navier–Stokes equations with a body force for weakly-compressible flows [25,28,29]

An LB algorithm is decomposed in 2 steps: the collision step and the streaming step. The collision step corresponds to the right-hand-side of Eq. (1). Once the f_i are updated, the streaming step takes place according to the left-hand-side of Eq. (1).

2.2. *Turbulence simulation: Large-eddy approach*

Usually, the LES is implemented within the LB framework by replacing the molecular viscosity ν with an effective viscosity ν_{eff} [30]. The ν_{eff} allows to model the non-resolved scales by adding a turbulent viscosity ν_{turb}. The Smagorinsky–Lilly model [31] was used in this research. The ν_{eff} is given by

$$\nu_{eff} = \nu + \nu_{turb}, \quad \textit{with} \quad \nu_{turb} = (C\Delta)^2|\bar{\mathbf{S}}|, \tag{10}$$

where C is the Smagorinsky constant; $\Delta = (\Delta x\Delta y\Delta z)^{1/3}$ is the grid filter; and $|\bar{\mathbf{S}}| = \sqrt{2\,\bar{\mathbf{S}}_{\alpha\beta}\bar{\mathbf{S}}_{\alpha\beta}}$ is the magnitude of the filtered strain rate $\bar{\mathbf{S}}_{\alpha\beta} = \frac{1}{2}\left(\frac{\partial\bar{u}_\alpha}{\partial x_\beta} + \frac{\partial\bar{u}_\beta}{\partial x_\alpha}\right)$.

It is well known that the Smagorinsky–Lilly model is not adapted for wall-bounded flows because it is too dissipative for the near-wall region [32]. One way to overcome this limitation is to use a van Driest damping function [33] defined as

$$\nu_{turb} = \tilde{\rho}[\kappa y[1 - e^{-y^+/A^+}]]^2|\partial u/\partial y|\,, \tag{11}$$

where $\tilde{\rho}$ is the average density; $\kappa = 0.4$ is the von Karman constant, this parameter varies between 0.37 and 0.41 [34]; $|\partial u/\partial y|$ is the magnitude of the streamwise velocity gradient along the wall-normal direction; $A^+ = 26$ is the van Driest parameter; $y^+ = y\tilde{u}_\tau/\nu$ is the dimensionless normal distance, y, away from the wall, with $\tilde{u}_\tau$ the friction velocity given by

$$\tilde{u}_\tau = \sqrt{\tilde{\tau}_w/\tilde{\rho}}. \tag{12}$$

where $\tilde{\tau}_w$ is the average shear stress.

Malaspinas and Sagaut [35] presented a consistent framework to implement LES within LBM framework. They have shown that for weakly compressible turbulent flows the relaxation time τ can be replaced by an effective relaxation time τ_{eff} via

$$\tau_{eff} = \tau + \tau_{turb}, \qquad \tau_{turb} = \nu_{turb}/c_s^2\,, \tag{13}$$

where τ_{turb} is the turbulent relaxation time.

From a macroscopic approach, the filtered strain rate $\bar{\mathbf{S}}$ needs to be computed in order to estimate the turbulent or effective viscosity parameter. Malaspinas and Sagaut [35] obtained an explicit expression for the BGK model without external body force using a local method. From a mesoscopic approach, the turbulent relaxation time τ_{turb} is the interesting quantity to be computed in order to obtain the effective relaxation time τ_{eff}, which is needed for the collision step on Eq. (1). The turbulent relaxation time τ_{turb} with a local method is given by

$$\tau_{turb} = \sqrt{\tau^2 + \frac{2(C\Delta)^2}{\bar{\rho}\; c_s^4}\sqrt{2\,\breve{\Pi}^{(1)} : \breve{\Pi}^{(1)}}} - \frac{\tau}{2}, \tag{14}$$

where $\breve{\Pi}^{(1)} = \bar{\rho}(\mathbf{F}\mathbf{u}^* + \mathbf{u}^*\mathbf{F})/2 + \Pi^{(1)}$ is the modified momentum flux; and $\bar{\rho} = \sum \bar{f}_i$ is the filtered density. It should be noted that the distribution function f_i becomes the filtered distribution function $\bar{f}_i$ within the LES framework. Eq. (14) is used for the fluid lattices, whereas Eq. (11) is for the boundary lattices.

2.3. Lattice Boltzmann boundary conditions

A Dirichlet velocity condition is used in this research to impose the velocity at the boundary. The interested reader for boundary conditions within LB framework could find a detailed introduction and overview within the book of Krüger et al. [36].

In this work only wet-node approaches are addressed. The basic idea of a wet node approach is the reconstruction of every particle distribution function $\bar{f}_i$ in the boundary cell, which can be split up in an equilibrium part $\bar{f}_i^{eq}$ and a non-equilibrium part $\bar{f}_i^{(1)}$

$$\bar{f}_i(t,\mathbf{x}) = \bar{f}_i^{eq}(\bar{\rho}, \bar{\mathbf{u}}^*) + \bar{f}_i^{(1)}\,. \tag{15}$$

After, the reconstruction the collision step is performed without modifications.

We are considering two different wet-node approaches. The first one is the equilibrium scheme [37,38]. Every $\bar{f}_i$ on the boundary is substituted by the equilibrium function

$$\bar{f}_i(t,\mathbf{x}) = \bar{f}_i^{eq}(\bar{\rho}, \bar{\mathbf{u}}^*)\,. \tag{16}$$

The second approach is the extrapolation scheme proposed by Guo et al. [39,40]. Hereby, the non-equilibrium distribution function $\bar{f}_i^{(1)}$ is substituted with zeroth order extrapolation scheme, which uses the value from the cell in inwards normal direction

$$\bar{f}_i(t,\mathbf{x}) = \bar{f}_i^{eq}(\bar{\rho}, \bar{\mathbf{u}}^*) + \bar{f}_i^{(1)}\left(t, \mathbf{x} - |\mathbf{c_j}|\mathbf{n}\right)\,. \tag{17}$$

These two approaches are chosen due to simplicity and the ability to deal with edges and corners in a stair case approximation.

2.3.1. Computation of density

The density at the boundary is not given, but necessary to calculate the equilibrium part, see Eq. (15). For a flat wall, the density can be approximated with local or non-local methods. A local method uses only the information of the boundary nodes, i.e. the distribution $\bar{f}_i(t,\mathbf{x})$ and the macroscopic constraints. A non-local method needs information from neighbour lattice nodes. A very accurate approach to calculate the density in a local manner is the Zou and He's method [41]. They propose to compute the density $\bar{\rho}_{bc} := \bar{\rho}(x)$ at wall node x via

$$\bar{\rho}_{bc} = \frac{1}{1 + \bar{\mathbf{u}}_{bc}^{\perp}}\left(2\sum_{i\in\{i|c_i\cdot\mathbf{n}>0\}} f_i + \sum_{i\in\{i|c_i\cdot\mathbf{n}=0\}} f_i\right), \tag{18}$$

where $\bar{\mathbf{u}}_{bc}^{\perp} = \left(\bar{\mathbf{u}}_{bc}^{*} - \frac{1}{2}\mathbf{F}\right) \cdot \mathbf{n}$ is the perpendicular component of the velocity vector $\bar{\mathbf{u}}_{bc}^{*}$ along the outward unity normal vector $\mathbf{n}$.

Although Zou and He's method is a highly accurate and mass conserving formulation, the method is restricted to flat boundaries. Therefore, this research only uses the formulation by Guo et al. [39] in order to deal with arbitrary shaped boundaries. The method uses the density of the neighbour lattice node in the inwards normal direction, $-|\mathbf{c}_j|\mathbf{n}$, via

$$\bar{\rho}_{bc} = \sum \bar{f}_i \left(t, \mathbf{x} - |\mathbf{c}_j|\mathbf{n}\right) \tag{19}$$

with $\mathbf{c}_j$ denoting the lattice velocity direction that respects the condition $(\mathbf{c}_j \cdot \mathbf{n})/|\mathbf{c}_j| = -1$.

2.4. Wall functions

The flow close to the wall is modelled using near-wall functions. These functions are often based on a logarithmic or a power-law profile for the predominated velocity. A near-wall function allows to obtain the average wall shear stress $\tilde{\tau}_w$ and turbulent fluctuations. In this work, the authors tested three different wall function approaches.

The first one is the Musker profile [42] given by

$$\begin{aligned} u^+ = {} & 5.424 \arctan\left(\frac{2.0y^+ - 8.15}{16.7}\right) \\ & + \log_{10}\left(\frac{(y^+ + 10.6)^{9.6}}{({y^+}^2 - 8.15y^+ + 86.0)^2}\right) \\ & - 3.5072790194, \end{aligned} \tag{20}$$

where $u^+ = \frac{\tilde{u}}{\tilde{u}_\tau}$ is the normalized velocity in stream-wise direction. The function is an implicit equation based on the logarithmic profile and it is applicable from the viscous sublayer ($y^+ \geq 1$). A Newton method is used to approximate the average wall shear stress $\tilde{\tau}_{wall}$.

Another possibility to circumvent the implicit calculation of wall shear stress is the approach by Werner and Wengle [5]. The wall function is split into two layers:

$$u^+ = \begin{cases} y^+ & 0 \leq y^+ < 11.81 \\ C_m (y^+)^m & 11.81 \leq y^+ \end{cases} \tag{21}$$

where $m = \frac{1}{7}$ and $C_m = 8.3$. By the use of the power-law function for the upper layer, the wall shear stress can be calculated explicitly and is given by

$$\tilde{\tau}_w = \begin{cases} \dfrac{2\rho\nu\bar{u}_F}{y_F} & \bar{u}_F \leq \dfrac{\nu}{2y_F}(11.81)^2 \\ \rho\left[\dfrac{1-m}{2}C_m^{\frac{1+m}{1-m}}(\dfrac{\nu}{y_F})^{1+m} + \dfrac{1+m}{C_m}(\dfrac{\nu}{y_F})^m \bar{u}_F\right]^{\frac{2}{1+m}} & \bar{u}_F > \dfrac{\nu}{2y_F}(11.81)^2 \end{cases} \tag{22}$$

The drawback of the two region formulation is the kink in the middle of the buffer layer, see 5(a). Therefore, a three layer formulation can be used. According to the work of Schmitt [6], one can use a logarithmic function to cover the buffer layer. A three layer model yields

$$u^+ = \begin{cases} y^+ & 0 \leq y^+ < 5 \\ a \log_{10}(y^+) + b & 5 \leq y^+ < 30 \\ C_m (y^+)^m & 30 \leq y^+ \end{cases} \tag{23}$$

where $a = \frac{\frac{1}{\kappa}\log_{10}(30) + B - 5}{\log_{10}(6)}$ and $b = 5 - a\log_{10}(5)$ and $B = 5.2$ and $\kappa = 0.4$.

The average wall shear stress $\tilde{\tau}_w$ calculation in the tree layer model is given by

$$\begin{aligned} & \tilde{\tau}_w = \frac{2\rho\nu\bar{u}_F}{y_F} && \bar{u}_F < \frac{\nu}{2y_F}(5)^2 \\ & \frac{\tilde{u}}{\sqrt{\frac{\tilde{\tau}_w}{\rho}}} = a \log_{10}(\frac{\sqrt{\frac{\tilde{\tau}_w}{\rho}}y_F}{\nu}) + b \quad \text{solve for } \tilde{\tau}_w && \frac{\nu}{2y_F}(5)^2 \leq \bar{u}_F < \frac{\nu}{2y_F}(30)^2 \\ & \tilde{\tau}_w = \rho\left[\frac{1-m}{2}C_m^{\frac{1+m}{1-m}}(\frac{\nu}{y_F})^{1+m} + \frac{1+m}{C_m}(\frac{\nu}{y_F})^m \bar{u}_F\right]^{\frac{2}{1+m}} && \frac{\nu}{2y_F}(30)^2 \leq \bar{u}_F \end{aligned} \tag{24}$$

In the buffer region, the average wall shear stress $\tilde{\tau}_w$ is implicitly calculated by a Newton method. However, the calculation in the linear ($y^+ < 5$) and the logarithmic ($y^+ > 30$) region is explicitly given according to the work of Werner and Wengle [5].

The influence of these different formulations on the turbulence statistics and an error estimation with respect to the DNS data [43] is presented and discussed in Section 3.2.

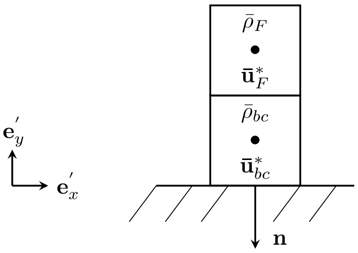

Fig. 1. Sketch of the used and calculated quantities form the boundary node (bc) and the adjacent fluid node (F) in normal direction.

2.5. Near-wall treatment

The idea of the used wall model approach was proposed by Malaspinas and Sagaut [13]. The objective is the computation of the velocity at the boundary $\bar{\mathbf{u}}^*_{bc}$. The used filtered velocity vector $\bar{\mathbf{u}}^*_F$ and position vector $\mathbf{x}$ notation are given by

$$\bar{\mathbf{u}}^* = (\bar u, \bar v, \bar w), \qquad \mathbf{x} = (x, y, z). \tag{25}$$

If a staircase approximation is considered, the distance to the boundary y_{bc} is given by

$$y_{bc} = 0.5\Delta x\|\mathbf{n}\|, \tag{26}$$

where Δx is the distance between two lattice nodes and $\|\mathbf{n}\|$ is the magnitude of the boundary unity normal n. The distance from the wall to the neighbour fluid node in wall-normal direction y_F is written as

$$y_F = y_{bc} + \Delta x\|\mathbf{n}\|. \tag{27}$$

The boundary node and the corresponding fluid node is shown in Fig. 1. Because the wall function profiles are only valid for stream-wise direction, it is necessary to extract this component from the wall-normal neighbour filtered velocity $\bar{\mathbf{u}}^*_F$. To do so, the local stream-wise unit vector $\mathbf{e}'_x$ is computed by

$$\mathbf{e}'_x = \frac{\bar{\mathbf{u}}^*_F - (\bar{\mathbf{u}}^*_F \cdot \mathbf{n})\mathbf{n}}{\|\bar{\mathbf{u}}^*_F - (\bar{\mathbf{u}}^*_F \cdot \mathbf{n})\mathbf{n}\|}. \tag{28}$$

The stream-wise component $\bar u_F$ of $\bar{\mathbf{u}}^*_F$ and the wall-normal neighbour distance respect to the wall y_F are given by

$$\bar u_F = \bar{\mathbf{u}}^*_F \cdot \mathbf{e}'_x. \tag{29}$$

The average wall shear stress $\tilde\tau_w$ is computed by solving the Musker profile Eq. (20) for $\bar u_F = \tilde u\,(y_F, \tilde\tau_w)$ or can directly computed by Eq. (22). Then, the streamwise velocity at the boundary is computed by $\bar u_{bc} = \tilde u\,(y_{bc}, \tilde\tau_w)$. Finally, the boundary velocity is obtained by $\bar{\mathbf{u}}^*_{bc} = \bar u_{bc}\mathbf{e}'_x$.

2.5.1. Summary of the used wall model algorithm

The following listing summarizes the necessary formulas to reconstruct the filtered particle distribution functions $\bar f_i$ and to calculate the turbulent viscosity ν_t in order to perform the collide and stream step.

1. Compute $\bar{\mathbf{u}}^*_F$ with Eq. (6)–(7).
2. Compute $\mathbf{e}'_x$ with Eq. (28).
3. Compute $\bar u_F$ and y_F with Eq. (29) and Eq. (27).
4. Approximate $\tilde\tau_w$ by solving the Musker profile (Eq. (20)) with $\bar u'_F$ and y_F or explicit with Eq. (22)
5. Compute $\bar{\mathbf{u}}^*_{bc} = \tilde u\,(y_{bc}, \tilde\tau_w)\,\mathbf{e}'_x$, with $\tilde u\,(y_{bc}, \tilde\tau_w)$ defined by Eq. (20), Eq. (21) or Eq. (23) and y_{bc} with Eq. (26)
6. Compute $\bar\rho_{bc}$ with Eq. (19)
7. Reconstruct $\bar f_i$ with either Eq. (17) or Eq. (16).
8. Compute ν_{turb} with Eq. (11) and τ_{turb} with Eq. (13)
9. Compute collision and streaming steps with Eq. (1).

3. Results of the validation benchmark: Bi-periodic turbulent flow

The proposed wall function approach, see Section 2.5.1, is validated against the benchmark case of a 3D bi-periodic turbulent channel flow. The bi-periodic channel flow is a very common benchmark case for wall-bounded turbulent flows

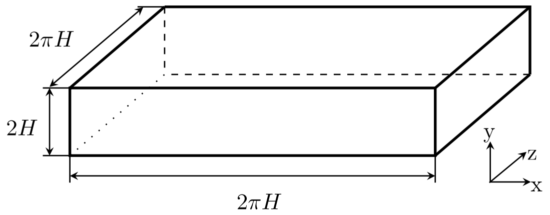

Fig. 2. Sketch of the geometry: periodicity in stream-wise (x-direction) and span-wise (z-direction), walls in lateral direction (y-direction), channel half $H = 1\,\mathrm{m}$.

and therefore a wide spectrum of experimental and numerical data is available. The channel is periodic in stream-wise (x-direction) and span-wise (z-direction) direction. Two parallel walls are perpendicular to the normal direction (y-direction). A $D3Q19$ descriptor set is chosen according to the work of Malaspinas and Sagaut [13]. The grid is aligned to the Cartesian axis of the channel geometry. In the case of a non axis-aligned grid configuration a descriptor with a higher amount of lattice directions (e.g. $D3Q27$) should be chosen to improve the rotational invariance [44]. The dimensions of the channel flow geometry are given by Fig. 2. The half of the channel height is $H = 1\,\mathrm{m}$. The Re_τ number and the bulk Reynolds number Re_{bulk} for the channel can be estimated by

$$\mathrm{Re}_\tau = \frac{H\tilde{u}_\tau}{\nu}, \tag{30}$$

$$\mathrm{Re}_{bulk} = \frac{2Hu_m}{\nu}, \tag{31}$$

where u_m is the mean bulk velocity and ν is the kinematic viscosity.

The flow is forced in stream-wise direction according the forcing scheme of Cabrit [45], which is written as

$$F = \frac{\tilde{u}_\tau^2}{H} + (u_{m,DNS} - \tilde{u}_x)\frac{u_{m,DNS}}{H}, \tag{32}$$

where $u_{m,DNS}$ is the mean velocity given by the DNS data and $\tilde{u}_x$ is the yz plane averaged velocity at $x = \pi H$. The flow is initialized with a power-law profile, see Eq. (21), perturbated by a turbulence intensity of 5 percent. Thereby, the turbulence is seeded with random fluctuations to reduce the amount of flow through cycles before the statistics are obtained. The turbulence intensity is given by

$$I = \frac{u'}{u_m}, \tag{33}$$

where u' is the velocity fluctuation in stream-wise direction. The statistics are spatial and temporal averaged to ensure a high accuracy. The spatial average is realized by a line L in z direction that is positioned at $x = \pi H$. The time for the statistics is started after 400 channel passages $cp = \frac{2\pi H}{u_m}$ and lasts 150 channel passages. The amount of ensembles is related to a statistic frequency of 25 Hz. Assuming $u_m \approx 1\,\frac{\mathrm{m}}{\mathrm{s}}$ the total amount of ensembles is about 23560. The recorded statistics consist of the normalized stream-wise velocity profile, which is defined as

$$\langle u \rangle^+ = \frac{1}{N_t}\sum_{t=t_0}^{t_n}\frac{1}{N_L}\sum_{\mathbf{x}\in L}\frac{\bar{u}(t,\mathbf{x})}{\tilde{u}_\tau}. \tag{34}$$

where N_t is the amount of ensembles, t_0 denotes the start time step and t_n the end time step of the statistics, N_L is the number of grid points in the according line. Also the normalized Reynolds normal stress $\langle u'u' \rangle^+$ in stream-wise direction is tracked and given by

$$\langle u'u' \rangle^+ = \langle uu \rangle^+ - (\langle u \rangle^+)^2, \tag{35}$$

$$\langle uu \rangle^+ = \frac{1}{N_t}\sum_{t=t_0}^{t_n}\frac{1}{N_L}\sum_{\mathbf{x}\in L}\frac{(\bar{u}(t,\mathbf{x}))^2}{\tilde{u}_\tau^2}. \tag{36}$$

The calculation for the normalized normal stresses in span-wise $\langle w'w' \rangle^+$ and lateral $\langle v'v' \rangle^+$ direction is analogous. The normalized Reynolds shear stress is given by

$$\langle u'v' \rangle^+ = \langle uv \rangle^+ - \langle u \rangle^+ \langle v \rangle^+, \tag{37}$$

Table 1
Discretization parameter for the three different grid resolutions $N = 10$, $N = 20$ and $N = 40$.

N	Δt	Δx	u_L	Ma
10	0.005466	0.1053	0.0519298	0.08995
20	0.001297	0.05128	0.0252991	0.04382
40	0.0003162	0.02531	0.0124895	0.02163

$$\langle uv\rangle^+ = \frac{1}{N_t}\sum_{t=t_0}^{t_n}\frac{1}{N_L}\sum_{\mathbf{x}\in L}\frac{\bar{u}(t,\mathbf{x})\bar{v}(t,\mathbf{x})}{\tilde{u}_\tau^2}, \quad \langle v\rangle^+ = \frac{1}{N_t}\sum_{t=t_0}^{t_n}\frac{1}{N_L}\sum_{\mathbf{x}\in L}\frac{\bar{v}(t,\mathbf{x})}{\tilde{u}_\tau}. \tag{38}$$

For all simulations a Smagorinsky constant of $C = 0.12$ is chosen, because the low dissipative characteristics of the BGK scheme should be taken into account [30]. The chosen resolutions $N = 10$, $N = 20$ and $N = 40$ are defined as the number of grid points related to the half channel height H. The used discretization parameters are depicted in Table 1. Diffusive scaling $\Delta t \propto \Delta x^2$ is used and the Mach number Ma is chosen to fulfil the incompressibility condition $\mathrm{Ma} < 0.1$. The Mach number Ma is given by

$$\mathrm{Ma} = \frac{u_L}{c_s}, \tag{39}$$

where c_s is the lattice speed of sound and u_L is the lattice velocity. The DNS results of Lee and Moser [43] have been used to compare the normalized velocity profiles and the Reynolds stresses.

3.1. Comparison of velocity boundary approaches at $\mathrm{Re}_\tau = 1000$

In the following section we analyse the influence of the reconstruction of the non-equilibrium particle distribution function $\bar{f}_i^{(1)}$ on the flow field. Therefore, the two velocity boundary schemes, which are described in Section 2.3, are applied on the turbulent channel flow.

The normalized stream-wise mean velocity u^+ is shown in Fig. 3 for the three different mesh resolutions, N equal to 10, 20 and 40. These three resolutions correspond to a dimensionless wall distance y^+ of 12.5, 25 and 50, respectively. The equilibrium (EQ) scheme underestimates the stream-wise velocity at the first few lattice nodes, up to 3 away from the wall, for all resolutions. Furthermore, the underestimation error increases as the first node gets closer to the wall, see Figs. 3(a) and 3(c). The neglected non-equilibrium part of f_i by the EQ scheme impacts the 1st order turbulent statistics (i.e. the mean velocity). On the other hand, the extrapolation (EP) scheme gives a better approximation of the stream-wise velocity for all the mesh resolutions. This scheme fairly well approximates it if the first node is located at the buffer region ending ($5 < y^+ < 30$), see Fig. 3(c). Both schemes, the EQ and the EP, should not be used below the logarithmic layer ($y^+ < 30$) if the velocity at the first node needs to be correctly simulated.

The normalized Reynolds normal stress in stream-wise direction $\langle u'u'\rangle$ and the shear stress $\langle u'v'\rangle$ for both boundary schemes are depicted in Fig. 4. The normal stress $\langle u'u'\rangle$ for both schemes is in good agreement to the DNS results [43] for the coarse and fine resolutions ($N = 10$ and 40). However, at $N = 20$ the EQ scheme does not follow the DNS profile but it fluctuates around it. These fluctuations are unexpected with the stabilizing effect of the EQ scheme by cutting off the non-equilibrium part of f_i. On the other hand the EP scheme is able to describe the profile of the DNS results. At the higher resolution ($N = 40$), the location of the peak value is better approximated by the EP scheme. However, the EQ scheme gives a closer DNS peak value than the EP scheme. The Reynolds shear stress $\langle u'v'\rangle$ is better recovered by the EQ scheme than the EP scheme $N = 10$, the EP scheme gives a fluctuation profile. These fluctuations vanish at higher grid resolutions. Although the EQ scheme seems to smooth the fluctuations at $N = 10$ (see Fig. 4(b)), the near-wall prediction at higher resolutions is less accurate than the EP scheme (see Figs. 4(d) and 4(e)). Furthermore, fluctuations in the EQ scheme course by $N = 20$ are visible, see Fig. 4(d).

Overall, the EQ scheme is only suitable to stabilize the Reynolds stresses for low resolutions (i.e. $N = 10$). In contrast, the use of the EP scheme at higher grid resolutions increases the accuracy due to the reconstruction of the non-equilibrium part of f_i.

3.2. Comparison of different wall functions for $\mathrm{Re}_\tau = 1000$

We tested three different wall functions: the continuous Musker equation (Eq. (20)), the two equation proposed by Werner and Wengle (Eq. (21)) and a three equations model (Eq. (23)) based on the work of Schmitt [6]. These wall functions are described in detail in Section 2.4. All three models are based on empirical equations to approximate the boundary layer profile. The three wall functions are plotted for $\mathrm{Re}_\tau = 1000$ in Fig. 5(a) and the relative deviation from the DNS data is tracked in Fig. 5(b). The relative deviation corresponds to the approximation error defined as

$$err_{WF} := \frac{u^+_{WF}(y^+) - u^+_{DNS}(y^+)}{u^+_{DNS}(y^+)}, \tag{40}$$

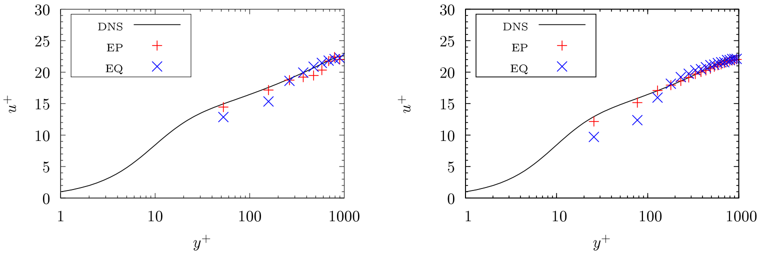

(a) $N = 10$, $\mathrm{Re}_\tau = 1000$, Musker (b) $N = 20$, $\mathrm{Re}_\tau = 1000$, Musker

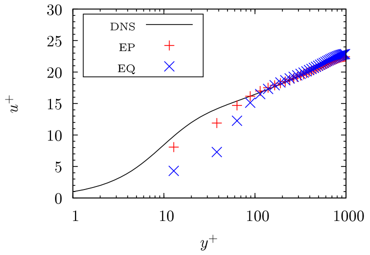

(c) $N = 40$, $\mathrm{Re}_\tau = 1000$, Musker

Fig. 3. Normalized stream-wise velocity u^+ profiles for the equilibrium (EQ) and the extrapolation (EP) scheme with three grid resolutions $N = 10$, $N = 20$ and $N = 40$, for $\mathrm{Re}_\tau = 1000$ and wall function of Musker.

where u^+_{DNS} is the normalized stream-wise velocity for $\mathrm{Re}_\tau = 1000$ from the DNS data; and u^+_{WF} is the corresponding value from the wall function. It can be observed that the two equation formulation (WW) suffers from inaccuracy in the buffer layer ($5 < y^+ < 30$). The calculated error provides for the Werner and Wengle (WW) approach a peak error at $y^+ \approx 12$, which is close to 25 percent. This high error indicates that neither the power-law nor the linear law is able to describe this region adequately. This drawback vanishes, if a third equation for the buffer layer is introduced (i.e. SC). The continuous Musker formulation is also able to describe all three wall regions with sufficient accuracy (maximal error in the buffer layer of 3.3 percent).

The influence of these wall functions is investigated for the two grid resolutions $N = 10$ and $N = 40$ on the 1st and 2nd order turbulence statistics. Fig. 6 represents the normalized stream-wise velocity u^+, the normal stress on stream-wise direction$\langle u'u' \rangle^+$ and the shear stress $\langle u'v' \rangle^+$ profiles. Both grid resolutions are chosen in order to show the first point in the logarithmic layer ($y^+ \approx 50$) and in the middle of the buffer layer ($y^+ \approx 12.5$). If the first grid point is located in the logarithmic region, all three wall functions are able to cover the correct behaviour for the velocity profile and the Reynolds stresses, see Figs. 6(a), 6(c) and 6(e). However, if the first grid point is in the buffer layer, the velocity is overestimated with the WW function, see Fig. 6(b), and it is underestimated by the other wall functions. The normal stress $\langle u'u' \rangle^+$ is correctly recovered by the MU and SC functions regardless the mesh resolution (see Figs. 6(c) and 6(d)). The WW function overestimate it and shows a fluctuating course for the fine resolution (see Fig. 6(d)). The prediction of the shear stress $\langle u'v' \rangle^+$ is similar for all the wall functions. The WW formulation slightly overestimates it for the fine resolution (see Fig. 6(f)). This behaviour is explained by the error of the WW function on the buffer layer presented on Fig. 5(b). Therefore, the WW function should not be used in the buffer region ($5 < y^+ < 30$). On the contrary, the MU and SC functions are in good agreement to each other and they are able to cover the course of the reference DNS data for 1st and 2nd order turbulent statistics.

3.3. *Comparison for different values of* Re_τ

The same three resolutions ($N = 10$, $N = 20$ and $N = 40$) were applied on the bi-periodic channel flow for $\mathrm{Re}_\tau = 2000$ and $\mathrm{Re}_\tau = 5200$, which correspond to a bulk Reynolds number of $\mathrm{Re}_{bulk} \approx 80\,000$ and $\mathrm{Re}_{bulk} \approx 250\,000$, respectively. Based on the previous results from Sections 3.1 and 3.2, we choose the Musker (MU) equation as the wall function and the extrapolation (EP) scheme for the velocity boundary implementation.

The normalized stream-wise velocity u^+, the normal stress $\langle u'u' \rangle^+$ and the shear stress $\langle u'v' \rangle^+$ are compared again to the DNS data, see Fig. 7. For the smallest resolution ($N = 10$), the velocity profile u^+ fluctuates around the DNS solution for

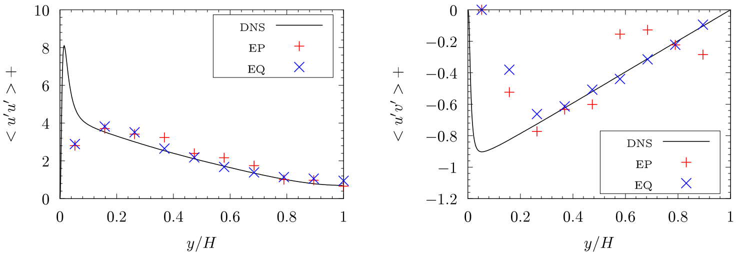

(a) $N = 10$, $\mathrm{Re}_\tau = 1000$, Musker (b) $N = 10$, $\mathrm{Re}_\tau = 1000$, Musker

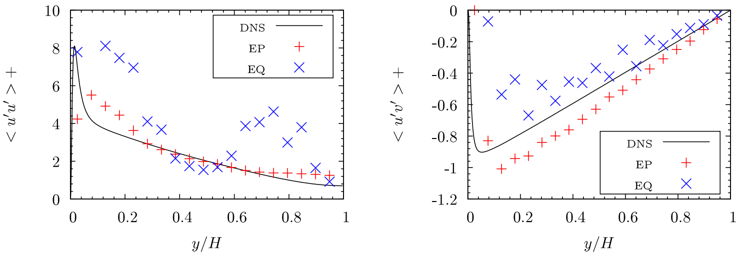

(c) $N = 20$, $\mathrm{Re}_\tau = 1000$, Musker (d) $N = 20$, $\mathrm{Re}_\tau = 1000$, Musker

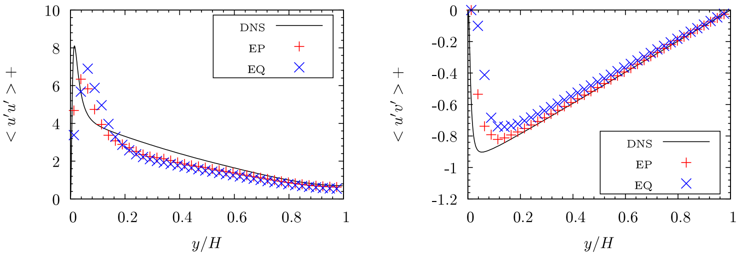

(e) $N = 40$, $\mathrm{Re}_\tau = 1000$, Musker (f) $N = 40$, $\mathrm{Re}_\tau = 1000$, Musker

Fig. 4. Normalized Reynolds normal stresses in streamwise direction $\langle u'u' \rangle^+$ and shear stresses $\langle u'v' \rangle^+$ profiles for the equilibrium (EQ) and the extrapolation (EP) scheme with three grid resolutions $N = 10$, $N = 20$ and $N = 40$, $\mathrm{Re}_\tau = 1000$ and wall function of Musker.

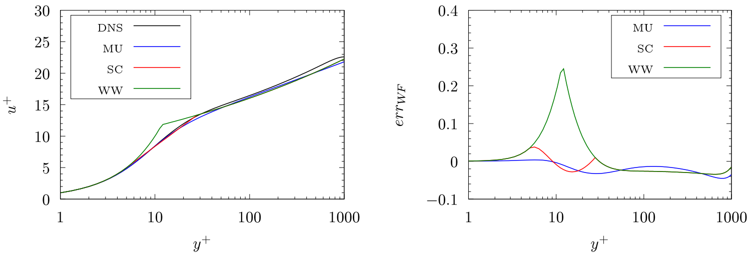

(a) velocity profiles (b) error estimation

Fig. 5. Normalized streamwise velocity u^+ for three wall functions: Musker (MU), Schmitt (SC) and Werner et Wengle (WW) in comparison to DNS data at $\mathrm{Re}_\tau = 1000$ and relative error calculation according Eq. (40).

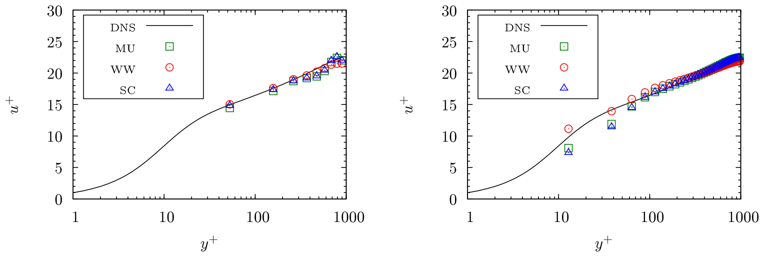

(a) $N = 10$, $\mathrm{Re}_\tau = 1000$, extrapolation (b) $N = 40$, $\mathrm{Re}_\tau = 1000$, extrapolation

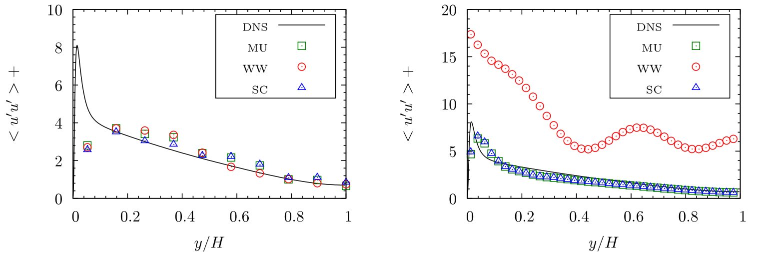

(c) $N = 10$, $\mathrm{Re}_\tau = 1000$, extrapolation (d) $N = 40$, $\mathrm{Re}_\tau = 1000$, extrapolation

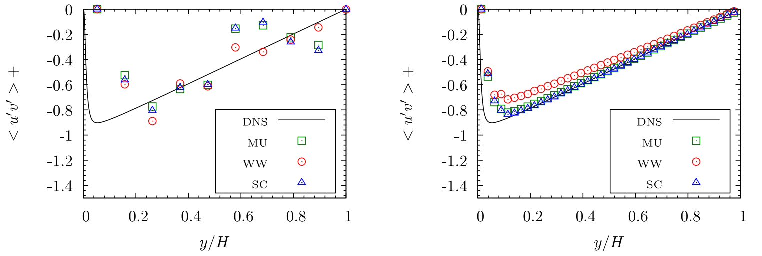

(e) $N = 10$, $\mathrm{Re}_\tau = 1000$, extrapolation (f) $N = 40$, $\mathrm{Re}_\tau = 1000$, extrapolation

Fig. 6. Normalized streamwise velocity u^+, Reynolds normal stresses in streamwise $\langle u'u' \rangle^+$ and the shear stresses $\langle u'v' \rangle^+$ profiles for the wall functions Musker (MU), Werner et Wengle (WW) and Schmitt (SC) with grid resolution $N = 10$ and $N = 40$, $\mathrm{Re}_\tau = 1000$ and extrapolation (EP) scheme.

both Re_τ. These fluctuations increase for $\mathrm{Re}_\tau = 5200$. At higher resolutions the approximation of u^+ is in good agreement to DNS, see Figs. 7(a) and 7(b).

The normal stresses are depicted in Fig. 7(c) and 7(d). The lowest resolution ($N = 10$) is again not able to describe the course with a sufficient accuracy for both Re_τ. The accordance to the course for grid resolution $N = 20$ is better, but the stresses are overestimated all along the profile. By contrast, the highest resolution $N = 40$ is close to DNS solution.

Fig. 7(e) presents the shear stress values for $\mathrm{Re}_\tau = 2000$, it is observed that for $N = 10$ the LES solution shows a high deviation from the DNS course. This behaviour increases by $\mathrm{Re}_\tau = 5200$, see Fig. 7(f). This reflects that the proposed scheme is not able to describe 2nd turbulent statistics with 10 grid points on the half-channel height. The mesh resolution of $N = 20$ allows to eliminate the fluctuations, but the shear stress is still underestimated. Only the mesh resolution of $N = 40$ fairly recover the DNS profiles.

In summary, the MU function coupled to EP scheme requires a mesh resolution for the half-channel height between $N = 20$ to $N = 40$ to fairly reproduce the DNS profiles of 1st and 2nd order turbulent statistics. Furthermore, only the Reynolds stresses at the highest resolution $N = 40$ are in good agreement with the DNS data.

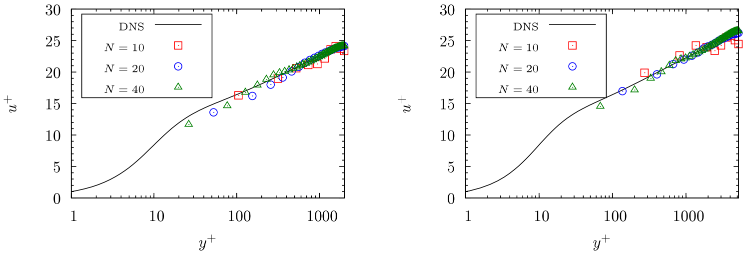

(a) $\mathrm{Re}_\tau = 2000$, extrapolation, Musker (b) $\mathrm{Re}_\tau = 5200$, extrapolation, Musker

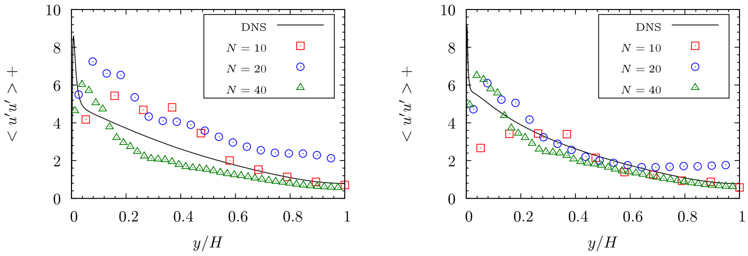

(c) $\mathrm{Re}_\tau = 2000$, extrapolation, Musker (d) $\mathrm{Re}_\tau = 5200$, extrapolation, Musker

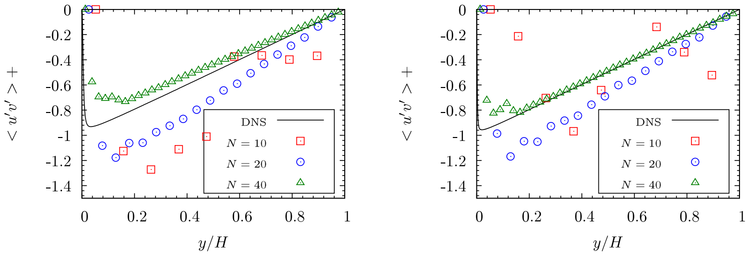

(e) $\mathrm{Re}_\tau = 2000$, extrapolation, Musker (f) $\mathrm{Re}_\tau = 5200$, extrapolation, Musker

Fig. 7. Normalized stream-wise velocity u^+, normal stress in stream-wise $\langle u'u'\rangle^+$ and the shear stress $\langle u'v'\rangle^+$ profiles for $\mathrm{Re}_\tau = 2000$ and $\mathrm{Re}_\tau = 5200$ with three grid resolutions $N = 10$, $N = 20$ and $N = 40$, wall function of Musker and extrapolation scheme.

3.4. Enhanced turbulence statistic data and error estimation

The results of the turbulent channel flow are quantitatively evaluated by an error criterion. The normalized mean absolute error *nMAE* criterion was chosen and it is given by

$$nMAE := \frac{\sum_{i=1}^{n} |Y_{i,SIM} - Y_{i,DNS}|}{\sum_{i=1}^{n} Y_{i,DNS}}, \tag{41}$$

where $Y_{i,SIM}$ is the simulation data of the wall function approach at a discrete point i; and $Y_{i,DNS}$ is the according DNS reference value. The DNS reference values are linearly interpolated to adapt them to the discrete positions of the LBM solution. A study of the effect of grid resolution for the normalized stream-wise velocity u^+ based on this error criterion is shown in Fig. 8 for three different Re_τ: 1000, 2000 and 5200. The experimental order of convergence (EOC) for the grid resolutions $N = 10$ and $N = 20$ is close to $EOC = 1$ for both $\mathrm{Re}_\tau = 1000$ and $\mathrm{Re}_\tau = 2000$. However, the *EOC* for $\mathrm{Re}_\tau = 5200$ is approximately $EOC = 2$. For the grid resolutions $N = 20$ and $N = 40$, the estimated error is still decreasing, but seems to reach a plateau, which decreases the *EOC*. The reasons for this could be the small error at $N = 20$ and the comparison to DNS data instead of wall function profiles. Despite the high quality of the reference solution, the accuracy

Table 2
Normalized mean absolute error *nMAE* of the normalized stream-wise velocity $\tilde{u}^+$, the Reynolds normal stresses in stream-wise $\langle u^{'}u^{'}\rangle^+$ wall-normal $\langle v^{'}v^{'}\rangle^+$ and span-wise $\langle w^{'}w^{'}\rangle^+$ directions, the Reynolds shear stress $\langle u^{'}v^{'}\rangle^+$ profiles with different wall function (WF) approaches (Musker (MU), Schmitt (SC) and Werner and Wengle (WW)), boundary schemes (BS) (extrapolation (EP) and equilibrium (EQ)), grid resolutions N and friction Reynolds numbers Re_τ.

Re_τ	N	*BS*	WF	u^+	$< u^{'}u^{'} >^+$	$< v^{'}v^{'} >^+$	$< w^{'}w^{'} >^+$	$< u^{'}v^{'} >^+$
1000	10	EP	MU	0.02846	0.1586	6.0277	7.2599	−0.2921
1000	10	EQ	MU	0.02798	0.1004	0.2922	2.9690	−0.1571
1000	20	EP	MU	0.01586	0.1856	0.4477	0.1158	−0.2026
1000	20	EQ	MU	0.03406	0.9066	0.3493	0.3799	−0.3173
1000	40	EP	MU	0.01178	0.1639	0.1215	0.1374	−0.0535
1000	40	EQ	MU	0.03067	0.2418	0.1540	0.1282	−0.1596
1000	10	EP	WW	0.02382	0.1211	5.8791	0.4744	−0.1969
1000	10	EP	SC	0.02643	0.1195	6.3565	5.1764	−0.3143
1000	20	EP	WW	0.02191	0.1469	0.6565	0.2671	−0.1205
1000	20	EP	SC	0.01839	0.2298	0.5152	0.1831	−0.1385
1000	40	EP	WW	0.02470	2.7632	0.2265	0.2180	−0.1783
1000	40	EP	SC	0.01281	0.1753	0.1261	0.1389	−0.0396
2000	10	EP	MU	0.02369	0.3453	4.9721	1.6562	−0.6237
2000	20	EP	MU	0.01488	0.6770	0.2845	0.1750	−0.3688
2000	40	EP	MU	0.01198	0.2568	0.0995	0.1237	−0.1508
5200	10	EP	MU	0.04122	0.1377	8.2053	2.6698	−0.6187
5200	20	EP	MU	0.00973	0.2071	1.1306	1.0366	−0.3133
5200	40	EP	MU	0.00788	0.1852	0.1366	0.1089	−0.0491

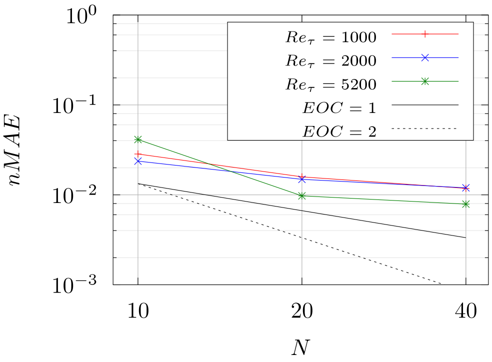

Fig. 8. Deviation from the normalized stream-wise velocity DNS profile for three different friction Reynolds numbers $\mathrm{Re}_\tau = 1000$, $\mathrm{Re}_\tau = 2000$, $\mathrm{Re}_\tau = 5200$.

is influenced by statistical uncertainties (<1%) [43]. In addition, the used spatial linear interpolation leads to an error term, especially in regions where the profile is not assumed to be linear ($y^+ > 5$). Since the LES grid spacing Δx_{LES} is larger than the DNS grid spacing Δx_{DNS} this error term is in order $\mathcal{O}((\Delta x_{DNS})^2)$.

Table 2 provides the *nMAE* of the normalized stream-wise velocity u^+, the normal stresses $\langle u'u'\rangle^+$ and the shear stress $\langle u'v'\rangle^+$ for all simulated channel flow configurations. The Reynolds stresses $\langle v'v'\rangle^+$, $\langle w'w'\rangle^+$ and $\langle u'v'\rangle^+$ show grid convergence for $\mathrm{Re}_\tau = 2000$ and $\mathrm{Re}_\tau = 5200$.

Furthermore, a high conformity to the DNS data for the configuration MU function and EP scheme at the resolution $N = 40$ is visible for the used Re_τ numbers. The wall function approach presented is suitable for simulating high Re number flows in underresolved grids with good accuracy.

4. Results of the application case: Coriolis mass flowmeter

A Coriolis mass flowmeter (CMF) measures the mass flow and the density of a fluid with a high accuracy. This device is part of many pipeline systems in plants, where a high precision is necessary to ensure a certain product quality or safety guideline. The installation of a CMF in a pipeline system requires reliable data of the pressure drop. In the following section, we present our numerical setup to simulate a RotaMASS Supreme RCxS38 CMF from the company *ROTA YOKOGAWA GmbH & Co. KG*. The geometry of the simulated domain is depicted in Fig. 9 and consists of a flow divider, two measuring tubes and a flow combiner.

The inflow and the outflow stretch are elongated to diminish the jet effects after the flow combiner (see Fig. 10), which influence the pressure measurement accuracy at the outflow. In stream-wise direction periodic boundary conditions are

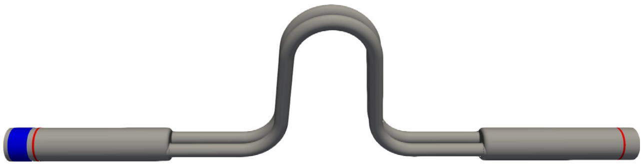

Fig. 9. Simulation domain of the Coriolis mass flowmeter and position of the forcing area (blue) and the two pressure measuring planes (red). The flow direction is from left to right. In flow direction a flow divider, two measuring tubes and a flow combiner are shown. (For interpretation of the references to colour in this figure legend, the reader is referred to the web version of this article.)

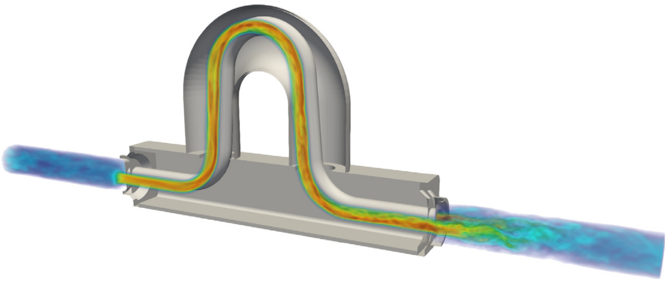

Fig. 10. Volume rendering representation of the instantaneous velocity at Re = 15 980.

Table 3
Discretization parameter for the three different grid resolutions $N = 21$, $N = 41$ and $N = 81$.

Re	N	Δt	Δx	u_L	Ma
15 980	21	0.0006469	0.002619	0.05786	0.1002
15 980	41	0.0001697	0.001341	0.02964	0.05133
15 980	81	4.348e−05	0.0006790	0.01500	0.02598
31 960	81	2.174e−05	0.0006790	0.01500	0.02598
63 910	81	1.087e−05	0.0006790	0.01500	0.02598
127 800	81	5.435e−06	0.0006790	0.01500	0.02598

applied due to stability and to guarantee an adequate distribution of turbulence intensity at the entrance. As a result, a force term is applied on a volume close to the inflow, see Fig. 9, and scaled to the set mass flow. The scaling of the force ensures the prescribed massflow by a control loop that covers a predefined turbulence intensity and the time averaged velocity in the forcing area. The expected pressure drop is neither used in the control loop nor in the scaling procedure. The wall of the CMF is described by three different boundary conditions. The first one is our wall function approach using the extrapolation scheme and the Musker equation. The curved walls are approximated by a staircase and the resulting discrete boundary normals are used in the wall function approach. The second scheme is the full way bounce back approach to show a boundary condition that uses a staircase approximation and implements a no-slip condition. On the contrary the third scheme, the Bouzidi approach [46] takes the distance to the physical boundary into account and resolves the staircase approximation. Four different Reynolds numbers are simulated: Re = 15 980, Re = 31 960, Re = 63 910 and 127 800. The characteristic length in the definition of the Reynolds number is related to the diameter of the measuring tube and the average velocity. The discretization parameters are given by Table 3. The Mach number Ma in the coarse grid is chosen with respect to the incompressibility condition and diffusive scaling is applied. The simulated fluid is water at a temperature of 293.15 K.

4.1. Pressure drop validation

The pressure drop is calculated by a pressure value at the inflow and the outflow region. Therefore, two planes are chosen one behind the forcing area close to the inlet and the other one near to the outlet, see Fig. 9. The plane averaged pressure p_E is given by

$$p_E(t) = \frac{1}{N_E}\sum_{\mathbf{x}\in E}\bar{p}(t,\mathbf{x}), \tag{42}$$

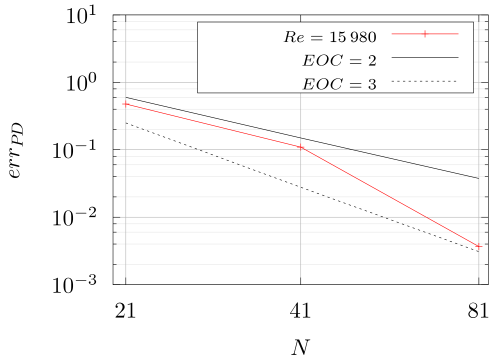

Fig. 11. Deviation from the experimental data for the wall function approach using the extrapolation scheme and the Musker equation at Reynolds number $\mathrm{Re}_\tau = 15\,980$.

where E is a given plane, N_E is the amount of grid points in the plane and x the position in the plane, which starts at $x = x_0$ and ends at $x = x_n$. The time averaged total pressure drop Δp_{total} is defined as

$$\Delta p_{total} = \frac{1}{N_t} \sum_{t=t_0}^{t_n} |p_{inflow}(t) - p_{outflow}(t)|, \tag{43}$$

where N_t is the amount of time steps, t_0 indicates the start time step and t_n the end time step of the statistics. The numerical statistics of the Coriolis flow meter are related to the residence time, which is given as

$$t_r = \frac{V_{CMF}}{\dot{V}}, \tag{44}$$

where V_{CMF} is the volume of the CMF and $\dot{V}$ is the volume flow through the CMF. The statistic starts after $20t_r$ and lasts for $10t_r$. The statistic frequency is also chosen to $\frac{1000}{t_r}$ with respect to the residence time. This leads to a total ensemble amount of $N_t = 10000$. The relative error for the pressure drop err_{PD} is defined as

$$err_{PD} = \left| \frac{\Delta p_{total,SIM} - \Delta p_{total,EXP}}{\Delta p_{total,EXP}} \right|, \tag{45}$$

where $\Delta p_{total,EXP}$ is the experimental pressure drop value and $\Delta p_{total,SIM}$ is the simulated pressure drop value.

Fig. 11 shows the calculated error err_{PD} for different grid resolutions N. The resolution is related to the diameter at the inflow section. The applied wall function scheme shows at $\mathrm{Re} = 15\,980$ by $N = 21$ and $N = 41$ an EOC close to $EOC = 2$. For $N = 41$ and $N = 81$ the EOC is greater than $EOC = 3$. Due to the fact that the experimental pressure drop takes into account a measuring error and a staircase approximation is used, this high EOC is based on mutually beneficial error terms. If the measurement error is of the same magnitude as the pressure error err_{PD}, the order of convergence can be increased or decreased due to the uncertainty of the experimental reference values. Further sources of error could be caused by the difference between the position of the numerical and the experimental position of the pressure measurement. The use of different boundary conditions and the influence on the pressure drop Δp_{total} is depicted in Fig. 12. It is observed that the Bouzidi scheme leads to a slightly better simulated pressure drop than the bounce back scheme. This behaviour is to be expected, because Bouzidi takes the correct wall spacing into account and the implemented bounce back approach operates on a staircase approximation. Nevertheless, both schemes suffer on a highly overestimated pressure drop. On the contrary, the wall function approach is in very good agreement to the experimental data.

A summary of all simulated cases is given by Table 4. The estimated error err_{PD} shows for Bouzidi and bounce back scheme that the higher the Reynolds number, the worse the pressure drop prediction. The wall function approach is able to cover the experimental data with a maximal error of 6.1% at the highest Reynolds number. In comparison to bounce back and Bouzidi the error is reduced by two orders of magnitude.

5. Conclusion and outlook

This paper aims at demonstrating the capacity to simulate wall-bounded turbulent flows in highly underresolved grids with a SRT-LES-LB model coupled to a wall function. The model was validated with the bi-periodic turbulent channel flow. Thereby, algorithm options, as velocity boundary schemes and wall functions, were estimated for a friction Reynolds number $\mathrm{Re}_\tau = 1000$. It was shown that the extrapolation scheme has an improved accuracy at higher resolutions. In the

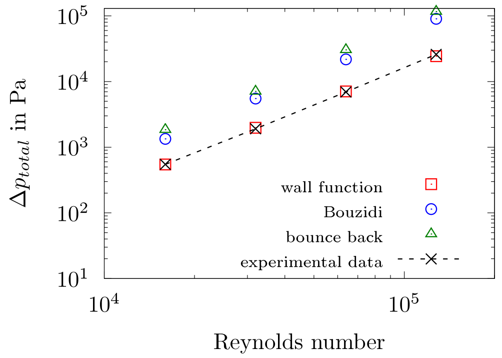

Fig. 12. Total pressure drop Δp_{total} data of the simulation with bounce back, Bouzidi and wall function approach for different Reynolds numbers with grid resolution $N = 81$ in comparison to the experimental data.

Table 4
Pressure drop Δp_{total} and the according relative error err_{PD} for different Reynolds numbers Re, boundary schemes and grid resolutions N.

Re	N	Boundary scheme	Δp_{total}	err_{PD}
15 980	21	Wall function	288	0.47628
15 980	41	Wall function	609	0.10966
15 980	81	Wall function	546	0.00367
15 980	81	Bouzidi	1 339	1.43989
15 980	81	Bounce back	1 849	2.36794
31 960	81	Wall function	1 979	0.03620
31 960	81	Bouzidi	5 497	1.87819
31 960	81	Bounce back	7 075	2.70418
63 910	81	Wall function	7 085	0.02242
63 910	81	Bouzidi	21 769	2.14128
63 910	81	Bounce back	30 388	3.38499
127 800	81	Wall function	24 321	0.06095
127 800	81	Bouzidi	90 035	2.47629
127 800	81	Bounce back	116 421	3.49501

case of the wall function, a three layer formulation and the Musker equation allow to handle the velocity at the first grid point in the buffer layer with sufficient precision ($err_{WF} < 3.3\%$). The extrapolation scheme and the Musker equation were applied on two higher friction Reynolds numbers: 2000 and 5200. The 1st and 2nd order turbulence statistics are well in line with the DNS reference data for higher grid resolutions. The smallest grid resolution, $N = 10$, is not able to recover the DNS profiles and suffers from fluctuations. However, grid convergence is observed for the normalized velocity profiles u^+.

The analysis of the pressure drop in the geometry of a Coriolis mass flowmeter shows a major improvement in comparison to different no-slip boundary conditions. The error is reduced by two orders of magnitude in the used under-resolved grid. Hence the developed approach is able to deal with application geometries and the simulated pressure drop by flows at high Reynolds numbers, up to Re $= 127\,800$, is in very good agreement to experimental data ($err_{PD} < 6.1\%$).

Further work has to been carrying out on the implementation of a curved boundary formulation that takes into account the position of the wall. Authors will refer to the work of Guo [40], which extends the used extrapolation scheme to curved boundaries. In principle, the proposed algorithm is also valid for non discrete normals in case of an arbitrary shaped boundary. Furthermore, the analysis of pressure gradients occurring at curved boundaries should be investigated and included in the wall function formulation.

Acknowledgements

The authors acknowledge *Valence Romans Agglo* and *ANRT* for financial support. Authors also warmly thank Dr. Christian OBRECHT for his scientific support.

References

[1] T. Cochran, Calculate pipeline flow of compressible fluids, Chem. Eng. 103 (2) (1996) 115–122.
[2] S.B. Pope, Turbulent Flows, first ed., Cambridge Univ. Pr., 2011.

[3] D.R. Chapman, Computational aerodynamics development and outlook, AIAA J. 17 (12) (1979) 1293–1313.

[4] B. Launder, D. Spalding, The numerical computation of turbulent flows, Comput. Methods Appl. Mech. Engrg. 3 (2) (1974) 269–289, http://dx.doi.org/10.1016/0045-7825(74)90029-2, URL http://www.sciencedirect.com/science/article/pii/0045782574900292.

[5] H. Werner, H. Wengle, Large-eddy simulation of turbulent flow over and around a cube in a plate channel, in: Turbulent Shear Flows 8, Springer, 1993, pp. 155–168.

[6] L. Schmitt, Grobstruktursimulation Turbulenter Grenzschicht-, Kanal-und Stufenströmungen, (Ph.D. thesis), 1988.

[7] M. Casey, T. Wintergerste, Best Practices Guidelines: ERCOFTAC Special Interest Group on "Quality and Trust in Industrial CFD", Ercoftac, 2000.

[8] J.W. Deardorff, A numerical study of three-dimensional turbulent channel flow at large Reynolds numbers, J. Fluid Mech. 41 (2) (1970) 453–480, http://dx.doi.org/10.1017/S0022112070000691.

[9] U. Schumann, Subgrid scale model for finite difference simulations of turbulent flows in plane channels and annuli, J. Comput. Phys. 18 (4) (1975) 376–404, http://dx.doi.org/10.1016/0021-9991(75)90093-5, URL http://www.sciencedirect.com/science/article/pii/0021999175900935.

[10] T.-H. Shih, L. Povinelli, N.-S. Liu, M. G. Potapczuk, J. Lumley, A generalized wall function, Tech. Rep. TM-1999-209398, NASA Glenn Research Center; Cleveland, OH United States (08 1999).

[11] C.M. Teixeira, Incorporating turbulence models into the lattice-Boltzmann method, Internat. J. Modern Phys. C 09 (08) (1998) 1159–1175, http://dx.doi.org/10.1142/S0129183198001060.

[12] O. Filippova, S. Succi, F. Mazzocco, C. Arrighetti, G. Bella, D. Hnel, Multiscale lattice Boltzmann schemes with turbulence modeling, J. Comput. Phys. 170 (2) (2001) 812–829, http://dx.doi.org/10.1006/jcph.2001.6764, URL http://www.sciencedirect.com/science/article/pii/S0021999101967646.

[13] O. Malaspinas, P. Sagaut, Wall model for large-eddy simulation based on the lattice Boltzmann method, J. Comput. Phys. 275 (2014) 25–40, http://dx.doi.org/10.1016/j.jcp.2014.06.020, URL http://www.sciencedirect.com/science/article/pii/S0021999114004276.

[14] S. Hoyas, J. Jimnez, Scaling of the velocity fluctuations in turbulent channels up to $Re_\tau = 2003$, Phys. Fluids 18 (1) (2006) 011702, http://dx.doi.org/10.1063/1.2162185, URL https://doi.org/10.1063/1.2162185.

[15] S. Hoyas, J. Jimnez, Reynolds number effects on the Reynolds-stress budgets in turbulent channels, Phys. Fluids 20 (10) (2008) 101511, http://dx.doi.org/10.1063/1.3005862, URL https://doi.org/10.1063/1.3005862.

[16] A. Schneider, A Consistent Large Eddy Approach for Lattice Boltzmann Methods and its Application to Complex Flows, (Ph.D. thesis), 2015, URL http://nbn-resolving.de/urn/resolver.pl?urn:nbn:de:hbz:386-kluedo-40568.

[17] A. Pasquali, M. Geier, M. Krafczyk, Near-wall treatment for the simulation of turbulent flow by the cumulant lattice Boltzmann method, Comput. Math. Appl. (2017) http://dx.doi.org/10.1016/j.camwa.2017.11.022, URL http://www.sciencedirect.com/science/article/pii/S0898122117307484.

[18] L.d.L.X. Augusto, J. Ross-Jones, G.C. Lopes, P. Tronville, J.A.S. Gonçalves, M. Rädle, M.J. Krause, Microfiber filter performance prediction using a lattice Boltzmann method, Commun. Comput. Phys. 23 (2018) 910–931.

[19] R. Trunk, T. Henn, W. Drfler, H. Nirschl, M.J. Krause, Inertial dilute particulate fluid flow simulations with an Euler–Euler lattice Boltzmann method, J. Comput. Sci. 17 (2016) 438–445, http://dx.doi.org/10.1016/j.jocs.2016.03.013, discrete Simulation of Fluid Dynamics 201. URL http://www.sciencedirect.com/science/article/pii/S1877750316300345.

[20] T. Henn, V. Heuveline, M.J. Krause, S. Ritterbusch, Aortic coarctation simulation based on the lattice Boltzmann method: benchmark results, in: O. Camara, T. Mansi, M. Pop, K. Rhode, M. Sermesant, A. Young (Eds.), Statistical Atlases and Computational Models of the Heart. Imaging and Modelling Challenges, Springer Berlin Heidelberg, Berlin, Heidelberg, 2013, pp. 34–43.

[21] V. Heuveline, M.J. Krause, J. Latt, Towards a hybrid parallelization of lattice Boltzmann methods, Comput. Math. Appl. 58 (5) (2009) 1071–1080, http://dx.doi.org/10.1016/j.camwa.2009.04.001, mesoscopic Methods in Engineering and Science. URL http://www.sciencedirect.com/science/article/pii/S0898122109002454.

[22] V. Heuveline, M.J. Krause, Openlb: towards an efficient parallel open source library for lattice Boltzmann fluid flow simulations, in: International Workshop on State-of-the-Art in Scientific and Parallel Computing. PARA, Vol. 9, 2010.

[23] P. Nathen, D. Gaudlitz, M.J. Krause, N.A. Adams, On the stability and accuracy of the BGK, MRT and RLB Boltzmann schemes for the simulation of turbulent flows, Commun. Comput. Phys. 23 (3) (2018) 846–876.

[24] P.L. Bhatnagar, E.P. Gross, M. Krook, A model for collision processes in gases. I. Small amplitude processes in charged and neutral one-component systems, Phys. Rev. 94 (1954) 511–525, http://dx.doi.org/10.1103/PhysRev.94.511.

[25] Z. Guo, C. Zheng, B. Shi, Discrete lattice effects on the forcing term in the lattice Boltzmann method, Phys. Rev. E 65 (2002) 046308, http://dx.doi.org/10.1103/PhysRevE.65.046308.

[26] X. He, L.-S. Luo, Theory of the lattice Boltzmann method: From the Boltzmann equation to the lattice Boltzmann equation, Phys. Rev. E 56 (1997) 6811–6817, http://dx.doi.org/10.1103/PhysRevE.56.6811.

[27] X. Shan, X.-F. Yuan, H. Chen, Kinetic theory representation of hydrodynamics: a way beyond the Navier–Stokes equation, J. Fluid Mech. 550 (2006) 413–441, http://dx.doi.org/10.1017/S0022112005008153.

[28] H. Huang, M. Krafczyk, X. Lu, Forcing term in single-phase and shan-chen-type multiphase lattice Boltzmann models, Phys. Rev. E 84 (2011) 046710, http://dx.doi.org/10.1103/PhysRevE.84.046710.

[29] G. Silva, V. Semiao, First-and second-order forcing expansions in a lattice Boltzmann method reproducing isothermal hydrodynamics in artificial compressibility form, J. Fluid Mech. 698 (2012) 282–303.

[30] S. Hou, J. Sterling, S. Chen, G. Doolen, A lattice Boltzmann subgrid model for high Reynolds number flows, 1994.

[31] J. Smagorinsky, General circulation experiments with the primitive equations: I. the basic experiment, Monthly Weather Rev. 91 (3) (1963) 99–164.

[32] F. Nicoud, F. Ducros, Subgrid-scale stress modelling based on the square of the velocity gradient tensor, Flow Turbul. Combust. 62 (3) (1999) 183–200, http://dx.doi.org/10.1023/A:1009995426001.

[33] E. Driest, On turbulent flow near a wall, J. Aeronaut. Sci. 23 (11) (1956) 1007–1011.

[34] H.M. Nagib, K.A. Chauhan, Variations of von Kármán coefficient in canonical flows, Phys. Fluids 20 (10) (2008) 101518, http://dx.doi.org/10.1063/1.3006423.

[35] O. Malaspinas, P. Sagaut, Consistent subgrid scale modelling for lattice Boltzmann methods, J. Fluid Mech. 700 (2012) 514–542.

[36] T. Krüger, H. Kusumaatmaja, A. Kuzmin, O. Shardt, G. Silva, E.M. Viggen, The Lattice Boltzmann Method, Springer, 2017.

[37] J. Latt, B. Chopard, O. Malaspinas, M. Deville, A. Michler, Straight velocity boundaries in the lattice Boltzmann method, Phys. Rev. E 77 (2008) 056703, http://dx.doi.org/10.1103/PhysRevE.77.056703.

[38] A.A. Mohamad, S. Succi, A note on equilibrium boundary conditions in lattice Boltzmann fluid dynamic simulations, Eur. Phys. J. Spec. Top. 171 (1) (2009) 213–221, http://dx.doi.org/10.1140/epjst/e2009-01031-9.

[39] G. Zhao-Li, Z. Chu-Guang, S. Bao-Chang, Non-equilibrium extrapolation method for velocity and pressure boundary conditions in the lattice Boltzmann method, Chin. Phys. 11 (4) (2002) 366, URL http://stacks.iop.org/1009-1963/11/i=4/a=310.

[40] Z. Guo, C. Zheng, B. Shi, An extrapolation method for boundary conditions in lattice Boltzmann method, Phys. Fluids 14 (6) (2002) 2007–2010, http://dx.doi.org/10.1063/1.1471914.

[41] Q. Zou, X. He, On pressure and velocity boundary conditions for the lattice Boltzmann BGK model, Phys. Fluids 9 (6) (1997) 1591–1598.

[42] A. Musker, Explicit expression for the smooth wall velocity distribution in a turbulent boundary layer, AIAA J. 17 (6) (1979) 655–657.

[43] M. Lee, R.D. Moser, Direct numerical simulation of turbulent channel flow up to $Re_\tau \approx 5200$, J. Fluid Mech. 774 (2015) 395–415, http://dx.doi.org/10.1017/jfm.2015.268.

[44] S.K. Kang, Y.A. Hassan, The effect of lattice models within the lattice Boltzmann method in the simulation of wall-bounded turbulent flows, J. Comput. Phys. 232 (1) (2013) 100–117, http://dx.doi.org/10.1016/j.jcp.2012.07.023, URL http://www.sciencedirect.com/science/article/pii/S0021999112003968.

[45] O. Cabrit, F. Nicoud, Direct simulations for wall modeling of multicomponent reacting compressible turbulent flows, Phys. Fluids 21 (5) (2009) 055108, http://dx.doi.org/10.1063/1.3123528.

[46] M. Bouzidi, M. Firdaouss, P. Lallemand, Momentum transfer of a Boltzmann-lattice fluid with boundaries, Phys. Fluids 13 (11) (2001) 3452–3459.

5

Near-Wall-Modeled Large-Eddy Simulation of an Engine Relevant Flow

This chapter was published in the following article:

M. Haussmann, F. Ries, J. B. Jeppener-Haltenhoff, Y. Li, M. Schmidt, C. Welch, L. Illmann, B. Böhm, H. Nirschl, M. J. Krause and A. Sadiki
Evaluation of a Near-Wall-Modeled Large Eddy Lattice Boltzmann Method for the Analysis of Complex Flows Relevant to IC Engines
Computation, 8.43 (2020)
https://doi.org/10.3390/computation8020043

My contribution according to the contributor role taxonomy system [14] included conceptualization, methodology, software, validation, formal analysis, investigation, data curation, writing – original draft, visualization and project administration.

computations

MDPI

Article

Evaluation of a Near-Wall-Modeled Large Eddy Lattice Boltzmann Method for the Analysis of Complex Flows Relevant to IC Engines

Marc Haussmann [1,2], Florian Ries [3,*], Jonathan B. Jeppener-Haltenhoff [1,2], Yongxiang Li [3], Marius Schmidt [3], Cooper Welch [3], Lars Illmann [3], Benjamin Böhm [3], Hermann Nirschl [2], Mathias J. Krause [1,2] and Amsini Sadiki [3]

[1] Lattice Boltzmann Research Group, Institute for Mechanical Process Engineering and Mechanics, Karlsruhe Institute of Technology, Straße am Forum 8, 76131 Karlsruhe, Germany; marc.haussmann@kit.edu (M.H.); jonathan@jeppener.de (J.B.J.-H.); mathias.krause@kit.edu (M.J.K.)

[2] Process Machines, Institute for Mechanical Process Engineering and Mechanics, Karlsruhe Institute of Technology, Straße am Forum 8, 76131 Karlsruhe, Germany; hermann.nirschl@kit.edu

[3] Reactive Flows and Diagnostics, Department of Mechanical Engineering, Technical University of Darmstadt, Otto-Berndt-Str. 3, 64287 Darmstadt, Germany; yongxiang.li@ekt.tu-darmstadt.de (Y.L.); schmidt@rsm.tu-darmstadt.de (M.S.); welch@rsm.tu-darmstadt.de (C.W.); illmann@rsm.tu-darmstadt.de (L.I.); boehm@rsm.tu-darmstadt.de (B.B.); sadiki@ekt.tu-darmstadt.de (A.S.)

* Correspondence: ries@ekt.tu-darmstadt.de

Received: 4 April 2020; Accepted: 30 April 2020; Published: 5 May 2020

Abstract: In this paper, we compare the capabilities of two open source near-wall-modeled large eddy simulation (NWM-LES) approaches regarding prediction accuracy, computational costs and ease of use to predict complex turbulent flows relevant to internal combustion (IC) engines. The applied open source tools are the commonly used OpenFOAM, based on the finite volume method (FVM), and OpenLB, an implementation of the lattice Boltzmann method (LBM). The near-wall region is modeled by the Musker equation coupled to a van Driest damped Smagorinsky-Lilly sub-grid scale model to decrease the required mesh resolution. The results of both frameworks are compared to a stationary engine flow bench experiment by means of particle image velocimetry (PIV). The validation covers a detailed error analysis using time-averaged and root mean square (RMS) velocity fields. Grid studies are performed to examine the performance of the two solvers. In addition, the differences in the processes of grid generation are highlighted. The performance results show that the OpenLB approach is on average 32 times faster than the OpenFOAM implementation for the tested configurations. This indicates the potential of LBM for the simulation of IC engine-relevant complex turbulent flows using NWM-LES with computationally economic costs.

Keywords: turbulent flow; large-eddy simulation; wall function; IC engine; OpenLB; OpenFOAM; particle image velocimetry

1. Introduction

Due to the complex turbulent nature of internal combustion (IC) engine flows, their accurate prediction is a major challenge to numerical and experimental investigations. Additional difficulties arise from the interconnection of multiphysical processes, including multiphase flow phenomena, heat transfer and chemical reactions. Each process features different time and length scales, often varying in orders of magnitude, which further increases the complexity.

A particularly important turbulent flow structure for the analysis of IC engines is the intake jet [1]. This high-speed flow over the valves is critical in generating a charge motion, which is commonly referred to as a tumble motion. The tumble breakdown in engine compression results in turbulent structures, which dominate the mixing, ignition and combustion processes and in turn, the engine efficiency and pollutant emissions. Therefore, it is necessary to understand the complex processes in turbulent IC engine intake flows to improve the combustion performance and reduce cycle-to-cycle variability [2–7].

Optically accessible research engines enable the detailed investigation and visualization of the processes inside IC engines, often with simplified geometries for numerical validation. High-speed laser diagnostics have long been utilized in engine experiments and have provided more insight into the turbulent structures present in engine flows [8–11]. Simplified flow bench setups with steady state or transient operation are common tools to optimize cylinder head or intake port geometries and have been used to investigate the intake flow in industrial and scientific research [12,13]. Recent studies examined intake phenomena using magnetic resonance velocimetry (MRV) in a steady water flow bench [1] or low-speed particle image velocimetry (PIV) in a steady air flow bench [14,15]. The data from these experiments have been used as validation for large eddy simulation (LES) approaches [14–18].

However, high-speed PIV data for a flow bench with a realistic engine geometry is limited. Therefore, numerical simulations are another essential tool for the analysis of IC engine flows. In particular, the 3D flow data and turbulence structures obtained with LES offer data which are nearly impossible to obtain in experimental investigations. The choice of LES instead of commonly used Reynolds-averaged Navier–Stokes (RANS) approaches is justified by its ability to resolve the intrinsic unsteady flow motion resulting from the moving valves and pistons. The study of unsteady phenomena such as cycle-to-cycle variability, misfire and knock are especially important factors influencing the geometric design and the operating conditions [2]. The use of LES, which is known to be computationally expensive, is often favored with moderate Reynolds numbers ($10,000 < \text{Re} < 30,000$) and relatively small regions of interest. However, the fast prediction of accurate and detailed LES results to accelerate design cycles is still a challenge due to the increased number of cells and time required to generate adequate statistics when comparison with RANS approaches.

LES studies of fired and non-fired engine cases including moving piston and valves are reported by many researchers, e.g., [3–7]. Most of these numerical studies are focused on the analysis of cycle-to-cycle variations of in-cylinder flow fields and its influence on the mixing dynamics, combustion and pollutant emission. In this respect, it is worth mentioning that systematic evaluation studies of different LES approaches and models under engine-like operating conditions are rarely reported in the literature. This is mainly because of the considerable numerical effort required to carry out LES of many engine cycles of fired and non-fired cases with moving piston/valves. Furthermore, the complexity of in-cylinder flows impedes in-depth studies of individual processes and model evaluation. Therefore, it is useful to reduce the complexity of the engine configuration and evaluate LES approaches and numerical models by means of simplified flow bench configurations that represent most of the flow and mixing phenomena relevant to IC engines.

The aforementioned studies are based on traditional discretization methods like the finite volume method (FVM). In recent years, an alternative approach called the lattice Boltzmann method (LBM) has gained increasing attention in research and industry. LBM is useful in a wide range of applications, e.g., thermal flow simulations [19,20] or flows in complex geometries [21,22], due to its highly efficient parallel algorithm [23,24]. Such efficiency offers a high potential in reducing computation times for the simulation of high Reynolds number flows using DNS or LES approaches, which is usually a bottleneck in the field of turbulent flow simulations.

Qualitative and quantitative comparisons were made to estimate the capabilities of LBM based implementations for the simulation of turbulent flows in comparison with FVM-based implementations. In 2014 Kajzer et al. [25] evaluated the performance differences between an LBM and FVM implementation for the simulation of homogeneous isotropic turbulence. They found that in particular the scalability of LBM methods and the adaptivity for computations on graphics processing units (GPU) lead to a significant performance advantage compared with the tested FVM implementation in OpenFOAM. Two years later Pasquali et al. [26] showed that the calculation of the external aerodynamics of a car also benefits from the use of LBM on GPUs. A further comparison between LBM and FVM depicted that the higher grid resolution obtained by LBM leads to more resolved vortex structures in the outer layer of turbulent channel flows [27]. Barad et al. [28] compared a higher order finite difference method (FDM) with LBM in a software framework that uses the same Cartesian mesh structure. They showed that for the simulation of airframe noise the LBM implementation is 15 times faster than the higher order FDM scheme at a similar accuracy.

Most of the LBM studies related to engine flows that have been conducted to date deal with the injection process. Therefore, a multiphase approach is chosen to simulate spray formation, bubble break up and flow induced cavitation. A summary of these studies can be found in the book of Montessori and Falcucci [29]. A moving valve/pistion arrangement was simulated by Dorschner et al. [30] using the parameter-free Karlin–Bösch–Chikatamarla (KBC) collision operator. They showed that the results are in good agreement with a DNS reference.

In contrast to all these previous contributions, we focus on the implementation of open source near-wall-modeled LES (NWM-LES) to achieve fast and accurate results, which is relevant to users in academia and industry. Therefore, a recent version of the established FVM-based implementation of OpenFOAM is compared with OpenLB [31], an open source LBM framework. To get a fair comparison, we solve the same target equation in both software frameworks, including an explicit sub-grid scale (SGS) modeling and the use of a wall function. Furthermore, we do not limit the grid to a certain amount of cells or type of mesh elements so that each implementation can show its advantages. The grid generation process is also taken into account to compare the time spent on pre-processing. This is one of the first studies where in-house-conducted experimental data are used to validate two open source implementations. Moreover, a detailed error analysis of both methods covering the grid convergence of time-averaged and root mean square (RMS) velocity fields in the context of engine flows is a novelty. Additionally, a performance analysis compares the solver runtime of each implementation that is needed to calculate the statistics for the different grids. The comparison in the theory section aims to highlight the differences between both discretization methods. In addition, the differences in the implementation of wall-modeled LES in LBM and FVM are described. The NWM-LES implementation in LBM is ongoing research due to the complex boundary treatment in LBM. As a result, a new LBM wall function approach is proposed which extends the previous approaches [32,33] to curved boundaries.

This paper is organized as follows: Section 2 introduces the applied modeling approaches and shows the differences and similarities using LBM or FVM. Next, the experimental and numerical setup is described in Section 3. The related results using NWM-LES obtained with OpenFOAM and OpenLB for different grid resolutions are presented and compared to the PIV results in Section 4. Finally, Section 5 summarizes the results and draws a conclusion.

2. Applied Modeling Approaches

2.1. Filtered Navier–Stokes Equations

The filtered incompressible Navier–Stokes equations consist of the continuity equation

$$\frac{\partial \overline{u}_\alpha}{\partial x_\alpha} = 0, \tag{1}$$

and the momentum equation according Leonard's decomposition [34] which reads

$$\frac{\partial \overline{u}_\alpha}{\partial t} + \frac{\partial \overline{u}_\alpha \overline{u}_\beta}{\partial x_\beta} = \nu \frac{\partial}{\partial x_\beta}\left(\frac{\partial \overline{u}_\alpha}{\partial x_\beta} + \frac{\partial \overline{u}_\beta}{\partial x_\alpha}\right) - \frac{\partial T^{\mathrm{SGS}}_{\alpha\beta}}{\partial x_\beta} - \frac{1}{\rho}\frac{\partial \overline{p}}{x_\alpha}, \tag{2}$$

where Greek indices obey the Einstein notation, $\overline{u}_\alpha$ is the filtered velocity, $\overline{p}$ is the filtered pressure field, $T^{\mathrm{SGS}}_{\alpha\beta}$ is the SGS stress tensor, ρ is the density and ν is the viscosity. This set of equations can be closed by using a linear eddy viscosity hypothesis for the SGS stress tensor

$$T^{\mathrm{SGS}}_{\alpha\beta} = -\nu^{\mathrm{SGS}} \left(\frac{\partial \overline{u}_\alpha}{\partial x_\beta} + \frac{\partial \overline{u}_\beta}{\partial x_\alpha} \right), \tag{3}$$

where ν^{SGS} is the SGS viscosity that can be modeled by an SGS viscosity model (see Section 2.2). In Equation (2) no volume force is applied and will not be considered hereafter.

2.1.1. Finite Volume Method

In dealing with the FVM of incompressible fluid flow, the discretization process of the balance laws of fluid motion can be divided into two steps: (1) the spatial and temporal discretization of the solution domain and (2) the discretization of the spatial and temporal terms in the Navier–Stokes equations [35]. Then, the partial differential equations can be converted into a corresponding set of algebraic equations and solved numerically. Additionally, nonlinearities in the Navier–Stokes equations and the pressure-velocity coupling require some special numerical treatment. The second-order solution procedure employed in the open source C++ library OpenFOAM 2.4.0, which is used in the present LES study, is briefly outlined in the following. A detailed description can be found, e.g., in [36–38].

In the standard FVM framework of OpenFOAM, the continuum space and time domain are divided into a finite number of discrete regions called control volumes (CV) and time intervals, respectively. Thereby, the CVs completely bound the solution domain and the solution variables, such as velocity and pressure, are colocated at the cell centroids of the CVs [39]. In contrast to a staggered grid arrangement, this allows an arbitrary topology of CVs, e.g., hexahedrons, tetrahedrons, prisms, pyramids or general polyhedrons, which has significant advantages in the discretization of complex solution domains.

Several approximation schemes and solution procedures are available in the OpenFOAM framework to discretize and solve the Navier-Stokes equations. In this study, the standard pimpleFOAM solver of OpenFOAM 2.4.0 is applied, which is based on a merged PISO [40]-SIMPLE [41] algorithm for the coupling of pressure and velocity. Thereby, the governing equations are numerically solved in a segregated manner using a momentum predictor, pressure solver and momentum corrector. This iterative solution procedure is applied with a second-order implicit backward-differencing scheme for the time integration. Regarding spatial terms, a low-dissipative second-order flux-limiting differencing scheme is employed for the convection terms and a conservative scheme is used for the Laplacian and gradient terms. The resulting systems of linear equations are iteratively solved using a geometric agglomerated algebraic multigrid solver. Thereby, convergence of the overall procedure is obtained if all normalized residuals are smaller than 10^{-4}. Validation and verification studies of this specific solution procedure for LES of complex fluid flows relevant to IC engines are provided in [18,42,43].

2.1.2. Lattice Boltzmann Method

The lattice Boltzmann equation discretizes the velocity space of the kinetic Boltzmann equation to a discrete set of lattice velocities c_i, $i = 0, 1, \dots, q-1$. Common velocity sets to recover the three-dimensional incompressible Navier–Stokes equations are $D3Q15$, $D3Q19$ and $D3Q27$. The present work uses a discrete velocity $D3Q19$ set, which is given by

$$c_i = \begin{cases} (0,0,0) & i = 0 \\ (\pm1,0,0),\ (0,\pm1,0),\ (0,0,\pm1) & i = 1,2,\dots,6 \\ (\pm1,\pm1,0),\ (\pm1,0,\pm1),\ (0,\pm1,\pm1) & i = 7,8,\dots,18 \end{cases} \tag{4}$$

The descriptor set is chosen due to the higher computation performance and the lower memory demand in the used LBM implementation. However, higher errors due to a violation of the rotational invariance are taken into account in comparison with a $D3Q27$ stencil [44].

The filtered lattice Boltzmann equation without external forces is given by

$$\overline{f}_i\left(x^{\mathrm{LB}}+c_i,t^{\mathrm{LB}}+1\right)=\overline{f}_i\left(x^{\mathrm{LB}},t^{\mathrm{LB}}\right)+\overline{\Omega}_i, \tag{5}$$

where $\overline{f}_i$ is the filtered particle distribution function at discrete lattice position x^{LB} and time step t^{LB}. The filtered collision operator $\overline{\Omega}_i$ is implemented by a single-relaxation time model proposed by Bhatnagar, Gross and Krook [45]. It can be written as

$$\overline{\Omega}_i=-\frac{1}{\tau^{eff}}\left(\overline{f}_i(t^{\mathrm{LB}},x^{\mathrm{LB}})-\overline{f}_i^{eq}(\overline{\rho}^{\mathrm{LB}},\overline{u}^{\mathrm{LB}})\right), \tag{6}$$

where τ^{eff} is the effective relaxation time towards the filtered discrete particle distribution function at equilibrium state $\overline{f}_i^{eq}$, $\overline{\rho}$ is the filtered lattice density and $\overline{u}$ the filtered velocity field. The collision operator satisfies the conservation of mass and momentum. The particle distribution function equilibrium is described by a low Mach number truncated Maxwell-Boltzmann distribution

$$\overline{f}_i^{eq}\left(\overline{\rho}^{\mathrm{LB}},\overline{u}^{\mathrm{LB}}\right)=\overline{\rho}^{\mathrm{LB}}\omega_i\left[1+\frac{c_{i\alpha}\overline{u}_\alpha^{\mathrm{LB}}}{c_s^2}+\frac{\overline{u}_\alpha^{\mathrm{LB}}\overline{u}_\beta^{\mathrm{LB}}(c_{i\alpha}c_{i\beta}-c_s^2\delta_{\alpha\beta})}{2c_s^4}\right], \tag{7}$$

where ω_i are the lattice weights obtained by the Gauss-Hermite quadrature [46,47], $c_s=1/\sqrt{3}$ is the speed of sound of the lattice and $\delta_{\alpha\beta}$ is the Kronecker operator.

The moments of the particle distribution functions $\overline{f}_i$ yield macroscopic flow quantities. The density $\overline{\rho}^{\mathrm{LB}}$, the momentum $\overline{\rho}^{\mathrm{LB}}\overline{u}^{\mathrm{LB}}$ and momentum flux $\overline{\Pi}$ are obtained by the zeroth, first and second moments, which are given by

$$\overline{\rho}^{\mathrm{LB}}=\sum_{i=0}^{q-1}\overline{f}_i\,, \tag{8}$$

$$\overline{\rho}^{\mathrm{LB}}\overline{u}^{\mathrm{LB}}=\sum_{i=0}^{q-1}c_i\overline{f}_i, \tag{9}$$

$$\overline{\Pi}_{\alpha\beta}=\sum_{i=0}^{q-1}c_{i\alpha}c_{i\beta}\overline{f}_i\,. \tag{10}$$

The lattice effective kinematic viscosity of the fluid ν^{eff} is connected to the effective relaxation time τ^{eff} as follows

$$\nu^{\mathrm{LB},eff}=c_s^2\left(\tau^{eff}-0.5\right). \tag{11}$$

Assuming a simplified isothermal equation of state the filtered lattice pressure is related to the filtered density by

$$\overline{p}^{\mathrm{LB}}=c_s^2\overline{\rho}^{\mathrm{LB}}. \tag{12}$$

Finally, the lattice Boltzmann algorithm is divided in 2 steps: the collision step and the streaming step. The local collision step is represented by the right-hand side of Equation (5) and the subsequent streaming step is associated with the left-hand side of Equation (5).

2.2. Sub-Grid Scale Modeling

The introduced eddy viscosity ν^{SGS} in Equation (3) is estimated by an SGS viscosity model, which can be generally written as

$$\nu^{\mathrm{SGS}} = (C_M \Delta_{grid})^2 D_M, \tag{13}$$

where C_M is a model coefficient, Δ_{grid} is the grid filter and D_M a model-related operator. The present work uses a Smagorinsky-Lilly model [48], where the model operator is defined as

$$D_M = \sqrt{2\overline{S}_{\alpha\beta}\overline{S}_{\alpha\beta}}, \tag{14}$$

where $\overline{S}_{\alpha\beta}$ is the filtered strain rate. The literature values for the Smagorinsky-Lilly model constant C_M are in the range of $C_M = 0.065...0.24$ [49,50]. For a complex turbulent flow, a Smagorinsky-Lilly constant of $C_M = 0.1$ is a common choice [51]. The Smagorinsky–Lilly model suffers from a too dissipative behavior in the near-wall region [42,52]. One possibility to prevent this aspect is the introduction of a damping function that reduces the SGS viscosity depending on the wall distance. The van Driest damping function [53] can be incorporated in the grid filter Δ_{grid} by

$$\Delta_{grid} = \min\left[\sqrt[3]{\Delta_x \Delta_y \Delta_z},\ \frac{\kappa y}{C_\Delta}\left(1 - e^{(-\frac{y^+}{A^+})}\right)\right], \tag{15}$$

where y is the wall distance, $A^+ = 26$ is the van Driest parameter, $C_\Delta = 0.158$ is a model constant and $\kappa = 0.41$ is the von Kármán constant [54]. The dimensionless wall distance y^+ in Equation (15) is defined as

$$y^+ = \frac{u_\tau y}{\nu}, \tag{16}$$

where $u_\tau = \sqrt{\frac{T_w}{\rho}}$ is the friction velocity and T_w the wall shear stress.

2.2.1. SGS Model for Finite Volume Method

In the FVM framework of OpenFOAM, the SGS viscosity ν^{SGS} is calculated explicitly for each time step using the resolved velocity field. Then, the turbulent and molecular diffusion contributions are combined into an effective stress tensor by means of the Boussinesq approximation as

$$\begin{aligned} T^{eff}_{\alpha\beta} &= -\left(\nu + \nu^{\mathrm{SGS}}\right)\left(\frac{\partial \overline{u}_\alpha}{\partial x_\beta} + \frac{\partial \overline{u}_\beta}{\partial x_\alpha}\right), \\ &= -\nu^{eff}\left(\frac{\partial \overline{u}_\alpha}{\partial x_\beta} + \frac{\partial \overline{u}_\beta}{\partial x_\alpha}\right), \end{aligned} \tag{17}$$

where ν^{eff} represents the effective viscosity. For the sake of computational efficiency, the velocity gradient and transposed velocity gradient terms in Equation (17) are treated separately. Thereby, the velocity gradient term is treated implicitly as a diffusion, while the transposed velocity is treated as an explicit source term. The latter is therefore calculated using the velocity at the previous iteration. Further information on the implementation of eddy viscosity turbulence in OpenFOAM can be found, e.g., in [55].

2.2.2. SGS Model for Lattice Boltzmann Method

Eddy viscosity models are often introduced in LBM by adding turbulent viscosity to the molecular viscosity [56], which results in an effective viscosity

$$\nu^{\mathrm{LB},eff} = \nu^{\mathrm{LB}} + \nu^{\mathrm{LB,SGS}}. \tag{18}$$

A consistent approach to implement eddy viscosity models in LBM was derived by Malaspinas and Sagaut [57]. They presented that due to the connection between lattice viscosity and lattice relaxation time (see Equation (11)), the relaxation time is also divided in a molecular and SGS contribution

$$\tau^{eff} = \tau + \tau^{\mathrm{SGS}}, \tag{19}$$

where $\tau^{\mathrm{SGS}} = \frac{\nu^{\mathrm{LB,SGS}}}{c_s^2}$ is the eddy contribution. The filtered strain rate $\overline{S}^{\mathrm{LB}}_{\alpha\beta}$ in the SGS operator formulation in Equation (14) can be obtained by a finite difference scheme or locally in the LBM framework by

$$\overline{S}^{\mathrm{LB}}_{\alpha\beta} = -\frac{\overline{\Pi}^{neq}_{\alpha\beta}}{2\overline{\rho}^{\mathrm{LB}}\tau^{eff}c_s^2}, \tag{20}$$

where $\overline{\Pi}^{neq}_{\alpha\beta}$ is the second moment of the non-equilibrium parts of the particle distribution function, which can be calculated according to Equation (10) by replacing $\overline{f}_i$ with $\overline{f}^{neq}_i = (\overline{f}_i - \overline{f}^{eq}_i)$. This implicit relation of the effective relaxation time τ^{eff} and the filtered strain rate $\overline{S}^{\mathrm{LB}}_{\alpha\beta}$ can be replaced by an explicit expression for the Bhatnagar–Gross–Krook (BGK) collision operator by a local method proposed by Malaspinas and Sagaut [57]. This explicit expression for determining the effective relaxation time τ^{eff} is given by

$$\tau^{eff} = \sqrt{\tau^2 + \frac{2C_M^2}{\overline{\rho}^{\mathrm{LB}}\,c_s^4}\sqrt{2\overline{\Pi}^{neq}_{\alpha\beta}\overline{\Pi}^{neq}_{\alpha\beta}}} + \frac{\tau}{2}. \tag{21}$$

2.3. *Wall Function Approach*

In contrast to a near-wall resolved LES, the NWM-LES requires additional effort to model the effects occurring in the boundary layer. However, NWM-LES allows grid spacing up to $y^+ = 200$, which results in a significantly smaller amount of grid points. In the present work, we use the idea of Werner and Wengle [58], which describes an instantaneous connection between the wall shear stress and the velocity. This consideration only applies for averaged quantities and therefore a RANS hypothesis is assumed for the boundary node. A fully developed turbulent boundary layer can be described by the Musker profile [59] which reads

$$\begin{aligned} u^+ = {} & 5.424 \arctan\left(\frac{2.0y^+ - 8.15}{16.7}\right) \\ & + \log_{10}\left(\frac{(y^+ + 10.6)^{9.6}}{(y^{+2} - 8.15y^+ + 86.0)^2}\right) \\ & - 3.5072790194. \end{aligned} \tag{22}$$

This empirical formulation is based on a logarithmic law and is able to describe the turbulent boundary layer from the viscous sublayer ($y^+ \geq 1$). The solution of the implicit function (22) requires an iterative scheme.

2.3.1. Wall Function for Finite Volume Method

Analogous to wall-shear stress models often used in the context of RANS, the boundary condition of the SGS viscosity ν^{SGS} is corrected for each time step by means of a wall function in the NWM-LES approach of OpenFOAM. The numerical procedure can be divided into two steps. First, the friction velocity u_τ is approximated iteratively according to Musker's wall function. Thereby, the Newton–Raphson method is applied to find the root of the wall function. Then, in the second step, ν^{SGS} at the wall is calculated as

$$\nu^{\mathrm{SGS}} = u_\tau^2 \frac{y_p}{u_\parallel}, \tag{23}$$

where y_p denotes the wall distance of the cell centroid and $u_\parallel$ the stream-wise velocity. It is important to note that a boundary condition of ν^{SGS} based on Musker's wall function is not available in OpenFOAM and was therefore added to the standard framework. A detailed description of the wall function approach in OpenFOAM including comprehensive validation studies in turbulent channel and impinging flows were provided by the authors in [60].

2.3.2. Wall Function for Lattice Boltzmann Method

The implementation of wall functions in the context of LBM is not straightforward due to numerous boundary scheme approaches. The idea of the wall model approach applied in this work was proposed by Malaspinas and Sagaut [32] and adapted to the BGK collision operator by Haussmann et al. [33]. They validated the wall function scheme using a bi-periodic turbulent channel flow. We adapt this scheme to curved boundaries using a curved link-wise instead of a wet-node boundary scheme. Our proposed algorithm is parted in two steps: the curved boundary approach and a velocity correction step according to the wall function. For better comprehension, the used indexing convention for the following two paragraphs is depicted in Figure 1.

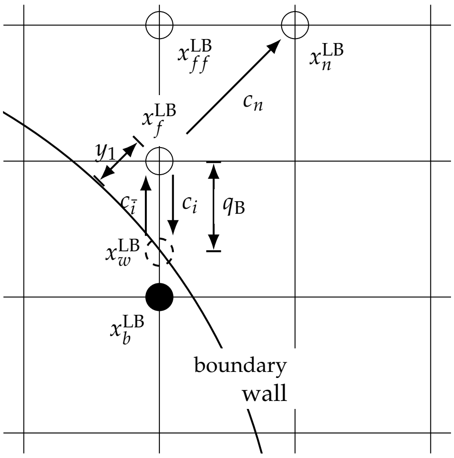

Figure 1. Illustration of the indexing convention for the curved wall function approach applied in this work.

Curved Boundary Step

In the present work, we use the curved boundary approach proposed by Bouzidi et al. [61]. This approach is an extension of a half-way bounce back scheme and characterized as precise, stable and computationally efficient for the simulation of turbulent flows [62]. The interpolated bounce-back approach uses a linear interpolation based on the dimensionless distance q_{B}, which is defined as:

$$q_{\mathrm{B}} = \frac{|x_f^{\mathrm{LB}} - x_w^{\mathrm{LB}}|}{|x_f^{\mathrm{LB}} - x_b^{\mathrm{LB}}|}. \tag{24}$$

Without altering the streaming step for boundary cells the unknown particle distribution function after the streaming step $f_{\bar{i}}(x_f^{\mathrm{LB}}, t^{\mathrm{LB}} + 1)$ can be replaced by

$$f_{\bar{i}}(x_f^{\mathrm{LB}}, t^{\mathrm{LB}}+1) = \begin{cases} \frac{1}{2q_{\mathrm{B}}} f_i(x_b^{\mathrm{LB}}, t^{\mathrm{LB}}+1) + \frac{2q_{\mathrm{B}}-1}{2q_{\mathrm{B}}} f_{\bar{i}}(x_{ff}^{\mathrm{LB}}, t^{\mathrm{LB}}+1) & \text{for } q_{\mathrm{B}} \geq \frac{1}{2}, \\ 2q_{\mathrm{B}} f_i(x_b^{\mathrm{LB}}, t^{\mathrm{LB}}+1) + (1-2q_{\mathrm{B}}) f_i(x_f^{\mathrm{LB}}, t^{\mathrm{LB}}+1) & \text{for } q_{\mathrm{B}} < \frac{1}{2}, \end{cases} \tag{25}$$

where index $\bar{i}$ indicates the particle distribution function in the opposite direction of index i. For $q_{\mathrm{B}} = 0.5$ the approach is equal to the half-way bounce back boundary condition.

Velocity Correction Step

The velocity correction step is used to correct the velocity in the particle distribution functions at node position x_f^{LB} according the wall function. Firstly, the distance to the boundary y_1^{LB} is defined in the discrete normal direction c_n. Accordingly, the distance from the neighbor fluid node at position x_n^{LB} to the boundary is given by

$$y_2^{\mathrm{LB}} = y_1^{\mathrm{LB}} + |c_n|. \tag{26}$$

Due to the fact that the wall profile uses only the stream-wise velocity component, a local stream-wise unit vector $\mathbf{e}_s$ is obtained by

$$\mathbf{e}_s = \frac{\overline{u}_n^{\mathrm{LB}} - (\overline{u}_n^{\mathrm{LB}} \cdot c_n)c_n}{|\overline{u}_n^{\mathrm{LB}} - (\overline{u}_n^{\mathrm{LB}} \cdot c_n)c_n|}. \tag{27}$$

Subsequently, the stream-wise component $\overline{u}_2^{\mathrm{LB}}$ of $\overline{\mathbf{u}}_n^{\mathrm{LB}}$ is calculated by

$$\overline{u}_2^{\mathrm{LB}} = \overline{u}_n^{\mathrm{LB}} \cdot \mathbf{e}_s. \tag{28}$$

The boundary distance y_2^{LB} and the stream-wise velocity component $\overline{u}_2^{\mathrm{LB}}$ are inserted in the Musker profile Equation (22) to obtain the averaged wall shear stress $\tilde{T}_w^{\mathrm{LB}}$. Therefore, the solution of the implicit equation is approximated by the Newton method. Afterwards, the stream-wise component $\tilde{u}_1^{\mathrm{LB}}$ of $\tilde{u}_f^{\mathrm{LB}}$ is calculated by the Musker profile Equation (22) using the boundary distance y_1^{LB} and the averaged wall shear stress $\tilde{T}_w^{\mathrm{LB}}$. Then, the velocity $\tilde{u}_f^{\mathrm{LB}}$ of the first fluid is computed by

$$\tilde{u}_1^{\mathrm{LB}} = \tilde{u}_f^{\mathrm{LB}} \cdot \mathbf{e}_s. \tag{29}$$

Finally, the particle distribution function at node position x_f^{LB} is corrected as follows

$$f_i(x_f^{\mathrm{LB}}, t^{\mathrm{LB}}+1) = f_i^{eq}(\rho^{\mathrm{LB},*}, \tilde{u}_f^{\mathrm{LB}}) + f_i^{neq,*}, \tag{30}$$

where superscript $*$ denotes the quantities calculated after Equation (25). This means only the velocity is altered according the wall function, while the density and the non-equilibrium parts are preserved.

3. Setup of the IC Engine Test Case

In this work, a flow bench setup of an IC engine was chosen as a benchmark for the numerical comparison. With this setup, the intake flow with the focus on the intake jet over the valves into the cylinder can be examined in a realistic engine geometry and at the same time the overall complexity can be reduced compared with a real engine. The optically-accessible single cylinder engine at TU Darmstadt (*Darmstadt Engine*, [10]) was converted into a steady-state flow bench by removing and replacing the piston with an outlet channel open to ambient conditions (see Figure 2). As opposed to the previous flow bench studies of Freudenhammer et al. [63] in which the same spray-guided cylinder head geometry was fitted in a continuous water flow configuration for MRV measurements, the flow bench of the present study uses dry air and allows for instantaneous flow measurements. For this configuration, the cylinder liner was extended and the outlet channel geometry was optimized by means of unsteady RANS to suppress recirculation of the flow. For added simplicity to the engine geometry, the spark plug and fuel injector were replaced by flat plugs; but otherwise, the four-valve spray-guided pent-roof cylinder head (AVL) and fused-silica cylinder liner with a bore of 86 mm as well as the intake system remained unchanged. Figure 2 shows a diagram of the intake system and engine geometry of the flow bench experiment. As indicated by the red boxes, the flow bench has three optical access sections. The first section (I) represents the standard engine optical access which was fitted to the new flow bench extension (experimental sections II and III). Experimental section II allows for the characterization of the flow inside the flow bench extension for the verification of the flow structures present. Finally, experimental section III allows optical access and flow validation of the outflow through the bottom of the flow bench via a flat fused-silica plate and movable mirror. Intake valves were positioned at a fixed valve lift of 9.21 mm corresponding to 270 °CA (crank angles before top dead center) and exhaust valves were kept closed, thus mimicking the intake flow during regular engine operation.

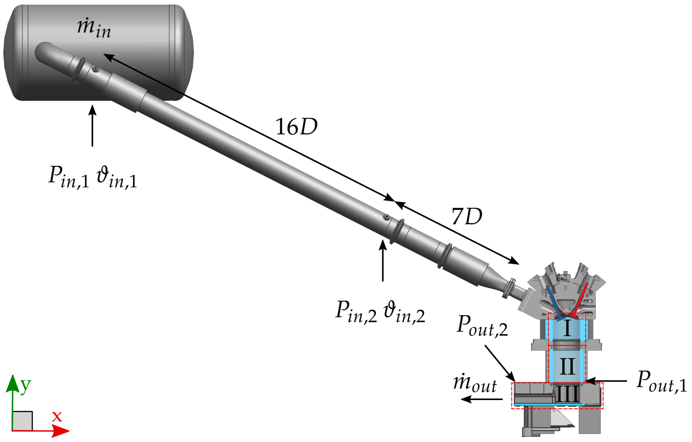

Figure 2. Flow bench and intake system overview. The inner diameter of the intake pipes D is 56.3 mm. Experimental sections include the standard engine- (I), the Flow bench- (II) and the Outlet duct optical access (III).

The flow bench experiment was conducted under controlled boundary conditions for consistent operation. Two mass flow controllers (Bronkhorst) were used to set a defined mass flow of 94.1 $\frac{\text{kg}}{\text{h}}$, which corresponds to the respective instantaneous mass flow at 270 °CA under normal engine operation with a speed of 800 rpm and intake pressure of 0.95 bar. Since the instantaneous mass flow of engine operation is not available, the velocities in the intake jet were compared and matched such that the phase-averaged velocity (average of 400 cycles at 270 °CA) in motored engine operation matched the average velocities of the flow bench near the intake valve. As indicated in Figure 2, two absolute pressure sensors ($P_{in,1}$, $P_{in,2}$, PAA-M8cool HB, Keller) measured the static pressure and two PT100 temperature sensors ($\vartheta_{in,1}$, $\vartheta_{in,2}$) measured the temperature of the flow within the intake pipe. Additionally, two more absolute pressure sensors ($P_{out,1}$, $P_{out,2}$, PMP4070, Kistler) measured the static pressure inside the flow bench. Table 1 summarizes the experimental boundary conditions.

Table 1. Flow bench boundary conditions. Values in brackets represent estimates of the measurement uncertainty (total error band corresponding to a rectangular distribution with mean ± uncertainty).

Valve Lift	**9.21(0.15) mm**
$\vartheta_{in,2}$	22.7(0.5) °C
$P_{in,2}$	1.000(0.001) bar
$P_{out,2}$	0.998(0.001) bar
$\dot{m}_{in}$	94.10(1.00) kg/hr
η	18.26×10^{-6} kg/(m s)
ρ	1.18 kg/m^3
ϑ_{wall} (estimated)	22(1) °C

3.1. Experimental Setup

High-speed PIV was used to measure the in-cylinder flow velocity field in the valve plane (VP, z = −19 mm) (see Figure 3). For this configuration a laser light sheet (850 µm thickness) from two high-speed frequency-doubled Nd:YAG cavities (IS4II-DE Edgewave), operated at 12.5 kHz each with a time separation of 8 µs, entered the cylinder volume via the bottom glass plate of the outlet channel. DOWSIL 510 (Dow Corning) silicone oil was atomized by a fluid seeder (AGF 10.0, Palas) with an average particle size of 0.5 µm and introduced to the intake system as tracer particles. The Mie-scattered light was imaged with a high-speed CMOS camera (Phantom v2640) equipped with a Nikon lens (85 mm f/1.4 with 35 mm distance rings) in HS Binned double-frame mode.

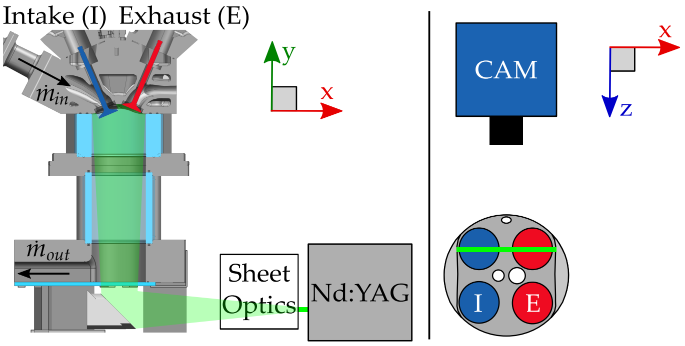

Figure 3. Arrangement of particle image velocimetry (PIV) measurement system.

The commercial software DaVis 10.0.5 (LaVision) was used to calculate flow fields. After a time filter background subtraction, a cross-correlation with multi-pass iterations of decreasing window size (twice: 48 × 48 pixel; twice: 24 × 24 pixel, 75% overlap) resulted in vector fields which where post-processed with a peak ratio threshold of 1.3 and a universal outlier median filter to remove spurious vectors. The dynamic range of the velocity measurement is limited by the minimum and maximum resolved pixel shift. The frame separation time of the setup was optimized to yield a pixel shift of maximum 4.5 pixels in the intake jet region, since the jet characteristics are the main interest.

The uncertainty of velocity measurements by means of PIV depends on parameters such as the optical setup defined by imaging optics, camera and light sheet as well as tracer properties, the PIV algorithm and the flow itself. Common approaches to estimate the uncertainty as a function of different influencing variables employ artificial PIV images generated by Monte Carlo simulations [64]. Newer methods use the actual experimental data to estimate the uncertainty [65–67] and have been validated by a benchmark experiment [68].

The commercial software DaVis estimates the uncertainty based upon a correlation statistics approach [67]. In this study, the time-averaged uncertainty of the instantaneous velocity magnitudes is approximately 3% to 6% (normalized to the global maximum velocity range of 35 m s^{-1}). This uncertainty range is valid for the jet region and lower velocity regions below the valves. Near the exhaust side cylinder walls, where the intake jet is curved downwards due to the influence of the walls, the normalized uncertainties increase to a maximum of 10%. This approach considers random errors inherent to the correlation process for particle images. Therefore, the reported uncertainties apply for instantaneous velocity fields and propagate to RMS velocity values, but are reduced to $\ll 1\%$ for the time-averaged velocity, since most of the 25,000 pairs of particle images are uncorrelated to each other.

Other sources of error introduce a bias in the velocity calculation. Sharp gradients in the flow, e.g., at the edge of the intake jet, are underestimated due to the spatial averaging of the PIV algorithm. Acknowledging reported uncertainty assessments [64], this normalized error is assumed to be on the order of 3% to 9% for the jet region in instantaneous velocity fields and is slightly lower in the time-averaged velocity field due to the non-stationary jet position. The spatial average of the normalized uncertainty due to flow gradients amounts to 1%.

Additional systematic errors stem from the non-zero light sheet thickness and strong out-of-plane velocity components, which are detected as in-plane components due to the camera's perspective. This error is zero in the center, increases linearly to the edges of the field-of-view and can amount to more than 10% [64]. However, if the averaged out-of-plane velocity component is zero this error source is statistically zero. In the central tumble plane this assumption is justified, but less so in the valve plane, where mean out-of-plane velocity components exist. The uncertainty due to perspective errors was calculated with the time-averaged LES flow field, which provides all three velocity components. This normalized uncertainty contribution amounts to up to 10% locally and to 0.2% in the spatial average. Altogether, the spatially averaged accumulated normalized uncertainty of the time-averaged PIV measurements within this work is estimated to be 1%.

3.2. Numerical Setup

The fluid domain is depicted in Figure 4 in a clip representation. The inlet patch is colored in blue and the outlet patch in red. In contrast to the experimental setup, both the inflow and outflow regions are shortened in order to reduce the computational effort. The reduction of the inflow length to $2.62D$ is justified by the applied inlet boundary condition (see Section 3.3). For the estimation of the outflow length as $1.88D$, the tumble flow area and the integral time scale were considered to ensure that the influence of the flow upstream is negligible.

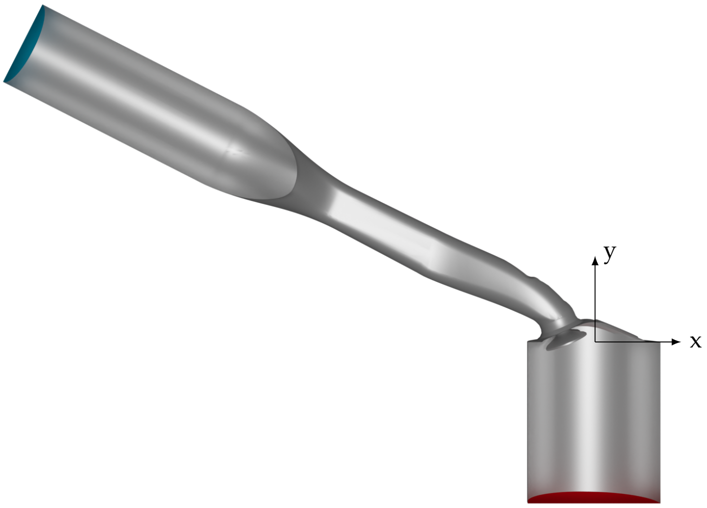

Figure 4. Clip representation of the simulation geometry with (x,y)-plane coordinate system. The boundary contains inlet (blue), outlet (red) and wall patches (metallic).

3.3. Boundary Conditions and Initial Conditions

The initial and boundary conditions play an important role in LES, because they mainly influence the time for statistically independent results. The inlet condition is especially challenging; the often used approaches that assume random fluctuations are not sufficient. The result is an energy signal, which equally distributes the energy in the wave number regime. Therefore, in the present study, we apply a digital filter-based operation proposed by Klein et al. [69]. This approach is able to reproduce prescribed Reynolds stresses. Considering the measured mass flow in the experiment and assuming a plug flow profile, the Dirichlet condition for the time-averaged inflow velocity is given by

$$\langle u \rangle_{in} = (7.941, -4.047, 0.0)\ \frac{\mathrm{m}}{\mathrm{s}}. \tag{31}$$

The superimposed fluctuations use an integral length of $L = 0.25D$ according to the work of Ries et al. [42]. The calculation of the prescribed Reynolds stress tensor $\langle u'_\alpha u'_\beta \rangle_{in}$, taking the hypothesis of homogeneous isotropic turbulence into account, reads

$$\langle u'_\alpha u'_\beta \rangle_{in} = \delta_{\alpha\beta}\, |\langle u \rangle_{in}|\, I, \tag{32}$$

where $I = 0.06$ is the turbulence intensity. The outlet condition is a free outflow condition, where the Dirichlet pressure condition is set to

$$p_{out} = 0\,\mathrm{Pa}. \tag{33}$$

3.3.1. Finite Volume Method

In the case setup of OpenFOAM, no-slip conditions are utilized for the velocity and the zero Neumann condition is used for the kinematic pressure at the solid walls. Furthermore, the wall function approach is employed for the SGS viscosity at the walls. At the outlet, a velocity inlet/outlet boundary condition is used to allow back-flow of air from downstream. Thereby, the incoming fluid velocity is obtained by the internal cell value, while the zero Neumann condition is employed in the case of outflow. Finally, as mentioned above, synthetic turbulent inflow conditions are employed at the inflow based on the digital filter method of Klein et al. [69].

3.3.2. Lattice Boltzmann Method

As previously mentioned in Section 2.3.2, the boundary conditions in the LBM are a critical challenge, especially in turbulent flows, where both accuracy and stability are important. The inflow condition is realized by a non-local regularized approach (see boundary scheme BC4 in [70]). The used inflow velocity is obtained by the digital filter approach, which is bilinear interpolated and mapped to each cell position. The outflow condition uses a wet-node equilibrium condition. Every particle distribution in each boundary cell before the regular collision occurs is replaced by

$$f_i(x^{\mathrm{LB}}, t^{\mathrm{LB}}) = f_i^{eq}(\rho_{out}^{\mathrm{LB}}, u^{\mathrm{LB}}(x^{\mathrm{LB}} + c_n, t^{\mathrm{LB}})), \tag{34}$$

where ρ_{out}^{LB} is the prescribed lattice density and $u^{\mathrm{LB}}(x^{\mathrm{LB}} + c_n, t^{\mathrm{LB}})$ the velocity of the neighbor cell in the normal direction. It is noteworthy that boundary approaches that also reconstruct the non-equilibrium part (e.g., BC3 and BC4 in [70]) show stability issues for this flow configuration.

The flow field is initialized by the equilibrium distribution $f_i^{eq}(\rho^{\mathrm{LB}}, u^{\mathrm{LB}})$, where $\rho^{\mathrm{LB}} = 1$ and $u^{\mathrm{LB}} = 0$. Then, the velocity at the inflow is increased at the inlet for $t = 0.05\,\mathrm{s}$ and is updated until the considered mass flow is reached. This procedure results in non-equilibrium parts of the particle distribution function that are adjusted according to the velocity field.

3.4. Statistics

The flow field is assumed to be statistically stationary after $t_{ss} = 0.5\,\mathrm{s}$. After this start-up time, sampling is started within the LBM and FVM frameworks. The statistics are used to calculate the time-averaged velocity $\langle u \rangle$ and the RMS velocity u_{RMS}, which can be calculated by

$$u_{\alpha,\mathrm{RMS}} = \sqrt{\langle (u'_\alpha)^2 \rangle} = \sqrt{\langle u_\alpha^2 \rangle - \langle u_\alpha \rangle^2}, \tag{35}$$

where $\langle u_\alpha^2 \rangle$ is the time-averaged square of the velocity. The averaging time for u_{RMS} is calculated according to the engineering correlation proposed by Ries et al. [42] as

$$t_{av} = \frac{L}{|\langle u \rangle|\,\epsilon_{\mathrm{RMS}}^2}, \tag{36}$$

where ϵ_{RMS} is the desired maximum sampling error. Inserting a sampling error $\epsilon_{\mathrm{RMS}} = 0.025$, the averaging time is calculated as $t_{av} = 2.524\,\mathrm{s}$.

3.4.1. Finite Volume Method

An adaptive time stepping technique is applied in the OpenFOAM setup in order to ensure a Courant–Friedrichs–Lewy (CFL) number smaller than one. Thereby, the time-averaged velocities are defined as

$$\langle u_\alpha \rangle = \frac{1}{t_{av}} \sum_{n=0}^{N_t} \left(u_\alpha^n \Delta t^n \right), \tag{37}$$

where Δt^n is the time step at t^n and N_t the total number of time steps within t_{av}. Analogously, the time-averaged square of the velocity $\langle u_\alpha^2 \rangle$ is given by

$$\langle u_\alpha^2 \rangle = \frac{1}{t_{av}^2} \sum_{n=0}^{N_t} \left(u_\alpha^n \Delta t^n \right)^2. \tag{38}$$

3.4.2. Lattice Boltzmann Method

Due to the use of fixed time steps, ensemble averaging is applied. The time-averaged velocity $\langle u_\alpha \rangle$ is given as

$$\langle u_\alpha \rangle = \frac{1}{N_e} \sum_{t_{ss}}^{t_{ss}+t_{av}} \left(u_\alpha(t) \right), \tag{39}$$

where number N_e is the number of independent ensembles. In the same way the time-averaged square of the velocity $\langle u_\alpha^2 \rangle$ is evaluated as

$$\langle u_\alpha^2 \rangle = \frac{1}{N_e^2} \sum_{t_{ss}}^{t_{ss}+t_{av}} \left(u_\alpha(t) \right)^2. \tag{40}$$

Assuming Taylor's hypothesis of frozen turbulence and a spatial decorrelation distance of two integral length scales L, the number of independent ensembles N_e is calculated by

$$N_e = \frac{t_{av} |\langle u \rangle_{in}|}{2L}. \tag{41}$$

This results in 800 independent ensembles.

3.5. Grid Configurations

Both OpenFOAM and OpenLB are evaluated with three different grids in this work. There are certain differences between the grid structures, see Figure 5.

OpenLB uses a uniform Cartesian mesh without grid refinement. The fluid cells are indicated by checking if each grid point is inside or outside the geometry. The resulting grid is not volume conservative. In contrast, body-fitted meshes are favored by OpenFOAM. Therefore, prisms and polyhedral mesh elements are applied to reconstruct the geometry shape and preserve the volume. Furthermore, refinement layers are used to resolve more scales, especially near the wall. A detailed comparison between the three grid configurations used: low resolution (LR), medium resolution (MR) and high resolution (HR) for both OpenFOAM and OpenLB can be found in Table 2.

Acoustic scaling $\Delta t \propto \Delta x$ is used for the presented OpenLB configuration, which provides a constant compressibility error with respect to the incompressible Navier–Stokes equations but in return, requires less computational increase for smaller grid spacing than diffusive scaling. The application of acoustic scaling leads to a constant lattice Mach number $\mathrm{Ma}^{\mathrm{LB}} = 0.026$ for the OpenLB setups. The resulting compressibility error is assumed to be sufficiently small. In terms of the inlet diameter D, Cartesian grid resolutions of $N = 53, 77$ and 111 are generated, approximately tripling the cell number in every configuration consisting of OpenFOAM meshes. Due to the adaptive time step and grid refinement in OpenFOAM, the size of the displayed grid spacing Δx and time step Δt is space- and time-averaged, respectively.

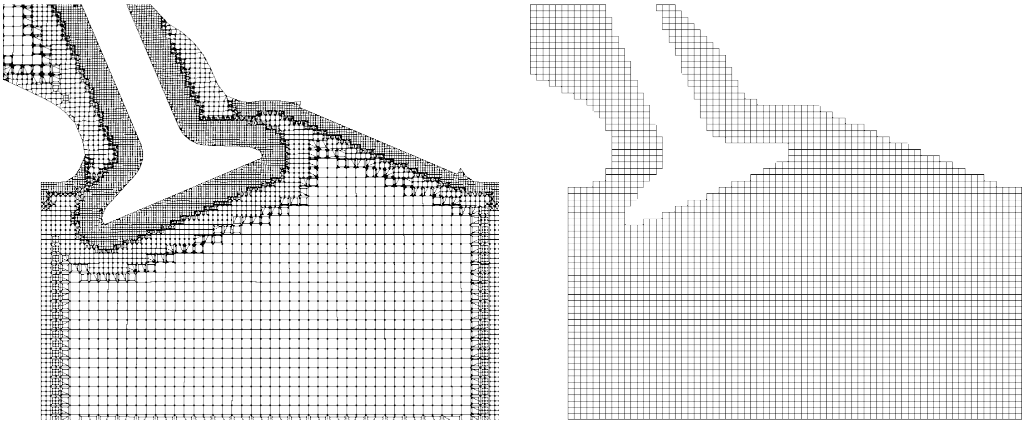

(**a**) OpenFOAM (**b**) OpenLB

Figure 5. Slice representation of the Finite Volume and Lattice Boltzmann computational meshes. For OpenFOAM (**a**) an unstructured graded mesh and for OpenLB (**b**) a uniform Cartesian mesh is used.

Table 2. Discretization parameters for the three grid configurations: low resolution (LR), medium resolution (MR) and high resolution (HR) for both OpenFOAM and OpenLB.

Solver	**Identifier**	N_{grid}	Δx	Δt	$\mathbf{Ma}^{\mathbf{LB}}$	**CFL**
OpenFOAM	$\mathrm{LR}_{\mathrm{FVM}}$	1.153×10^{6}	1.060×10^{-3}	3.000×10^{-6}	–	1
OpenFOAM	$\mathrm{MR}_{\mathrm{FVM}}$	3.121×10^{6}	7.610×10^{-4}	2.250×10^{-6}	–	1
OpenFOAM	$\mathrm{HR}_{\mathrm{FVM}}$	8.712×10^{6}	5.410×10^{-4}	1.600×10^{-6}	–	1
OpenLB	$\mathrm{LR}_{\mathrm{LBM}}$	1.300×10^{6}	1.061×10^{-3}	1.786×10^{-6}	0.026	–
OpenLB	$\mathrm{MR}_{\mathrm{LBM}}$	3.846×10^{6}	7.303×10^{-4}	1.230×10^{-6}	0.026	–
OpenLB	$\mathrm{HR}_{\mathrm{LBM}}$	1.123×10^{7}	5.066×10^{-4}	8.526×10^{-7}	0.026	–

4. Results of the IC Engine Test Case

In this section, PIV and LES results of the in-cylinder fluid flow are analyzed. At first, the ability of LBM and FVM to predict characteristic features of engine flows is assessed. Then, predicted time-averaged and RMS velocity profiles at several locations downstream of the valve are compared with each other and with the high-speed PIV measurements. Subsequently, the prediction accuracy of both numerical techniques are evaluated based on error analysis. Finally, the computational cost of OpenLB and OpenFOAM is appraised in terms of meshing and simulation performance.

4.1. Characterization of the In-Cylinder Flow

Figure 6 depicts the magnitude of the two dimensional time-averaged velocity $|\langle U \rangle|$ at the VP section obtained from (a) PIV measurements, (b) OpenLB and (c) OpenFOAM. Whereby $|\langle U \rangle|$ is defined by means of the in-plane velocity components as

$$|\langle U \rangle| = \sqrt{\langle u_x \rangle^2 + \langle u_y \rangle^2}. \tag{42}$$

The absence of the plane normal components is due to the two-dimensional PIV measurement data (see Section 3.1).

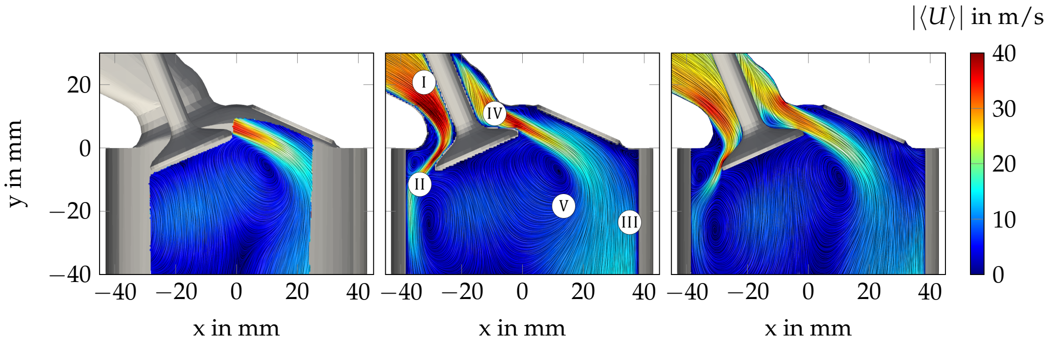

(**a**) PIV (**b**) $\mathrm{HR}_{\mathrm{LBM}}$ (**c**) $\mathrm{HR}_{\mathrm{FVM}}$

Figure 6. Line integral convolution visualization of the averaged velocity field with local characteristic flow patterns (I-V) of the PIV measurements (**a**), along with the OpenLB (**b**) and OpenFOAM (**c**) numerical results.

Characterized by strong flow/wall interaction processes, the turbulent flow inside IC engines features very complex flow and mixing dynamics. Considering Figure 6, some of the complex types of flow relevant to IC engines can also be found in the flow bench configuration; namely, (I) boundary layer flow, (II) impingement/stagnation, (III) wall-jets, (IV) flow separation/reattachment and (V) the so-called tumble flow. By comparing the LES results with the PIV measurements in Figure 6, it appears that LBM as well as FVM are able to properly predict such flow types. Furthermore, it can be clearly seen that predictions of LBM and FVM are quite similar to each other and also generally similar to the PIV measurements. This confirms the validity of LBM and FVM for such a fluid flow application.

The complex physics of engine flows are further analyzed and highlighted in Figure 7, which shows a snapshot of turbulent structures in the vicinity of the valve visualized by means of the Q-criterion [71]. Thereby, iso-surfaces of $Q = 7 \times 10^{-7}$ are colored by the magnitude of the instantaneous velocity.

As is visible in Figure 7, a highly turbulent flow is generated around the intake valve. This gas stream separates from the valve and initiates large-scale turbulent structures, which cascade into smaller ones until they dissipate further downstream. Such a complex disintegration process is essential in the context of IC engine flows since it influences the mixing and subsequent flow pattern inside the combustion chamber. It is nearly impossible to capture these three dimensional turbulent scales experimentally. However, as seen in Figure 7, it can be well represented by means of LBM and FVM techniques.

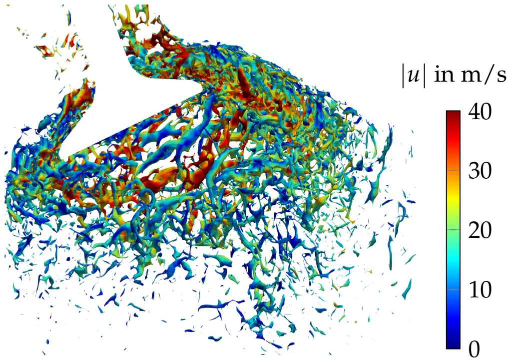

Figure 7. Turbulent structures as smoothed iso-surfaces of Q-criterion with $Q = 7 \times 10^{-7}$ and magnitude of velocity from $\mathrm{HR_{LBM}}$.

4.2. Validation of In-Cylinder Fluid Flow

For further comparison, the magnitudes for the two-dimensional time-averaged velocity $|\langle U \rangle|$ and RMS velocity $|U_{\mathrm{RMS}}|$ are plotted over three lines positioned at $y = -7$ mm, -12 mm and -17 mm, see Figure 8.

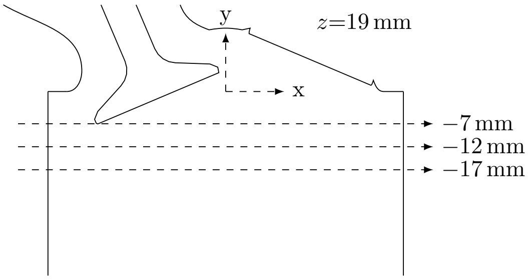

Figure 8. Positions of the three considered lines at $y = -7$ mm, -12 mm and -17 mm in the mid valve plane at $z = 19$ mm.

The magnitude for the two-dimensional RMS velocity vector is again obtained from the two in-plane components

$$|U_{\mathrm{RMS}}| = \sqrt{u^2_{\mathrm{RMS},x} + u^2_{\mathrm{RMS},y}}. \tag{43}$$

For these three lines, each grid configuration of both solvers and the PIV results are presented in Figure 9.

It can be seen that the highest grid resolutions $\mathrm{HR_{LBM}}$ and $\mathrm{HR_{FVM}}$ agree well with the trends of the PIV results. Furthermore, the different convergence behaviors in the near-wall region are observable. Due to the used grid refinement, the wall jet can be described more precisely by $\mathrm{LR_{FVM}}$ and $\mathrm{MR_{FVM}}$ compared with $\mathrm{LR_{LBM}}$ and $\mathrm{MR_{LBM}}$. In contrast, OpenLB is able to predict the transition area of the tumble flow to the right-side wall jet more accurately than OpenFOAM, even with the lower resolutions $\mathrm{LR_{LBM}}$ and $\mathrm{MR_{LBM}}$.

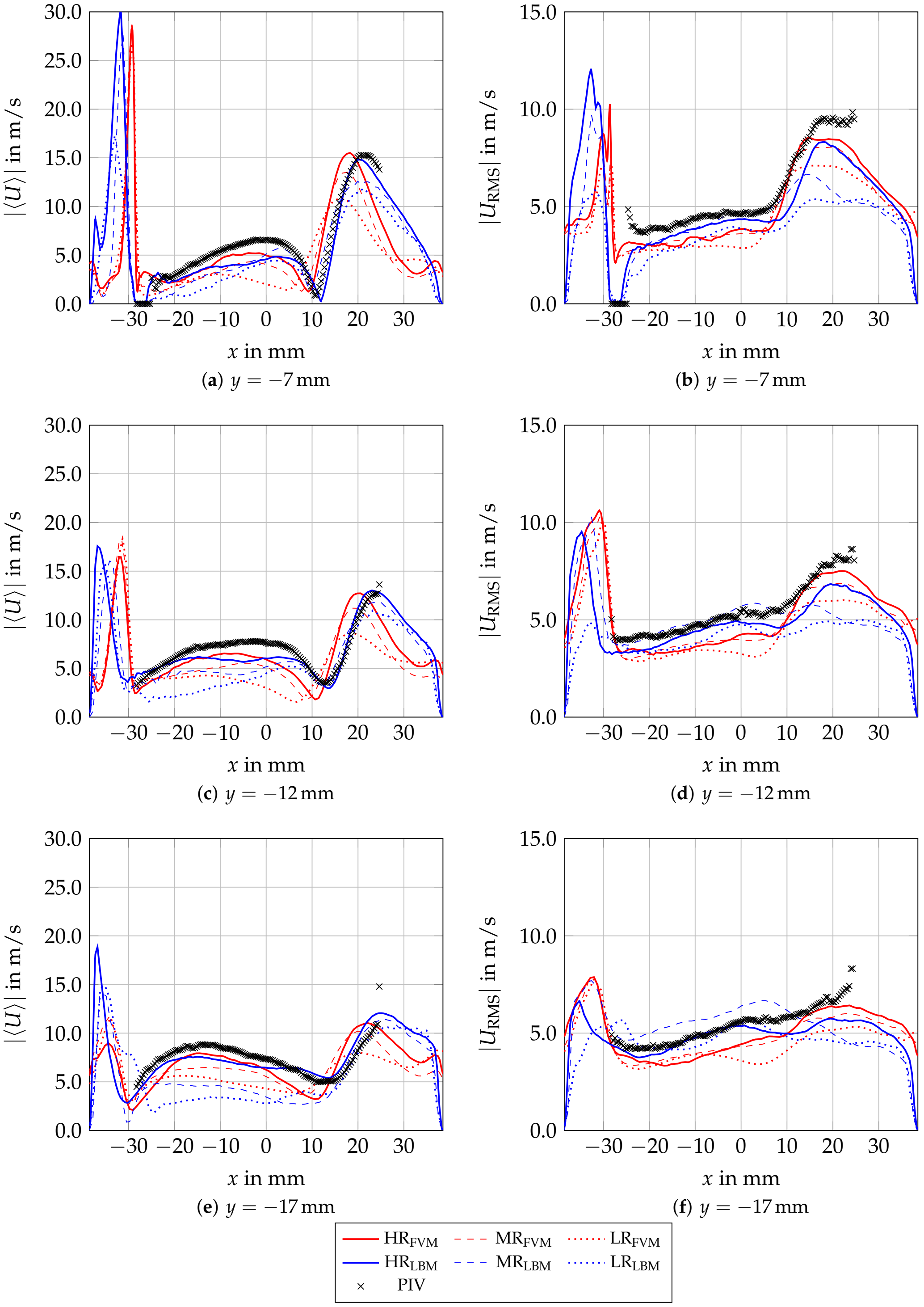

(**a**) $y = -7\,\mathrm{mm}$ (**b**) $y = -7\,\mathrm{mm}$

(**c**) $y = -12\,\mathrm{mm}$ (**d**) $y = -12\,\mathrm{mm}$

(**e**) $y = -17\,\mathrm{mm}$ (**f**) $y = -17\,\mathrm{mm}$

Figure 9. Magnitude of the two dimensional time-averaged velocity $|\langle U\rangle|$ and root mean square (RMS) velocity $|U_{\mathrm{RMS}}|$ at $y = -7\,\mathrm{mm}$,$y = -12\,\mathrm{mm}$ and $y = -17\,\mathrm{mm}$ in low, medium and high resolution grids for Lattice Boltzmann Method (LBM) and finite volume method (FVM) in comparison with PIV data.

4.3. Prediction Accuracy

The prediction accuracy of the numerical results calculated by OpenLB and OpenFOAM is compared with each other by means of the PIV measurement data. Therefore, we introduce the normalized absolute error nAE as the error criterion. The nAE for variable ϕ at position x is defined as

$$\mathrm{nAE}_{\phi}(x) = \frac{|\phi_{sim}(x) - \phi_{\mathrm{PIV}}(x)|}{\max(\phi_{\mathrm{PIV}}(x)) - \min(\phi_{\mathrm{PIV}}(x))}, \tag{44}$$

where ϕ_{sim} is the simulated data and ϕ_{PIV} is the PIV measurement data, which is used as the reference value. The normalization is obtained by the interval length of the experimental data. The $\mathrm{nAE}_{|\langle U \rangle|}$, concerning the time-averaged velocity $|\langle U \rangle|$, is depicted for the three different grid resolutions LR, MR and HR in Figure 10. The region of interest is in accordance with the experimental data (VP, see Figures 3 and 8).

For the low grid resolution LR, both OpenFOAM and OpenLB show the largest errors in the jet region (see Figure 10a,b. Also, the tumble flow prediction accuracy is diminished in comparison with higher grid resolutions. It can be observed that especially the approximation of the jet region in $\mathrm{LR}_{\mathrm{LBM}}$ is worse than $\mathrm{LR}_{\mathrm{FVM}}$, due to the larger grid spacing in the near-wall region around the valve. In contrast, the medium grid resolution exhibits in both cases that the error in the jet region is reduced (see Figure 10c,d. The high deviation region at the starting point of the jet is related to a shifted separation point of the boundary layer on the valve surface. Overall, the flow field of $\mathrm{MR}_{\mathrm{FVM}}$ approximates the PIV measurement data better than $\mathrm{MR}_{\mathrm{LBM}}$, which is due to the higher accuracy in the jet and tumble flow range. In Figure 10e,f, the error maps for the highest grid resolution are presented. The error maps for $\mathrm{HR}_{\mathrm{LBM}}$ and $\mathrm{HR}_{\mathrm{FVM}}$ are in good agreement with each other and to the PIV measurement. Both the jet and the tumble flow region are well predicted. Again, it is noticeable that the highest deviation in the jet region is related to a shifted separation point.

For the RMS velocity $|U_{\mathrm{RMS}}|$, high errors are more spread over the jet region compared with the mean velocity $|\langle U \rangle|$ errors, reaching into the tumble region as the fluctuation due to turbulent kinetic energy is amplified by the velocity (see Figure 11). For both LR and MR, OpenFOAM is able to predict the turbulent velocity fluctuations in the jet region better than OpenLB as a result of the graded mesh (see Figure 11a–d). For the same reason, OpenLB shows much smaller errors in the tumble region, while OpenFOAM suffers from greater errors at $\mathrm{MR}_{\mathrm{FVM}}$ and $\mathrm{LR}_{\mathrm{FVM}}$ (see Figure 11a,c). Similar to the $|\langle U \rangle|$ error map, $|U_{\mathrm{RMS}}|$ is in good agreement with the PIV measurements for $\mathrm{HR}_{\mathrm{LBM}}$ and $\mathrm{HR}_{\mathrm{FVM}}$ given in Figure 11e,f.

A global error criterion can be defined by the arithmetic mean of the normalized error nAE_{ϕ}. This normalized mean absolute error nMAE_{ϕ} is given by

$$\mathrm{nMAE}_{\phi} = \frac{1}{N_{\mathrm{PIV}}} \sum_{k=1}^{N_{\mathrm{PIV}}} \mathrm{nAE}_{\phi}(x_k), \tag{45}$$

where N_{PIV} is the number of experimental data points in the plane. Figure 12 depicts the normalized mean absolute error of the mean velocity $\mathrm{nMAE}_{|\langle U \rangle|}$ and the RMS velocity $\mathrm{nMAE}_{|U_{\mathrm{RMS}}|}$.

It can be seen that the nMAE decreases with an increasing number of cells. Both errors for the time-averaged velocity and the RMS velocity are lower than $\mathrm{nMAE}_{|\langle U \rangle|} < 0.08$ and $\mathrm{nMAE}_{|U_{\mathrm{RMS}}|} < 0.15$, respectively, which is satisfactory for such coarse meshes. The errors for the highest resolution are very similar, which is also indicated by the corresponding error maps (see Figure 10e,f). The convergence order for the OpenLB and OpenFOAM configurations is lower than the first order. This diminished convergence order can be justified by the experimental reference data, where the estimated PIV measurement uncertainty is $\mathrm{nMAE}_{|\langle U \rangle|} = 0.01$. Another source of error for the RMS velocity, besides the uncertainty of the PIV data, is the sampling error $\epsilon_{\mathrm{RMS}} = 0.025$. This may also affect the convergence order of $\mathrm{nMAE}_{|U_{\mathrm{RMS}}|}$.

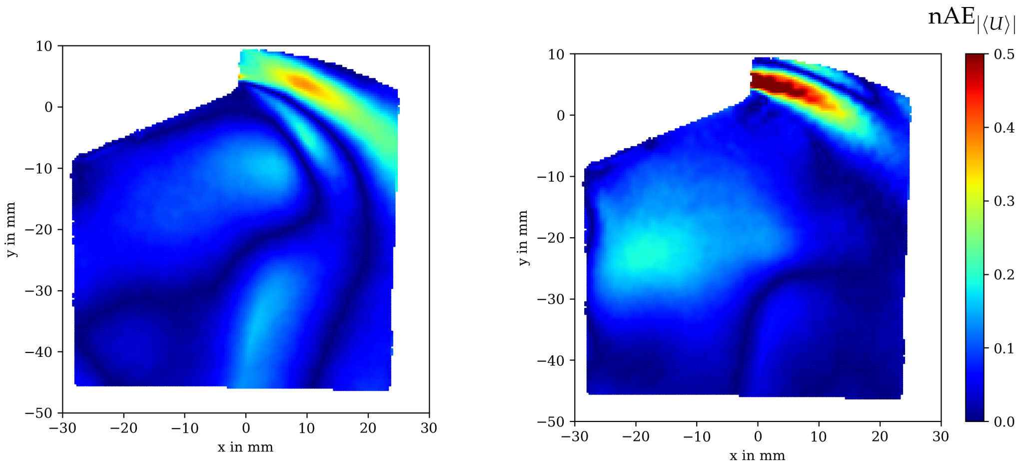

(**a**) LR$_{\mathrm{FVM}}$

(**b**) LR$_{\mathrm{LBM}}$

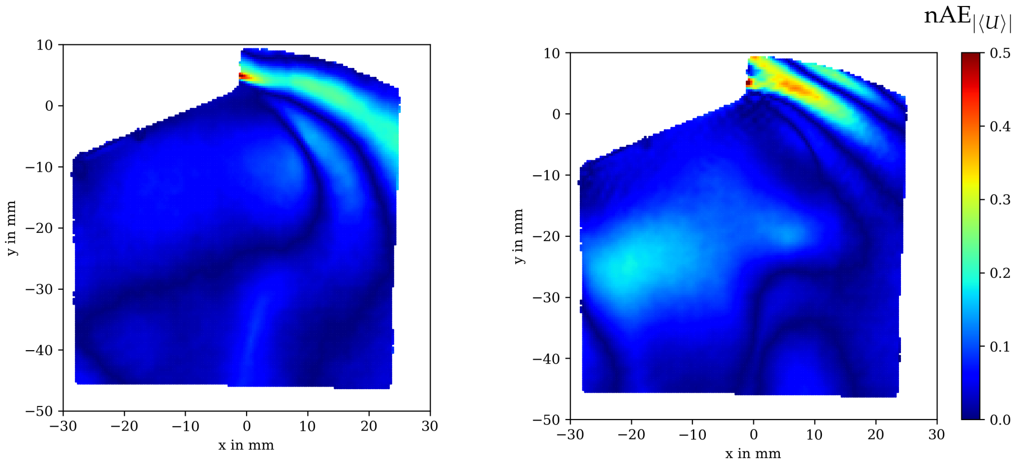

(**c**) MR$_{\mathrm{FVM}}$

(**d**) MR$_{\mathrm{LBM}}$

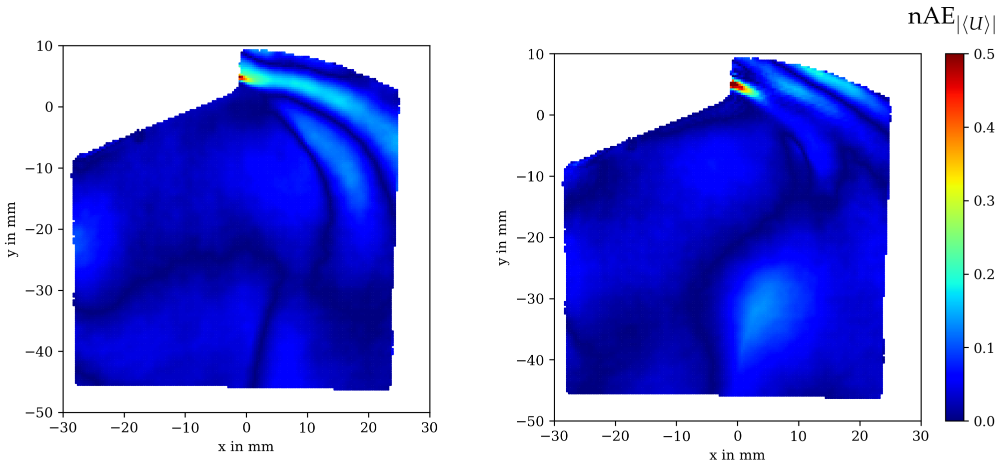

(**e**) HR$_{\mathrm{FVM}}$

(**f**) HR$_{\mathrm{LBM}}$

Figure 10. Normalized absolute error (nAE) map representation of the time-averaged velocity nAE$_{|\langle U \rangle|}$ for in-cylinder flow against PIV data for OpenFOAM (left) and OpenLB (right) at different grid resolutions.

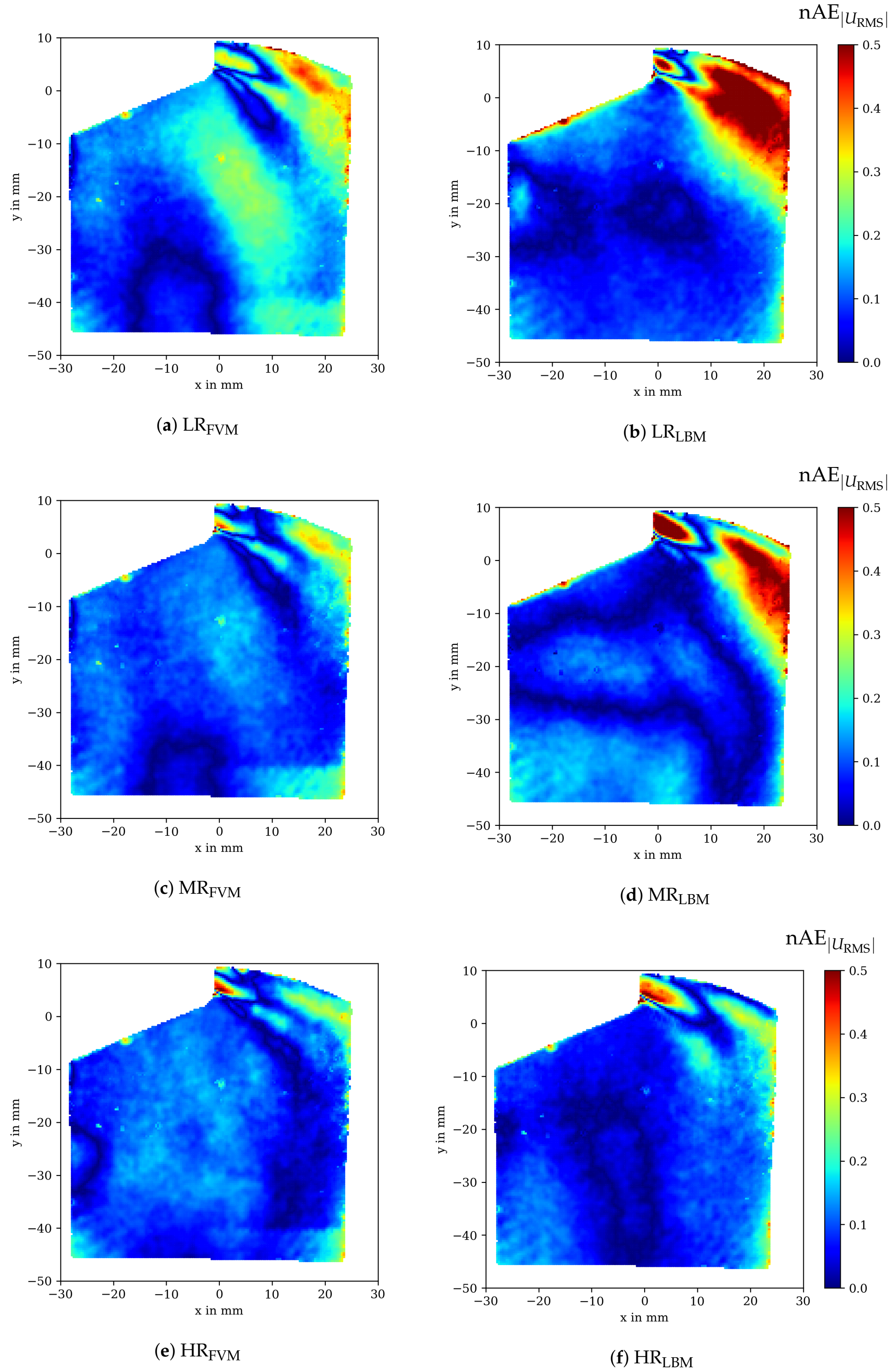

(**a**) $\mathrm{LR}_{\mathrm{FVM}}$

(**b**) $\mathrm{LR}_{\mathrm{LBM}}$

(**c**) $\mathrm{MR}_{\mathrm{FVM}}$

(**d**) $\mathrm{MR}_{\mathrm{LBM}}$

(**e**) $\mathrm{HR}_{\mathrm{FVM}}$

(**f**) $\mathrm{HR}_{\mathrm{LBM}}$

Figure 11. Normalized absolute error (nAE) map representation of the RMS velocity $\mathrm{nAE}_{|U_{\mathrm{RMS}}|}$ for in-cylinder flow against PIV data for OpenFOAM (left) and OpenLB (right) at different grid resolutions.

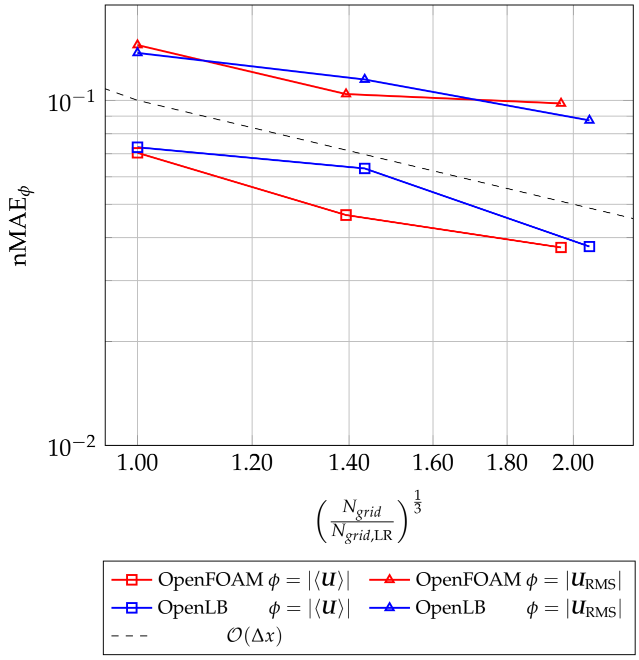

Figure 12. Normalized mean absolute error of the time-averaged velocity $\mathrm{nMAE}_{|\langle U \rangle|}$ and the RMS velocity $\mathrm{nMAE}_{|U_{\mathrm{RMS}}|}$ for three different grids: low resolution (LR), median resolution (MR) and high resolution (HR). The number of cells are normalized by the coarse grid LR.

4.4. Computational Cost

Besides the accuracy, the computational costs are a key factor to analyze the suitability of a numerical method. Therefore, the runtime of the mesh generation and the solver was evaluated on a single node which consists of two dodeca-core Intel Xeon processors E5-2680 v3 that support AVX2. The node provides 64 GB main memory. The use of a single node for estimating runtime performance was chosen because the parallel scalability is not in the scope of this study. The estimation of parallel scalability requires extensive testing due to the strong influence by the cells per core ratio, the load balancing method and the connection between the nodes of the cluster system. Comprehensive studies that deal with the parallel scalability of OpenFOAM and OpenLB can be found in [43,72,73].

4.4.1. Meshing Performance

Due to the straightforward approach in the case of OpenLB, the grid generation is fully automatic and does not require any additional preparation steps. On the contrary, the meshing process for FVM is very time-consuming if the grid is manually obtained. Internal OpenFOAM tools can drastically reduce the effort, but require an experienced user. This study uses the built-in OpenFOAM meshing tool snappyHexMesh. Still, writing a script for grid generation for a complex geometry can take several days. Nevertheless, we only take the runtime for the mesh generation into account. The meshing time is estimated by

$$t_{core,mesh} = N_{core}\, t_{node,mesh}\,, \tag{46}$$

where $t_{node,mesh}$ is the runtime on the node and N_{core} the amount of used cores. The comparison of the meshing time for the three different resolutions is represented in Figure 13.

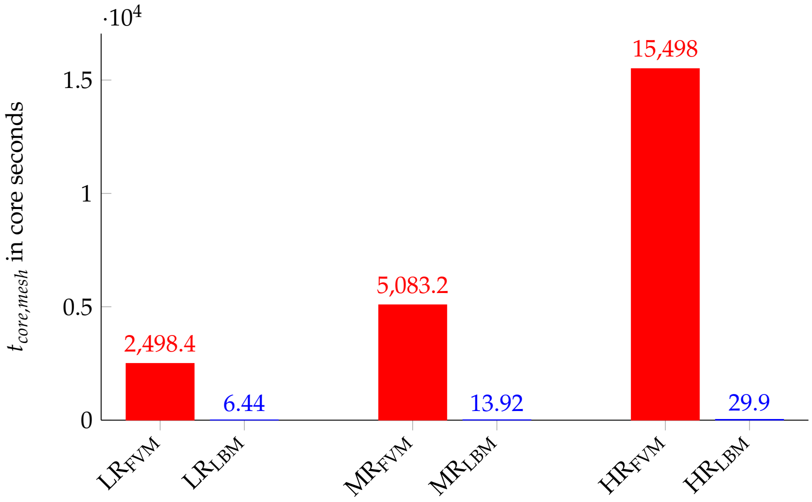

Figure 13. Meshing runtime $t_{core,mesh}$ comparison between OpenFOAM and OpenLB for the three grid configurations: LR, MR and HR.

It can be observed that the meshing time in OpenLB is more than doubled each time the higher grid resolution is used. In contrast, the results of OpenFOAM show a certain overhead with the high resolution grid, i.e. The grid generation for OpenFOAM takes considerably more time with each increase in resolution. This can be justified by the complex meshing procedure, which consists of a castellation, snapping and adding layers step including several optimization cycles. Overall, the meshing time in OpenLB is on average 424 times shorter than in OpenFOAM. In the case of a static mesh, this performance benefit is not decisive. However, the use of a moving mesh, e.g., if piston motions are taken into account, requires several mesh updates in one cycle. Therefore, a fast grid creation process, such as that with OpenLB, can be essential in the context of engine relevant flows. The suitability of LBM for describing moving boundaries has been demonstrated in extensive comparisons for different moving boundary methods, e.g., in [74,75].

4.4.2. Simulation Performance

For the comparison of the simulation performance difference for each grid, a runtime metric is introduced. At $t_{ss} = 0.5\,\mathrm{s}$, the beginning of the statistics computation, the runtime tracker is started. The tracked runtime $t_{node,solver}$ is divided by the according past simulation time $t_{sim,solver}$ and scaled with the number of cores N_{core}. This core time $t_{core,solver}$ is written as

$$t_{core,solver} = \frac{N_{core} t_{node,solver}}{t_{sim,solver}}. \tag{47}$$

This means that the runtime metric calculates the core hours for one second of simulation time including the additional time for processing the turbulence statistics. The direct comparison of each grid resolution is justified by the comparable accuracy, see Section 4.3. The performance results for the three different grid resolutions are presented in Figure 14.

The bar chart reveals that the simulations obtained by OpenLB are significantly faster than the OpenFOAM simulations. The resulting performance factor can be determined by dividing $t_{core,solver}$ for the corresponding grid resolutions. If each grid configuration is taken into account, the mean performance factor for OpenLB to OpenFOAM can be estimated as 32.03. It is noteworthy that the performance factor varies greatly between the different grid resolutions, 21.76 for LR and 46.49 for

HR. Additional quantities are introduced to further investigate the variance of the performance factor. The mean cells per core (MCPc) are given by

$$\mathrm{MCPc} = \frac{N_{grid}}{N_{core}}. \tag{48}$$

Another performance metric are the cell updates per core and second (CUPcs), which are defined as

$$\mathrm{CUPcs} = \frac{N_{grid}}{t_{core,solver}\Delta t}. \tag{49}$$

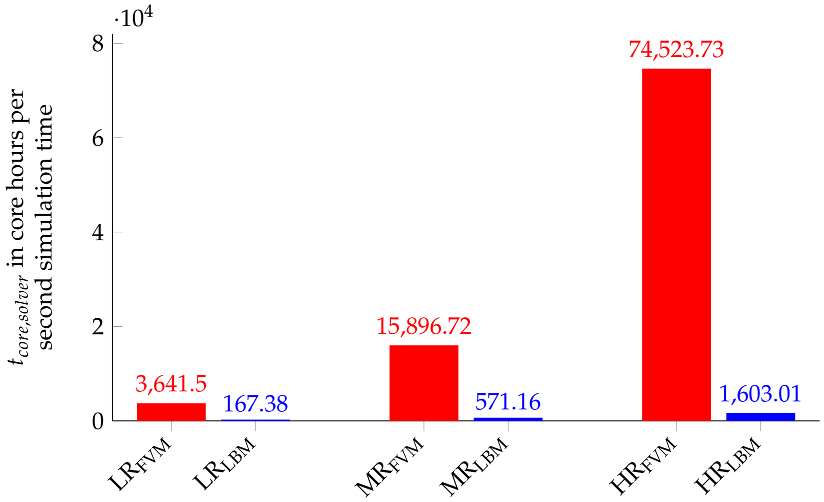

Figure 14. Solver runtime $t_{core,solver}$ comparison between OpenFOAM and OpenLB for the three grid configurations: LR, MR and HR.

Both quantities MCPc and CUPcs are listed for the three grid configurations in Table 3.

Table 3. Mean cells per core (MCPc) and cell updates per core and second (CUPcs) for the three grid configurations: low resolution (LR), medium resolution (MR) and high resolution (HR) for both OpenFOAM and OpenLB.

Solver	Identifier	MCPc	CUPcs
OpenFOAM	$\mathrm{LR_{FVM}}$	5.016×10^4	2.934×10^4
OpenFOAM	$\mathrm{MR_{FVM}}$	1.357×10^5	2.424×10^4
OpenFOAM	$\mathrm{HR_{FVM}}$	3.788×10^5	2.023×10^4
OpenLB	$\mathrm{LR_{LBM}}$	5.654×10^4	1.208×10^6
OpenLB	$\mathrm{MR_{LBM}}$	1.672×10^5	1.521×10^6
OpenLB	$\mathrm{HR_{LBM}}$	4.885×10^5	2.283×10^6

The solvers show a contrary behavior, while OpenLB benefits from an increased MCPc and almost doubles the CUPcs from LR to HR, OpenFOAM has a decrease of about 45 percent. Consequently, OpenFOAM seems to be less affected by the used MCPc. The reasons for the different behavior can be manifold and range from the influence of the load balancing method to cache effects and communication effects. A detailed discussion of these influencing factors can be found in [72,76,77].

5. Conclusions and Outlook

The purpose of this paper is to evaluate NWM-LES for complex turbulent flows using LBM by comparison with FVM simulations and PIV experiments. Thereby, a van Driest damped Smagorinsky model coupled to the Musker equation was used to model the turbulent boundary layer. Both LBM and FVM NWM-LES approaches were outlined in detail. Three different grid resolutions were used to simulate an engine relevant in-cylinder flow with the open source frameworks OpenLB and OpenFOAM. Characteristic flow features of the in-cylinder flow were highlighted and compared side-by-side. In addition to the quantitative comparison, the errors of the tested grid configuration were calculated against a highly precise PIV measurement and analyzed in detail. It was shown that the matching grid configurations of both numerical methods had similar errors. Surprisingly, OpenLB requires only slightly more cells than OpenFOAM to produce the same accuracy, although no grid refinement was used. This can be justified by the chosen region of interest, which is remote from the wall, and also the incorporated near-wall treatment based on the wall function approach. The time-averaged and the RMS velocity at the highest grid resolution for OpenLB and OpenFOAM were in good agreement with the PIV measurement ($\mathrm{nMAE}_{|\langle U \rangle|} < 0.038$ and $\mathrm{nMAE}_{|U_{\mathrm{RMS}}|} < 0.098$, respectively). The performance estimation revealed that the meshing process in OpenLB was 424 times faster and the simulation process approximately 32 times faster for the investigated setup. These significant performance differences in meshing and solver runtime indicate that LBM is a valuable and viable alternative to FVM in simulating IC engine relevant flows with NWM-LES. In particular, the fast grid generation process in OpenLB further reduces computational costs, if moving meshes are applied. The faster calculation speed for NWM-LES using LBM is advantageous to address industrial applications and to enable "overnight" calculations that previously took weeks. Therefore, faster design cycles and operating condition tests are feasible. The performance advantage can also be used to provide more precise results in the same time and finally paves the way for near-wall-resolved LES in the future [78].

Nevertheless, LBM still needs additional research to gain the maturity of NWM-LES with FVM. The applied equilibrium wall function approach based on Musker's law of the wall is strictly speaking only valid in fully developed turbulent boundary layers. In contrast, turbulent boundary layers of complex turbulent flows deal with pressure gradients, separation and recirculation, variable physical properties, compressibility effects and many more. Therefore, a further step is to implement a generalized wall function such as [79–81] in OpenLB that is able to model these flow features. In addition, the simple SGS model employed in this study can be replaced by more advanced turbulent models, e.g., models based on dynamic procedures [82], the scale similarity hypothesis [83] or wall-adapted SGS models [52], which have shown an increased accuracy for IC engine flows [2,42]. If reactive turbulent flows are considered, further investigations have to be done. In this respect, a modeling approach based on detailed chemistry with a large number of species as well as tabulated chemistry is a challenging task, especially for LBM due to the high memory requirements [84]. However, given the benefits of the mesh generation and computation time reductions shown in this work, LBM is a promising alternative to FVM in IC engine and many other complex turbulent flow applications in the future.

Author Contributions: Conceptualization, M.H. and F.R.; Methodology, M.H. and F.R.; Software, M.H., J.B.J.-H., M.J.K., F.R. and Y.L.; Validation, M.H., J.B.J.-H., F.R., Y.L., C.W., M.S. and L.I.; Formal analysis, M.H., F.R. and J.B.J.-H.; Investigation, M.H, J.B.J.-H., F.R., Y.L., C.W. and M.S.; Resources, M.J.K., B.B. and A.S.; Data curation, M.H, J.B.J.-H., M.J.K., F.R. and Y.L.; Writing–original draft preparation, M.H.; Writing–review and editing, F.R., J.B.J.-H., C.W., M.S., M.J.K., B.B. and A.S.; Visualization, M.H., C.W. and J.B.J.-H.; Supervision, M.J.K., H.N., B.B. and A.S.; Project administration, M.H. and F.R.; Funding acquisition, M.J.K., H.N., B.B. and A.S.; PIV measurements, C.W., M.S., L.I. and B.B. All authors have read and agreed to the published version of the manuscript.

Funding: This research was funded by the Deutsche Forschungsgemeinschaft (DFG) SFB-Transregio project number 237267381-TRR150 and by the Fritz und Margot Faudi-Stiftung under project number 94.

Acknowledgments: The authors gratefully acknowledge the financial support by the Deutsche Forschungsgemeinschaft (DFG) SFB-Transregio project number 237267381-TRR150, the support for the simulations on the Lichtenberg High Performance Computer (HHLR) at the Technical University of Darmstadt and the financial support by the Open Access Publishing Fund of the Technical University of Darmstadt. C.W. and B.B. acknowledge the financial support by the Fritz und Margot Faudi-Stiftung under project number 94. C.W., M.S., L.I. and B.B. kindly acknowledge Andreas Dreizler (Reactive Flows and Diagnostics, TU Darmstadt) for providing invaluable resources and advice in conducting the experiments. Additionally, C.W., M.S., L.I. and B.B. would like to acknowledge Andrea Pati and Christian Hasse (Simulation of reactive Thermo-Fluid Systems, TU Darmstadt) for fruitful discussion and for providing unsteady RANS data in optimizing the design of the flow bench.

Conflicts of Interest: The authors declare no conflict of interest.

Abbreviations

The following nomenclature is used in this manuscript:

BGK	Bhatnagar–Gross–Krook
CFL	Courant–Friedrichs–Lewy number
CUPcs	cell updates per core and second
CV	control volumes
FDM	finite difference method
FVM	finite volume method
GPU	graphics processing unit
HR	high resolution
IC	internal combustion
LBM	lattice Boltzmann method
LES	large eddy simulation
MCPc	mean cells per core
MR	medium resolution
MRV	magnetic resonance velocimetry
nMAE	normalized mean absolute error
nAE	normalized absolute error
NWM	near-wall-modeled
PIV	particle image velocimetry
RANS	Reynolds-averaged Navier–Stokes
RMS	root mean square
SGS	sub-grid scale
LR	low resolution
VP	valve plane

Roman

A^+	van Driest parameter
c	set of discrete lattice velocity vectors
c_n	discrete lattice normal velocity vector
C_Δ	van Driest model constant
C_M	sub-grid scale model coefficient
c_s	speed of sound of the lattice
D	intake pipe diameter
D_M	model related operator
e_s	stream-wise unit vector
$\overline{f}$	filtered particle distribution vector
$\overline{f}^{eq}$	filtered particle distribution vector at equilibrium state
$\overline{f}^{neq}$	non-equilibrium of the particle distribution function vector
I	turbulence intensity

L	integral length scale
$\mathrm{Ma}^{\mathrm{LB}}$	lattice Mach number
$\dot{m}_{in}$	massflow into the flow bench
$\dot{m}_{out}$	massflow out of the flow bench
N	resolution
N_{core}	number of cores
N_e	number of independent ensembles
N_{grid}	number of grid cells
N_{PIV}	number of PIV data points
N_t	total number of time steps within t_{av}
$\overline{p}$	filtered pressure
$\overline{p}^{\mathrm{LB}}$	filtered lattice pressure
p_{out}	pressure at the numerical outflow
$P_{in,1}$	absolute pressure at pressure sensor inlet 1
$P_{in,2}$	absolute pressure at pressure sensor inlet 2
$P_{out,1}$	absolute pressure at pressure sensor outlet 1
$P_{out,2}$	absolute pressure at pressure sensor outlet 2
q_{B}	dimensionless distance
Q	Q-criterion
Re	Reynolds number
$\overline{S}$	filtered strain rate tensor
$\overline{S}^{\mathrm{LB}}$	filtered lattice strain rate tensor
t	time
t_{av}	averaging time
t^{LB}	lattice time
$t_{core,mesh}$	runtime on the core for meshing
$t_{node,mesh}$	runtime on the node for meshing
$t_{core,solver}$	runtime on the core for the solver per second simulation time
$t_{node,solver}$	runtime on the node for the solver
$t_{sim,solver}$	passed simulation time
t_{ss}	time to a statistically stationary flowfield
T^{eff}	effective stress tensor
T^{SGS}	sub-grid scale stress tensor
T_w	wall shear stress
$\tilde{T}_w^{\mathrm{LB}}$	averaged wall shear stress assuming RANS hypothesis
$\overline{u}$	filtered velocity vector
$\overline{u}^{\mathrm{LB}}$	filtered lattice velocity vector
$\tilde{u}_f^{\mathrm{LB}}$	averaged velocity vector assuming RANS hypothesis
$\overline{\mathbf{u}}_n^{\mathrm{LB}}$	filtered lattice velocity vector at position x_n^{LB}
$\tilde{u}_1^{\mathrm{LB}}$	stream-wise component of $\tilde{u}_f^{\mathrm{LB}}$
$\overline{u}_2^{\mathrm{LB}}$	stream-wise component of $\overline{\mathbf{u}}_n^{\mathrm{LB}}$
u_τ	friction velocity
u^+	dimensionless friction velocity
$u_\parallel$	stream-wise velocity
$\langle u \rangle$	time-averaged velocity vector
$\langle u \rangle_{in}$	time-averaged velocity vector at the numerical inflow
u'	velocity fluctuation vector
$\langle u' \rangle$	time-averaged velocity fluctuation vector
$\langle u'u' \rangle$	Reynolds stress tensor
$\langle U \rangle$	two dimensional time-averaged velocity vector
U_{RMS}	two dimensional root mean square velocity vector

x	position vector
x^{LB}	lattice position vector
x_f^{LB}	lattice position vector in c_i direction
x_{ff}^{LB}	lattice position vector in $2c_i$ direction
x_n^{LB}	lattice position vector in c_n direction
x_w^{LB}	lattice wall position vector
y	wall distance
y_1^{LB}	lattice distance from the the node at position x_f^{LB} distance to the boundary
y_2^{LB}	lattice distance from the the node at position x_n^{LB} to the boundary
y^+	dimensionless wall distance
y_p	wall distance of the cell centroid

Greek

δ	Kronecker operator
Δ_{grid}	grid filter
Δt	time step
Δx	grid spacing
ϵ	maximal sampling error
η	dynamic viscosity
$\vartheta_{in,1}$	temperature at temperature sensor 1
$\vartheta_{in,2}$	temperature at temperature sensor 2
ϑ_{wall}	wall temperature
κ	von Kármán constant
ν	kinematic viscosity
ν^{eff}	effective kinematic viscosity
ν^{SGS}	sub-grid scale kinematic viscosity
ν^{LB}	lattice kinematic viscosity
$\nu^{\mathrm{LB},eff}$	lattice effective kinematic viscosity
$\nu^{\mathrm{LB,SGS}}$	lattice sub-grid scale kinematic viscosity
$\overline{\Pi}$	filtered lattice momentum flux
$\overline{\Pi}^{neq}$	filtered second moment of the non-equilibrium of the particle distribution function
ρ	density
$\overline{\rho}^{\mathrm{LB}}$	filtered lattice density
ρ_{out}^{LB}	lattice density at the outflow
τ	lattice relaxation time
τ^{SGS}	lattice sub-grid scale relaxation time
τ^{eff}	lattice effective relaxation time
ϕ_{PIV}	PIV measurement data
ϕ_{sim}	simulated data
ω	lattice weight vector
$\overline{\Omega}$	filtered collision operator vector

References

1. Freudenhammer, D.; Baum, E.; Peterson, B.; Böhm, B.; Jung, B.; Grundmann, S. Volumetric intake flow measurements of an IC engine using magnetic resonance velocimetry. *Exp. Fluids* **2014**, *55*, 1724. [CrossRef]
2. Rutland, C. Large-eddy simulations for internal combustion engines—A review. *Int. J. Eng. Res.* **2011**, *12*, 421–451. [CrossRef]
3. Vermorel, O.; Richard, S.; Colin, O.; Angelberger, C.; Benkenida, A.; Veynante, D. Towards the understanding of cyclic variability in a spark ignited engine using multi-cycle LES. *Combust. Flame* **2007**, 1525–1541. [CrossRef]
4. Goryntsev, D.; Sadiki, A.; Klein, M.; Janicka, J. Large eddy simulation based analysis of the effects of cycle-to-cycle variations on air-fuel mixing in realistic DISI engines. *Proc. Combust. Inst.* **2009**, 2759–2766. [CrossRef]

5. Enaux, B.; Granet, V.; Vermorel, O.; Lacour, C.; Thobois, L.; Dugué, V.; Poinsot, T. Large eddy simulation of a motored single-cylinder piston engine: Numerical strategies and validation. *Flow Turbul. Combust.* **2010**, 53–177. [CrossRef]
6. Granet, V.; Vermorel, O.; Lacour, C.; Enaux, B.; Dugué, V.; Poinsot, T. Large-Eddy Simulation and experimental study of cycle-to-cycle variations of stable and unstable operating points in a spark ignition engine. *Combust. Flame* **2012**, 1562–11575. [CrossRef]
7. Goryntsev, D.; Nishad, K.; Sadiki, A.; Janicka, J. Application of LES for analysis of unsteady effects on combustion processes and misfires in DISI engine. *Oil Gas Sci. Technol. Revue d'IFP Energies Nouvelles* **2014**, 129–140. [CrossRef]
8. Reuss, D.L.; Adrian, R.J.; Landreth, C.C.; French, D.T.; Fansler, T.D. Instantaneous planar measurements of velocity and large-scale vorticity and strain rate in an engine using particle-image velocimetry. *SAE Trans.* **1989**, 1116–1141. [CrossRef]
9. Peterson, B.; Sick, V. Simultaneous flow field and fuel concentration imaging at 4.8 kHz in an operating engine. *Appl. Phys. B* **2009**, *97*, 887. [CrossRef]
10. Baum, E.; Peterson, B.; Böhm, B.; Dreizler, A. On the validation of LES applied to internal combustion engine flows: Part 1: Comprehensive experimental database. *Flow Turbul. Combust.* **2014**, *92*, 269–297. [CrossRef]
11. Zentgraf, F.; Baum, E.; Böhm, B.; Dreizler, A.; Peterson, B. On the turbulent flow in piston engines: Coupling of statistical theory quantities and instantaneous turbulence. *Phys. Fluids* **2016**, *28*, 045108. [CrossRef]
12. Gale, N.F. Diesel engine cylinder head design: The compromises and the techniques. *SAE Trans.* **1990**, 415–438. [CrossRef]
13. Agnew, D.D. *What is Limiting your Engine Air Flow: Using Normalized Steady Air Flow Bench Data*; Technical Report, SAE Technical Paper; SAE: Warrendale, PA, USA, 1994. [CrossRef]
14. Hartmann, F.; Buhl, S.; Gleiss, F.; Barth, P.; Schild, M.; Kaiser, S.A.; Hasse, C. Spatially resolved experimental and numerical investigation of the flow through the intake port of an internal combustion engine. *Oil Gas Sci. Technol. Revue d'IFP Energies Nouvelles* **2016**, *71*, 2. [CrossRef]
15. Falkenstein, T.; Bode, M.; Kang, S.; Pitsch, H.; Arima, T.; Taniguchi, H. Large-Eddy Simulation study on unsteady effects in a statistically stationary SI engie port flow. *SAE Int.* **2015**. [CrossRef]
16. Buhl, S.; Hartmann, F.; Kaiser, S.A.; Hasse, C. Investigation of an IC engine intake flow based on highly resolved LES and PIV. *Oil Gas Sci. Technol. Revue d'IFP Energies Nouvelles* **2017**, *72*, 15. [CrossRef]
17. Falkenstein, T.; Kang, S.; Davidovic, M.; Bode, M.; Pitsch, H.; Kamatsuchi, T.; Nagao, J.; Arima, T. LES of Internal Combustion Engine Flows Using Cartesian Overset Grids. *Oil Gas Sci. Technol.–Revue d'IFP Energies Nouvelles* **2017**, *72*, 36. [CrossRef]
18. Nishad, K.; Ries, F.; Li, Y.; Sadiki, A. Numerical Investigation of Flow through a Valve during Charge Intake in a DISI-Engine using Large Eddy Simulation. *Energies* **2019**, *12*, 2620. [CrossRef]
19. Gaedtke, M.; Hoffmann, T.; Reinhardt, V.; Thäter, G.; Nirschl, H.; Krause, M.J. Flow and heat transfer simulation with a thermal large eddy lattice Boltzmann method in an annular gap with an inner rotating cylinder. *Int. J. Modern Phys. C* **2019**, *30*, 1950013. [CrossRef]
20. Gaedtke, M.; Wachter, S.; Kunkel, S.; Sonnick, S.; Rädle, M.; Nirschl, H.; Krause, M.J. Numerical study on the application of vacuum insulation panels and a latent heat storage for refrigerated vehicles with a large Eddy lattice Boltzmann method. *Heat Mass Transf.* **2020**, *56*, 1189–1201. [CrossRef]
21. Augusto, L.d.L.X.; Ross-Jones, J.; Lopes, G.C.; Tronville, P.; Gonçalves, J.A.S.; Rädle, M.; Krause, M.J. Microfiber filter performance prediction using a lattice Boltzmann method. *Commun. Comput. Phys.* **2018**, *23*, 910–931. [CrossRef]
22. Henn, T.; Heuveline, V.; Krause, M.J.; Ritterbusch, S. Aortic Coarctation Simulation Based on the Lattice Boltzmann Method: Benchmark Results. In *Statistical Atlases and Computational Models of the Heart. Imaging and Modelling Challenges*; Camara, O., Mansi, T., Pop, M., Rhode, K., Sermesant, M., Young, A., Eds.; Springer: Berlin/Heidelberg, Germany, 2013; pp. 34–43.
23. Heuveline, V.; Krause, M.J.; Latt, J. Towards a hybrid parallelization of lattice Boltzmann methods. *Comput. Math. Appl.* **2009**, *58*, 1071–1080. [CrossRef]
24. Heuveline, V.; Krause, M.J. OpenLB: Towards an efficient parallel open source library for lattice Boltzmann fluid flow simulations. In *International Workshop on State-of-the-Art in Scientific and Parallel Computing*; PARA: Trondheim, Norway, 2010; Volume 9.

25. Kajzer, A.; Pozorski, J.; Szewc, K. Large-eddy simulations of 3D Taylor-Green vortex: Comparison of smoothed particle hydrodynamics, lattice Boltzmann and finite volume methods. *J. Phys. Conf. Ser.* **2014**, *530*, 012019. [CrossRef]
26. Pasquali, A.; Schönherr, M.; Geier, M.; Krafczyk, M. Simulation of external aerodynamics of the DrivAer model with the LBM on GPGPUs. In *Parallel Computing: On the Road to Exascale*; IOS Press: Amsterdam, The Netherlands, 2016; Volume 27, pp. 391–400. [CrossRef]
27. Jin, Y.; Uth, M.; Herwig, H. Structure of a turbulent flow through plane channels with smooth and rough walls: An analysis based on high resolution DNS results. *Comput. Fluids* **2015**, *107*, 77–88. [CrossRef]
28. Barad, M.F.; Kocheemoolayil, J.G.; Kiris, C.C. Lattice Boltzmann and Navier-stokes cartesian cfd approaches for airframe noise predictions. In Proceedings of the 23rd AIAA Computational Fluid Dynamics Conference, Denver, CO, USA, 5–9 June 2017; p. 4404.
29. Montessori, A.; Falcucci, G. *Lattice Boltzmann Modeling of Complex Flows for Engineering Applications*; Morgan & Claypool Publishers: San Rafael, CA, USA, 2018.
30. Dorschner, B.; Bösch, F.; Chikatamarla, S.S.; Boulouchos, K.; Karlin, I.V. Entropic multi-relaxation time lattice Boltzmann model for complex flows. *J. Fluid Mech.* **2016**, *801*, 623–651. [CrossRef]
31. Krause, M.; Avis, S.; Dapalo, D.; Hafen, N.; Haußmann, M.; Gaedtke, M.; Klemens, F.; Kummerländer, A.; Maier, M.L.; Mink, A.; et al. OpenLB Release 1.3: Open Source Lattice Boltzmann Code, 2019. Available online: http://optilb.com/openlb/wp-content/uploads/2011/12/olb_ug-0.5r0.pdf (accessed on 30 April 2020).
32. Malaspinas, O.; Sagaut, P. Wall model for large-eddy simulation based on the lattice Boltzmann method. *J. Comput. Phys.* **2014**, *275*, 25–40. [CrossRef]
33. Haussmann, M.; Barreto, A.C.; Kouyi, G.L.; Rivière, N.; Nirschl, H.; Krause, M.J. Large-eddy simulation coupled with wall models for turbulent channel flows at high Reynolds numbers with a lattice Boltzmann method—Application to Coriolis mass flowmeter. *Comput. Math. Appl.* **2019**, *78*, 3285–3302. [CrossRef]
34. Leonard, A.; others. Energy cascade in large-eddy simulations of turbulent fluid flows. *Adv. Geophys. A* **1974**, *18*, 237–248.
35. Hirsch, C. *Numerical Computation of Internal & External Flows: Fundamentals of Computational Fluid Dynamics*, 2nd ed.; John Wiley & Sons: Burlington, MA, USA, 2007.
36. Jasak, H. Error Analysis and Estimation for the Finite Volume Method with Applications to Fluid Flows. Ph.D. Thesis, University of London, London, UK, 1996.
37. Greenshields, C.J. *OpenFOAM Programmer's Guide Version 3.0.1*; OpenFOAM Foundation Ltd.: England, UK, 13 December 2015.
38. Ferziger, J.; Perić, M. *Computational Methods for Fluid Dynamics*, 3rd ed.; Springer: Berlin/Heidelberg, Germany; New York, NY, USA, 2002.
39. Greenshields, C.; Weller, H.; Gasparini, L.; Reese, J. Implementation of semi-discrete, non-staggered central schemes in a colocated, polyhedral, finite volume framework, for high-speed viscous flows. *Int. J. Numer. Meth. Fluids* **2010**, *63*, 1–21. [CrossRef]
40. Issa, R. Solution of the implicitly discretised fluid flow equations by operator-splitting. *J. Comput. Phys.* **1985**, *62*, 40–65. [CrossRef]
41. Patankar, S.; Spalding, D. A calculation procedure for heat, mass and momentum transfer in three-dimensional parabolic flows. *Int. J. Heat Mass Trans.* **1972**, *15*, 1787–1806. [CrossRef]
42. Ries, F.; Nishad, K.; Dressler, L.; Janicka, J.; Sadiki, A. Evaluating large eddy simulation results based on error analysis. *Theor. Comput. Fluid Dyn.* **2018**, *32*, 733–752. [CrossRef]
43. Ries, F. Numerical Modeling and Prediction of Irreversibilities in Sub- and Supercritical Turbulent Near-Wall Flows. Ph.D. Thesis, Technische Universität Darmstadt, Darmstadt, Germany, 2019.
44. Kang, S.K.; Hassan, Y.A. The effect of lattice models within the lattice Boltzmann method in the simulation of wall-bounded turbulent flows. *J. Comput. Phys.* **2013**, *232*, 100–117. [CrossRef]
45. Bhatnagar, P.L.; Gross, E.P.; Krook, M. A Model for Collision Processes in Gases. I. Small Amplitude Processes in Charged and Neutral One-Component Systems. *Phys. Rev.* **1954**, *94*, 511–525. [CrossRef]
46. He, X.; Luo, L.S. Theory of the lattice Boltzmann method: From the Boltzmann equation to the lattice Boltzmann equation. *Phys. Rev. E* **1997**, *56*, 6811–6817. [CrossRef]
47. Shan, X.; Yuan, X.F.; Chen, H. Kinetic theory representation of hydrodynamics: A way beyond the Navier–Stokes equation. *J. Fluid Mech.* **2006**, *550*, 413–441. [CrossRef]

48. Smagorinsky, J. General circulation experiments with the primitive equations: I. The basic experiment. *Mon. Weather Rev.* **1963**, *91*, 99–164. [CrossRef]
49. Moin, P.; Kim, J. Numerical investigation of turbulent channel flow. *J. Fluid Mech.* **1982**, *118*, 341–377. [CrossRef]
50. Rogallo, R.S.; Moin, P. Numerical Simulation of Turbulent Flows. *Annu. Rev. Fluid Mech.* **1984**, *16*, 99–137. [CrossRef]
51. Fröhlich, J. *Large Eddy Simulation Turbulenter Strömungen*; Springer, B.G. Teubner Verlag/GWV Fachverlage GmbH: Wiesbaden, Gemany, 2006; Volume 1.
52. Nicoud, F.; Ducros, F. Subgrid-Scale Stress Modelling Based on the Square of the Velocity Gradient Tensor. *Flow Turbul. Combust.* **1999**, *62*, 183–200. [CrossRef]
53. Driest, E.V. On turbulent flow near a wall. *J. Aeronaut. Sci.* **1956**, *23*, 1007–1011. [CrossRef]
54. Nagib, H.M.; Chauhan, K.A. Variations of von Kármán coefficient in canonical flows. *Phys. Fluids* **2008**, *20*, 101518. [CrossRef]
55. de Villiers, E. The Potential of Large Eddy Simulation for the Modeling of Wall Bounded Flows. Ph.D Thesis, University of London, London, UK, 2006.
56. Hou, S.; Sterling, J.; Chen, S.; Doolen, G. A lattice Boltzmann subgrid model for high Reynolds number flows. *arXiv* **1998**, arXiv:comp-gas/9401004.
57. Malaspinas, O.; Sagaut, P. Consistent subgrid scale modelling for lattice Boltzmann methods. *J. Fluid Mech.* **2012**, *700*, 514–542. [CrossRef]
58. Werner, H.; Wengle, H. Large-eddy simulation of turbulent flow over and around a cube in a plate channel. In *Turbulent Shear Flows 8*; Springer: Berlin/Heidelberg, Germany, 1993; pp. 155–168.
59. Musker, A. Explicit expression for the smooth wall velocity distribution in a turbulent boundary layer. *AIAA J.* **1979**, *17*, 655–657. [CrossRef]
60. Li, Y.; Ries, F.; Nishad, K.; Sadiki, A. Near-wall modeling of LES for non-equilibrium turbulent flows in an inclined impinging jet with moderate Re-number. In Proceedings of the 6th European Conference on Computational Mechanics (ECCM 6), Glasgow, UK, 11–15 June 2018.
61. Bouzidi, M.; Firdaouss, M.; Lallemand, P. Momentum transfer of a Boltzmann-lattice fluid with boundaries. *Phys. Fluids* **2001**, *13*, 3452–3459. [CrossRef]
62. Stich, G.D.; Housman, J.A.; Kocheemoolayil, J.G.; Barad, M.F.; Kiris, C.C. Application of Lattice Boltzmann and Navier-Stokes Methods to NASA's Wall Mounted Hump. In Proceedings of the 2018 AIAA AVIATION Forum, Atlanta, GA, USA, 25–29 June 2018.
63. Freudenhammer, D.; Peterson, B.; Ding, C.P.; Boehm, B.; Grundmann, S. The influence of cylinder head geometry variations on the volumetric intake flow captured by magnetic resonance velocimetry. *SAE Int. J. Engines* **2015**, *8*, 1826–1836. [CrossRef]
64. Raffel, M.; Willert, C.E.; Wereley, S.T.; Kompenhans, J. *Particle Image Velocimetry*; Springer: Berlin/Heidelberg, Germany, 2007. [CrossRef]
65. Charonko, J.J.; Vlachos, P.P. Estimation of uncertainty bounds for individual particle image velocimetry measurements from cross-correlation peak ratio. *Meas. Sci. Technol.* **2013**, *24*, 065301. [CrossRef]
66. Sciacchitano, A.; Wieneke, B.; Scarano, F. PIV uncertainty quantification by image matching. *Meas. Sci. Technol.* **2013**, *24*, 045302. [CrossRef]
67. Wieneke, B. PIV uncertainty quantification from correlation statistics. *Meas. Sci. Technol.* **2015**, *26*, 074002. [CrossRef]
68. Sciacchitano, A.; Neal, D.R.; Smith, B.L.; Warner, S.O.; Vlachos, P.P.; Wieneke, B.; Scarano, F. Collaborative framework for PIV uncertainty quantification: Comparative assessment of methods. *Meas. Sci. Technol.* **2015**, *26*, 074004. [CrossRef]
69. Klein, M.; Sadiki, A.; Janicka, J. A digital filter based generation of inflow data for spatially developing direct numerical or large eddy simulations. *J. Comput. Phys.* **2003**, *186*, 652–665. [CrossRef]
70. Latt, J.; Chopard, B.; Malaspinas, O.; Deville, M.; Michler, A. Straight velocity boundaries in the lattice Boltzmann method. *Phys. Rev. E* **2008**, *77*, 056703. [CrossRef] [PubMed]
71. Kida, S.; Mirua, H. Identification and Analysis of Vortical Structures. *Eur. J. Mech. B/Fluids* **1998**, *17*, 471–488. [CrossRef]

72. Axtmann, G.; Rist, U. Scalability of OpenFOAM with Large Eddy Simulations and DNS on High-Performance Systems. In *High Perfromance Computing in Science and Engineering*; Springer: Cham, Switzerland, 2016; Volume 16, 413–424. [CrossRef]
73. Krause, M.; Kummerländer, A.; Avis, S.; Kusumaatmaja, H.; Dapelo, D.; Klemens, F.; Gaedtke, M.; Hafen, N.; Mink, A.; Trunk, R.; et al. OpenLB–Open Source Lattice Boltzmann Code. 2020, submitted.
74. Chen, L.; Yu, Y.; Lu, J.; Hou, G. A comparative study of lattice Boltzmann methods using bounce-back schemes and immersed boundary ones for flow acoustic problems. *Int. J. Numer. Methods Fluids* **2014**, *74*, 439–467. [CrossRef]
75. Peng, C.; Ayala, O.M.; de Motta], J.C.B.; Wang, L.P. A comparative study of immersed boundary method and interpolated bounce-back scheme for no-slip boundary treatment in the lattice Boltzmann method: Part II, turbulent flows. *Comput. Fluids* **2019**, *192*, 104251. [CrossRef]
76. Pohl, T.; Kowarschik, M.; Wilke, J.; Iglberger, K.; Rüde, U. Optimization and profiling of the cache performance of parallel lattice Boltzmann codes. *Parallel Process. Lett.* **2003**, *13*, 549–560. [CrossRef]
77. Fietz, J.; Krause, M.J.; Schulz, C.; Sanders, P.; Heuveline, V. Optimized hybrid parallel lattice Boltzmann fluid flow simulations on complex geometries. In *European Conference on Parallel Processing*; Springer: Cham, Switzerland, 2012; pp. 818–829.
78. Slotnick, J.; Khodadoust, A.; Alonso, J.; Darmofal, D.; Gropp, W.; Lurie, E.; Mavriplis, D. *CFD Vision 2030 Study: A Path to Revolutionary Computational Aerosciences*; NASA Center for AeroSpace Information: Hanover, MD, USA, 2014.
79. Shih, T.H.; Povinelli, L.A.; Liu, N.S.; Chen, K.H. Generalized wall function for complex turbulent flows. In Proceedings of the 38th Aerospace Sciences, Reno, NV, USA, 10–13 January 2000.
80. Craft, T.; Gerasimov, A.; Iacovides, H.; Launder, B. Progress in the generalization of wall-function treatments. *Int. J. Heat Fluid* **2002**, *23*, 148–160. [CrossRef]
81. Popvac, M.; Hanjalic, K. Compound Wall Treatment for RANS Computation of Complex Turbulent Flows and Heat Transfer. *Flow Turhul. Combust.* **2007**, *78*, 177–202. [CrossRef]
82. Germano, M. A dynamic subgrid-scale eddy viscosity model. *Phys. Fluids* **1991**, *3*, 1760–1765. [CrossRef]
83. Bardina, J.; Ferziger, J.; Reynolds, W. Improved subgrid-scale models for large-eddy simulation. In Proceedings of the 3th Fluid and Plasmadynamics Conference, Los Angeles, CA, USA, 29 June–1 July 1970; p. 1357.
84. Frouzakis, C.E. Lattice boltzmann methods for reactive and other flows. In *Turbulent Combustion Modeling*; Springer: Cham, Switzerland, 2011; pp. 461–486.

6

Evaluation of Fluid-Solid Interface Approaches for Vortex-Induced Vibrations

This chapter was published in the following article:

M. Haussmann, N. Hafen, F. Raichle, R. Trunk, H. Nirschl and M. J. Krause
Galilean Invariance Study on Different Lattice Boltzmann Fluid-Solid Interface Approaches for Vortex-Induced Vibrations
Computers & Mathematics with Applications, 80.5 (2020)
https://doi.org/10.1016/j.camwa.2020.04.022

My contribution according to the contributor role taxonomy system [14] included conceptualization, methodology, software, validation, formal analysis, investigation, data curation, writing – original draft, visualization and project administration.

Computers and Mathematics with Applications 80 (2020) 671–691

Contents lists available at ScienceDirect

Computers and Mathematics with Applications

journal homepage: www.elsevier.com/locate/camwa

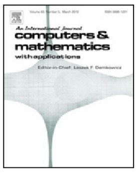

Galilean invariance study on different lattice Boltzmann fluid–solid interface approaches for vortex-induced vibrations

Marc Haussmann [a,b,*], Nicolas Hafen [a,b], Florian Raichle [a,b], Robin Trunk [a,b], Hermann Nirschl [b], Mathias J. Krause [a,b]

[a] *Lattice Boltzmann Research Group, Karlsruhe Institute of Technology, Germany*
[b] *Institute for Mechanical Process Engineering and Mechanics, Karlsruhe Institute of Technology, Germany*

ARTICLE INFO

Article history:
Received 14 September 2019
Received in revised form 1 April 2020
Accepted 22 April 2020
Available online xxxx

Keywords:
BGK
Benchmark
OpenLB
LBM
VIV

ABSTRACT

The present work compares fluid–solid interface approaches for the lattice Boltzmann method (LBM) to study vortex-induced vibrations (VIV). Two classes of fluid–solid interface approaches, namely the partially saturated methods (PSM) (Noble and Torczynski (1998), Holdych (2003), Krause et al. (2017), Trunk et al. (2018)) and moving boundary methods (MBM) (Bouzidi et al. (2001), Lallemand and Luo (2003), Yu et al. (2003), Ginzburg et al. (2008) and Filippova and Hänel (1998), Mei et al. (1999, 2000)), are investigated. First, the Galilean invariance of aerodynamic coefficients obtained by each scheme is examined. The Bhatnagar–Gross–Krook (BGK) LBM is utilized to simulate an eccentrically positioned cylinder in a transient Couette flow. In addition, various refill methods for MBM and volume approximation techniques for PSM are tested. Besides different error norms and a grid independence study of each method, the Galilean invariance violating frequencies are studied as well. These error calculations are used to choose a representative for each class to simulate vortex shedding. The VIV test case describes a transverse oscillation of a cylinder in a freestream at a Reynolds number of 100. Both free and forced cylinder oscillations are examined to study known phenomena as lock-in and lock-out zones. The results of MBM and PSM are in good agreement to literature values and prove the suitability for VIV simulations.

1. Introduction

The study of vortex-induced vibrations (VIV) plays a major role in many engineering applications e.g. the construction of bridges [1], pipelines [2], or submarine cables [3]. Therefore, the investigation of VIV phenomena is of topical interest to improve their durability, efficiency and safety.

One of the most important benchmark cases of VIV is the examination of the wake past a circular cylinder, a topic to which numerous experimental and numerical contributions have been made during the last 40 years. Interested readers are referred to the reviews of Bearman [4] and Sarpkaya [5]. Most of these simulations are based on traditional discretization methods such as the finite volume or finite element method. The present study, however, covers the lattice Boltzmann method (LBM), which has shown its applicability in distinct fields such as particle simulations [6,7] and flows

---

[*] Corresponding author at: Lattice Boltzmann Research Group, Karlsruhe Institute of Technology, Germany.
E-mail addresses: marc.haussmann@kit.edu (M. Haussmann), nicolas.hafen@kit.edu (N. Hafen), raichle.florian@gmail.com (F. Raichle), robin.trunk@kit.edu (R. Trunk), hermann.nirschl@kit.edu (H. Nirschl), mathias.krause@kit.edu (M.J. Krause).

https://doi.org/10.1016/j.camwa.2020.04.022
0898-1221/

in complex geometries [8,9] by reason of its underlying highly efficient parallel algorithm [10,11]. The previous VIV simulations using LBM covered various obstacle shapes and geometric arrangements.

The wake of a single cylinder with a prescribed transverse motion in the lock-in zone as well as free oscillations were analysed by Wang et al. [12]. Further studies with one free oscillating circular cylinder can be found [13,14]. Jiang et al. [15] depicted the influence of an altered shape to a cuboid and provided a validation for the static case. VIV of two cylinders in tandem configuration were performed by Xu et al. [16] at a Reynolds number of $Re = 100$ and by Lin et al. [17] at $Re = 200$. Also the influence of three moving cylinders were described by Hong et al. [18]. Furthermore, possibilities to suppress VIV and to control the wake were simulated [19]. Various VIV application simulations cover swimming fish [20], harbour seal vibrissae [21] or energy harvesting systems [22].

All previously mentioned VIV simulation studies deal with a fluid–solid interface approach to describe the movement of an obstacle. Fluid–solid interface approaches in the LBM can be classified into three main groups, namely the partially saturated methods (PSM), the moving boundary methods (MBM) and the immersed boundary methods (IBM). The latter group of schemes based on a Lagrangian description of the boundary is not considered in this study, the focus is set on the comparison between MBM and PSM.

PSM are characterized by a continuous description of the simulation domain obtained by a solid volume fraction approximation. In contrast, MBM use a boundary formulation coupled to a cell reconstruction method for moving geometries. Based on these different approaches, numerous algorithms were compared in the last decade focusing on a great variety of different applications. In 2008, Kao et Yang [23] proposed a novel mass and momentum conserving bounce back scheme and compared it to established MBM. Peng et al. [24] showed the difference between MBM and IBM for a fixed cylinder configuration. The influence of several collision operators were examined in [25]. Furthermore, Tao et al. [26] evaluated different momentum exchange and refill methods for the MBM. One of the first extensive comparisons between MBM, PSM and IBM can be found in [27], which mainly focuses on flow acoustic problems. In addition to the comparison of different methods, the study covers multiple refill methods. Rettinger et Rüde [28] compared MBM and PSM for several 3D particle benchmarks.

The present study, in contrast, evaluates the mentioned methods with respect to their suitability for VIV simulations. In that context, a transient analysis of aerodynamic quantities and frequencies is indispensable. The investigated simulation data can be affected by temporal and spatial discretization depending on the movement of the obstacle in the flowfield. The Galilean invariance as a transformation property of the Navier–Stokes equations is numerically investigated. In contrast, Galilean invariance defects of collision operators, equilibria or descriptor sets, which are often addressed by row expansions using Taylor or Hermite polynomials (see e.g. Dellar [29]) are not part of this study. The present Galilean invariance study is dealing with two inertial frames. Therefore, a static and a moving obstacle configuration is applied to precisely differentiate between grid errors and Galilean invariance errors. Various PSM and MBM coupled to distinct refill algorithms and volume approximation approaches are compared. For the first time, different resolutions are used to evaluate the force signals and to quantify the errors with various error norms. Moreover, to the knowledge of the authors, PSM have never before been used to simulate VIV phenomena. The comparison of MBM and PSM in the context of VIV represents a novel study.

The resulting data of the present work allows to quantify the influence of the grid resolution and the ability to describe moving obstacles for each methods. The discrete motion of the fluid–solid interface interacts with the numerical discretization and introduces periodically reoccurring pressure fluctuations. The frequencies of these upcoming fluctuations are parasitic frequencies, since they violate the Galilean invariance properties. Therefore, a detailed error analysis is used to choose algorithm configurations with regard to accuracy or occurring fluctuations depending on the respective resolution. Especially for VIV, the parasitic frequencies play a central role since they can drastically influence the overall quality of the results.

This paper is structured in the following way: Section 2 introduces the used PSM and MBM approaches. Here, refill methods, volume approximation techniques and force calculations are described in detail. The next section (Section 3) describes a cylinder in a Couette flow. This setup is used to rate each configuration regarding their suitability to perform VIV simulations. Based on this validation two representatives are chosen to simulate a transverse oscillating cylinder in Section 4. The results are summarized in Section 5 and potential future studies are pointed out.

2. Theoretical background and modelling

2.1. Lattice Boltzmann method

The LBM discretizes a simulation domain by a voxel mesh on which a set of velocity distribution functions $f_i(\boldsymbol{x}, t)$ are solved numerically at position $\boldsymbol{x}$ and time t. This set is specified by d dimensions and q lattice velocities $\boldsymbol{c}_i$, $i = 0, 1, \dots, q-1$. All terms in Section 2 are written in lattice units with the usual choice of $\delta x = \delta t = 1$, for the grid spacing δx and the lattice time step δt. In the subsequent sections quantities in lattice units are explicitly identified with the superscript L. A common choice to recover the incompressible Navier–Stokes equations in two dimensions is the $D2Q9$ descriptor set. The corresponding lattice velocities $\boldsymbol{c}_i$ can be defined as

$$\boldsymbol{c}_i = \begin{cases} (0,0) & \text{for } i = 0, \\ (\pm 1, 0), (0, \pm 1) & \text{for } i = 1, \dots, 4, \\ (\pm 1, \pm 1) & \text{for } i = 5, \dots, 8. \end{cases} \tag{1}$$

The general form of the external force free lattice Boltzmann equation (LBE) reads

$$f_i(\boldsymbol{x}+\boldsymbol{c}_i, t+1) = f_i(\boldsymbol{x}, t) + \Omega_i(\boldsymbol{x}, t). \tag{2}$$

The collision operator $\Omega_i(\boldsymbol{x}, t)$ can be chosen in different ways, the present work uses the single-relaxation time Bhatnagar–Gross–Krook (BGK) [30] form, which reads

$$\Omega_i(\boldsymbol{x}, t) = -\frac{1}{\tau}\left(f_i(\boldsymbol{x}, t) - f_i^{(eq)}(\boldsymbol{x}, t)\right). \tag{3}$$

The velocity distribution functions $f_i(\boldsymbol{x}, t)$ are linearly relaxed with the lattice relaxation time τ towards their equilibria $f_i^{(eq)}(\boldsymbol{x}, t)$.

A truncated Maxwell–Boltzmann equilibrium function $f_i^{(eq)}(\boldsymbol{u}, \rho)$ to solve a weakly compressible flow is obtained by

$$f_i^{(eq)}(\boldsymbol{u}, \rho) = w_i\rho\left[1+\left(\frac{\boldsymbol{c}_i\cdot\boldsymbol{u}}{c_s^2}+\frac{(\boldsymbol{c}_i\cdot\boldsymbol{u})^2}{2c_s^4}+\frac{\boldsymbol{u}^2}{2c_s^2}\right)\right], \tag{4}$$

where $\boldsymbol{u}$ is the lattice velocity, ρ denotes the lattice density, w_i are lattice weights received from the Gauss–Hermite quadrature [31,32] and $c_s = \frac{1}{\sqrt{3}}$ represents the lattice speed of sound. The lattice shear kinematic viscosity ν is connected to the lattice relaxation time τ in the incompressible limit by

$$\nu = c_s^2\left(\tau - \frac{1}{2}\right). \tag{5}$$

The macroscopic quantities lattice density ρ and momentum $\rho\boldsymbol{u}$ are accessible through the moments of the populations. The zeroth and first order moments are calculated as

$$\rho = \sum_{i=0}^{q-1} f_i \tag{6}$$

and

$$\rho\boldsymbol{u} = \sum_{i=0}^{q-1} \boldsymbol{c}_i f_i, \tag{7}$$

respectively. The relation of lattice pressure p and density ρ using an isothermal equation of state is given by

$$p = c_s^2\rho. \tag{8}$$

The lattice Mach number Ma^{L} is written as

$$\mathrm{Ma}^{\mathrm{L}} = \frac{u^{\mathrm{L}}}{c_s}, \tag{9}$$

where u^{L} is the characteristic lattice velocity.

An LBM algorithm is divided into a collision step corresponding to the right side of Eq. (2) and a streaming step associated with the left side of Eq. (2).

2.2. Moving boundary methods (MBM)

A moving solid object inside the fluid domain is described by the position of its boundary, which changes over time. According to this boundary position, we distinguish between fluid and solid nodes. In the particular case where a former solid node becomes a fluid node, the unknown velocity distribution functions have to be determined by a refill algorithm. Therefore, MBM consist of a velocity boundary formulation which is coupled to a refill algorithm. The following boundary schemes are curved boundary formulations and take the distance to the boundary into account to improve the accuracy. For the sake of clarity, the introduced position indices are depicted in Fig. 1. Index b is associated with the boundary node located inside the solid region. In direction $\boldsymbol{c}_i$ the wall is intersected at $\boldsymbol{x}_w$. $\boldsymbol{x}_f$, $\boldsymbol{x}_{ff}$ and $\boldsymbol{x}_{fff}$ denoting the corresponding fluid nodes in this direction. The distance between $\boldsymbol{x}_w$ and $\boldsymbol{x}_f$ is defined by the normalized distance q, which is calculated by

$$q = \frac{|\boldsymbol{x}_f - \boldsymbol{x}_w|}{|\boldsymbol{x}_f - \boldsymbol{x}_b|}. \tag{10}$$

Position x_{new} is related to nodes, where a refill algorithm needs to be applied. The nodes in discrete normal direction $\boldsymbol{c}_n$ are denoted by $\boldsymbol{x}_n$, $\boldsymbol{x}_{nn}$ and $\boldsymbol{x}_{nnn}$. This indexing convention is also used for velocity $\boldsymbol{u}$ and density ρ. The index $\bar{i}$ accompanies a quantity in the opposite direction of one with index i.

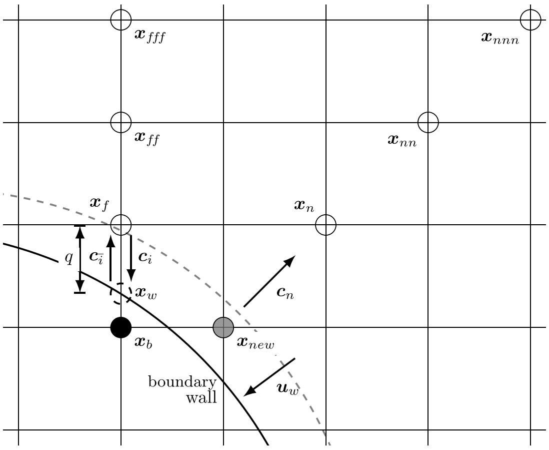

Fig. 1. Illustration of the used indexing convention.

2.2.1. Boundary schemes

Bouzidi boundary (BOUZIDI). The boundary condition proposed by Bouzidi et al. [33] represents an extension of a half-way bounce back scheme to handle curved boundaries. The boundary scheme can be classified as an interpolated bounce-back approach [34]. The unknown populations after the streaming step $f_{\bar{i}}(\boldsymbol{x}_f, t+1)$ are calculated by a linear interpolation:

$$f_{\bar{i}}(\boldsymbol{x}_f, t+1) = \begin{cases} 2qf_i(\boldsymbol{x}_b, t+1) + (1-2q)f_i(\boldsymbol{x}_f, t+1) - 2\frac{w_i}{c_s^2}\boldsymbol{c}_i \cdot \boldsymbol{u}_w(t) & \text{for } q < \frac{1}{2}, \\ \frac{1}{2q}f_i(\boldsymbol{x}_b, t+1) + \frac{2q-1}{2q}f_{\bar{i}}(\boldsymbol{x}_{ff}, t+1) - \frac{1}{q}\frac{w_i}{c_s^2}\boldsymbol{c}_i \cdot \boldsymbol{u}_w(t) & \text{for } q \geq \frac{1}{2}. \end{cases} \tag{11}$$

For $q = 1/2$ this is equivalent to a half-way bounce back condition. The last terms in Eq. (11) are an addition for moving boundaries using the wall velocity $\boldsymbol{u}_w(t)$.

Yu interpolation scheme (YU). Another interpolated bounce back approach is found in Yu et al. [35]. In contrast to Bouzidi et al. [33], they present a unified interpolation for $q \geq 1/2$ and $q < 1/2$. The present paper uses the linear formulation. The populations at a fictitious wall node $\boldsymbol{x}_w$ are calculated as

$$f_i(\boldsymbol{x}_w, t+1) = f_i(\boldsymbol{x}_f, t+1) + q\left[f_i(\boldsymbol{x}_b, t+1) - f_i(\boldsymbol{x}_f, t+1)\right]. \tag{12}$$

Assuming a velocity bounce back condition on the wall, it follows

$$f_{\bar{i}}(\boldsymbol{x}_w, t+1) = f_i(\boldsymbol{x}_w, t+1) - 2\frac{w_i}{c_s^2}\boldsymbol{c}_i \cdot \boldsymbol{u}_w(t). \tag{13}$$

So that, the missing populations $f_{\bar{i}}(\boldsymbol{x}_f, t+1)$ are calculated by

$$f_{\bar{i}}(\boldsymbol{x}_f, t+1) = f_{\bar{i}}(\boldsymbol{x}_w, t+1) + \frac{q}{1+q}\left[f_{\bar{i}}(\boldsymbol{x}_{ff}, t+1) - f_i(\boldsymbol{x}_w, t+1)\right], \tag{14}$$

where a linear interpolation with the boundary node $\boldsymbol{x}_b$ is applied.

Central linear interpolation (CLI). Ginzburg et al. [36] used an interpolated bounce back approach as well in order to obtain a curved boundary formulation. The boundary condition utilizes a central linear interpolation around the fluid node. With the coefficients $\kappa_0 = \frac{1-2q}{1+q}$ and $\alpha = \frac{4}{1+2q}$ the resulting form reads

$$f_{\bar{i}}(\boldsymbol{x}_f, t+1) = f_i(\boldsymbol{x}_b, t+1) + \kappa_0 f_i(\boldsymbol{x}_f, t+1) - \kappa_0 f_{\bar{i}}(\boldsymbol{x}_{ff}, t+1) - \alpha\frac{w_i}{c_s^2}\boldsymbol{c}_i \cdot \boldsymbol{u}_w(t). \tag{15}$$

This scheme reduces to the half-way bounce back boundary condition for $q = 1/2$.

Filippova and Hänel scheme (FH). In contrast to the previously mentioned boundary schemes, the work of Filippova and Hänel [37,38] employs extrapolations to deal with curved boundaries. The unknown velocity distribution after the streaming step $f_{\bar{i}}(\boldsymbol{x}_f, t+1)$ can be calculated by

$$f_{\bar{i}}(\boldsymbol{x}_f, t+1) = (1-\chi)f_i(\boldsymbol{x}_b, t+1) + \chi f_i^{(\star)}(\boldsymbol{x}_b, t) - 2\frac{w_i}{c_s^2}\boldsymbol{c}_i \cdot \boldsymbol{u}_w(t). \tag{16}$$

The linear combination in Eq. (16) uses a fictitious equilibrium $f_i^{(\star)}$ that is defined as

$$f_i^{(\star)}(\boldsymbol{x}_b, t) = w_i \rho_f(t) \left[1 + \frac{\boldsymbol{c}_i \cdot \boldsymbol{u}_{bf}(t)}{c_s^2} + \frac{(\boldsymbol{c}_i \cdot \boldsymbol{u}_f(t))^2}{2c_s^4} - \frac{\boldsymbol{u}_f(t) \cdot \boldsymbol{u}_f(t)}{2c_s^2} \right]. \tag{17}$$

The fictitious velocity $\boldsymbol{u}_{bf}$ and the weighting factor χ are chosen according to Mei et al. [39]

$$\boldsymbol{u}_{bf}(t) = \frac{(q-1)}{q}\boldsymbol{u}_f(t) + \frac{\boldsymbol{u}_w(t)}{q} \qquad \text{and } \chi = \frac{2q-1}{\tau + 1/2} \qquad \text{for } q \geq \frac{1}{2}, \tag{18}$$

$$\boldsymbol{u}_{bf}(t) = \boldsymbol{u}_{ff}(t) \qquad \text{and } \chi = \frac{2q-1}{\tau - 2} \qquad \text{for } q < \frac{1}{2}. \tag{19}$$

Changing these parameters in comparison to the original one proposed by Filippova and Hänel [38] results in a higher accuracy [39–41].

2.2.2. Boundary force calculation

The force calculation for MBM is usually based on a momentum exchange approach. In the present work we use a Galilean invariant momentum exchange approach [42]. The boundary force is calculated by a sum over all boundary nodes

$$\boldsymbol{F}(t) = \sum_{\boldsymbol{x}_b} \sum_{i \in L} \left[(\boldsymbol{c}_i - \boldsymbol{u}_w(t)) f_i(\boldsymbol{x}_b, t+1) - (\boldsymbol{c}_{\bar{i}} - \boldsymbol{u}_w(t)) f_{\bar{i}}(\boldsymbol{x}_f, t+1) \right], \tag{20}$$

where L denotes the set of fluid–solid links. This formulation is able to describe the boundary force of moving obstacles accurately and circumvents the drawbacks of a conventional momentum exchange calculation [26,42].

2.2.3. Refill algorithms

Equilibrium refill algorithm (EQ). A simple choice for the refill algorithm is the equilibrium distribution function refill algorithm [43]. The unknown particle distribution functions at the new fluid node $f_i(\boldsymbol{x}_{new}, t)$ are set to the equilibrium distribution function

$$f_i(\boldsymbol{x}_{new}, t) = f_i^{(eq)}(\rho_{new}(t), \boldsymbol{u}_w(t)). \tag{21}$$

The density $\rho_{new}(t)$ entering Eq. (21) is calculated by averaging the density of the surrounding fluid nodes and the used velocity is the wall velocity $\boldsymbol{u}_w(t)$.

Non-equilibrium refill algorithm (NEQ). Based on the idea of Guo et al. [44], the non-equilibrium parts of the unknown velocity distribution function are obtained by extrapolation. Both zeroth order [45] and second order [27] extrapolation are proposed. For the sake of accuracy we use the second order formulation in the present work. The unknown velocity distribution functions $f_i(\boldsymbol{x}_{new}, t)$ are decomposed into equilibrium and non-equilibrium contributions

$$f_i(\boldsymbol{x}_{new}, t) = f_i^{eq}(\rho_{new}(t), \boldsymbol{u}_w(t)) + f_i^{neq}(\boldsymbol{x}_{new}, t). \tag{22}$$

Both, the missing density $\rho_{new}(t)$ and the non-equilibrium distribution function $f_i^{neq}(\boldsymbol{x}_{new}, t)$, are obtained by

$$\rho_{new}(t) = 3\rho_f(t) - 3\rho_{ff}(t) + \rho_{fff}(t), \tag{23}$$

and

$$f_i^{neq}(\boldsymbol{x}_{new}, t) = 3f_i^{neq}(\boldsymbol{x}_f, t) - 3f_i^{neq}(\boldsymbol{x}_{ff}, t) + f_i^{neq}(\boldsymbol{x}_{fff}, t), \tag{24}$$

where the second order extrapolation is in $\boldsymbol{c}_i$ direction.

Normal extrapolation refill algorithm (EXTRA). Another second order extrapolation scheme is found in [43]

$$f_i(\boldsymbol{x}_{new}, t) = 3f_i(\boldsymbol{x}_n, t) - 3f_i(\boldsymbol{x}_{nn}, t) + f_i(\boldsymbol{x}_{nnn}, t). \tag{25}$$

Here, the velocity distributions $f_i(\boldsymbol{x}_{new}, t)$ are extrapolated by the velocity distribution functions in discrete normal direction $\boldsymbol{c}_n$.

2.3. Partially saturated methods (PSM)

Instead of using a velocity boundary formulation (Section 2.2), PSM employ a level-set function in form of a continuous description of a solid volume fraction approximation $d(\boldsymbol{x}, t) \in [0, 1]$ over the entire simulation domain. Its contribution can be modelled by modifying the collision operator $\Omega_i(\boldsymbol{x}, t)$ or by adding an additional source term $S_i(\boldsymbol{x}, t)$ to the LBE (Eq. (2)) depending on the approach being used, which yields the general form

$$f_i(\boldsymbol{x} + \boldsymbol{c}_i, t+1) = f_i(\boldsymbol{x}, t) + \Omega_i(\boldsymbol{x}, t) + S_i(\boldsymbol{x}, t). \tag{26}$$

In either way, a weighting factor $B(\boldsymbol{x}, t)$ depending on the solid volume fraction approximation has to be introduced. According to Rettinger and Rüde [28], this can be achieved in two different variants

$$\textbf{B1}: \quad B(\boldsymbol{x}, t) = d(\boldsymbol{x}, t), \tag{27}$$

$$\textbf{B2}: \quad B(\boldsymbol{x}, t) = \frac{d(\boldsymbol{x}, t)\left(\tau - \frac{1}{2}\right)}{(1 - d(\boldsymbol{x}, t)) + \left(\tau - \frac{1}{2}\right)}. \tag{28}$$

2.3.1. Approaches

Homogenized lattice Boltzmann method (HLBM). One way of modelling a fluid–solid interface by means of a continuous field description is to use a moving porous media approach. A corresponding framework for LBM is provided by the HLBM. Adapted from a lattice Boltzmann description of fluid flow in heterogeneous porous media [46], the influence of submerged solid objects on the fluid flow is achieved by scaling an effective velocity $\boldsymbol{u}^{eff}(\boldsymbol{x}, t)$. This scaling consists of a simple convex combination, directly depending on the solid volume fraction $d(\boldsymbol{x}, t)$ with a **B1** weighting formulation

$$\boldsymbol{u}^{eff}(\boldsymbol{x}, t) = B(\boldsymbol{x}, t)\boldsymbol{u}^{F}(\boldsymbol{x}, t) + (1 - B(\boldsymbol{x}, t))\,\boldsymbol{u}^{S}(\boldsymbol{x}, t). \tag{29}$$

Here, $\boldsymbol{u}^{F}(\boldsymbol{x}, t)$ and $\boldsymbol{u}^{S}(\boldsymbol{x}, t)$ are the velocities of the fluid and the solid object, respectively. A porous momentum loss force accounts for the reduced momentum due to the fluid flow retardation. As proposed by Kupershtokh [47], this force can implicitly be incorporated into the LBE by shifting the distribution functions $f_i(\boldsymbol{x}, t)$ in velocity space with a source term

$$S_i(\boldsymbol{x}, t) = f_i^{\mathrm{eq}}\left(\rho(\boldsymbol{x}, t), \boldsymbol{u}^{eff}(\boldsymbol{x}, t)\right) - f_i^{\mathrm{eq}}\left(\rho(\boldsymbol{x}, t), \boldsymbol{u}^{F}(\boldsymbol{x}, t)\right). \tag{30}$$

PSM$_{M2}$ and PSM$_{M3}$. Another way to account for the influence of a submerged solid object can be realized by modifying the LBM collision operator rather than including an additional source term [48,49]. This modification consists analogously to Eq. (29) of a weighted average of a fluid collision operator $\Omega_i^f(\boldsymbol{x}, t)$ and one specifically designed to model solid sites $\Omega_i^s(\boldsymbol{x}, t)$

$$\Omega_i(\boldsymbol{x}, t) = B(\boldsymbol{x}, t)\Omega_i^s(\boldsymbol{x}, t) + (1 - B(\boldsymbol{x}, t))\Omega_i^f(\boldsymbol{x}, t). \tag{31}$$

While $\Omega_i^f(\boldsymbol{x}, t)$ represents the standard BGK collision operator (Eq. (3)), the solid one $\Omega_i^s(\boldsymbol{x}, t)$ can be modelled in different ways

$$\textbf{M1}: \quad \Omega_i^s(\boldsymbol{x}, t) = \left[f_{\bar{i}}(\boldsymbol{x}, t) - f_{\bar{i}}^{\mathrm{eq}}(\rho, \boldsymbol{u})\right] - \left[f_i(\boldsymbol{x}, t) - f_i^{\mathrm{eq}}(\rho, \boldsymbol{u}_s)\right], \tag{32}$$

$$\textbf{M2}: \quad \Omega_i^s(\boldsymbol{x}, t) = \left[f_i^{\mathrm{eq}}(\rho, \boldsymbol{u}_s) - f_i(\boldsymbol{x}, t)\right] + \left(1 - \frac{1}{\tau}\right)\left[f_i(\boldsymbol{x}, t) - f_i^{\mathrm{eq}}(\rho, \boldsymbol{u})\right], \tag{33}$$

$$\textbf{M3}: \quad \Omega_i^s(\boldsymbol{x}, t) = \left[f_{\bar{i}}(\boldsymbol{x}, t) - f_{\bar{i}}^{\mathrm{eq}}(\rho, \boldsymbol{u}_s)\right] - \left[f_i(\boldsymbol{x}, t) - f_i^{\mathrm{eq}}(\rho, \boldsymbol{u}_s)\right]. \tag{34}$$

As formulation **M2** and **M3** in combination with **B2** (Eq. (28)) were reported as superior [28], only these are considered in the present study and referred to as PSM$_{\mathrm{M2}}$ and PSM$_{\mathrm{M3}}$.

2.3.2. Boundary force calculation

In PSM the hydrodynamic force acting on a solid object is calculated by summing up the force contribution of all individual nodes $\boldsymbol{x}_S$ occupied by the solid object. In HLBM this contribution is accounted for by the source term $S_i(\boldsymbol{x}, t)$ representing the porous momentum loss force (Section 2.3.1)

$$\boldsymbol{F}(t) = \sum_{\boldsymbol{x}_S}\left[\sum_i \left(S_i(\boldsymbol{x}_S, t)\boldsymbol{c}_i\right)\right]. \tag{35}$$

In PSM$_{\mathrm{M2}}$ and PSM$_{\mathrm{M3}}$ the contribution consists of the weighting factor $B(\boldsymbol{x}, t)$, the oppositely directed lattice velocity $\boldsymbol{c}_{\bar{i}}$ and the solid collision operator $\Omega_i^s(\boldsymbol{x}, t)$ according to the M2 or M3 formulation in Eqs. (33) and (34) respectively

$$\boldsymbol{F}(t) = \sum_{\boldsymbol{x}_S}\left[B(\boldsymbol{x}_S, t)\sum_i \left(\Omega_i^s(\boldsymbol{x}_S, t)\boldsymbol{c}_{\bar{i}}\right)\right]. \tag{36}$$

2.3.3. Volume approximation algorithms

As the weighting factor $B(\boldsymbol{x}, t)$ employed in all PSM approaches heavily depends on the solid volume fraction approximation $d(\boldsymbol{x}, t)$, its calculation poses a decisive factor to the accuracy and performance of the overall algorithm. For that, the intersections of the quadrilateral cells and the solid object have to be evaluated. While this is a trivial task in case of an analytical description of the solid objects boundary, in most cases such a description does not exist which leads to the necessity of volume approximation algorithms.

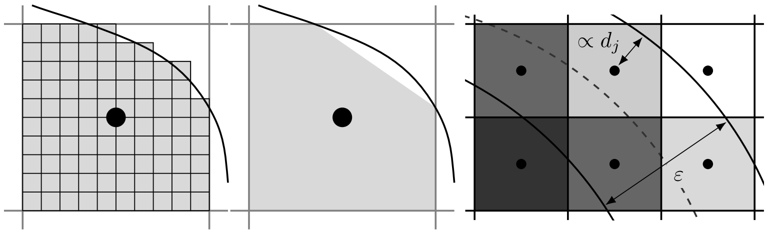

(a) SS (b) POLYGON (c) EPSILON

Fig. 2. Illustration of the three volume approximations algorithms SS, POLYGON and EPSILON. The black dots represent the cell centres.

Supersampling algorithm (SS). In order to increase the accuracy while sticking to a simple step function, the SS represents an alternative approach. As demonstrated by Owen [50], each intersected cell can be subdivided into a number of subcells (Fig. 2(a)) depending on a chosen refinement level n_{ref}. The solid fraction of each cell can then be calculated by simply checking which subcells are located within the solid objects boundary and by subsequently summing over those that do. The present study uses a refinement level of $n_{ref} = 10$, which results in 100 subcells for every intersected cell. This approach is straightforward to implement, but eventually becomes computationally expensive for large refinement levels. Its applicability to a wide range of boundary geometries, however, often poses a crucial advantage over different approaches.

Polygon approximation algorithm (POLYGON). A more sophisticated approach is the approximation of the volume fraction in each cell by one single sufficiently simple shape. A polygon can be constructed by intersecting the boundary with the cell sides and computing the length of the edges that are inside the boundary [51]. Its area corresponds to the solid fraction in that cell. This is shown in Fig. 2(b).

Epsilon boundary layer algorithm (EPSILON). In the case of moving objects a simple step function leads to abrupt changes from solid to fluid cells, which potentially leads to fluctuations and numerical errors. These can be avoided by using a continuous function with a smooth transition from solid to fluid instead (Fig. 2(c)). In case of a circular cylinder, this function can be described via

$$d(\boldsymbol{x},t) = \begin{cases} 1 & \text{for} \quad \|\boldsymbol{x}-\boldsymbol{X}_k\|_2 \le R - \frac{\varepsilon}{2}, \\ \cos^2\left(\frac{\pi}{2\varepsilon}(\|\boldsymbol{x}-\boldsymbol{X}_k\|_2)\right) & \text{for} \quad R-\frac{\varepsilon}{2} < \|\boldsymbol{x}-\boldsymbol{X}_k\|_2 < R+\frac{\varepsilon}{2}, \\ 0 & \text{for} \quad \|\boldsymbol{x}-\boldsymbol{X}_k\|_2 \ge R+\frac{\varepsilon}{2}. \end{cases} \tag{37}$$

Here, $\boldsymbol{X}_k(t)$ is the object's centre of mass, R its radius and $\varepsilon \ge 0$ the smoothing parameter ε controlling the width of the continuous transition area [6]. In the present study, we set the smoothing parameter to $\varepsilon = \sqrt{2}$. Resulting from the $D2Q9$ descriptor set with $\max(\|\boldsymbol{c}_i\|_2) = \sqrt{2}$, this choice ensures that a solid cell ($d(\boldsymbol{x},t) = 1$) is not a direct neighbour of a fluid cell ($d(\boldsymbol{x},t) = 0$).

3. Results of the Galilean invariance benchmark

3.1. Benchmark description

We simulate a moving cylinder in a transient Couette flow. The geometrical setup is inspired by [43] and illustrated in Fig. 3. The channel has a length of $L_1 + L_2 = 8D$ and a height of $L_4 = 4D$, where D denotes the cylinder diameter. The cylinder is eccentrically positioned in y-direction inside the channel at $L_3 = \left(1+\frac{1}{15}\right)2D$. Initially the flow field is set to $U_0 = 0.02\,\frac{\mathrm{m}}{\mathrm{s}}$ in x-direction. The velocity of the moving cylinder in x-direction is prescribed and set to $U_C = 0.02\,\frac{\mathrm{m}}{\mathrm{s}}$. The upper and lower walls move with a velocity of $U_W = 0.1\,\frac{\mathrm{m}}{\mathrm{s}}$ and $-U_W = -0.1\,\frac{\mathrm{m}}{\mathrm{s}}$ respectively in x-direction. The mentioned values for the wall and cylinder velocities are set at time $t = 0\,\mathrm{s}$, which corresponds to an impulsive motion [43]. The velocity boundaries at the walls are implemented by a non-local regularized approach (see boundary scheme BC4 in [52]), which is second order accurate for straight walls. In x-direction of the channel periodic boundaries [53] are applied. For the description of the cylinder boundary both MBM and PSM are utilized. The shear rate of the flow is defined as

$$\kappa = \frac{2U_W}{L_4}. \tag{38}$$

The Reynolds number is given by

$$Re = \frac{D^2\kappa}{\nu}, \tag{39}$$

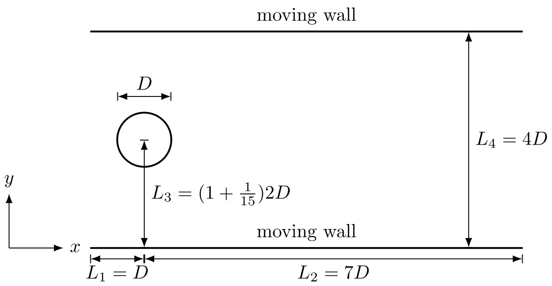

Fig. 3. Geometrical description of the Galilean invariance benchmark case.

Table 1
Discretization parameters for resolutions $N = 20, 40, 80, 160, 320$.

N	u^{L}	Ma^{L}	$\Delta x/\mathrm{m}$	$\Delta t/\mathrm{s}$	τ
20	0.041	0.070	2.500×10^{-3}	2.029×10^{-3}	0.714
40	0.020	0.035	1.250×10^{-3}	5.071×10^{-4}	0.714
80	0.010	0.018	6.250×10^{-4}	1.268×10^{-4}	0.714
160	0.005	0.009	3.125×10^{-4}	3.170×10^{-5}	0.714
320	0.003	0.004	1.563×10^{-4}	7.924×10^{-6}	0.714

where ν is the kinematic viscosity. The Reynolds number is set to 11.36. If a reference frame is assumed with reference speed $U_{ref} = -0.02\,\frac{\mathrm{m}}{\mathrm{s}}$ in x-direction, the cylinder is static with $U_C + U_{ref} = 0.0\,\frac{\mathrm{m}}{\mathrm{s}}$. Therefore, the upper wall velocity and lower wall velocity is $U_W + U_{ref} = 0.08\,\frac{\mathrm{m}}{\mathrm{s}}$ and $-U_W + U_{ref} = -0.12\,\frac{\mathrm{m}}{\mathrm{s}}$ respectively. Accordingly, the initial condition of the flow field is changed to $U_0 + U_{ref} = 0.0\,\frac{\mathrm{m}}{\mathrm{s}}$. These two reference frames allow the estimation of the Galilean invariance. The used error criterions err_{L^2} and err_{L^∞} are based on the L^2 and the L^∞ norm. The err_{L^2} for the quantity χ is given by

$$err_{L^2}(\chi) = \sqrt{\frac{\sum_{m=0}^{M}\left[\chi^{\mathrm{ref}}(t_m) - \chi(t_m)\right]^2}{\sum_{m=0}^{M}\left[\chi^{\mathrm{ref}}(t_m)\right]^2}}, \tag{40}$$

where M denotes the number of considered time steps and χ^{ref} is a reference solution. Analogously, the $err_{L^\infty}(\chi)$ can be written as

$$err_{L^\infty}(\chi) = \frac{\sum_{m=0}^{M}\max|\chi^{\mathrm{ref}}(t_m) - \chi(t_m)|}{\sum_{m=0}^{M}\max|\chi^{\mathrm{ref}}(t_m)|}. \tag{41}$$

Eqs. (40) and (41) are used to calculate both grid and Galilean invariance errors. For the estimation of the grid error only the results of the static configuration ($U_{ref} = -0.02\,\frac{\mathrm{m}}{\mathrm{s}}$) are taken into account. The reference solution in the error norms $\chi^{\mathrm{ref}}(t_m)$ is set to the corresponding highest grid resolution obtained by the static cylinder configuration. In contrast, the calculation of Galilean invariance errors $\chi(t_m)$ is carried out with the moving cylinder configuration. The related reference solution $\chi^{\mathrm{ref}}(t_m)$ is computed in the static configuration at the same resolution. This choice separates the grid error of the static configuration from the Galilean invariance error. The considered quantities in this benchmark case are the force signals in x- and y-direction F_x and F_y.

$$gerr_{L^2}\left(F_x, F_y\right) = \frac{1}{2}\left[err_{L^2}(F_x) + err_{L^2}\left(F_y\right)\right]. \tag{42}$$

In Eq. (42), a global error $gerr_{L^2}\left(F_x, F_y\right)$ out of these two quantities can be computed as the arithmetic mean of $err_{L^2}(F_x)$ and $err_{L^2}\left(F_y\right)$.

3.2. Influence of refill and volume approximation methods

For the evaluation of the refill methods we use BOUZIDI and for the volume approximation techniques $\mathrm{PSM}_{\mathrm{M2}}$. The benchmark case is simulated for 5 different resolutions $N = 20, 40, 80, 160, 320$, where N is related to the diameter of the cylinder D. We use diffusive scaling $\Delta t \propto \Delta x^2$ to decrease the Mach number error term with the resolution. The used discretization parameter are depicted in Table 1.

Additionally the parasitic frequencies due to the tested refill and volume approximation methods are investigated. Firstly, the force signals of F_x and F_y are filtered by a high-pass filter (HP) to filter out the underlying frequency that is

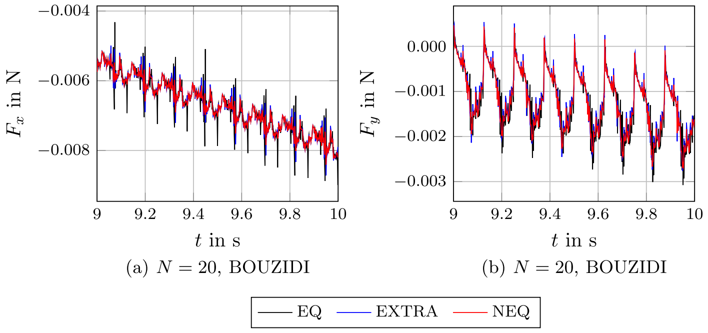

(a) $N = 20$, BOUZIDI (b) $N = 20$, BOUZIDI

Fig. 4. Force signals F_x and F_y for BOUZIDI at $N = 20$ using EQ, NEQ and EXTRA refill algorithms.

induced by the eccentricity of the cylinder. The high-pass filter cutoff frequency of 2 Hz is estimated based on the static cylinder configuration. Then, power spectra (PS) of the filtered force signals are calculated. The characterization of the power spectrum is done by the frequency of the highest peak

$$f_{para}(\chi) = f\left(\max(\mathrm{PS}(\mathrm{HP}(\chi)))\right), \tag{43}$$

which describes the parasitic frequency with the highest power. As a reference value, the frequency of the cylinder motion with respect to the used grid resolution can be estimated by

$$f_{grid} = \frac{U_C}{\Delta x}. \tag{44}$$

Additionally, the total power is calculated by integrating the power spectrum over the observed frequency range

$$P_{total}(\chi) = 2\int_2^{f_{max}} \mathrm{PS}(\mathrm{HP}(\chi))df, \tag{45}$$

where the maximal frequency is related to the time step size by $f_{max} = 1/(2\Delta t)$. Consequently, the total power P_{total} is a measure to characterize the intensity of the occurring parasitic frequencies.

The instantaneous force signals F_x and F_y, using refill methods, for the resolution of $N = 20$ are illustrated in Fig. 4. It can be seen that the EQ exhibits the highest fluctuations in comparison to NEQ and EXTRA. This insight coincides with earlier studies [26,43]. For the quantification of the increased parasitic frequencies the L^2 and L^∞ errors are calculated in Table 3. These errors are given by Eqs. (40) and (41) using the time interval $t \in [3, 10]$ and Δt as ensemble time to capture fluctuations at high frequencies. The $err_{L^\infty}(F_x)$ for the EQ at $N = 20$ is nearly doubled in comparison to NEQ and EXTRA. The effect is also visible for F_y, but shifted to higher resolutions. With increasing resolution the difference between EQ in comparison to NEQ and EXTRA is more pronounced. This can be deduced from the smaller averaged experimental order of convergence $\overline{EOC}$ (see Table 4). The total power of the force signals P_{total} supports these statements, because both $P_{total}(F_x)$ and $P_{total}(F_y)$ of EQ are significantly higher in comparison to NEQ and EXTRA (see Table 2). At higher grid resolutions this leads to an increase in power by an order of magnitude. The frequencies $f_{para}(F_x)$ and $f_{para}(F_y)$ are in good agreement with the grid frequencies f_{grid}. Exceptions for $f_{para}(F_x)$ are found at $N = 20$ for EXTRA and EQ, where $f_{para}(F_x)$ represents a multiple of f_{grid}. The higher errors and the lower convergence speed can be explained by the neglection of the non-equilibrium contribution in the refill scheme. The results of EXTRA and NEQ are hardly different. The significant differences is that the extrapolation direction is in lattice link direction $\boldsymbol{c}_i$ in case of NEQ and in discrete normal direction $\boldsymbol{c}_n$ for EXTRA. Furthermore, the velocity in the equilibrium distribution is extrapolated in case of EXTRA and set to the wall velocity in NEQ. This implies that neither the extrapolation direction nor the used velocity have a substantial influence on the results. The slightly reduced $gerr_{L^2}(F_x, F_y)$ and the lower total power of $P_{total}(F_x)$ and $P_{total}(F_y)$ justify our selection to use NEQ in the subsequent studies.

The temporal evolution of F_x and F_y, using volume approximation techniques, for $N = 20$ is shown in Fig. 5. The course of POLYGON and EPSILON is significantly smoother, because the secondary violating Galilean invariance peaks have disappeared. The intrinsic continuous nature of POLYGON and EPSILON are responsible for this favourable feature. In contrast, SS shows secondary peaks. Therefore, the Galilean invariance L^2 and L^∞ errors depicted in Table 3 are greatly increased. This is due to the higher total power P_{total} of the parasitic frequencies, see Table 2. Although 100 subcells were used for the SS, the $err_{L^\infty}(F_x)$ at $N = 20$ is increased approximately sevenfold in comparison to POLYGON and EPSILON. This behaviour can be linked to the used subgrid in SS. The volume approximation in each cell results in discrete values for the solid fraction. The jump from one discrete value to the next introduces the secondary peaks. This influence of the secondary peaks is also visible, if the parasitic frequencies $f_{para}(F_x)$ with the highest power are considered. The parasitic

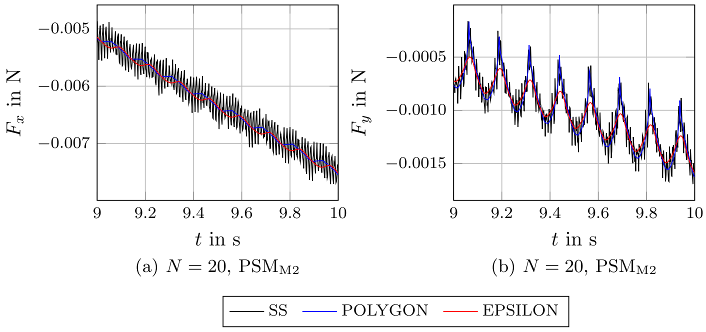

(a) $N = 20$, $\mathrm{PSM_{M2}}$

(b) $N = 20$, $\mathrm{PSM_{M2}}$

Fig. 5. Force signals F_x and F_y for $\mathrm{PSM_{M2}}$ at $N = 20$ using SS, POLYGON and EPSILON volume approximation algorithms.

Table 2
Power spectrum related quantities $P_{total}(F_x)$, $P_{total}(F_y)$, $f_{para}(F_x)$ and $f_{para}(F_y)$ of computations with EQ, EXTRA, NEQ, EPSILON, POLYGON, SS at $N = 20, 40, 80, 160, 320$.

	N	EQ	EXTRA	NEQ	EPSILON	POLYGON	SS
$P_{total}(F_x)/(\mathrm{N})^2$	20	3.46×10^{-08}	2.01×10^{-08}	1.34×10^{-08}	4.62×10^{-10}	8.26×10^{-11}	1.01×10^{-08}
	40	9.89×10^{-09}	3.90×10^{-09}	3.29×10^{-09}	1.86×10^{-11}	6.62×10^{-11}	1.91×10^{-09}
	80	2.15×10^{-09}	3.25×10^{-10}	2.87×10^{-10}	3.72×10^{-11}	1.33×10^{-11}	5.18×10^{-10}
	160	4.81×10^{-10}	4.05×10^{-11}	3.76×10^{-11}	3.21×10^{-12}	1.63×10^{-12}	6.75×10^{-11}
	320	1.38×10^{-11}	1.90×10^{-12}	1.88×10^{-12}	2.52×10^{-13}	2.93×10^{-13}	2.76×10^{-12}
$f_{para}(F_x)/\mathrm{Hz}$	20	112.00	24.00	7.97	8.03	7.92	80.00
	40	15.98	15.98	15.98	16.00	15.96	160.00
	80	31.98	31.98	31.98	31.99	31.99	320.00
	160	63.98	63.98	63.98	63.98	63.98	640.01
	320	127.71	127.71	127.71	127.96	128.22	1,280.40
$P_{total}(F_y)/(\mathrm{N})^2$	20	7.57×10^{-08}	6.85×10^{-08}	6.69×10^{-08}	1.84×10^{-09}	5.67×10^{-09}	6.60×10^{-09}
	40	6.28×10^{-09}	3.12×10^{-09}	2.84×10^{-09}	3.34×10^{-10}	2.70×10^{-10}	9.72×10^{-10}
	80	1.34×10^{-09}	2.99×10^{-10}	2.58×10^{-10}	1.67×10^{-10}	8.16×10^{-11}	3.93×10^{-10}
	160	3.37×10^{-10}	3.59×10^{-11}	3.16×10^{-11}	3.53×10^{-11}	3.24×10^{-11}	9.08×10^{-11}
	320	6.02×10^{-12}	3.54×10^{-13}	3.36×10^{-13}	3.50×10^{-13}	2.76×10^{-13}	1.50×10^{-12}
$f_{para}(F_y)/\mathrm{Hz}$	20	8.04	8.03	8.03	7.98	8.03	8.03
	40	16.02	16.02	16.01	16.05	16.03	160.01
	80	32.01	32.01	32.01	31.98	32.04	319.97
	160	63.98	63.98	63.98	63.98	63.98	63.98
	320	127.71	256.18	256.18	128.22	128.22	5,119.82

frequency $f_{para}(F_x)$ for SS is in fact ten times the grid frequency f_{grid} due to the refinement level of $n_{ref} = 10$. The higher the refinement level n_{ref} and the associated set of discrete values, the smaller the amplitudes of the secondary fluctuations. As a consequence P_{total} is decreased. Since an increase in the refinement level $n_{ref} > 10$ leads to a significant rise in computing time, higher refinement levels are not considered here. In Table 4, the averaged experimental order of convergence $\overline{EOC}$ of SS and EPSILON is close to one, whereas the $\overline{EOC}$ for POLYGON is slightly higher with a value of $\overline{EOC} = 1.18$. The higher convergence speed and the physically motivated volume approximation method, which is also suitable for arbitrarily shaped objects, lead us to the decision to use POLYGON for further studies.

If we compare the Galilean invariance errors based on the refill methods and volume approximation methods, it is clearly visible that the volume approximation method errors are smaller (see Fig. 6). Also the total power P_{total} is significantly reduced, if volume approximation methods are applied. This is to be expected and corresponds with findings of previous studies [27]. The destruction and creation of fluid nodes in MBM induce the highly oscillating course at small resolutions. Nevertheless, the higher convergence speed of the refill based methods leads to comparable results for MBM and PSM at high resolutions.

3.3. Influence of fluid–solid interface approaches

For the selection of one suitable scheme, each for MBM and PSM, it is necessary to take into account the grid error and the Galilean invariance error. The grid error is estimated for the case of the non-moving cylinder to isolate the grid dependency. The L^2 and L^∞ grid errors and Galilean invariance errors are depicted in Tables 6 and 7. These error calculations use the time interval $t \in [3, 10]$ and Δt as ensemble time to resolve fluctuations at high frequencies.

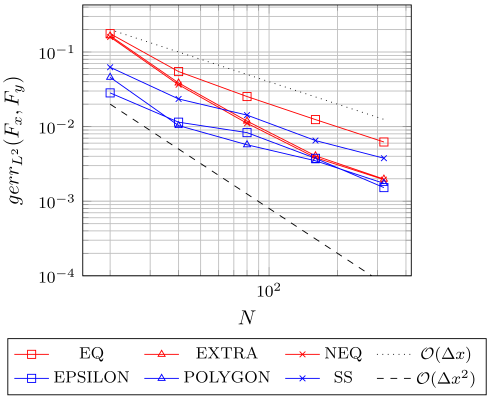

Fig. 6. Global Galilean invariance error $gerr_{L^2}(F_x, F_y)$ for $t \in [3, 10]$ of computations with SS, POLYGON, EPSILON, EQ, NEQ and EXTRA.

Table 3
Force signal Galilean invariance errors $err_{L^2}(F_x)$, $err_{L^\infty}(F_x)$, $err_{L^2}(F_y)$ and $err_{L^\infty}(F_y)$ for $t \in [3, 10]$ of computations with EQ, EXTRA, NEQ, EPSILON, POLYGON, SS at $N = 20, 40, 80, 160, 320$ against the corresponding static configuration solution.

	N	EQ	EXTRA	NEQ	EPSILON	POLYGON	SS
$err_{L^2}(F_x)$	20	0.05974	0.04696	0.03839	0.00750	0.00495	0.03332
	40	0.03068	0.01935	0.01765	0.00141	0.00281	0.01363
	80	0.01464	0.00608	0.00573	0.00193	0.00109	0.00746
	160	0.00686	0.00198	0.00190	0.00060	0.00048	0.00265
	320	0.00384	0.00163	0.00162	0.00021	0.00050	0.00207
$err_{L^\infty}(F_x)$	20	0.19335	0.11521	0.07754	0.00881	0.00807	0.05792
	40	0.08908	0.04420	0.03257	0.00146	0.00315	0.02459
	80	0.05469	0.01719	0.01638	0.00186	0.00135	0.01507
	160	0.02791	0.00430	0.00371	0.00081	0.00071	0.00839
	320	0.02730	0.00233	0.00214	0.00026	0.00066	0.00538
$err_{L^2}(F_y)$	20	0.29286	0.28290	0.27955	0.04912	0.08672	0.09165
	40	0.07871	0.05767	0.05521	0.02152	0.01783	0.03334
	80	0.03597	0.01764	0.01642	0.01468	0.01032	0.02107
	160	0.01797	0.00614	0.00577	0.00691	0.00649	0.01035
	320	0.00860	0.00233	0.00227	0.00284	0.00297	0.00547
$err_{L^\infty}(F_y)$	20	0.69075	0.72356	0.67947	0.08161	0.23721	0.25333
	40	0.22019	0.14832	0.15505	0.03419	0.05379	0.11422
	80	0.15194	0.06826	0.06083	0.02257	0.01641	0.06062
	160	0.10692	0.02304	0.02115	0.01035	0.00981	0.03420
	320	0.05206	0.00736	0.00645	0.00458	0.00453	0.01921

Table 4
Experimental order of convergence (EOC) obtained by the Galilean invariance (GI) global error $gerr_{L^2}(F_x, F_y)$ for $t \in [3, 10]$ of computations with SS, POLYGON, EPSILON, EQ, NEQ and EXTRA.

		EQ	EXTRA	NEQ	EPSILON	POLYGON	SS
GI	$EOC_{20,40}$	1.69	2.10	2.13	1.30	2.15	1.41
	$EOC_{40,80}$	1.11	1.70	1.72	0.47	0.85	0.72
	$EOC_{80,160}$	1.03	1.55	1.53	1.14	0.71	1.13
	$EOC_{160,320}$	1.00	1.04	0.98	1.30	1.01	0.79
	$\overline{EOC}$	1.21	1.60	1.59	1.05	1.18	1.01

The averaged global errors $gerr_{L^2}(F_x, F_y)$ are illustrated in Fig. 7. The course of the grid errors are quite similar for all MBM: BOUZIDI, CLI, FH and YU. In contrast, the Galilean invariance errors exhibit larger differences. The CLI shows the highest Galilean invariance errors at small and intermediate resolutions. Since both YU and CLI are a unified interpolated bounce back approach, YU should be preferred due to smaller errors and a higher Galilean invariance convergence rate (Table 5). BOUZIDI and FH produce similar results, notwithstanding the different idea behind these schemes. In summary, YU is chosen as the representative of MBM for the following VIV simulations due to the best averaged grid and Galilean invariance $\overline{EOC}$.

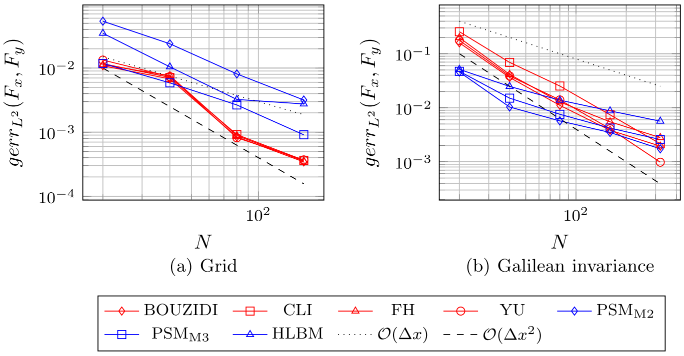

(a) Grid (b) Galilean invariance

Fig. 7. Global Galilean invariance and grid errors $gerr_{L^2}(F_x, F_y)$ for $t \in [3, 10]$ of computations with BOUZIDI, CLI, FH, YU, $\mathrm{PSM_{M2}}$, $\mathrm{PSM_{M3}}$ and HLBM.

Table 5
Experimental order of convergence (EOC), obtained by the global Galilean invariance (GI) and grid (G) error $gerr_{L^2}(F_x, F_y)$ for $t \in [3, 10]$ of computations with BOUZIDI, CLI, FH, YU, $\mathrm{PSM_{M2}}$, $\mathrm{PSM_{M3}}$ and HLBM.

		BOUZIDI	CLI	FH	YU	$\mathrm{PSM_{M2}}$	$\mathrm{PSM_{M3}}$	HLBM
G	$EOC_{20,40}$	0.68	0.71	0.57	0.85	1.17	1.01	1.74
	$EOC_{40,80}$	3.01	2.96	3.10	3.17	1.56	1.14	1.69
	$EOC_{80,160}$	1.30	1.33	1.32	1.15	1.35	1.55	0.23
	$\overline{EOC}$	1.66	1.67	1.66	1.72	1.36	1.23	1.22
GI	$EOC_{20,40}$	2.13	1.89	2.26	2.19	2.15	1.65	1.05
	$EOC_{40,80}$	1.72	1.45	1.69	1.47	0.85	0.99	0.84
	$EOC_{80,160}$	1.53	1.77	1.22	1.77	0.71	0.85	0.66
	$EOC_{160,320}$	0.98	1.78	0.97	2.06	1.01	0.70	0.63
	$\overline{EOC}$	1.59	1.72	1.54	1.87	1.18	1.05	0.80

All PSM configurations reveal a distinct convergence speed. Examining the approaches individually in Table 5, it can be seen, that $\mathrm{PSM_{M2}}$ results in higher values for both grid and Galilean invariance $\overline{EOC}$. While $\mathrm{PSM_{M2}}$ and HLBM show comparable results considering the grid errors at high resolutions (Fig. 7(a)), HLBM performs significantly worse than both $\mathrm{PSM_{M2}}$ and $\mathrm{PSM_{M3}}$ for the Galilean invariance (Fig. 7(b)). Despite its superior convergence behaviour, the $\mathrm{PSM_{M2}}$ approach exhibits a grid error $err_{L^2}(F_x)$, that is three times larger than $\mathrm{PSM_{M3}}$ with HLBM residing in between for $N = 20$. Increasing the grid resolution does slightly change the relation of $\mathrm{PSM_{M2}}$ and $\mathrm{PSM_{M3}}$. Since the grid errors for each scheme use different reference solutions, the direct comparison of the relative errors is only reliable for small resolutions. This statement results from the assumption that the differences between the respective reference solutions are smaller than the grid errors at coarse resolutions. The grid error of HLBM indicates a reduced convergence speed at high resolutions. If we look at the Galilean invariance error, it can be seen that the $\mathrm{PSM_{M2}}$ configuration has the smallest $err_{L^\infty}(F_x)$ and $err_{L^\infty}(F_y)$ at each resolution. For the following VIV simulations it is recommended to use the configuration with fluctuations as small as possible. Therefore, we decided to use $\mathrm{PSM_{M2}}$ from here on.

The comparison of the class of PSM and MBM clearly displays the advantages and drawbacks. PSM are known for their small fluctuations due to the continuous description of the simulation domain. Therefore, all tested PSM are characterized by small Galilean invariance errors. Only with resolutions of $N = 160$ and $N = 320$, MBM return comparable errors. As a further remark, the interpolated MBM suffer from inaccuracy in the estimation of the momentum transfer at boundaries [23,43]. This leads to a net mass flux, that impedes mass conservation near the boundary. On the contrary, PSM avoid this issue due to the continuous description of the flowfield. This represents a distinct advantage of PSM due to superior mass conservation. The grid convergence study for the static cylinder shows an increased error for PSM and a worse grid convergence order. The fact that the position information of the boundary is taken into account in the MBM explains the higher grid convergence order.

4. Results of the vortex-induced vibration benchmark

4.1. Benchmark description

A cylinder in a freestream is investigated. The geometrical description is depicted in Fig. 8. The position of the cylinder and the size of the simulation domain are inspired by [54,55]. The cylinder is centrally positioned in y-direction at $L_4 = 10D$, where D is the cylinder diameter. On the upper and lower boundary, slip conditions are applied. The original

Table 6
Force signal Galilean invariance errors $err_{L^2}(F_x)$, $err_{L^\infty}(F_x)$, $err_{L^2}(F_y)$ and $err_{L^\infty}(F_y)$ for $t \in [3, 10]$ of computations with BOUZIDI, CLI, FH, YU, PSM_{M2}, PSM_{M3} and HLBM at $N = 20, 40, 80, 160, 320$ against the corresponding static configuration solution.

	N	BOUZIDI	CLI	FH	YU	PSM_{M2}	PSM_{M3}	HLBM
$err_{L^2}(F_x)$	20	0.03839	0.08928	0.05101	0.03628	0.00495	0.01617	0.01413
	40	0.01765	0.02662	0.02046	0.01146	0.00281	0.00891	0.00960
	80	0.00573	0.01389	0.00708	0.00551	0.00109	0.00527	0.00872
	160	0.00190	0.00361	0.00244	0.00210	0.00048	0.00282	0.00530
	320	0.00162	0.00090	0.00214	0.00038	0.00050	0.00160	0.00264
$err_{L^\infty}(F_x)$	20	0.07754	0.26045	0.13193	0.07699	0.00807	0.02462	0.01722
	40	0.03257	0.07085	0.04274	0.03091	0.00315	0.01710	0.01097
	80	0.01638	0.03258	0.01985	0.01428	0.00135	0.00713	0.01075
	160	0.00371	0.00896	0.00507	0.00479	0.00071	0.00507	0.00613
	320	0.00214	0.00257	0.00309	0.00088	0.00066	0.00243	0.00348
$err_{L^2}(F_y)$	20	0.27955	0.42179	0.34597	0.31647	0.08672	0.07827	0.08855
	40	0.05521	0.11165	0.06237	0.06607	0.01783	0.02120	0.03995
	80	0.01642	0.03658	0.01851	0.02244	0.01032	0.00985	0.01890
	160	0.00577	0.01119	0.00854	0.00607	0.00649	0.00558	0.01220
	320	0.00227	0.00340	0.00347	0.00158	0.00297	0.00356	0.00864
$err_{L^\infty}(F_y)$	20	0.67947	1.16934	0.90536	0.79474	0.23721	0.26282	0.12937
	40	0.15505	0.37760	0.20399	0.22751	0.05379	0.06593	0.06261
	80	0.06083	0.11486	0.07386	0.07413	0.01641	0.01803	0.02950
	160	0.02115	0.03358	0.03002	0.01923	0.00981	0.00992	0.02190
	320	0.00645	0.01061	0.00888	0.00551	0.00453	0.00733	0.01596

Table 7
Force signal grid errors $err_{L^2}(F_x)$, $err_{L^\infty}(F_x)$, $err_{L^2}(F_y)$ and $err_{L^\infty}(F_y)$ for $t \in [3, 10]$ of computations with BOUZIDI, CLI, FH, YU, PSM_{M2}, PSM_{M3} and HLBM at $N = 20, 40, 80, 160$ against the corresponding resolution $N = 320$.

	N	BOUZIDI	CLI	FH	YU	PSM_{M2}	PSM_{M3}	HLBM
$err_{L^2}(F_x)$	20	0.01714	0.01953	0.01831	0.01928	0.03819	0.01298	0.02888
	40	0.00434	0.00477	0.00463	0.00498	0.02080	0.00533	0.01381
	80	0.00076	0.00090	0.00082	0.00073	0.00709	0.00318	0.00285
	160	0.00023	0.00025	0.00023	0.00025	0.00295	0.00083	0.00280
$err_{L^\infty}(F_x)$	20	0.01619	0.01841	0.01706	0.01658	0.03630	0.01436	0.02021
	40	0.00321	0.00358	0.00339	0.00342	0.02001	0.00487	0.01273
	80	0.00097	0.00111	0.00102	0.00093	0.00669	0.00339	0.00250
	160	0.00018	0.00019	0.00018	0.00018	0.00284	0.00077	0.00235
$err_{L^2}(F_y)$	20	0.00458	0.00390	0.00425	0.00740	0.06959	0.01066	0.04099
	40	0.00923	0.00953	0.01061	0.00978	0.02707	0.00642	0.00708
	80	0.00092	0.00093	0.00095	0.00090	0.00913	0.00214	0.00363
	160	0.00046	0.00048	0.00048	0.00049	0.00339	0.00099	0.00271
$err_{L^\infty}(F_y)$	20	0.00447	0.00407	0.00409	0.00541	0.08291	0.01228	0.03627
	40	0.00751	0.00767	0.00861	0.00808	0.03050	0.00580	0.00637
	80	0.00084	0.00085	0.00087	0.00083	0.00945	0.00241	0.00332
	160	0.00041	0.00042	0.00042	0.00043	0.00368	0.00105	0.00262

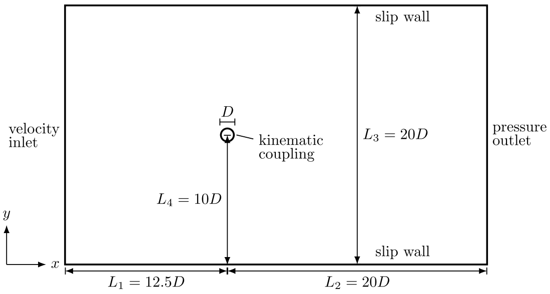

Fig. 8. Geometrical description of the VIV benchmark case.

proposed domain by Placzek et al. [54] suggested a height of $L_3 = 10D$. In the present study the height of the simulation domain is doubled to $L_3 = 20D$ in order to reduce the influence of the slip boundaries on the results. The algorithm of the employed straight slip boundary condition is described in [56]. The velocity inlet and pressure outlet boundaries follow a non-local regularized approach (see boundary scheme BC4 in [52]). The velocity at the inflow is slowly increased by a smooth function during the first two simulation seconds to avoid instabilities due to non-equilibrium contributions. At $t = 2$ s the velocity in x-direction is kept constant to the freestream velocity $U_\infty = 2\,\frac{\mathrm{m}}{\mathrm{s}}$. The Reynolds number for this flow is given by

$$Re = \frac{U_\infty D}{\nu}. \tag{46}$$

The Reynolds number is set to 100 in order to be able to study the Karman vortex street regime. The wake flow is therefore laminar and two-dimensional [57]. The investigated aerodynamic quantities are the drag coefficient

$$C_D = \frac{F_x}{0.5\rho D U_\infty^2} \tag{47}$$

and the lift coefficient

$$C_L = \frac{F_y}{0.5\rho D U_\infty^2}. \tag{48}$$

Another important quantity is the Strouhal number that is defined as

$$St = f_{st}\frac{D}{U_\infty}, \tag{49}$$

where f_{st} is the Strouhal frequency. The Strouhal frequency is the vortex shedding frequency of the cylinder at rest. However, the vortex shedding frequency of the cylinder in motion is denoted by f_{vs}. The dimensionless vortex shedding frequency of the moving cylinder f_{vs}^*, also named reduced frequency is defined analogous to the Strouhal number as

$$f_{vs}^* = f_{vs}\frac{D}{U_\infty}. \tag{50}$$

Three different configurations of this benchmark are examined. The first one is a static configuration, i.e. the cylinder is fixed. The other two configurations deal with a moving cylinder. The forced oscillation of the cylinder is obtained by prescribing the cylinder motion. The cylinder motion is assumed to be purely sinusoidal and can be described by

$$y(t) = y_{max}\sin(2\pi f_{ex} t) \tag{51}$$

where y is the transverse displacement of the cylinder centre, y_{max} is the amplitude and f_{ex} the prescribed excitation frequency. Thus, the cylinder motion and the occurring wake regimes are adjustable by the two parameter y_{max}, f_{ex}. For convenience, we nondimensionalize the set of variables to the non-dimensional amplitude

$$A^* = \frac{y_{max}}{D} \tag{52}$$

and a frequency ratio

$$F = \frac{f_{ex}}{f_{st}}. \tag{53}$$

This configuration can be seen as a one-way coupled fluid–solid interface approach: The flowfield is affected by the cylinder motion, however the flow influence on the motion is neglected. In contrast, the free oscillation of the cylinder covers the effects of the flowfield on the cylinder motion. Therefore, the vertical motion is governed by the differential equation of an undamped oscillator

$$m\ddot{y} + ky = F_y, \tag{54}$$

where m is the mass of the cylinder and k the spring constant of the elastic mounting. Since no external forces are present, the natural frequency of the cylinder is given by

$$f_n = \frac{1}{2\pi}\sqrt{\frac{k}{m}}. \tag{55}$$

The time integration of Eq. (54) is done by a blended procedure [58]. The prediction of the cylinder acceleration $\ddot{y}^{n+1}$ for the time step t_{n+1} can be written as

$$\ddot{y}^{n+1} = \frac{F_y^n}{m} - \frac{k}{m}y^n. \tag{56}$$

This acceleration is used via linear approximations to evaluate the cylinder velocity $\dot{y}^{n+1}$ and the displacement y^{n+1}. At timestep $t+1$ they are written as

$$\dot{y}^{n+1} = \dot{y}^n + \Delta t\ddot{y}^{n+1}, \tag{57}$$

Table 8
Discretization parameters for resolutions $N = 10, 20, 40, 80$.

N	u^{L}	Ma^{L}	$\Delta x/\mathrm{m}$	$\Delta t/\mathrm{s}$	τ
10	0.1	0.173	5.00×10^{-3}	2.500×10^{-4}	0.53
20	0.05	0.087	2.50×10^{-3}	6.250×10^{-5}	0.53
40	0.025	0.043	1.25×10^{-3}	1.563×10^{-5}	0.53
80	0.0125	0.022	6.25×10^{-4}	3.906×10^{-6}	0.53

Table 9
Strouhal number St, mean drag coefficient $\bar{C}_D$ and maximum lift coefficient $C_{L,max}$ of computations with YU and $\mathrm{PSM}_{\mathrm{M2}}$ at $N = 10, 20, 40, 80$. Comparison against reference data of Stansby et Slaouti [60], Anagnostopoulos [61], Henderson [62], Zhou et al. [63], Shiels et al. [59], Placzek et al. [54].

Reference		St	$\bar{C}_D$	$C_{L,max}$
Stansby et Slaouti [60]		0.166	1.32	0.35
Anagnostopoulos [61]		0.167	1.20	0.27
Henderson [62]		0.166	1.35	0.33
Zhou et al. [63]		0.162	1.48	0.31
Shiels et al. [59]		0.167	1.33	0.33
Placzek et al. [54]		0.169	1.37	0.33
Lower bound		0.162	1.20	0.27
Upper bound		0.169	1.48	0.35
Method	N			
$\mathrm{PSM}_{\mathrm{M2}}$	10	0.171	1.46	0.32
$\mathrm{PSM}_{\mathrm{M2}}$	20	0.171	1.41	0.35
$\mathrm{PSM}_{\mathrm{M2}}$	40	0.169	1.39	0.34
$\mathrm{PSM}_{\mathrm{M2}}$	80	0.170	1.38	0.34
YU	10	0.166	1.38	0.30
YU	20	0.169	1.38	0.32
YU	40	0.168	1.37	0.33
YU	80	0.168	1.37	0.34

and

$$y^{n+1} = y^n + \Delta t[(1-\theta)\dot{y}^n + \theta\dot{y}^{n+1}], \tag{58}$$

where θ is the blending factor. The blending factor is set to $\theta = 0.5$ so that the numerical damping is small [58]. Both parameter m and k of Eq. (54) can be transferred to non-dimensional parameters

$$m^* = \frac{m}{0.5\rho D^2}, \tag{59}$$

and

$$k^* = \frac{k}{0.5\rho U_\infty^2}, \tag{60}$$

according to the work of Shiels et al. [59]. Furthermore, Shiels et al. [59] introduce the effective rigidity

$$k^*_{eff} = k^* - 4(\pi f^*_{vs})^2 m^*, \tag{61}$$

and shows that this single parameter is able to describe distinct pairs of k^* and m^* even if they are equal to zero.

4.2. Fixed cylinder

The simulations are performed for a static cylinder. In Table 8, the used discretization parameters for the four grid resolutions $N = 10, 20, 40, 80$ are displayed, where N is related to the diameter of the cylinder. The physical time steps Δt are diffusively scaled with the physical grid spacing, i.e. $\Delta t \propto \Delta x^2$.

In Table 9, the mean drag coefficient $\bar{C}_D$, the Strouhal number St and the maximum occurring lift coefficient $C_{L,max}$ are depicted for different references. Additionally the results of the present study for different grid resolutions are shown. The statistics for the results are obtained after 40 Strouhal periods $t_{st} = \frac{1}{f_{st}}$ and last for 60 Strouhal periods. It can be seen that the reference values vary in a certain interval marked with upper and lower bound. The span of the intervals is related to different methods, resolutions and geometrical configurations. The chosen methods YU and $\mathrm{PSM}_{\mathrm{M2}}$ show even for the smallest resolution of $N = 10$ aerodynamic coefficients that are inside the reference interval.

However, the Strouhal number for $\mathrm{PSM}_{\mathrm{M2}}$ is slightly higher in comparison to the reference data. Both methods show that the quantities are converging at high grid resolutions. At a grid resolution of $N = 40$ each quantity differs to its

Table 10
Mean drag coefficient $\bar{C}_D$, maximum lift coefficient $C_{L,max}$ and lift coefficient amplitude based on the power spectrum $C_{L,max,\mathrm{PS}}$ of computations with YU and PSM$_{\mathrm{M2}}$ at $N = 40$. Comparison against reference data of Placzek et al. [54].

	F	$\bar{C}_D$	$C_{L,max}$		
Placzek et al. [54]	0.9	1.50	0.14		
Placzek et al. [54]	1.1	1.75	0.72		
				$C_{L,max,\mathrm{PS}}$	$err(C_{L,max})$
PSM$_{\mathrm{M2}}$	0.9	1.52	0.15	0.13	0.135
PSM$_{\mathrm{M2}}$	1.1	1.77	0.78	0.77	0.018
YU	0.9	1.51	0.20	0.14	0.422
YU	1.1	1.76	0.80	0.77	0.042

corresponding quantity at a grid resolution of $N = 80$ by less than one percent. Additionally, the temporal discretization at $N = 40$ uses approximately 940 time steps to describe one Strouhal period t_{st}. Therefore, we decided to use $N = 40$ for the moving cylinder configurations.

4.3. Forced cylinder oscillations

The cylinder motion is now prescribed by Eq. (51) and characterized by the non-dimensional parameters amplitude A^* and frequency ratio F. The amplitude is fixed to $A = 0.25$ and the frequency ratio is varied to obtain different types of responses.

4.3.1. Locked region

The lock-in region is defined as the pure sinusoidal lift response that follows the frequency of the cylinder motion f_{ex}. These locked configurations are investigated for a frequency ratio of $F = 0.9$ and $F = 1.1$. The lift coefficient signals for YU and PSM$_{\mathrm{M2}}$ and the according spectral analyses are illustrated in Fig. 9. The dimensionless frequency f^* is defined as

$$f^* = \frac{f}{f_{ex}}. \tag{62}$$

Analogously, the dimensionless time t^* is given by

$$t^* = t f_{ex}. \tag{63}$$

The spectral analyses clearly indicates for both schemes and frequency ratios that the main frequency is $f^* \approx 1.0$. Consequently, the lift response follows f_{ex} instead of the Strouhal frequency f_{st}. The amplitude is enhanced with a higher frequency ratio and suppressed with a lower frequency ratio in comparison to the static case. If we look at the instantaneous lift signal for $F = 0.9$, parasitic fluctuations of both signals are visible. The error estimation of the parasitic frequencies is obtained by the use of the power spectrum (PS). The root mean square (rms) amplitude of lift coefficient $C_{L,rms,\mathrm{PS}}$ is defined as

$$C_{L,rms,\mathrm{PS}} = \sqrt{\max|\mathrm{PS}(C_L)|}. \tag{64}$$

Under the assumption of a pure sinusoidal signal the amplitude based on the power spectrum $C_{L,max,\mathrm{PS}}$ can be obtained by

$$C_{L,max,\mathrm{PS}} = \sqrt{2} C_{L,rms,\mathrm{PS}}. \tag{65}$$

The related error criterion $err(C_{L,max})$ to estimate the highest fluctuations is calculated by

$$err(C_{L,max}) = \frac{|C_{L,max} - C_{L,max,\mathrm{PS}}|}{|C_{L,max,\mathrm{PS}}|}. \tag{66}$$

Table 10 shows the results for PSM$_{\mathrm{M2}}$ and YU in comparison to the reference data [54] and the error criterion $err(C_{L,max})$. YU demonstrates higher fluctuations ($err(C_{L,max}) = 0.422$) as PSM$_{\mathrm{M2}}$ ($err(C_{L,max}) = 0.135$) for $F = 1.1$. This insight coincides with the results of Section 3.3 and can be traced back to the algorithm. Remarkably, the fluctuations are much smaller when $F = 1.1$. For YU the fluctuations are smaller by one magnitude. The comparison to the reference data shows that the mean drag coefficients $\bar{C}_D$ of both schemes and frequency ratios are in good agreement. However, the maximum lift coefficient $C_{L,max}$ shows higher deviations, in particular the value of YU at $F = 0.9$. This is reasoned by the high fluctuations. If, on the other hand, the amplitude based on the power spectrum $C_{L,max,\mathrm{PS}}$ is taken into account, the lift values show a higher consistency to the reference values.

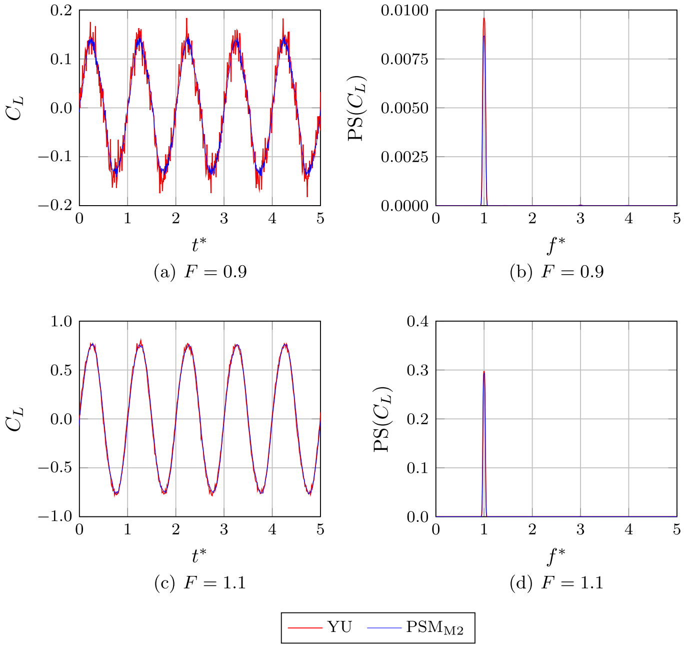

(a) $F = 0.9$ (b) $F = 0.9$

(c) $F = 1.1$ (d) $F = 1.1$

Fig. 9. Lift coefficient response C_L and power spectrum PS(C_L) for frequency ratios $F = 0.9$ and $F = 1.1$ of computations with YU and PSM$_{M2}$ at $N = 40$.

4.3.2. Unlocked region

The simulation of the unlocked wake is done by frequency ratios $f = 0.5$ and $F = 1.5$. The unlocked region is characterized by a non pure sinusoidal signal. A certain beating behaviour is now visible [64]. Both the Strouhal frequency f_{st} and the motion frequency f_{ex} influence the lift course. Therefore, we can define a beating frequency f_b to describe the periodicity of the signal. In Fig. 10 the instantaneous lift signal for YU and PSM$_{M2}$ are depicted for $F = 0.5$ and $F = 1.5$. For $F = 0.5$ the beating frequency corresponds to f_{ex}. If we look at the spectral analysis, f_{st} and f_{ex} are covered in the spectral plot 10(b) at $f^* \approx 1.00$ and $f^* \approx 2.00$. This is in good agreement with the reference data [54]. YU indicates higher fluctuations in the course in comparison to the PSM$_{M2}$.

In the case of $F = 1.5$, the beating frequency is estimated to $f^* = 0.125$. The related PS(C_L) in Fig. 10(d) again shows two peaks at $f^* = 0.67$ and $f^* = 1.00$. The missing peak of the beating frequency is traced back to the low differences between the amplitudes indicating a less energetic beating [54]. Both lift signals obtained by YU and PSM$_{M2}$ exhibit only minor fluctuations. It can be seen that the single amplitudes in one beating period are slightly different, which is justified by the enlarged beating period at $F = 1.5$.

4.4. Free cylinder oscillations

The motion of the cylinder is now governed by the differential Eq. (4.1). The utilized time integration algorithm for this two-way coupled fluid–solid interface approach is depicted in Section 4.1. Different parameter pairs of mass m and spring constant k are inserted to simulate a range of effective rigidities k^*_{eff}. In Fig. 11, the mean drag coefficient $\bar{C}_D$, the maximum lift $C_{L,max}$, the non-dimensional amplitude A^* and the reduced frequency f^* are plotted against k^*_{eff} for YU and PSM$_{M2}$. Furthermore the reference data of Shiels et al. [59] is chosen for comparison. In Fig. 11(a), it can be seen that in the region of $k^*_{eff} \in [0, 5]$ that A^* reaches a maximum and the corresponding aerodynamic coefficients are also increased. The reduced frequency in Fig. 11(b) exhibits that the frequency is shifted to the natural frequency of the cylinder f_n. Therefore this region is named resonant. Shiels et al. [59] emphasize that the lock-in region, i.e. the coincidence of the cylinder motion frequency and the Strouhal frequency, only occurs at $k^*_{eff} = 0$ and should not be mixed up with the resonant region. At higher values $k^*_{eff} > 5$, the Strouhal frequency f_{st} and the aerodynamic coefficients of the static case are recovered. Also, in the region of $k^*_{eff} < 0$, the considered values asymptotically converge towards the values of the fixed cylinder configuration. The maximum lift coefficient values $C_{L,max}$ for $k^*_{eff} < 0$ in Fig. 11(c) are plotted with opposite sign. This is related to the phase shift between the cylinder motion and the lift signal [59]. The comparison of both methods

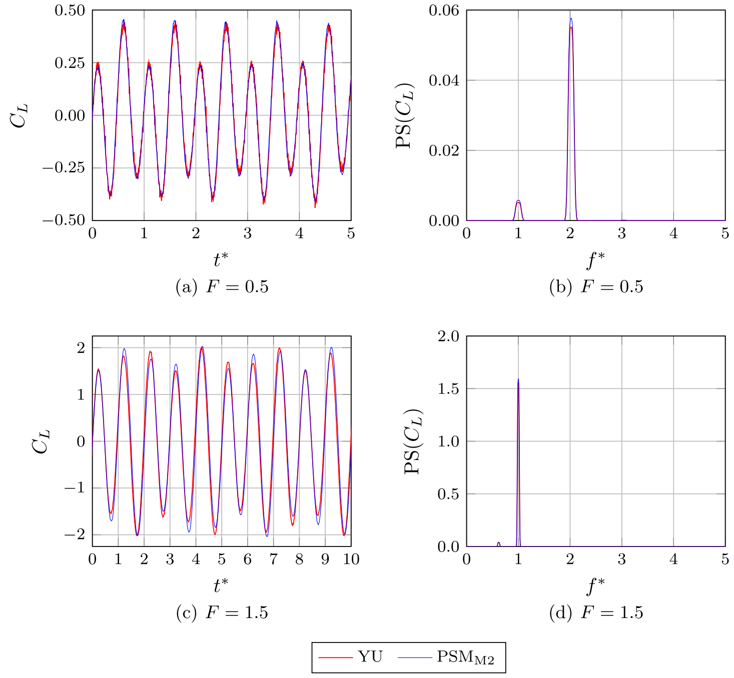

(a) $F = 0.5$ (b) $F = 0.5$

(c) $F = 1.5$ (d) $F = 1.5$

Fig. 10. Lift coefficient response C_L and power spectrum (PS(C_L)) for frequency ratios $F = 0.5$ and $F = 1.5$ of computations with YU and PSM$_{\mathrm{M2}}$ at $N = 40$.

to the reference data shows that both methods are able to cover the courses of the reference data. Minor deviations are recorded in the mean drag coefficients in Fig. 11(d), which are slightly overestimated. One reason for this is the higher mean drag coefficient in the fixed configuration of $\bar{C}_D = 1.37$ for YU and $\bar{C}_D = 1.39$ for PSM$_{\mathrm{M2}}$ in comparison to $\bar{C}_D = 1.33$. Also, the reduced frequencies are overestimated, which can be explained by the increased Strouhal number (Table 9).

5. Conclusion and outlook

The present work demonstrates the suitability of distinct MBM and PSM to simulate VIV. The force signals of a cylinder in a Couette flow were examined in two different reference frames. Firstly, three refill methods and volume approximation methods were tested regarding Galilean invariance. NEQ refill method for MBM and POLYGON approximation were chosen by reason of the increased averaged Galilean invariance $\overline{EOC} = 1.59$, respectively $\overline{EOC} = 1.18$. Four different MBM and three different PSM were then applied and benchmarked with respect to Galilean invariance and grid convergence. It could be shown that the YU scheme had a high grid convergence order of $\overline{EOC} = 1.72$ and a high Galilean Invariance convergence order of $\overline{EOC} = 1.87$. In the group of PSM the PSM$_{\mathrm{M2}}$ configuration showed preferable features such as low fluctuations in the moving case. The YU and PSM$_{\mathrm{M2}}$ were used in the simulation of transverse oscillation cylinder in a freestream at $Re = 100$. Both configurations were able to predict the reference data in the static case. At a resolution of $N = 40$ the relative error of both configurations was less than 1% in comparison to $N = 80$. The forced oscillation simulation for PSM and YU showed a high conformity to the reference solution both in the lock-in and the lock-out region for the aerodynamic coefficients and the spectral analysis results. YU suffered from higher parasitic secondary fluctuations by comparison to PSM$_{\mathrm{M2}}$. In case of the free oscillation simulation both schemes were able to follow the course of the reference data with varying effective rigidity k^*_{eff}. In summary, YU and PSM$_{\mathrm{M2}}$ are suitable methods to simulate VIV phenomena. The Galilean invariance benchmark results indicate that at low resolutions PSM$_{\mathrm{M2}}$ is the preferable method due to less parasitic fluctuations. At higher resolutions the increased grid and Galilean invariance convergence order of YU leads to a higher accuracy. The choice of a suitable scheme should therefore be made on the used grid resolution.

Further work should be done to integrate fluctuation suppressing schemes as the local iteration refilling scheme [27] to improve the results of MBM VIV simulations. Also the inclusion of IBM in the test framework is preferable, especially if deformable geometries are to be considered.

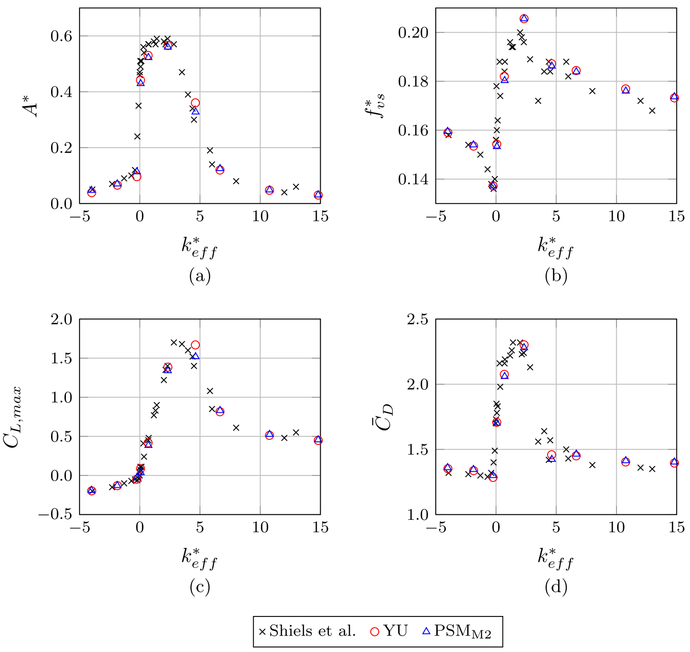

Fig. 11. Amplitude A^*, reduced frequency f^*_{vs}, maximum lift coefficient $C_{L,max}$ and mean drag coefficient $\bar{C}_D$ for different effective rigidities k^*_{eff} of computations with YU and $\mathrm{PSM}_{\mathrm{M2}}$ at $N = 40$. Comparison against the reference data of Shiels et al. [59].

CRediT authorship contribution statement

Marc Haussmann: Conceptualization, Methodology, Software, Validation, Formal analysis, Investigation, Writing - original draft, Project administration, Visualization, Data curation. **Nicolas Hafen:** Validation, Software, Writing - review & editing. **Florian Raichle:** Investigation, Data curation, Formal analysis, Visualization, Writing - review & editing. **Robin Trunk:** Methodology, Software. **Hermann Nirschl:** Supervision, Funding acquisition. **Mathias J. Krause:** Resources, Software, Supervision, Funding acquisition, Writing - review & editing.

Acknowledgement

This study was funded by the Deutsche Forschungsgemeinschaft (DFG, German Research Foundation) – 422374351

References

[1] Y. Fujino, Y. Yoshida, Wind-induced vibration and control of Trans-Tokyo Bay crossing bridge, J. Struct. Eng. 128 (8) (2002) 1012–1025.
[2] B. Yang, F.-P. Gao, D.-S. Jeng, Y.-X. Wu, Experimental study of vortex-induced vibrations of a pipeline near an erodible sandy seabed, Ocean Eng. 35 (3–4) (2008) 301–309.
[3] F. Hover, S. Miller, M. Triantafyllou, Vortex-induced vibration of marine cables: experiments using force feedback, J. Fluids Struct. 11 (3) (1997) 307–326.
[4] P. Bearman, Circular cylinder wakes and vortex-induced vibrations, J. Fluids Struct. 27 (5–6) (2011) 648–658.
[5] T. Sarpkaya, A critical review of the intrinsic nature of vortex-induced vibrations, J. Fluids Struct. 19 (4) (2004) 389–447.
[6] M.J. Krause, F. Klemens, T. Henn, R. Trunk, H. Nirschl, Particle flow simulations with homogenised lattice Boltzmann methods, Particuology 34 (2017) 1–13.
[7] R. Trunk, J. Marquardt, G. Thäter, H. Nirschl, M.J. Krause, Towards the simulation of arbitrarily shaped 3D particles using a homogenised lattice Boltzmann method, Comput. & Fluids 172 (2018) 621–631.
[8] T. Henn, V. Heuveline, M.J. Krause, S. Ritterbusch, Aortic coarctation simulation based on the lattice Boltzmann method: Benchmark results, in: O. Camara, T. Mansi, M. Pop, K. Rhode, M. Sermesant, A. Young (Eds.), Statistical Atlases and Computational Models of the Heart. Imaging and Modelling Challenges, Springer Berlin Heidelberg, Berlin, Heidelberg, 2013, pp. 34–43.
[9] L.d.L.X. Augusto, J. Ross-Jones, G.C. Lopes, P. Tronville, J.A.S. Gonçalves, M. Rädle, M.J. Krause, Microfiber filter performance prediction using a lattice Boltzmann method, Commun. Comput. Phys. 23 (2018) 910–931.
[10] V. Heuveline, M.J. Krause, J. Latt, Towards a hybrid parallelization of lattice Boltzmann methods, Comput. Math. Appl. 58 (5) (2009) 1071–1080, http://dx.doi.org/10.1016/j.camwa.2009.04.001, URL http://www.sciencedirect.com/science/article/pii/S0898122109002454.

[11] V. Heuveline, M.J. Krause, Openlb: towards an efficient parallel open source library for lattice Boltzmann fluid flow simulations, in: International Workshop on State-of-the-Art in Scientific and Parallel Computing, PARA, Vol. 9, 2010.
[12] Y. Wang, C. Shu, C. Teo, J. Wu, An immersed boundary-lattice Boltzmann flux solver and its applications to fluid–structure interaction problems, J. Fluids Struct. 54 (2015) 440–465.
[13] S. Hirabayashi, Numerical analysis of vortex-induced motion of two-dimensional circular cylinder by lattice Boltzmann method, J. Mar. Sci. Technol. 21 (3) (2016) 426–433.
[14] A. De Rosis, G. Falcucci, S. Ubertini, F. Ubertini, S. Succi, Lattice Boltzmann analysis of fluid-structure interaction with moving boundaries, Commun. Comput. Phys. 13 (3) (2013) 823–834.
[15] X. Jiang, Y. Andreopoulos, T. Lee, Z. Wang, Numerical investigations on the vortex-induced vibration of moving square cylinder by using incompressible lattice Boltzmann method, Comput. & Fluids 124 (2016) 270–277.
[16] Y. Xu, Y. Liu, Y. Xia, F. Wu, Lattice-Boltzmann simulation of two-dimensional flow over two vibrating side-by-side circular cylinders, Phys. Rev. E 78 (4) (2008) 046314.
[17] J. Lin, R. Jiang, Z. Chen, X. Ku, Poiseuille flow-induced vibrations of two cylinders in tandem, J. Fluids Struct. 40 (2013) 70–85.
[18] Y. Hong-Bing, L. Yang, X. You-Sheng, K. Jian-Long, Numerical simulation of two-dimensional flow over three cylinders by lattice Boltzmann method, Commun. Theor. Phys. 54 (5) (2010) 886.
[19] C. Wang, H. Tang, F. Duan, C. Simon, Control of wakes and vortex-induced vibrations of a single circular cylinder using synthetic jets, J. Fluids Struct. 60 (2016) 160–179.
[20] F.-B. Tian, H. Luo, L. Zhu, J.C. Liao, X.-Y. Lu, An efficient immersed boundary-lattice Boltzmann method for the hydrodynamic interaction of elastic filaments, J. Comput. Phys. 230 (19) (2011) 7266–7283.
[21] H.E. Morrison, M. Brede, G. Dehnhardt, A. Leder, Simulating the flow and trail following capabilities of harbour seal vibrissae with the lattice Boltzmann method, J. Comput. Sci. 17 (2016) 394–402.
[22] S. Zhou, J. Wang, Dual serial vortex-induced energy harvesting system for enhanced energy harvesting, AIP Adv. 8 (7) (2018) 075221.
[23] P.-H. Kao, R.-J. Yang, An investigation into curved and moving boundary treatments in the lattice Boltzmann method, J. Comput. Phys. 227 (11) (2008) 5671–5690.
[24] Y. Peng, L.-S. Luo, A comparative study of immersed-boundary and interpolated bounce-back methods in LBE, Prog. Comput. Fluid Dyn. 8 (1–4) (2008) 156–167.
[25] L. Wang, Z. Guo, B. Shi, C. Zheng, Evaluation of three lattice Boltzmann models for particulate flows, Commun. Comput. Phys. 13 (4) (2013) 1151–1172.
[26] S. Tao, J. Hu, Z. Guo, An investigation on momentum exchange methods and refilling algorithms for lattice Boltzmann simulation of particulate flows, Comput. & Fluids 133 (2016) 1–14.
[27] L. Chen, Y. Yu, J. Lu, G. Hou, A comparative study of lattice Boltzmann methods using bounce-back schemes and immersed boundary ones for flow acoustic problems, Internat. J. Numer. Methods Fluids 74 (6) (2014) 439–467.
[28] C. Rettinger, U. Rüde, A comparative study of fluid-particle coupling methods for fully resolved lattice Boltzmann simulations, Comput. & Fluids 154 (2017) 74–89.
[29] P.J. Dellar, Lattice Boltzmann algorithms without cubic defects in Galilean invariance on standard lattices, J. Comput. Phys. 259 (2014) 270–283.
[30] P.L. Bhatnagar, E.P. Gross, M. Krook, A model for collision processes in gases. I. Small amplitude processes in charged and neutral one-component systems, Phys. Rev. 94 (1954) 511–525, http://dx.doi.org/10.1103/PhysRev.94.511, URL https://link.aps.org/doi/10.1103/PhysRev.94.511.
[31] X. He, L.-S. Luo, Theory of the lattice Boltzmann method: From the Boltzmann equation to the lattice Boltzmann equation, Phys. Rev. E 56 (1997) 6811–6817, http://dx.doi.org/10.1103/PhysRevE.56.6811, URL https://link.aps.org/doi/10.1103/PhysRevE.56.6811.
[32] X. Shan, X.-F. Yuan, H. Chen, Kinetic theory representation of hydrodynamics: a way beyond the Navier–Stokes equation, J. Fluid Mech. 550 (2006) 413–441, http://dx.doi.org/10.1017/S0022112005008153.
[33] M. Bouzidi, M. Firdaouss, P. Lallemand, Momentum transfer of a Boltzmann-lattice fluid with boundaries, Phys. Fluids 13 (11) (2001) 3452–3459.
[34] T. Krüger, H. Kusumaatmaja, A. Kuzmin, O. Shardt, G. Silva, E.M. Viggen, The Lattice Boltzmann Method, Springer, 2017.
[35] D. Yu, R. Mei, W. Shyy, A unified boundary treatment in lattice Boltzmann method, in: 41st Aerospace Sciences Meeting and Exhibit, 2003, p. 953.
[36] I. Ginzburg, F. Verhaeghe, D. d'Humieres, Two-relaxation-time lattice Boltzmann scheme: About parametrization, velocity, pressure and mixed boundary conditions, Commun. Comput. Phys. 3 (2) (2008) 427–478.
[37] O. Filippova, D. Hänel, Grid refinement for lattice-BGK models, J. Comput. Phys. 147 (1) (1998) 219–228.
[38] O. Filippova, S. Succi, F. Mazzocco, C. Arrighetti, G. Bella, D. Hänel, Multiscale lattice Boltzmann schemes with turbulence modeling, J. Comput. Phys. 170 (2) (2001) 812–829, http://dx.doi.org/10.1006/jcph.2001.6764, URL http://www.sciencedirect.com/science/article/pii/S0021999101967646.
[39] R. Mei, D. Yu, W. Shyy, L.-S. Luo, Force evaluation in the lattice Boltzmann method involving curved geometry, Phys. Rev. E 65 (4) (2002) 041203.
[40] R. Mei, L.-S. Luo, W. Shyy, An accurate curved boundary treatment in the lattice Boltzmann method, J. Comput. Phys. 155 (2) (1999) 307–330.
[41] R. Mei, W. Shyy, D. Yu, L.-S. Luo, Lattice Boltzmann method for 3-D flows with curved boundary, J. Comput. Phys. 161 (2) (2000) 680–699.
[42] B. Wen, C. Zhang, Y. Tu, C. Wang, H. Fang, Galilean invariant fluid–solid interfacial dynamics in lattice Boltzmann simulations, J. Comput. Phys. 266 (2014) 161–170.
[43] P. Lallemand, L.-S. Luo, Lattice Boltzmann method for moving boundaries, J. Comput. Phys. 184 (2) (2003) 406–421.
[44] G. Zhao-Li, Z. Chu-Guang, S. Bao-Chang, Non-equilibrium extrapolation method for velocity and pressure boundary conditions in the lattice Boltzmann method, Chin. Phys. 11 (4) (2002) 366, URL http://stacks.iop.org/1009-1963/11/i=4/a=310.
[45] A. Caiazzo, Analysis of lattice Boltzmann nodes initialisation in moving boundary problems, Prog. Comput. Fluid Dyn. 8 (1–4) (2008) 3–10.
[46] M.A.A. Spaid, F.R. Phelan, Lattice Boltzmann methods for modeling microscale flow in fibrous porous media, Phys. Fluids 9 (9) (1997) 2468–2474, http://dx.doi.org/10.1063/1.869392.
[47] A. Kupershtokh, New method of incorporating a body force term into the lattice Boltzmann equation, in: Proc. 5th International EHD Workshop, University of Poitiers, Poitiers, France, 2004, pp. 241–246.
[48] D. Noble, J. Torczynski, A lattice-Boltzmann method for partially saturated computational cells, Internat. J. Modern Phys. C 9 (08) (1998) 1189–1201.
[49] D.J. Holdych, Lattice Boltzmann Methods for Diffuse and Mobile Interfaces (Ph.D. thesis), University of Illinois at Urbana-Champaign, 2003.
[50] D. Owen, C. Leonardi, Y. Feng, An efficient framework for fluid–structure interaction using the lattice Boltzmann method and immersed moving boundaries, Internat. J. Numer. Methods Engrg. 87 (1–5) (2011) 66–95.
[51] S. Galindo-Torres, A coupled discrete element lattice Boltzmann method for the simulation of fluid–solid interaction with particles of general shapes, Comput. Methods Appl. Mech. Engrg. 265 (2013) 107–119.
[52] J. Latt, B. Chopard, O. Malaspinas, M. Deville, A. Michler, Straight velocity boundaries in the lattice Boltzmann method, Phys. Rev. E 77 (2008) 056703, http://dx.doi.org/10.1103/PhysRevE.77.056703, URL https://link.aps.org/doi/10.1103/PhysRevE.77.056703.
[53] R.S. Maier, R.S. Bernard, D.W. Grunau, Boundary conditions for the lattice Boltzmann method, Phys. Fluids 8 (7) (1996) 1788–1801.

[54] A. Placzek, J.-F. Sigrist, A. Hamdouni, Numerical simulation of an oscillating cylinder in a cross-flow at low Reynolds number: Forced and free oscillations, Comput. & Fluids 38 (1) (2009) 80–100.
[55] M.S. Guerouache, Etude Numerique de l'Instabilite de Benard-Karman Derriere un Cylindre Fixe ou en Mouvement Periodique. Dynamique de l'Ecoulement et Advection Chaotique (Ph.D. thesis), Nantes, 2000.
[56] S. Succi, The Lattice Boltzmann Equation: For Fluid Dynamics and beyond, Oxford university press, 2001.
[57] F. Saltara, A. Neto, J. Lopez, et al., 3D CFD simulation of vortex-induced vibration of cylinder, Int. J. Offshore Polar Eng. 21 (03) (2011).
[58] A. Placzek, J.-F. Sigrist, A. Hamdouni, Numerical simulation of vortex shedding past a circular cylinder in a cross-flow at low Reynolds number with finite volume technique: Part 2—flow-induced vibration, in: ASME 2007 Pressure Vessels and Piping Conference, American Society of Mechanical Engineers, 2007, pp. 21–30.
[59] D. Shiels, A. Leonard, A. Roshko, Flow-induced vibration of a circular cylinder at limiting structural parameters, J. Fluids Struct. 15 (1) (2001) 3–21.
[60] P. Stansby, A. Slaouti, Simulation of vortex shedding including blockage by the random-vortex and other methods, Internat. J. Numer. Methods Fluids 17 (11) (1993) 1003–1013.
[61] P. Anagnostopoulos, Numerical investigation of response and wake characteristics of a vortex-excited cylinder in a uniform stream, J. Fluids Struct. 8 (4) (1994) 367–390.
[62] R.D. Henderson, Details of the drag curve near the onset of vortex shedding, Phys. Fluids 7 (9) (1995) 2102–2104.
[63] C. Zhou, R. So, K. Lam, Vortex-induced vibrations of an elastic circular cylinder, J. Fluids Struct. 13 (2) (1999) 165–189.
[64] M. Nobari, H. Naderan, A numerical study of flow past a cylinder with cross flow and inline oscillation, Comput. & Fluids 35 (4) (2006) 393–415.

Glossary

The following abbreviations are used in this manuscript.

BOUZIDI: Bouzidi boundary
CLI: central linear interpolation
EOC: experimental order of convergence
EPSILON: epsilon boundary layer algorithm
EQ: equilibrium refill algorithm
EXTRA: normal extrapolation refill algorithm
FH: Filippova and Hänel scheme
HLBM: homogenized lattice Boltzmann method
HP: high-pass filter
IBM: immersed boundary methods
LBE: lattice Boltzmann equation
LBM: lattice Boltzmann method
MBM: moving boundary methods
NEQ: non-equilibrium refill algorithm
POLYGON: polygon approximation algorithm
PS: power spectrum
PSM: partially saturated methods
PSM$_{\mathrm{M2}}$: partially saturated method B2M2
PSM$_{\mathrm{M3}}$: partially saturated method B2M3
rms: root mean square
SS: supersampling algorithm
VIV: vortex-induced vibrations
YU: Yu interpolation scheme

7

Fluid-Structure Interaction of a Coriolis Mass Flowmeter

This chapter was published in the following preprint:

M. Haussmann, P. Reinshaus, S. Simonis, H. Nirschl and M. J. Krause
Fluid-Structure Interaction Simulation of a Coriolis Mass Flowmeter using a Lattice Boltzmann Method
arXiv physics.comp-ph, 2005.04070 (2020)
https://arxiv.org/abs/2005.04070

My contribution according to the contributor role taxonomy system [14] included conceptualization, methodology, software, validation, formal analysis, investigation, data curation, writing – original draft, visualization and project administration.

FLUID-STRUCTURE INTERACTION SIMULATION OF A CORIOLIS MASS FLOWMETER USING A LATTICE BOLTZMANN METHOD

Marc Haussmann
Lattice Boltzmann Research Group
Karlsruhe Institute of Technology
Karlsruhe 76131, Germany
`marc.haussmann@kit.edu`

Peter Reinshaus
ROTA YOKOGAWA GmbH & Co. KG
Wehr 79664, Germany
`peter.reinshaus@de.yokogawa.com`

Stephan Simonis
Lattice Boltzmann Research Group
Karlsruhe Institute of Technology
Karlsruhe 76131, Germany
`stephan.simonis@kit.edu`

Hermann Nirschl
Department of Mechanical Engineering
Karlsruhe Institute of Technology
Karlsruhe 76131, Germany
`hermann.nirschl@kit.edu`

Mathias J. Krause
Lattice Boltzmann Research Group
Karlsruhe Institute of Technology
Karlsruhe 76131, Germany
`mathias.krause@kit.edu`

May 11, 2020

ABSTRACT

In this paper we use a fluid-structure interaction (FSI) approach to simulate a Coriolis mass flowmeter (CMF). The fluid dynamics are calculated by the open source framework OpenLB, based on the lattice Boltzmann method (LBM). For the structural dynamics we employ the open source software Elmer, an implementation of the finite element method (FEM). A staggered coupling approach between the two software packages is presented. The finite element mesh is created by the mesh generator Gmsh to ensure a complete open source workflow. The Eigenmodes of the CMF, which are calculated by modal analysis are compared with measurement data. Using the estimated excitation frequency, a fully coupled, partitioned, FSI simulation is applied to simulate the phase shift of the investigated CMF design. The calculated phaseshift values are in good agreement to the measurement data and verify the suitability of the model to numerically describe the working principle of a CMF.

Keywords OpenLB · Elmer · Open source · FSI · LBM

1 Introduction

The exact measurement of mass flow of fluids is important in many branches of technology, for example chemical, oil and gas industry. It is needed to control processes and ensure safety, filling batches, inventory and others. The Coriolis mass flow meter (CMF) is an accurate instrument, which is becoming increasingly important in various applications [1]. It consists of one or multiple measuring tubes that are stimulated to vibrate by an electromagnetic pulse generator. The fluid to be investigated is directed through the tubes. Due to inertia, the Coriolis force causes a phase shift of the vibration, which is detected by sensors on both ends of the system. As the mass flow of the conveyed fluid is proportional to the Coriolis force, it can be determined directly.

CMFs have been widely described by analytical and structural models [2, 3, 4, 5, 6, 7]. These models have helped to understand the fundamental principle of CMF devices. Nevertheless, the influence of the fluid was greatly simplified and the practical operation could not be described completely. Therefore, fluid-structure interaction (FSI) models were developed to realize the operating principle, which means that the fluid motion is affected by the measuring pipe oscillation and the pipe motion in turn by the hydrodynamic forces. In recent years, iterative two-way FSI models, which consist of a separated computational fluid dynamics (CFD) solver and a computational structural mechanics (CSM) solver, were applied to simulate CMF.

Bobovnik et al. [8] used two different solvers to simulate a straight tube. Commercially available finite volume code for three dimensional turbulent fluid flow and finite element code for a shell structure were coupled. Five different tube lengths were studied simulating free tube vibration. The results for phase shift and frequency were similar to an analytical Flügge shell and potential flow model. In 2008, Mole et al. [9] extended the three dimensional numerical model of Bobovnik et al. [8] to deal with forced vibration. The study comprises the investigation of meter sensitivity at different Reynolds numbers. A maximum decrease of $0.4\,\%$ was observed for the lowest Reynolds number. This deviation is known as the low Reynolds number effect. The same numerical model was used by Bobovnik et al. [10] to study the influence of the design parameters on the installation effects of a CMF. Installation effects are measured as change of meter sensitivities from fully developed to disturbed fluid flow. Considering a single straight tube the errors vary with sensor positions and decrease with increasing tube length. In contrast, Kumar [11] claimed that a CMF is not sensitive to flow profiles. The FSI model of ANSYS-CFX was used to consider a straight single tube. The results were quite similar for the shorter tube lengths in comparison to previous studies [8]. In contrast, the longer tubes showed a higher deviation, which was attributed to the different resolution. By changing the viscosity, the Reynolds number was varied and the deviation in meter sensitivity could be captured. It was found that at low Reynolds numbers the oscillating viscous fluid forces become relatively strong and interact with the oscillating Coriolis force, which changes the measurement results. To further investigate the effect of the Reynolds numbers, Kumar and Anklin [12] investigated a curved double tube CMF with an FSI simulation. The meter deviation at low Reynolds numbers were found in good agreement to measurement data. The low Reynolds number effect was indicated as correctable, if the viscosity of the examined fluid is known. Also Rongmo and Jian [13] used the ANSYS-CFX FSI module to study the low Reynolds number effect in a U-tube CMF. They assumed that arising deviations may be due to those different damping factors. Damping influences the natural frequency of the tube and was expected to change the meter sensitivity.

The aforementioned studies employ traditional discretization methods like the finite volume method (FVM) for the fluid solver. Meanwhile, alternative approaches, such as the lattice Boltzmann method (LBM), have received increasing attention. Its highly efficient parallel algorithm [14, 15] and the applicability to a wide range of flow phenomena, e.g. flows in complex geometry [16, 17] or turbulent flows [18, 19] offer a high potential.

One of the first approaches that couple LBM to a structural solver can be found by Scholz et al. [20]. They propose an anisotropic p-adaptive method for elastodynamic problems and show a higher convergence rate in comparison to a uniform p-version. Especially, the load transfer between the fluid and structural mesh were discussed. Geller et al. [21] used a partitioned approach to address the famous two-dimensional FSI benchmark case proposed by Turek and Hron [22]. The proposed coupling approach by Geller et al. [21] leads to consistent quantitative result. A further study to validate an LBM solver coupled to a p-FEM solver with the Turek and Hron [22] benchmark was published by Kollmannsberger et al. [23]. The staggered coupling was shown to be sufficient for simulating the reference case due to the weaker impact of the additional mass effect at small time steps. In contrast, Li et al. [24] claimed that the added mass effect has a major influence on accuracy and stability. They shown that the use of a non-staggered coupling approach based on subiterations reduce the effect of artificially added mass. Based on the previously mentioned studies [23, 21, 20], Geller et al. [25] extended the developed FSI approach to address three dimensional benchmark problems.

In contrast, this paper aims to demonstrate the feasibility of a complete open source FSI workflow to simulate a CMF. Therefore, OpenLB [26, 27], an open source implementation of LBM, is coupled to the open source FEM framework Elmer [28]. The implemented coupling procedure uses a staggered approach. A modal analysis of the CMF geometry is executed to extract the excitation frequency. The obtained excitation frequency is applied in a frequency response test to evaluate the transient structural setting. The partitioned FSI approach is used to calculate the phase shift. Both the Eigenfrequencies and the phase shift values are compared to measurement data. The evaluation and validation of a complex engineering problem with a partitioned FSI approach using LBM is a novelty. As a further highlight the new FSI workflow is built on open source frameworks to ensure additional adaptions in the coupling interface.

The paper is structured as follows, Section 2 introduces the applied FSI approach covering the fluid and structural models. In Section 3 the CMF test case is depicted in detail. The related modal analysis and the subsequent phase shift calculation results, using the FSI approach, are presented and compared to the measurement data in Section 4. Finally, Section 5 summarizes the findings and draws a conclusion.

2 Methodology

Firstly, the governing equations for the fluid domain presented. Afterwards the LBM and the moving boundary approach is introduced. Next, the Navier–Cauchy equation and the applied solution routine for the structural domain are shown. Finally, the FSI approach to coupling the structural an the fluid domain is presented, including the coupling conditions and implementation details.

2.1 Fluid Domain

2.1.1 Navier–Stokes Equations

The incompressible Navier–Stokes equations consist of the continuity equation

$$\frac{\partial u_\alpha^f}{\partial x_\alpha} = 0, \tag{1}$$

and the momentum equation, which reads

$$\frac{\partial u^f_\alpha}{\partial t} + \frac{\partial u^f_\alpha u^f_\beta}{\partial x_\beta} = \frac{\partial T^f_{\alpha\beta}}{\partial x_\beta} - \frac{1}{\rho^f}\frac{\partial p}{x_\alpha}, \tag{2}$$

where Greek indices obey the Einstein notation, u^f_α is the fluid velocity, p is the pressure field, $T^f_{\alpha\beta}$ is the fluid stress tensor and ρ^f is the fluid density. Assuming a Newtonian fluid, the fluid stress tensor is given by

$$T^f_{\alpha\beta} = \nu^f \left(\frac{\partial u^f_\alpha}{\partial x_\beta} + \frac{\partial u^f_\beta}{\partial x_\alpha} \right), \tag{3}$$

where ν^f is the kinematic viscosity.

2.1.2 Lattice Boltzmann Method

The discretization of the kinetic Boltzmann equation on an equidistant Cartesian grid yields a finite number of particle distribution functions f_i . The resulting lattice is defined by d dimensions and q lattice velocities $\boldsymbol{c}_i$, $i = 0, 1, ..., q-1$. In the present work the $D3Q19$ velocity set is applied, which is given by

$$\boldsymbol{c}_i = \begin{cases} (0,0,0), & i = 0, \\ (\pm1,0,0),\ (0,\pm1,0),\ (0,0,\pm1), & i = 1,2,...,6, \\ (\pm1,\pm1,0),\ (\pm1,0,\pm1),\ (0,\pm1,\pm1), & i = 7,8,...,18. \end{cases} \tag{4}$$

The choice of the collision operator is justified by the higher computation performance and the lower memory demand in the used LBM implementation. The violation of the rotational invariance [29] in comparison to $D3Q27$ can be neglected in the laminar flow regime.

The lattice Boltzmann equation without external forces is given by

$$f_i\left(\boldsymbol{x}^{\mathrm{LB}} + \boldsymbol{c}_i, t^{\mathrm{LB}} + 1\right) = f_i\left(\boldsymbol{x}^{\mathrm{LB}}, t^{\mathrm{LB}}\right) + \Omega_i, \tag{5}$$

where f_i is the particle distribution function at discrete lattice position $\boldsymbol{x}^{\mathrm{LB}}$ and time step t^{LB}. The collision operator Ω_i is implemented by a single-relaxation time model proposed by Bhatnagar, Gross and Krook [30]. It can be defined as

$$\Omega_i = -\frac{1}{\tau}\left(f_i(t^{\mathrm{LB}}, \boldsymbol{x}^{\mathrm{LB}}) - f_i^{eq}(\rho^{\mathrm{LB}}, \boldsymbol{u}^{\mathrm{LB}})\right), \tag{6}$$

where τ is the relaxation time towards the discrete particle distribution function at equilibrium state f_i^{eq}, ρ^{LB} is the lattice density and $\boldsymbol{u}^{\mathrm{LB}}$ the velocity field. Hence, the collision operator conserve mass and momentum. The particle distribution function equilibrium f_i^{eq} is described by a low Mach number truncated Maxwell-Boltzmann distribution

$$f_i^{eq}\left(\rho^{\mathrm{LB}}, \boldsymbol{u}^{\mathrm{LB}}\right) = \rho^{\mathrm{LB}}\omega_i \left[1 + \frac{c_{i\alpha}u_\alpha^{\mathrm{LB}}}{c_s^2} + \frac{u_\alpha^{\mathrm{LB}}u_\beta^{\mathrm{LB}}(c_{i\alpha}c_{i\beta} - c_s^2\delta_{\alpha\beta})}{2c_s^4}\right], \tag{7}$$

where ω_i are the lattice weights obtained by the Gauss-Hermite quadrature [31, 32], $c_s = 1/\sqrt{3}$ is the speed of sound of the lattice and $\delta_{\alpha\beta}$ is the Kronecker delta.

The discrete moments of the particle distribution functions f_i result in macroscopic flow quantities. The density ρ^{LB}, the momentum $\rho^{\mathrm{LB}}\boldsymbol{u}^{\mathrm{LB}}$ and the momentum flux $\boldsymbol{\Pi}$ are respectively obtained by the zeroth, first and second moments, which are given by

$$\rho^{\mathrm{LB}} = \sum_{i=0}^{q-1} f_i\ , \tag{8}$$

$$\rho^{\mathrm{LB}}\boldsymbol{u}^{\mathrm{LB}} = \sum_{i=0}^{q-1} \boldsymbol{c}_i f_i, \tag{9}$$

$$\boldsymbol{\Pi}_{\alpha\beta} = \sum_{i=0}^{q-1} c_{i\alpha} c_{i\beta} f_i \ . \tag{10}$$

The relaxation time τ is coupled with the lattice kinematic viscosity ν^{LB} through

$$\nu^{\mathrm{LB}} = c_s^2 \left(\tau - 0.5\right). \tag{11}$$

Taking a simplified isothermal equation of state into account, the lattice pressure is related to the lattice density by

$$p^{\mathrm{LB}} = c_s^2 \rho^{\mathrm{LB}}. \tag{12}$$

The lattice Mach number $\mathrm{Ma}^{\mathrm{LB}}$ is written as

$$\mathrm{Ma}^{\mathrm{LB}} = \frac{u_{char}^{\mathrm{LB}}}{c_s}, \tag{13}$$

where u_{char}^{LB} is the characteristic lattice velocity. In the incompressible limit $(\mathrm{Ma}^{\mathrm{LB}} \rightarrow 0)$, the incompressible Navier–Stokes equations (see Eqs. (1) and (2)) are recovered.

Finally, the lattice Boltzmann algorithm is parted into two steps: local collision step and subsequent streaming step. The local collision step is represented by the right-hand side of Eq. (5) and the streaming step is associated with the left-hand side of Eq. (5).

2.1.3 Moving Boundary Methods

A fluid-solid interface is required for the simulation of FSI. The lattice Boltzmann method typically uses three groups of approaches to describe this type of interface, namely the partially saturated methods [33, 34], the immersed boundary methods [35, 36, 37] and the moving boundary methods [38, 39, 40]. In the present study, the latter type of interface description is applied.

A moving fluid-solid interface inside the fluid domain can be described by the position of its boundary, which changes over time. The current boundary position indicates fluid and solid nodes. If a former solid becomes a fluid node, a refill algorithm is applied to reconstruct the unknown particle distribution functions. Hence, moving boundary methods are conceptually parted into a velocity boundary formulation and a refill algorithm. For a better comprehension, the introduced index conventions are displayed in Fig. 1. The index b is related to the boundary node positioned inside the solid domain. In direction $\boldsymbol{c}_i$ the wall is intersected at $\boldsymbol{x}_w^{\mathrm{LB}}$. The locations $\boldsymbol{x}_f^{\mathrm{LB}}$, $\boldsymbol{x}_{ff}$ and $\boldsymbol{x}_{fff}$ denote the corresponding fluid nodes in this direction. The distance between $\boldsymbol{x}_w$ and $\boldsymbol{x}_f$ is given by the normalized distance q, which is calculated by

$$q = \frac{|\boldsymbol{x}_f^{\mathrm{LB}} - \boldsymbol{x}_w^{\mathrm{LB}}|}{|\boldsymbol{x}_f^{\mathrm{LB}} - \boldsymbol{x}_b^{\mathrm{LB}}|}. \tag{14}$$

Position x_{new}^{LB} indicates nodes, where a refill algorithm is necessary. The nodes in discrete normal direction $\boldsymbol{c}_n$ are identified by $\boldsymbol{x}_n^{\mathrm{LB}}$, $\boldsymbol{x}_{nn}^{\mathrm{LB}}$ and $\boldsymbol{x}_{nnn}^{\mathrm{LB}}$. This subscript convention is also used for velocity $\boldsymbol{u}^{\mathrm{LB}}$ and density ρ^{LB}.

The present work uses the curved boundary condition proposed by Bouzidi et al. [41], which represents an extension of a half-way bounce back boundary scheme. Thereby a linear interpolation

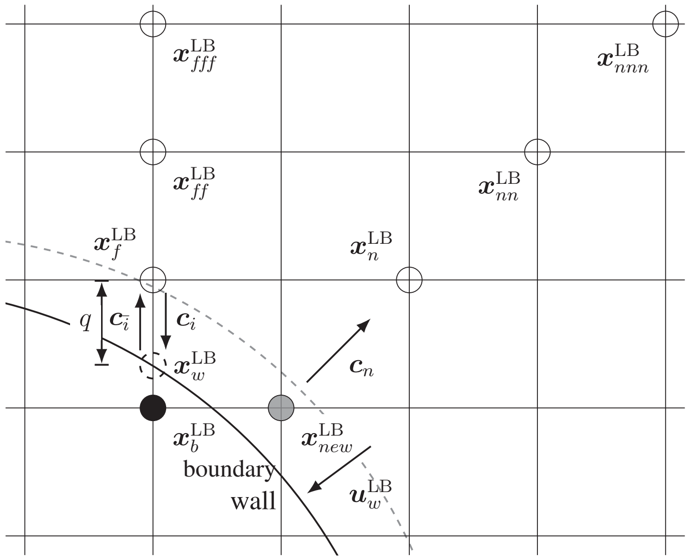

Figure 1: Illustration of the used indexing convention.

is utilized to take the distance to the boundary into account for increased accuracy. The unknown populations $f_{\bar{i}}(\boldsymbol{x}_f^{\mathrm{LB}}, t^{\mathrm{LB}}+1)$ after the streaming step are calculated by

$$f_{\bar{i}}(\boldsymbol{x}_f^{\mathrm{LB}}, t^{\mathrm{LB}}+1) = \begin{cases} 2q f_i(\boldsymbol{x}_b^{\mathrm{LB}}, t^{\mathrm{LB}}+1) + (1-2q) f_i(\boldsymbol{x}_f^{\mathrm{LB}}, t^{\mathrm{LB}}+1) - 2\frac{w_i}{c_s^2}\boldsymbol{c}_i \cdot \boldsymbol{u}_w^{\mathrm{LB}}(t) & \text{for } q < \frac{1}{2}, \\ \frac{1}{2q} f_i(\boldsymbol{x}_b, t^{\mathrm{LB}}+1) + \frac{2q-1}{2q} f_{\bar{i}}(\boldsymbol{x}_{ff}^{\mathrm{LB}}, t^{\mathrm{LB}}+1) - \frac{1}{q}\frac{w_i}{c_s^2}\boldsymbol{c}_i \cdot \boldsymbol{u}_w^{\mathrm{LB}}(t) & \text{for } q \geq \frac{1}{2}, \end{cases} \tag{15}$$

where index $\bar{i}$ denotes a quantity in the opposite direction of the one with index i. The half-way bounce back condition is recovered for $q = 1/2$.

For the refill algorithm, a second order extrapolation scheme can be found in [40]

$$f_i(\boldsymbol{x}_{new}^{\mathrm{LB}}, t^{\mathrm{LB}}) = 3 f_i(\boldsymbol{x}_n^{\mathrm{LB}}, t^{\mathrm{LB}}) - 3 f_i(\boldsymbol{x}_{nn}^{\mathrm{LB}}, t^{\mathrm{LB}}) + f_i(\boldsymbol{x}_{nnn}^{\mathrm{LB}}, t^{\mathrm{LB}}). \tag{16}$$

Hereby the particle distributions $f_i(\boldsymbol{x}_{new}^{\mathrm{LB}}, t^{\mathrm{LB}})$ are extrapolated by the particle distribution functions in discrete normal direction $\boldsymbol{c}_n$.

A further necessary step for FSI is the calculation of the hydrodynamic forces that act on the interface. Therefore, a Galilean invariant momentum exchange approach [42] is used. The boundary force that acts on a solid node $\boldsymbol{x}_b^{\mathrm{LB}}$ can be calculated by

$$\boldsymbol{F}^{\mathrm{LB}}(\boldsymbol{x}_b^{\mathrm{LB}}, t^{\mathrm{LB}}) = \sum_{i \in L} \left[(\boldsymbol{c}_i - \boldsymbol{u}_w^{\mathrm{LB}}(t)) f_i(\boldsymbol{x}_b^{\mathrm{LB}}, t+1) - (\boldsymbol{c}_{\bar{i}} - \boldsymbol{u}_w^{\mathrm{LB}}(t)) f_{\bar{i}}(\boldsymbol{x}_f^{\mathrm{LB}}, t^{\mathrm{LB}}+1) \right], \tag{17}$$

where L is the set of fluid-solid links. This formulation is suitable for the precise description of the boundary force of moving fluid-solid interfaces and avoids the disadvantages of a conventional momentum exchange calculation [43, 42].

2.2 Structural Domain

2.2.1 Navier–Cauchy Equation

The present work uses the Navier–Cauchy equation to describe the structural motion. Therefore, the structral moition is assumed to be linear elastic. The equation of motion for a linear elastic structure in differential form reads

$$\rho^s \frac{\partial^2 \Phi_\beta}{\partial t^2} = \frac{\partial T^s_{\alpha\beta}}{\partial x_\alpha} + \rho^s F^s_\beta, \tag{18}$$

where Φ_β is the structural displacement, ρ^s is the solid density, F^s_β is the body-force acting on the structure. Thereby, the Cauchy stress tensor $T^s_{\alpha\beta}$ can be written as

$$T^s_{\alpha\beta} = \mu^s \left(\frac{\partial \Phi_\alpha}{\partial x_\beta} + \frac{\partial \Phi_\beta}{\partial x_\alpha} \right) + \lambda^s \frac{\partial \Phi_\gamma}{\partial x_\gamma} \delta_{\alpha\beta}, \tag{19}$$

where μ^s and λ^s represents the first and second Lamé constants. Both Lamé constants can be defined by Young's modulus E and the Poisson's ratio ν^s as

$$\mu^s = \frac{E}{2\left((1+\nu^s\right)} \tag{20}$$

and

$$\lambda^s = \frac{\nu^s E}{\left(1+\nu^s\right)\left(1-2\nu^s\right)}. \tag{21}$$

2.2.2 Direct Methods

This linear Navier–Cauchy equation can be solved by a direct method. Therefore, the Elmer solver module is used, which provides the LAPACK collection to address band matrices. Direct methods are known for their robustness, but their scaling of order n^3 leads to a high memory demand. Nevertheless, the present work uses a direct method solution procedure due the stability advantages. Further information can be found, e.g. in the book of Larson and Bengzon [44].

2.3 Fluid-Structure Interaction

2.3.1 Coupling Conditions

The FSI problem has to fulfill certain coupling conditions on the interface $\mathcal{I}(t)$, based on physical principles [45].

Kinematic condition The kinematic condition describes the continuity of the velocities on the interface, i.e.

$$\boldsymbol{u}^f(\boldsymbol{x},t) = \mathbf{u}^s(\boldsymbol{x},t) \quad \text{on}\, \mathcal{I}(t). \tag{22}$$

The use of Lagrangian and Eulerian coordinate systems for the different solvers requires a mapping procedure.

Dynamic condition The dynamic condition ensures that the forces that act on the interface are balanced due to Newton's third law 'Actio est Reactio'. The coupling condition reads

$$\boldsymbol{F}^f(\boldsymbol{x},t) = -\boldsymbol{F}^s(\boldsymbol{x},t) \quad \text{on}\, \mathcal{I}(t). \tag{23}$$

Due to the different coordinate systems, a mapping procedure is also required here.

Geometric condition The third coupling condition is the geometric condition. The condition ensures that the domain is continuous at the interface, i.e.

$$\boldsymbol{x}^f(t) = \boldsymbol{x}^s(t) \quad \text{on}\, \mathcal{I}(t). \tag{24}$$

Hence, the fluid and solid domains cannot overlap or separate at the interface.

2.3.2 Segregated Approaches

There are several mathematical and technical problems involved in the analysis of FSI. In most cases, two different subsystems are used for the governing equations. Even for one subsystem the uniqueness of the solution can be shown only locally in time. One fundamental problem is the different nature of the partial differential equations. Incompressible Navier–Stokes are of parabolic type, but the structural equation is of hyperbolic type. Therefore, the different coupling conditions are difficult to ensure on the interface.

Segregated approaches are typically used to address FSI. The idea is to combine two different solvers, where each solver is specialized to solve either a fluid or a structural problem. The coupling is then fulfilled by an outer control instance. Due the maturity of each solver, this approach is often a quick possibility to treat complex application problems. A common segregated two-way coupled FSI workflow is illustrated in Fig. 2. The CFD solver on the left side of the sketch, numerically solves the Navier–Stokes equations on the fluid domain. The solution of the fluid field allows to extract the hydrodynamic forces at each grid point in the solid fluid interface that act on the solid. This force information is transferred to the CSM solver by an interface. The CSM solver (right side of the sketch) uses the transferred force information as a boundary condition in the structural simulation. The result of the numerical solution of the Navier–Cauchy equation provides the deformed fluid solid interface and the according displacement velocity on each grid point. Next, the information is transferred again by the interface operation to the fluid solver. The fluid solver in turn, uses the deformed interface and the displacement velocity as a boundary condition. This whole process is executed in each coupling period, until a certain time or convergence criterion is fulfilled.

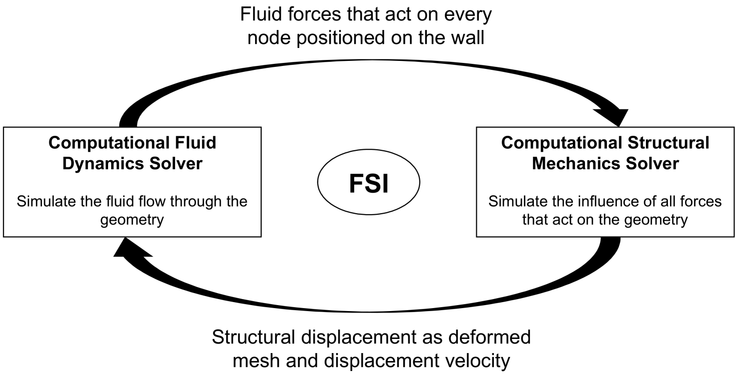

Figure 2: Segregated two-way coupled fluid structure interaction workflow.

2.3.3 Implementation

The FSI process which uses Elmer and OpenLB is depicted in Fig. 3. Note that a data based workflow is used to exchange information between the applications. Currently, the interface allows parallel execution of OpenLB, while Elmer is running in serial mode. A detailed explanation of each step in the workflow is given in the following procedure, which is executed for every coupling step.

1. The OpenLB instance calculates the hydrodynamic forces acting on the boundary for each solid node according to Eq. (17).

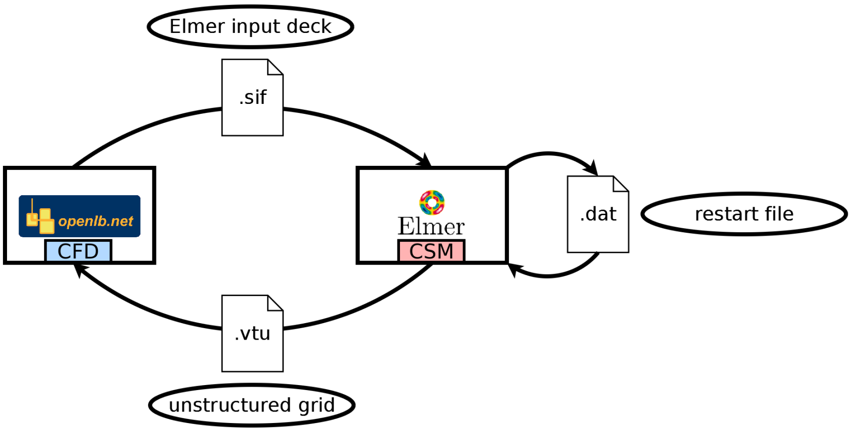

Figure 3: Fluid structure interaction workflow using OpenLB and Elmer.

2. The hydrodynamic forces are communicated and collected from each worker to the master process.
3. The master process maps the collected boundary forces to the finite element grid by integrating the force on each finite element mesh point.
4. The mapped boundary forces are written into an Elmer input deck file (.sif).
5. Elmer is restarted by the master process using the input deck file (.sif) and a related restart file (.dat).
6. The Elmer instance is closed after the displacement velocity and the deformed mesh is written to disk as an unstructured mesh file (.vtu) and a new Elmer restart file (.dat) is created.
7. The master process reads the mesh file (.vtu) and uses the built-in OpenLB voxelizer, which decides whether a point is outside or inside the fluid domain and allows the later distance calculation.
8. The master process maps the displacement velocity of the FEM grid to the LBM link intersection points $\boldsymbol{x}_w$ by a linear interpolation procedure and distributes the information to each worker process.
9. The OpenLB instance reconstructs the particle distribution functions for the fresh nodes by using the extrapolation refill algorithm (see Eq. (16)).
10. The collide and stream algorithm is executed (see Eq. (5)).
11. After the streaming step is executed, the unknown particle distribution function are calculated by the curved boundary approach using the mapped displacement velocity (see Eq. (15)).

3 Setup of the Coriolis Mass Flowmeter Test Case

The investigated CMF geometry is depicted in Figure 4. The CMF geometry consists of a flow divider that distributes the incoming mass flow in two U-shaped measuring pipes. After the flow passed both measuring pipes, a flow combiner unite the streams. The oscillation of the measuring pipe is initialized by an electromagnetic exciter at the top of both measuring pipes. The resulting oscillation signal is captured at sensor position 1 and 2. In addition, two node plates are used to damp the oscillation at the end of the pipes. The structural and fluid properties used in the simulations are listed in Table 1 unless otherwise specified. The structural properties correspond to steel. The fluid density ρ^f is chosen according to the density of water, but the dynamic viscosity η^f is greatly increased to ensure a laminar flow.

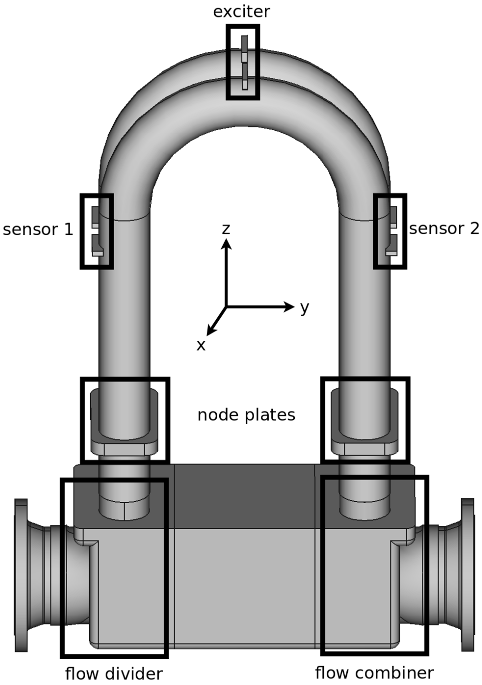

Figure 4: Geometry representation and description of the investigated CMF without outer housing.

Table 1: Structural and fluid properties.

Structural properties		Fluid properties	
ρ^s	$7870\,\mathrm{kg/m^3}$	ρ^f	$998\,\mathrm{kg/m^3}$
E	$210\,\mathrm{GPa}$	η^f	$0.207\,\mathrm{Pas}$
ν^s	0.3		

3.1 Boundary Conditions and Initial Conditions

3.1.1 Structural Domain

For the structural simulation setting, a zero displacement condition at the flanges is used, i.e.

$$\mathbf{\Phi}_{flanges} = \mathbf{0}\,\mathrm{m}. \tag{25}$$

Figure 5 indicates the flange faces in green, where this boundary condition is set. At the sensor

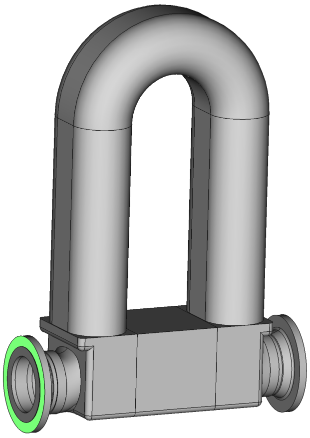

Figure 5: Boundary faces at the flanges (green).

exciter position an excitation load is applied

$$F_x = F_{x,max} \sin(2\pi f_{exc} t) \text{ for } t < \frac{1}{f_{exc}}, \tag{26}$$

where $F_{x,max} = 100\,N$ and f_{exc} is the excitation frequency. The force is only acting in the first period to excite the Eigenmode.

3.1.2 Fluid Domain

A Dirichlet velocity condition is applied as a boundary condition for the fluid domain at the inlet

$$u^f_{y,inlet} = \left[1 - \left(\frac{r}{R}\right)^2\right] u^f_{y,max}, \tag{27}$$

where R is the inlet radius and $u_{y,max}$ is the maximum velocity calculated according the used mass flow. This Poiseuille profile assumes a fully developed laminar pipe flow which is justified by an inlet Reynolds number of $\mathrm{Re}_{inlet} < 337$. The pressure on the outlet is set by a Dirichlet condition to

$$p_{outlet} = 0\,\mathrm{Pa}. \tag{28}$$

As FSI is known to be time-consuming it is recommended to start the simulation with a converged flow field. Therefore, the fluid geometry is simulated without the structural simulation to initialize the flow field. On the measuring pipe walls no-slip boundary conditions are set. The flow velocity at the inflow is increased at the inlet for 5 seconds until the desired mass flow is reached. This initialization procedure prevents occurring pressure waves due to high gradients and adjusts the non-equilibrium parts of the particle distribution functions.

3.1.3 Coupling Conditions

On each grid point at the interface $\mathcal{I}(t)$ of fluid and solid, the mapped time dependent hydrodynamic force is applied via

$$\boldsymbol{F}^s(t) = \boldsymbol{F}^f(t) \quad \text{on } \mathcal{I}(t). \tag{29}$$

Thus the dynamic coupling condition is fulfilled. The velocity on the fluid structure interface is given by

$$\boldsymbol{u}^f(t) = \boldsymbol{u}^s(t + \Delta t_c) \quad \text{on } \mathcal{I}(t + \Delta t_c), \tag{30}$$

where Δt_c is the coupling period. The occurring time shift is related to the staggered coupling scheme (see Sec. 2.3.2). The geometric condition of the interface is also influenced by the coupling period and is written as

$$\boldsymbol{x}^f(t) = \boldsymbol{x}^s(t + \Delta t_c) \quad \text{on } \mathcal{I}(t + \Delta t_c). \tag{31}$$

3.2 Mesh Generation

3.2.1 Structural Domain

The computational mesh for the structural simulation is generated by the open source FEM pre-processor Gmsh [46]. The mesh element is chosen according to the geometry pre-processor of OpenLB, because the extraction of a triangulated surface mesh out of tetrahedral volume mesh is straightforward. The choice of other mesh element shapes would lead to an additional triangulation step in every coupling period. In Table 2, the characteristic length scales of the FEM elements in the according regions are shown. Regions, where simulation results are extracted or high gradients may occur, are refined. Therefore, the sensor positions and the measuring pipes require small mesh elements. The maximal mesh element size is chosen with respect to the largest mesh element size that is used for the housing $\Delta x^s = 0.035\,\mathrm{m}$. The generated volume mesh in clip representation is depicted in Figure 6. The mesh contains 52624 nodes and 163164 elements. The five predefined regions support different refinement layers. This geometry adaptive mesh allows to reduce the amount of mesh points by consistent accuracy of the displacement signal at the sensor positions. The quality of the mesh was evaluated with the mesh criteria of Gmsh. Furthermore, the connection of critical mesh regions were checked, see Figure 7. Particularly in locations where elements are perpendicular to each other, defects may occur.

Table 2: Averaged characteristic length scales of the finite element mesh regions.

Region	Δx^s in m
Outer housing	0.035
Body	0.030
Sensors and exciter	0.005
Measuring pipes	0.010
Node plates	0.005

3.2.2 Fluid Domain

The meshing procedure for LBM is straightforward due to the equidistant uniform Cartesian mesh. The used discretization parameters for the two desired mass flows $20\,000\,\frac{\mathrm{kg}}{\mathrm{h}}$ and $40\,000\,\frac{\mathrm{kg}}{\mathrm{h}}$ are shown in Table 3. The resulting grid consists of 1.286 million grid cells. Figure 8 shows the voxelized measuring tubes at the beginning of the simulation. Additional two layers of solid cells cover the measuring pipes to allow the fluid-solid interface motion due to the pipe oscillation.

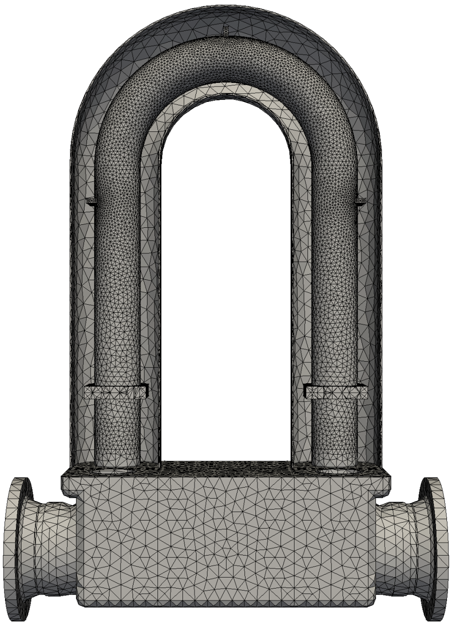

Figure 6: Clip representation of the volume mesh.

Table 3: LBM discretization parameters for the both investigated mass flows.

Mass flow in $\frac{\mathrm{kg}}{\mathrm{h}}$	Δx^f in m	Δt^f in s	$\mathrm{Ma}^{\mathrm{LB}}$
20 000	$4.056 \cdot 10^{-3}$	$1.177 \cdot 10^{-4}$	$8.660 \cdot 10^{-3}$
40 000	$4.056 \cdot 10^{-3}$	$5.885 \cdot 10^{-5}$	$8.660 \cdot 10^{-3}$

4 Results of the Coriolis Mass Flowmeter Test Case

After the mesh generation is completed, the Eigenfrequencies for the FEM mesh are calculated. The detection of the excitation frequency is a preliminary for the later phase shift calculation. Therefore, a modal analysis is performed with the structural solver Elmer.

4.1 Modal Analysis

The first modal analysis describes the condition for the measuring pipes filled with resting air. The structural parameters of steel are listed in Table 1. Due to the low density of air compared to steel, the additional mass of air can be neglected.

Using the zero displacement boundary condition (see Eq. (25)), the first ten Eigenfrequencies of the FEM grid are calculated. The resulting values are shown in Table 4. A closer look to each Eigenfrequency reveals the physical meaning. The searched excitation mode is found at mode number 2 and the Coriolis twist mode corresponds to mode number 8. The excitation mode is related to a parallel movement of the pipes towards and away from each other. On the contrary, the

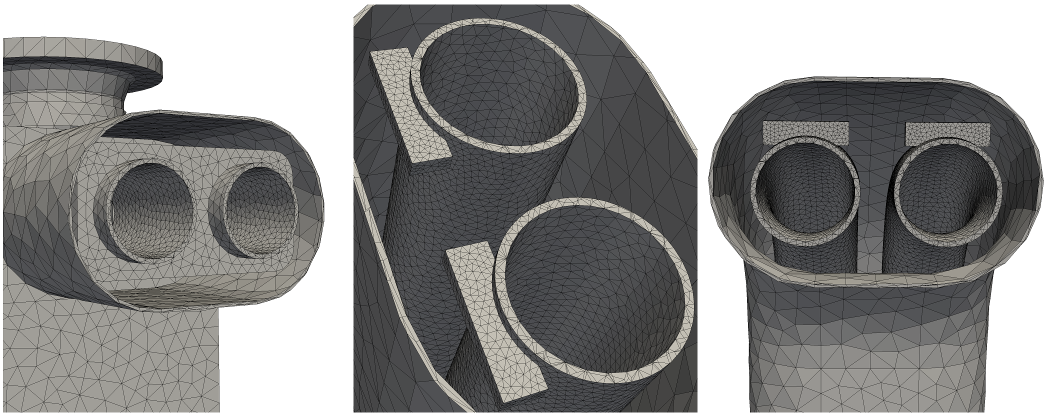

(a) Node plate – measuring pipes (b) Sensor – measuring pipes (c) Exciter – measuring pipes

Figure 7: Connection of the critical mesh regions.

Table 4: First ten Eigenfrequencies of the modal analysis and their physical meaning.

Mode	ω^2 in Hz^2	f in Hz	Physical meaning
1	$2.92 \cdot 10^5$	86.02	
2	$\mathbf{4.29 \cdot 10^5}$	**104.28**	**excitation mode**
3	$6.01 \cdot 10^5$	123.42	
4	$9.50 \cdot 10^5$	155.14	
5	$1.11 \cdot 10^6$	167.65	
6	$1.48 \cdot 10^6$	193.85	
7	$2.25 \cdot 10^6$	238.87	
8	$\mathbf{3.03 \cdot 10^6}$	**277.26**	**Coriolis twist mode**
9	$6.40 \cdot 10^6$	402.60	
10	$8.05 \cdot 10^6$	451.44	

Coriolis twist introduces an additional twist of the pipes. For a better illustration both modes are displayed in a front and top view in Figure 9. The next step is the test of the transient structural simulation. Two major aspects are investigated: on the one hand the stability of the transient settings are estimated and on the other hand the resonant behavior are tested. The used structural boundary conditions are described in Section 3.1.1. In the first case, an excitation frequency different from the Eigenfrequency is selected to $f_{exc} = 50\,\mathrm{Hz}$. In Figure 10, the structural response over time is plotted. It can be seen that the amplitude is strongly decreasing after the first period and no resonance is observable. This behavior was expected, because the excitation frequency and the Eigenfrequency are mismatched. Nevertheless, the transient simulation is stable over the entire simulation time. In the second configuration the excitation frequency is chosen with the Eigenfrequency to $f_{exc} = 104.28\,\mathrm{Hz}$. The displacement signal is depicted in Figure 11. The resonance is now clearly visible, which indicates that the results of the modal analysis are reliable and the transient simulation is also stable in the resonant case.

Additionally a further modal analysis is examined for water conveying tubes, which are used in the FSI case. Hereby, the additional mass of water cannot be neglected. The water filled tubes are approximated by a fictitious density of the tubes $\rho^s_{fictitious} = 12\,319\,\frac{\mathrm{kg}}{\mathrm{m}^3}$, which is calculated by the total mass of the measuring pipes divided by the volume of the structural pipe domain. The results

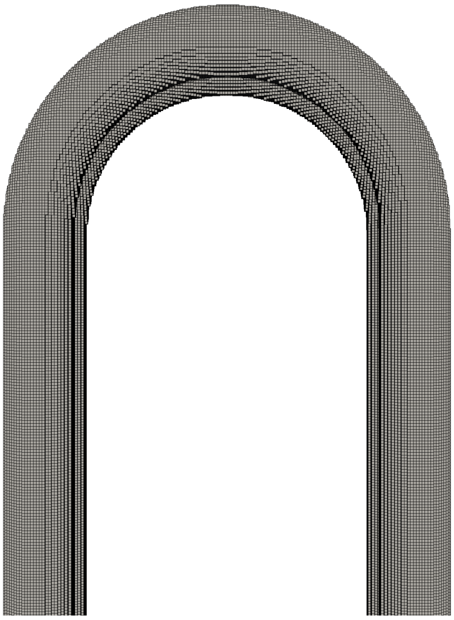

Figure 8: Voxelized measuring pipes of the LBM grid.

are summarized and compared to the measurement data in Table 5. The excitation frequencies for air and water are in good agreement to the measurement data (error $\approx 3\%$). The errors for the Coriolis frequency seems to be squared due to the higher mode.

Table 5: Excitation and Coriolis twist frequency for water and air filled tubes in comparison to measurement data.

	Simulation	Measurement	Error in $\%$
$f_{exc,air}$	104.28	101.00	3.24
$f_{exc,water}$	83.94	81.41	3.11
$f_{Coriolis,air}$	277.26	249.00	11.35
$f_{Coriolis,water}$	222.92	205.00	8.74

4.2 Phase Shift Calculation

After the modal analysis has determined the Eigenfrequency of the pipes filled with water, the transient fluid structure simulation is used to extract the phase shift. Firstly, the fluid field is initialized according to Section 3.1.2. The simulation procedure, which is described in Section 2.3.3, is executed in every coupling step Δt_c. The coupling period is chosen to the fluid time step Δt^f to minimize the time shift problem of the staggered approach. The simulation takes a total of 15 cycles which corresponds to approx. $0.18\,\mathrm{s}$ at the Eigenfrequency. Every cycle consists of 202 coupling steps. The displacement signal is extracted at the sensor positions S1_plus, S1_minus, S2_plus and S2_minus, where plus and minus indicate the left and right measuring pipe, respectively. The written data files are post processed to extract the phase shift and the frequency of the displacement signals. The displacement signals of sensor S1_plus and S2_plus are depicted in Figure 12. It can

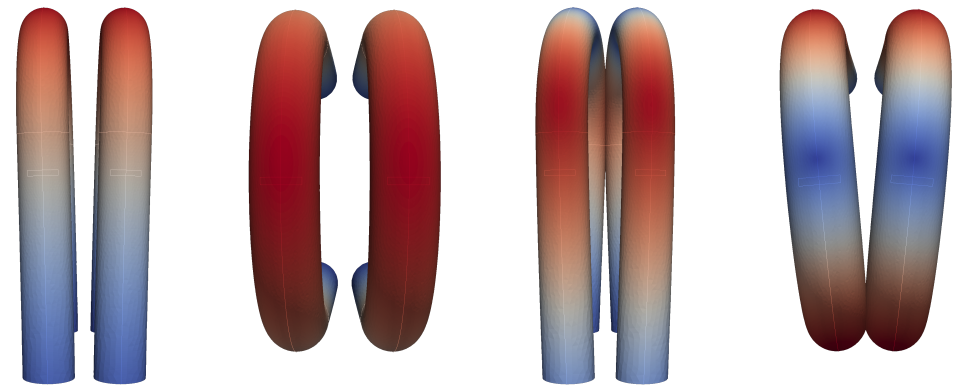

(a) Mode 2, front view (b) Mode 2, top view (c) Mode 8, front view (d) Mode 8, top view

Figure 9: Geometry displacement due to excitation mode (mode 2) and Coriolis twist mode (mode 8).

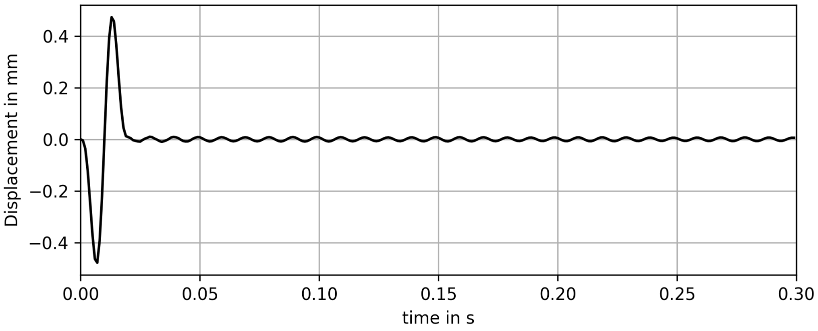

Figure 10: Structural response at frequency $f_{exc} = 50.00\,\mathrm{Hz}$.

be seen that the signal is almost sinusoidal in the first 5 cycles and the amplitude slowly decays over time. The last depicted periods show irregularities and differ from the expected pure sinusoidal course of the displacement signal. Furthermore a frequency analysis is performed to estimate resonance frequency. The results can be seen in Figure 13. The highest peak at $84.12\,\mathrm{Hz}$ in the frequency analysis is in good agreement with the estimated excitation frequency. A discrete Hilbert transformation is applied on the displacement signal to calculate the phase shift, see Figure 14. The stability of the FSI system is given for the first 8 cycles of the simulation. The symmetry condition, which should be fulfilled due to a axial-symmetric geometry, is only slightly violated. The error of the averaged phase shift value ϕ_{sim} with respect to the experimental data ϕ_{ref} is smaller than 5%, which is shown in Table 6. The relative errors for a mass flow of $20\,000$ and $40\,000\,\frac{\mathrm{kg}}{\mathrm{h}}$ are less than 5%. Numerical experiments with a lower amount of coupling steps are diverging in the first period, which indicates that the reduction of coupling steps does not lead to satisfactory results. Consequentially, 202 coupling periods are necessary to stabilize the simulation.

The simulation runtime was evaluated on a single node which consists of two deca-core Intel Xeon E5-2660 v3 processors. The comparison of the runtime to other numerical FSI simulations is depicted in Table 7. It can be seen that both computation time and calculated periods of the present

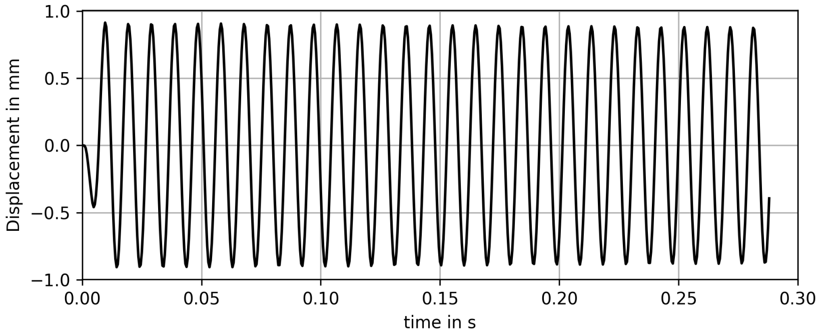

Figure 11: Structural response at frequency $f_{exc} = 104.28\,\mathrm{Hz}$.

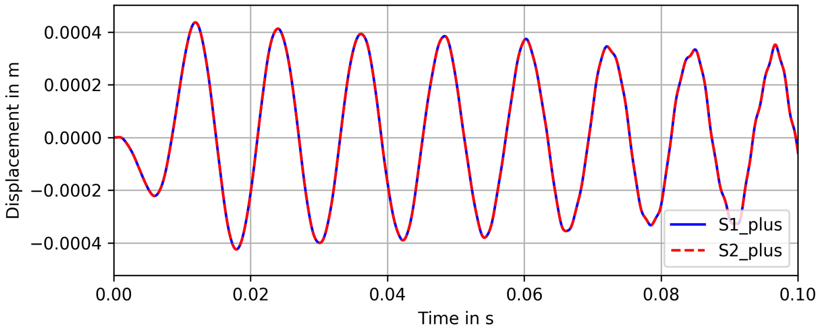

Figure 12: Displacement signal of sensor position S1_plus and S2_plus.

study are comparable to literature values. The computation runtime is estimated to 65 hours and over 3000 coupling steps are performed. It is noticeable that the computing time has hardly changed over the years. This is a consequence of the segregated approach, if two solvers are involved in the FSI approach. The partitioning of the fluid and the solid domain differs due to the numerical method and geometrical constraints. This implies that the exchanged information are collected and communicated between the solvers, which is a time consuming step that is very difficult to parallelize.

Table 6: Phaseshift errors for different mass flows and coupling steps per period.

Mass flow in $\frac{\mathrm{kg}}{\mathrm{h}}$	ϕ_{sim} in mrad	ϕ_{ref} in mrad	Error in %	Coupling steps
20 000	-	0.62	Instable	51
20 000	-	0.62	Instable	101
20 000	0.59	0.62	4.7	202
40 000	1.18	1.23	4.1	202

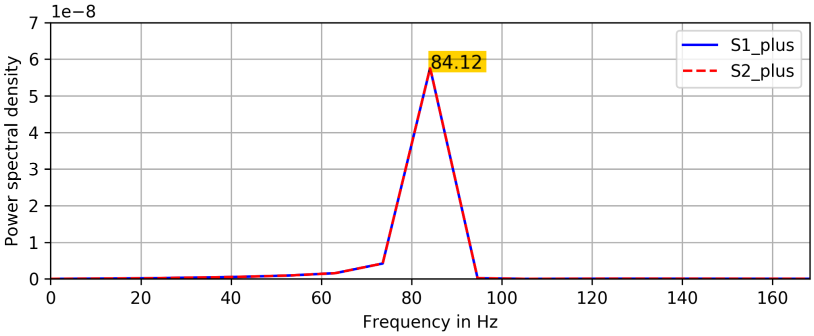

Figure 13: Discrete Fourier analysis of the displacement signal.

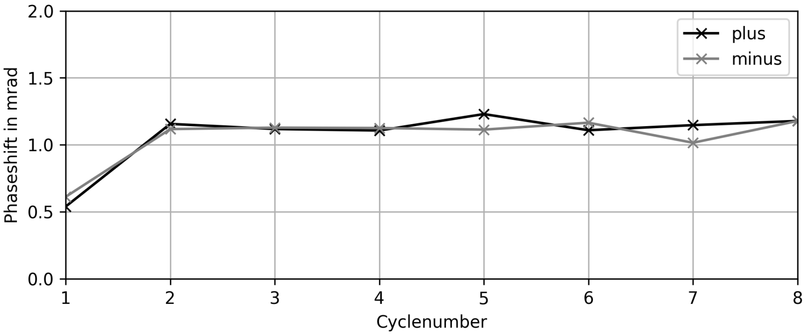

Figure 14: Phaseshift of the displacement signal.

5 Conclusion and Outlook

An FSI approach was presented for the simulation of a CMF. Thereby, the open source framework OpenLB and Elmer were used to create a segregated approach. The target equations of the structural and fluid domain were described. In addition, the coupling conditions and the implementation were outlined in detail. The FEM mesh generation process utilized the open source meshing tool Gmsh to ensure a complete open source workflow. A modal analysis was performed to extract the excitation frequency of water and air conveying pipes. The found excitation frequency was in good agreement to experimental measurements (error $\approx 3\%$). Afterwards, the FSI simulation, which uses the determined excitation frequency, was executed. The FSI simulation was stable for several cycles and allows to extract the phase shift with a sufficient precision (error $\approx 5\%$).

Table 7: Comparison of computation time between the present approach to literature values.

Study	Coupling resolution	Periods	Computation time in h
Bobovnik et al. (2013) [10]	70	43	72-96
Kumar et al. (2011) [12]	20	15	60
Mole et al. (2008) [9]	140	15	72
Present	202	15	65

Therefore, the presented FSI approach for CMF is able to describe the operating principle of a CMF. Furthermore, the runtime time of the created FSI coupling were comparable to literature approaches using commercial software.

Nevertheless, certain issues should be addressed in future studies. The FSI simulation becomes unstable after several periods. The reasons for this upcoming instability could be diverse. Firstly, the coupling time step could be decreased to reduce the time shift problem of the staggered coupling approach. Unfortunately this leads to an extended calculation time. Another possibility is the introduction of a subiteration scheme [47] that reduces the added mass effect due to the time shift. Further improvements can be made by the calculation of the hydrodynamic force, because momentum exchange based approaches suffer from inaccuracy, if too few points are used for integration. Therefore, a stress based calculation proposed in Geller et al. [21] may be an alternative. Furthermore, the applied linear mapping method between the uniform Cartesian LBM grid and the unstructured FEM grid can be improved by using more complex mapping methods [25].

References

[1] Tao Wang and Roger Baker. Coriolis flowmeters: a review of developments over the past 20 years, and an assessment of the state of the art and likely future directions. *Flow Measurement and Instrumentation*, 40:99–123, 2014.

[2] A Belhadj, R Cheesewright, and C Clark. The simulation of Coriolis meter response to pulsating flow using a general purpose fe code. *Journal of fluids and structures*, 14(5): 613–634, 2000.

[3] R Cheesewright and C Clark. The effect of flow pulsations on Coriolis mass flow meters. *Journal of Fluids and Structures*, 12(8):1025–1039, 1998.

[4] John Hemp. The weight vector theory of Coriolis mass flowmeters. *Flow measurement and Instrumentation*, 5(4):247–253, 1994.

[5] Masahiro Kazahaya. A mathematical model and error analysis of Coriolis mass flowmeters. *IEEE Transactions on Instrumentation and Measurement*, 60(4):1163–1174, 2010.

[6] Jože Kutin and I Bajsić. An analytical estimation of the Coriolis meter's characteristics based on modal superposition. *Flow Measurement and Instrumentation*, 12(5-6):345–351, 2002.

[7] LJ Wang, L Hu, ZC Zhu, P Ye, and X Fu. Analytical calculation of sensitivity for Coriolis mass flowmeter. *Measurement*, 44(6):1117–1127, 2011.

[8] G. Bobovnik, N. Mole, J. Kutin, B. Štok, and I. Bajsić. Coupled finite-volume/finite-element modelling of the straight-tube Coriolis flowmeter. *Journal of Fluids and Structures*, 20(6): 785–800, 2005. ISSN 08899746. doi: 10.1016/j.jfluidstructs.2005.04.008.

[9] N. Mole, G. Bobovnik, J. Kutin, B. Štok, and I. Bajsić. An improved three-dimensional coupled fluid–structure model for Coriolis flowmeters. *Journal of Fluids and Structures*, 24 (4):559–575, 2008. ISSN 08899746. doi: 10.1016/j.jfluidstructs.2007.10.004.

[10] G. Bobovnik, J. Kutin, N. Mole, B. Štok, and I. Bajsić. Numerical analysis of installation effects in Coriolis flowmeters: A case study of a short straight tube full-bore design. *Flow*

Measurement and Instrumentation, 34:142–150, 2013. ISSN 09555986. doi: 10.1016/j.flowmeasinst.2013.10.004.

[11] Vivek Kumar. FSI Simulations of Flow Measurement Devices using ANSYS-CFX.

[12] Vivek Kumar and Martin Anklin. Numerical simulations of Coriolis flow meters for low Reynolds number flows. *Journal of Metrology Society of India, Vol. 26*, (3):225–235, 2011.

[13] Luo Rongmo and Wu Jian. Fluid-structure coupling analysis and simulation of viscosity effect on Coriolis mass flowmeter.

[14] Vincent Heuveline, Mathias J. Krause, and Jonas Latt. Towards a hybrid parallelization of lattice Boltzmann methods. *Computers & Mathematics with Applications*, 58(5):1071–1080, 2009. ISSN 0898-1221. doi: https://doi.org/10.1016/j.camwa.2009.04.001. URL `http://www.sciencedirect.com/science/article/pii/S0898122109002454`. Mesoscopic Methods in Engineering and Science.

[15] Vincent Heuveline and Mathias J Krause. Openlb: towards an efficient parallel open source library for lattice Boltzmann fluid flow simulations. In *International Workshop on State-of-the-Art in Scientific and Parallel Computing. PARA*, volume 9, 2010.

[16] Thomas Henn, Vincent Heuveline, Mathias J. Krause, and Sebastian Ritterbusch. Aortic coarctation simulation based on the lattice Boltzmann method: Benchmark results. In Oscar Camara, Tommaso Mansi, Mihaela Pop, Kawal Rhode, Maxime Sermesant, and Alistair Young, editors, *Statistical Atlases and Computational Models of the Heart. Imaging and Modelling Challenges*, pages 34–43, Berlin, Heidelberg, 2013. Springer Berlin Heidelberg. ISBN 978-3-642-36961-2.

[17] Liliana de Luca Xavier Augusto, Jesse Ross-Jones, Gabriela Cantarelli Lopes, Paolo Tronville, José Antônio Silveira Gonçalves, Matthias Rädle, and Mathias J Krause. Microfiber filter performance prediction using a lattice Boltzmann method. *Commun Comput Phys*, 23:910–931, 2018.

[18] Marc Haussmann, Alejandro CLARO BARRETO, Gislain LIPEME KOUYI, Nicolas Rivière, Hermann Nirschl, and Mathias J Krause. Large-eddy simulation coupled with wall models for turbulent channel flows at high reynolds numbers with a lattice Boltzmann method—application to Coriolis mass flowmeter. *Computers & Mathematics with Applications*, 2019.

[19] Marc Haussmann, Stephan Simonis, Hermann Nirschl, Mathias J Krause, et al. Direct numerical simulation of decaying homogeneous isotropic turbulence—numerical experiments on stability, consistency and accuracy of distinct lattice Boltzmann methods. *International Journal of Modern Physics C (IJMPC)*, 30(09):1–29, 2019.

[20] Dominik Scholz, Stefan Kollmannsberger, Alexander Düster, and Ernst Rank. Thin solids for fluid-structure interaction. In *Fluid-Structure Interaction*, pages 294–335. Springer, 2006.

[21] Sebastian Geller, Jonas Tölke, and Manfred Krafczyk. Lattice-Boltzmann method on quadtree-type grids for fluid-structure interaction. In *Fluid-Structure Interaction*, pages 270–293. Springer, 2006.

[22] Stefan Turek and Jaroslav Hron. Proposal for numerical benchmarking of fluid-structure interaction between an elastic object and laminar incompressible flow. In *Fluid-structure interaction*, pages 371–385. Springer, 2006.

[23] Stefan Kollmannsberger, Sebastian Geller, Alexander Düster, Jonas Tölke, Christian Sorger, Manfred Krafczyk, and Ernst Rank. Fixed-grid fluid–structure interaction in two dimensions based on a partitioned lattice Boltzmann and p-FEM approach. *International journal for numerical methods in engineering*, 79(7):817–845, 2009.

[24] Pedro Valero-Lara. *Analysis and Applications of Lattice Boltzmann Simulations*. IGI Global, 2018.

[25] S Geller, S Kollmannsberger, M El Bettah, M Krafczyk, D Scholz, A Düster, and E Rank. An explicit model for three-dimensional fluid-structure interaction using LBM and p-FEM. In *Fluid Structure Interaction II*, pages 285–325. Springer, 2011.

[26] M.J. Krause, S. Avis, D. Dapalo, N Hafen, M. Haußmann, M Gaedtke, F. Klemens, A. Kummerländer, M.-L. Maier, A. Mink, J. Ross-Jones, S. Simonis, and R. Trunk. OpenLB Release 1.3: Open Source Lattice Boltzmann Code. May 2019. doi: 10.5281/zenodo.3625967. URL `https://doi.org/10.5281/zenodo.3625967`.

[27] M.J. Krause, A. Kummerländer, S.J. Avis, H. Kusumaatmaja, D. Dapelo, F. Klemens, M. Gaedtke, N. Hafen, A. Mink, R. Trunk, J. Marquardt, M.L. Maier, M. Haussmann, and S. Simonis. Openlb—open source lattice Boltzmann code. accepted for publication in CAMWA (2020).

[28] Elmer FEM open source multiphysical simulation software. `https://www.csc.fi/web/elmer`.

[29] Shin K. Kang and Yassin A. Hassan. The effect of lattice models within the lattice Boltzmann method in the simulation of wall-bounded turbulent flows. *Journal of Computational Physics*, 232(1):100 – 117, 2013. ISSN 0021-9991. doi: https://doi.org/10.1016/j.jcp.2012.07.023. URL `http://www.sciencedirect.com/science/article/pii/S0021999112003968`.

[30] P. L. Bhatnagar, E. P. Gross, and M. Krook. A model for collision processes in gases. I. Small amplitude processes in charged and neutral one-component systems. *Phys. Rev.*, 94:511–525, May 1954. doi: 10.1103/PhysRev.94.511. URL `https://link.aps.org/doi/10.1103/PhysRev.94.511`.

[31] Xiaoyi He and Li-Shi Luo. Theory of the lattice Boltzmann method: From the Boltzmann equation to the lattice Boltzmann equation. *Phys. Rev. E*, 56:6811–6817, Dec 1997. doi: 10.1103/PhysRevE.56.6811. URL `https://link.aps.org/doi/10.1103/PhysRevE.56.6811`.

[32] Xiaowen Shan, Xue-Feng Yuan, and Hudong Chen. Kinetic theory representation of hydrodynamics: a way beyond the Navier–Stokes equation. *Journal of Fluid Mechanics*, 550:413–441, 2006. doi: 10.1017/S0022112005008153.

[33] D. J. Holdych. *Lattice Boltzmann methods for diffuse and mobile interfaces*. PhD thesis, University of Illinois at Urbana-Champaign, 2003.

[34] DR Noble and JR Torczynski. A lattice-Boltzmann method for partially saturated computational cells. *International Journal of Modern Physics C*, 9(08):1189–1201, 1998.

[35] Zhi-Gang Feng and Efstathios E Michaelides. The immersed boundary-lattice Boltzmann method for solving fluid–particles interaction problems. *Journal of Computational Physics*, 195(2):602 – 628, 2004. ISSN 0021-9991. doi: https://doi.org/10.1016/j.jcp.2003.10.013. URL `http://www.sciencedirect.com/science/article/pii/S0021999103005758`.

[36] Shin K Kang and Yassin A Hassan. A comparative study of direct-forcing immersed boundary-lattice Boltzmann methods for stationary complex boundaries. *International Journal for Numerical Methods in Fluids*, 66(9):1132–1158, 2011.

[37] Yongguang Cheng, Luoding Zhu, and Chunze Zhang. Numerical study of stability and accuracy of the immersed boundary method coupled to the lattice Boltzmann BGK model. *Communications in Computational Physics*, 16(1):136–168, 2014.

[38] Olga Filippova and Dieter Hänel. Grid refinement for lattice-BGK models. *Journal of Computational physics*, 147(1):219–228, 1998.

[39] Dazhi Yu, Renwei Mei, and Wei Shyy. A unified boundary treatment in lattice Boltzmann method. In *41st Aerospace Sciences Meeting and Exhibit*, page 953, 2003.

[40] Pierre Lallemand and Li-Shi Luo. Lattice Boltzmann method for moving boundaries. *Journal of Computational Physics*, 184(2):406–421, 2003.

[41] M’hamed Bouzidi, Mouaouia Firdaouss, and Pierre Lallemand. Momentum transfer of a Boltzmann-lattice fluid with boundaries. *Physics of fluids*, 13(11):3452–3459, 2001.

[42] Binghai Wen, Chaoying Zhang, Yusong Tu, Chunlei Wang, and Haiping Fang. Galilean invariant fluid–solid interfacial dynamics in lattice Boltzmann simulations. *Journal of Computational Physics*, 266:161–170, 2014.

[43] Shi Tao, Junjie Hu, and Zhaoli Guo. An investigation on momentum exchange methods and refilling algorithms for lattice Boltzmann simulation of particulate flows. *Computers & Fluids*, 133:1–14, 2016.

[44] Mats G Larson and Fredrik Bengzon. *The finite element method: theory, implementation, and applications*, volume 10. Springer Science & Business Media, 2013.

[45] Thomas Richter. *Fluid-structure interactions: models, analysis and finite elements*, volume 118. Springer, 2017.

[46] Christophe Geuzaine and J-F Remacle. Gmsh: a three-dimensional finite element mesh generator with built-in pre-and post-processing facilities. In *Proceedings of the Second Workshop on Grid Generation for Numerical Computations, Tetrahedron II*, 2007.

[47] Matthias Heil. An efficient solver for the fully coupled solution of large-displacement fluid–structure interaction problems. *Computer Methods in Applied Mechanics and Engineering*, 193(1-2):1–23, 2004.

8

Conclusion and Outlook

The main objective of this thesis is to show that LBM is an outstanding tool for the simulation of engineering applications, particularly when turbulent flows are considered. This thesis makes important contributions to all four areas of numerical simulation: method development, implementation, validation and application. The individual contributions to each area are highlighted in the following paragraphs.

Method Development A novel LBM NWM-LES method was proposed that is able to simulate high Reynolds number flows on highly underresolved grids. Based on the collision operator study, the BGK collision operator was chosen due to its low numerical dissipation. The near wall region is modeled by a wall function and a wall-adaptive SGS model controls the introduced turbulent viscosity.

Implementation The LBM NWM-LES method was implemented in a highly modular fashion to allow extensibility to various boundary schemes and wall functions. This made it possible to extend the approach by a velocity boundary formulation that is able to handle curved boundaries. Furthermore, distinct fluid-solid interfaces were implemented in OpenLB. A coupling procedure between the fluid solver OpenLB and the structural solver Elmer was established to simulate FSI.

Validation The collision operator comparison revealed that BGK is suitable for DNS simulation due to its low dissipative behavior, if the spatial and temporal solution is chosen with respect to the Kolmogorov scales. The occurring instabilities at underresolved grid configurations are visible for TRT, BGK and ELB. The proposed literature value for the “magic parameter” [40, 41] required further scaling to yield any stable results. A constant “magic parameter” was not able to enhance the stability in comparision to BGK. The ELB scheme showed neither increased stability due to entropy correction nor improved accuracy. In contrast, the RLB scheme leads to stable results at each setting tested. The increased energy dissipation at low grids, however, greatly limits the accuracy. The stability of MRT is strongly influenced by the Mach number. If the Mach number is kept constant, the scheme is stable even at low resolutions. On the other hand, if the Mach number is reduced, an overestimated energy budget at high wave numbers leads to instabilities. The validation of the wall function algorithm showed that the choice of the extrapolation scheme as velocity boundary scheme and the Musker profile as wall function leads to accurate results in comparison to a DNS reference solution. The grid convergence of the proposed algorithm could be shown for both, the validation and within the application case. The investigation of different fluid-solid interface approaches revealed that the Yu scheme [111] as a representative of the moving boundary methods and the $\mathrm{PSM}_{\mathrm{M2}}$ configuration [73, 49, 81] as a representative of the partially saturated methods showed preferable features. At low resolutions, $\mathrm{PSM}_{\mathrm{M2}}$ is the preferable method due to less parasitic fluctuations. In contrast, the increased grid and Galilean invariance convergence order of the Yu scheme leads to a higher accuracy at higher resolutions.

Application The novel NWM-LES method was applied to simulate a CMF and an IC-engine. The pressure drop simulation of the CMF was in good agreement with the experimental data and showed to be suitable for addressing engineering applications at high Reynolds numbers. A comparison for the IC-engine test case between OpenLB using the NWM-LES implementation and OpenFOAM showed that both solvers were able to predict the time-averaged and the RMS velocity of the PIV experiment with a high accuracy. A comparison of the computational demand revealed that the simulation process in OpenLB is approximately 32 times faster for the investigated setup. This significant difference in performance with comparable accuracy underlines the suitability of the proposed LBM algorithm for NWM-LES and indicates that LBM is a valuable and viable alternative to FVM. Especially industrial applications can benefit from the faster calculation speed to perform simulations “overnight”, which previously took weeks to conduct. The investigation of the transversely oscillating cylinder in a free stream demonstrated that the tested Yu scheme and $\mathrm{PSM}_{\mathrm{M2}}$ scheme are both suitable methods to simulate VIV phenomena. The CMF investigation showed that the found excitation frequency of the modal analysis were in good agreement with the experimental measurements. The FSI simulation was stable over several cycles and the estimated phase shift values corresponded well with the experimental data. Thus, it could be shown that the proposed FSI approach can reproduce the working principle of a CMF. In addition, the runtime of the generated FSI coupling was comparable to literature approaches using commercial software.

The main aim of this thesis, the demonstration that LBM is able to simulate engineering applications, was reached. The application to a CMF, IC-engine and VIV revealed that both turbulent flow and FSI simulation with LBM lead to precise and reliable results compared to experimental and numerical reference data. Moreover, the fast and efficient implementation of the new LBM NWM-

LES method in OpenLB surpasses recent implementations of the FVM in terms of calculation speed.

Future Studies

Nevertheless, future studies have to be carried out to extend the presented studies and to allow further application cases. The study of DHIT for distinct collision operators should be expanded to include recently developed LBM schemes such as the cumulant lattice Boltzmann [35, 32, 33], the Karlin–Bösch–Chikatamarla (KBC) model [51, 11] or the recursive regularization procedure [63, 20]. Different canonical flow types should also be investigated to determine the suitability of the individual collision operators as an implicit LES model.

The proposed wall model should be tested with wall functions capable of describing, inter alia, pressure gradients, separation and recirculation, variable physical properties and compressibility effects. The implementation of a generalized wall function [96, 21, 78], which is able to model these flow phenomena, is therefore a further important step towards the modeling of complex turbulent boundary layers. Additionally, the evaluation of more advanced turbulent models, e.g., models based on dynamic procedures [39], the scale similarity hypothesis [6] or wall-adapted SGS models [72], is recommended to further improve the accuracy [89, 85]. Especially for the simulation of IC engine flows, turbulent reactive flows play a decisive role. Therefore, further modeling approaches based on detailed chemistry with a large number of species as well as tabulated chemistry should be investigated. This represents a special challenge for LBM due to the high memory requirements [30].

In the case of fluid-solid interfaces, pressure fluctuation schemes such as the local iteration refilling scheme [16] should be tested to improve the results of VIV simulations using moving boundary methods and for the interface description in the FSI simulation. Especially for FSI, the introduction of a subiteration scheme [46] that reduces the added mass effect due to the time shift should be considered. Furthermore, the calculation of the hydrodynamic force can be improved, if a stress based calculation [37] is used instead of the momentum exchange based calculation. The used linear mapping method between the uniform Cartesian LBM grid and the unstructured FEM grid can be improved by using more complex mapping methods [36].

Finally, LBM needs additional research, especially in the field of turbulent flows to reach the maturity of traditional methods. Nevertheless, the development of implicit and explicit LES models using mesoscopic information could substantially improve the accuracy and applicability of LBM LES. Combined with the shown high performance capabilities and the possibility to address multiphysical phenomena, LBM is a promising method for LES. Also, the wide field of turbulent FSI application could become available in the future.

Bibliography

[1] C. K. Aidun and J. R. Clausen. „Lattice-Boltzmann method for complex flows.“ In: *Annual review of fluid mechanics* 42 (2010), pp. 439–472.

[2] J. D. Anderson Jr. *Fundamentals of aerodynamics*. Tata McGraw-Hill Education, 2010.

[3] S. Ansumali, I. Karlin, C. E. Frouzakis, and K. Boulouchos. „Entropic lattice Boltzmann method for microflows.“ In: *Physica A: Statistical Mechanics and its Applications* 359 (2006), pp. 289–305.

[4] S. Ansumali and I. V. Karlin. „Single relaxation time model for entropic lattice Boltzmann methods.“ In: *Physical Review E* 65.5 (2002), p. 056312.

[5] C. Bailly and G. Comte-Bellot. „Homogeneous and Isotropic Turbulence.“ In: *Turbulence*. 2015, pp. 129–177.

[6] J. Bardina, J. Ferziger, and W. Reynolds. „Improved subgrid-scale models for large-eddy simulation.“ In: *13th fluid and plasmadynamics conference*. 1980, p. 1357.

[7] R. Benzi, S. Succi, and M. Vergassola. „The lattice Boltzmann equation: theory and applications.“ In: *Physics Reports* 222.3 (1992), pp. 145–197.

[8] P. L. Bhatnagar, E. P. Gross, and M. Krook. „A Model for Collision Processes in Gases. I. Small Amplitude Processes in Charged and Neutral One-Component Systems.“ In: *Phys. Rev.* 94 (3 1954), pp. 511–525.

[9] K. Y. Billah and R. H. Scanlan. „Resonance, Tacoma Narrows bridge failure, and undergraduate physics textbooks.“ In: *American Journal of Physics* 59.2 (1991), pp. 118–124.

[10] F. Bösch. „Entropic Lattice Boltzmann Models for Fluid Dynamics.“ PhD thesis. ETH Zurich, 2017.

[11] F. Bösch, S. S. Chikatamarla, and I. V. Karlin. „Entropic multirelaxation lattice Boltzmann models for turbulent flows.“ In: *Physical Review E* 92.4 (2015), p. 043309.

[12] J. Boussinesq. „Theorie de l'ecoulement tourbillant.“ In: *Mem. Acad. Sci.* 23 (1877), p. 46.

[13] M. Bouzidi, M. Firdaouss, and P. Lallemand. „Momentum transfer of a Boltzmann-lattice fluid with boundaries.“ In: *Physics of fluids* 13.11 (2001), pp. 3452–3459.

[14] A. Brand, L. Allen, M. Altman, M. Hlava, and J. Scott. „Beyond authorship: attribution, contribution, collaboration, and credit.“ In: *Learned Publishing* 28.2 (2015), pp. 151–155.

[15] D. R. Chapman. „Computational aerodynamics development and outlook.“ In: *AIAA journal* 17.12 (1979), pp. 1293–1313.

[16] L. Chen, Y. Yu, J. Lu, and G. Hou. „A comparative study of lattice Boltzmann methods using bounce-back schemes and immersed boundary ones for flow acoustic problems.“ In: *International Journal for Numerical Methods in Fluids* 74.6 (2014), pp. 439–467.

[17] S. Chen and G. D. Doolen. „Lattice Boltzmann method for fluid flows.“ In: *Annual review of fluid mechanics* 30.1 (1998), pp. 329–364.

[18] S. Chikatamarla, S. Ansumali, and I. Karlin. „Entropic lattice Boltzmann models for hydrodynamics in three dimensions.“ In: *Physical review letters* 97.1 (2006), p. 010201.

[19] T. Cochran. „Calculate pipeline flow of compressible fluids.“ In: *Chemical Engineering* 103.2 (1996), pp. 115–122.

[20] C. Coreixas, G. Wissocq, G. Puigt, J.-F. Boussuge, and P. Sagaut. „Recursive regularization step for high-order lattice Boltzmann methods.“ In: *Physical Review E* 96.3 (2017), p. 033306.

[21] T. Craft, A. Gerasimov, H. Iacovides, and B. Launder. „Progress in the generalization of wall-function treatments.“ In: *Int. J. Heat Fluid Fl.* 23 (2002), pp. 148–160.

[22] D. d'Humières. „Multiple-relaxation-time lattice Boltzmann models in three dimensions.“ In: *Philosophical Transactions of the Royal Society of London A: Mathematical, Physical and Engineering Sciences* 360.1792 (2002), pp. 437–451.

[23] E. V. Driest. „On turbulent flow near a wall.“ In: *Journal of the Aeronautical Sciences* 23.11 (1956), pp. 1007–1011.

[24] *Elmer FEM open source multiphysical simulation software*. https://www.csc.fi/web/elmer.

[25] J. H. Ferziger and M. Peric. *Computational methods for fluid dynamics*. Springer Science & Business Media, 2012.

[26] J. H. Ferziger and M. Peric. *Numerische Strömungsmechanik*. Springer-Verlag, 2008.

[27] J. H. Ferziger and M. Peric. *Numerische Strömungsmechanik*. Springer-Verlag, 2008.

[28] O. Filippova, S. Succi, F. Mazzocco, C. Arrighetti, G. Bella, and D. Hänel. „Multiscale Lattice Boltzmann Schemes with Turbulence Modeling.“ In: *Journal of Computational Physics* 170.2 (2001), pp. 812–829.

[29] J. Fröhlich. *Large eddy simulation turbulenter Strömungen*. Vol. 1. Springer, 2006.

[30] C. E. Frouzakis. „Lattice boltzmann methods for reactive and other flows.“ In: *Turbulent Combustion Modeling*. 2011, pp. 461–486.

[31] Y. Fujino and Y. Yoshida. „Wind-induced vibration and control of Trans-Tokyo Bay crossing bridge.“ In: *Journal of Structural Engineering* 128.8 (2002), pp. 1012–1025.

[32] M. Geier, A. Pasquali, and M. Schönherr. „Parametrization of the cumulant lattice Boltzmann method for fourth order accurate diffusion part I: Derivation and validation.“ In: *Journal of Computational Physics* 348 (2017), pp. 862–888.

[33] M. Geier, A. Pasquali, and M. Schönherr. „Parametrization of the cumulant lattice Boltzmann method for fourth order accurate diffusion Part II: Application to flow around a sphere at drag crisis.“ In: *Journal of Computational Physics* 348 (2017), pp. 889–898.

[34] M. Geier, M. Schönherr, A. Pasquali, and M. Krafczyk. „The cumulant lattice Boltzmann equation in three dimensions: Theory and validation.“ In: *Computers & Mathematics with Applications* 70.4 (2015), pp. 507–547.

[35] M. Geier, M. Schönherr, A. Pasquali, and M. Krafczyk. „The cumulant lattice Boltzmann equation in three dimensions: Theory and validation.“ In: *Computers & Mathematics with Applications* 70.4 (2015), pp. 507–547.

[36] S. Geller, S. Kollmannsberger, M. El Bettah, M. Krafczyk, D. Scholz, A. Düster, and E. Rank. „An explicit model for three-dimensional fluid-structure interaction using LBM and p-FEM.“ In: *Fluid Structure Interaction II*. 2011, pp. 285–325.

[37] S. Geller, J. Tölke, and M. Krafczyk. „Lattice-Boltzmann method on quadtree-type grids for fluid-structure interaction.“ In: *Fluid-Structure Interaction*. 2006, pp. 270–293.

[38] W. K. George. „Lectures in Turbulence for the 21st Century.“ In: *Chalmers University of Technology* (2013).

[39] M. Germano. „A dynamic subgrid-scale eddy viscosity model.“ In: *Phys. Fluids* 3.7 (1991), pp. 1760–1765.

[40] I. Ginzburg, D. d’Humières, and A. Kuzmin. „Optimal stability of advection-diffusion lattice Boltzmann models with two relaxation times for positive/negative equilibrium.“ In: *Journal of Statistical Physics* 139.6 (2010), pp. 1090–1143.

[41] I. Ginzburg, F. Verhaeghe, and D. d’Humieres. „Two-relaxation-time lattice Boltzmann scheme: About parametrization, velocity, pressure and mixed boundary conditions.“ In: *Communications in computational physics* 3.2 (2008), pp. 427–478.

[42] M. Haussmann, A. C. Barreto, G. L. Kouyi, N. Rivière, H. Nirschl, and M. J. Krause. „Large-eddy simulation coupled with wall models for turbulent channel flows at high Reynolds numbers with a lattice Boltzmann method—Application to Coriolis mass flowmeter.“ In: *Computers & Mathematics with Applications* 78.10 (2019), pp. 3285–3302.

[43] M. Haussmann, F. Ries, J. B. Jeppener-Haltenhoff, Y. Li, M. Schmidt, C. Welch, L. Illmann, B. Böhm, H. Nirschl, M. J. Krause, et al. „Evaluation of a Near-Wall-Modeled Large Eddy Lattice Boltzmann Method for the Analysis of Complex Flows Relevant to IC Engines.“ In: *Computation* 8.2 (2020), p. 43.

[44] M. Haussmann, S. Simonis, H. Nirschl, M. J. Krause, et al. „Direct numerical simulation of decaying homogeneous isotropic turbulence—numerical experiments on stability, consistency and accuracy of distinct lattice Boltzmann methods.“ In: *International Journal of Modern Physics C (IJMPC)* 30.09 (2019), pp. 1–29.

[45] X. He and L.-S. Luo. „Theory of the lattice Boltzmann method: From the Boltzmann equation to the lattice Boltzmann equation.“ In: *Phys. Rev. E* 56 (6 1997), pp. 6811–6817.

[46] M. Heil. „An efficient solver for the fully coupled solution of large-displacement fluid–structure interaction problems.“ In: *Computer Methods in Applied Mechanics and Engineering* 193.1-2 (2004), pp. 1–23.

[47] V. Heuveline and M. J. Krause. „OpenLB: towards an efficient parallel open source library for lattice Boltzmann fluid flow simulations.“ In: *International Workshop on State-of-the-Art in Scientific and Parallel Computing. PARA*. Vol. 9. 2010.

[48] V. Heuveline, M. J. Krause, and J. Latt. „Towards a hybrid parallelization of lattice Boltzmann methods.“ In: *Computers & Mathematics with Applications* 58.5 (2009). Mesoscopic Methods in Engineering and Science, pp. 1071–1080.

[49] D. J. Holdych. „Lattice Boltzmann methods for diffuse and mobile interfaces.“ PhD thesis. University of Illinois at Urbana-Champaign, 2003.

[50] S. Hou, J. Sterling, S. Chen, and G. Doolen. „A lattice Boltzmann subgrid model for high Reynolds number flows.“ In: 1994.

[51] I. V. Karlin, F. Bösch, and S. Chikatamarla. „Gibbs' principle for the lattice-kinetic theory of fluid dynamics.“ In: *Physical Review E* 90.3 (2014), p. 031302.

[52] A. N. Kolmogorov. „Dissipation of energy in locally isotropic turbulence.“ In: *Dokl. Akad. Nauk SSSR*. Vol. 32. 1. 1941, pp. 16–18.

[53] M. J. Krause. „Fluid Flow Simulation and Optimisation with Lattice Boltzmann Methods on High Performance Computers - Application to the Human Respiratory System.“ PhD thesis. 2010.

[54] T. Krüger, H. Kusumaatmaja, A. Kuzmin, O. Shardt, G. Silva, and E. M. Viggen. *The lattice Boltzmann method*. Vol. 10. Springer, 2017, pp. 978–3.

[55] P. Lallemand and L.-S. Luo. „Theory of the lattice Boltzmann method: Acoustic and thermal properties in two and three dimensions.“ In: *Physical review E* 68.3 (2003), p. 036706.

[56] P. Lallemand and L.-S. Luo. „Theory of the lattice Boltzmann method: Dispersion, dissipation, isotropy, Galilean invariance, and stability.“ In: *Physical Review E* 61.6 (2000), p. 6546.

[57] P. Lammers, K. Beronov, R. Volkert, G. Brenner, and F. Durst. „Lattice BGK direct numerical simulation of fully developed turbulence in incompressible plane channel flow.“ In: *Computers & fluids* 35.10 (2006), pp. 1137–1153.

[58] J. Latt and B. Chopard. „Lattice Boltzmann method with regularized pre-collision distribution functions.“ In: *Mathematics and Computers in Simulation* 72.2-6 (2006), pp. 165–168.

[59] B. Launder and D. Spalding. „The numerical computation of turbulent flows.“ In: *Computer Methods in Applied Mechanics and Engineering* 3.2 (1974), pp. 269–289.

[60] A. Leonard et al. „Energy cascade in large-eddy simulations of turbulent fluid flows.“ In: *Adv. Geophys. A* 18.A (1974), pp. 237–248.

[61] E. Lévêque, F. Toschi, L. Shao, and J.-P. Bertoglio. „Shear-improved Smagorinsky model for large-eddy simulation of wall-bounded turbulent flows.“ In: *Journal of Fluid Mechanics* 570 (2007), pp. 491–502.

[62] O. Malaspinas and P. Sagaut. „Wall model for large-eddy simulation based on the lattice Boltzmann method.“ In: *Journal of Computational Physics* 275 (2014), pp. 25–40.

[63] O. Malaspinas. „Increasing stability and accuracy of the lattice Boltzmann scheme: recursivity and regularization.“ In: *arXiv preprint arXiv:1505.06900* (2015).

[64] O. Malaspinas, M. Deville, and B. Chopard. „Towards a physical interpretation of the entropic lattice Boltzmann method.“ In: *Physical Review E* 78.6 (2008), p. 066705.

[65] O. Malaspinas and P. Sagaut. „Advanced large-eddy simulation for lattice Boltzmann methods: The approximate deconvolution model.“ In: *Physics of Fluids* 23.10 (2011), p. 105103.

[66] O. Malaspinas and P. Sagaut. „Consistent subgrid scale modelling for lattice Boltzmann methods.“ In: *Journal of Fluid Mechanics* 700 (2012), pp. 514–542.

[67] P. Moin and J. Kim. „Numerical investigation of turbulent channel flow.“ In: *Journal of Fluid Mechanics* 118 (1982), pp. 341–377.

[68] A. Musker. „Explicit expression for the smooth wall velocity distribution in a turbulent boundary layer.“ In: *AIAA Journal* 17.6 (1979), pp. 655–657.

[69] H. M. Nagib and K. A. Chauhan. „Variations of von Kármán coefficient in canonical flows.“ In: *Physics of Fluids* 20.10 (2008), p. 101518.

[70] P. Nathen, M. Haussmann, M. Krause, and N. Adams. „Adaptive filtering for the simulation of turbulent flows with lattice Boltzmann methods.“ In: *Computers & Fluids* 172 (2018), pp. 510–523.

[71] P. Nathen, D. Gaudlitz, M. J. Krause, and N. A. Adams. „On the stability and accuracy of the BGK, MRT and RLB Boltzmann schemes for the simulation of turbulent flows.“ In: *J. Commun. Comput. Phys* 23 (2017), pp. 846–876.

[72] F. Nicoud and F. Ducros. „Subgrid-scale stress modelling based on the square of the velocity gradient tensor.“ In: *Flow Turbul. Combust.* 62 (1999), pp. 183–200.

[73] D. Noble and J. Torczynski. „A lattice-Boltzmann method for partially saturated computational cells.“ In: *International Journal of Modern Physics C* 9.08 (1998), pp. 1189–1201.

[74] A. Pasquali, M. Geier, and M. Krafczyk. „Near-wall treatment for the simulation of turbulent flow by the cumulant lattice Boltzmann method.“ In: *Computers & Mathematics with Applications* (2017).

[75] O. M. Phillips. *The dynamics of the upper ocean*. Cambridge university press, 1966.

[76] U. Piomelli and J. R. Chasnov. „Large-eddy simulations: theory and applications.“ In: *Turbulence and transition modelling*. 1996, pp. 269–336.

[77] S. B. Pope. *Turbulent flows*. 2001.

[78] M. Popvac and K. Hanjalic. „Compound Wall Treatment for RANS Computation of Complex Turbulent Flows and Heat Transfer.“ In: *Flow Turhul. Combust.* 78 (2007), pp. 177–202.

[79] L. Prandtl, K. Oswatitsch, and K. Wieghardt. *Führer durch die Strömungslehre*. Springer-Verlag, 2013.

[80] K. N. Premnath, M. J. Pattison, and S. Banerjee. „Dynamic subgrid scale modeling of turbulent flows using lattice-Boltzmann method.“ In: *Physica A: Statistical Mechanics and its Applications* 388.13 (2009), pp. 2640–2658.

[81] C. Rettinger and U. Rüde. „A comparative study of fluid-particle coupling methods for fully resolved lattice Boltzmann simulations.“ In: *Computers & Fluids* 154 (2017), pp. 74–89.

[82] O. Reynolds. „On the dynamical theory of incompressible viscous fluids and the determination of the criterion.“ In: *Philosophical transactions of the royal society of london.(a.)* 186 (1895), pp. 123–164.

[83] L. F. Richardson. „Weather prediction by numerical process.“ In: *Quarterly Journal of the Royal Meteorological Society* 48.203 (1922), pp. 282–284.

[84] D. Ricot, S. Marié, P. Sagaut, and C. Bailly. „Lattice Boltzmann method with selective viscosity filter.“ In: *Journal of Computational Physics* 228.12 (2009), pp. 4478–4490.

[85] F. Ries, K. Nishad, L. Dressler, J. Janicka, and A. Sadiki. „Evaluating large eddy simulation results based on error analysis.“ In: *Theoretical and Computational Fluid Dynamics* 32.6 (2018), pp. 733–752.

[86] W. Rodi, G. Constantinescu, and T. Stoesser. *Large-eddy simulation in hydraulics*. Crc Press, 2013.

[87] R. S. Rogallo and P. Moin. „Numerical Simulation of Turbulent Flows.“ In: *Annual Review of Fluid Mechanics* 16.1 (1984), pp. 99–137.

[88] R. Rubinstein and L.-S. Luo. „Theory of the lattice Boltzmann equation: Symmetry properties of discrete velocity sets.“ In: *Physical Review E* 77.3 (2008), p. 036709.

[89] C. Rutland. „Large-eddy simulations for internal combustion engines–a review.“ In: *International Journal of Engine Research* 12.5 (2011), pp. 421–451.

[90] P. Sagaut. „Toward advanced subgrid models for Lattice-Boltzmann-based Large-eddy simulation: theoretical formulations.“ In: *Computers & Mathematics with Applications* 59.7 (2010), pp. 2194–2199.

[91] L. Saint-Raymond. „From the BGK model to the Navier-Stokes equations.“ In: *Annales scientifiques de l’Ecole normale supérieure*. Vol. 36. 2. 2003, pp. 271–317.

[92] H. Sajjadi, M. Salmanzadeh, G. Ahmadi, and S. Jafari. „Simulations of indoor airflow and particle dispersion and deposition by the lattice Boltzmann method using LES and RANS approaches.“ In: *Building and Environment* 102 (2016), pp. 1–12.

[93] L. Schmitt. „Grobstruktursimulation turbulenter Grenzschicht-, Kanal-und Stufenströmungen.“ PhD thesis. 1988.

[94] A. Schneider. „A Consistent Large Eddy Approach for Lattice Boltzmann Methods and its Application to Complex Flows.“ PhD thesis. 2015.

[95] X. Shan, X.-F. Yuan, and H. Chen. „Kinetic theory representation of hydrodynamics: a way beyond the Navier–Stokes equation.“ In: *Journal of Fluid Mechanics* 550 (2006), pp. 413–441.

[96] T.-H. Shih, L. A. Povinelli, N.-S. Liu, and K.-H. Chen. „Generalized wall function for complex turbulent flows.“ In: (2000).

[97] J. Slotnick, A. Khodadoust, J. Alonso, D. Darmofal, W. Gropp, E. Lurie, and D. Mavriplis. „CFD vision 2030 study: a path to revolutionary computational aerosciences.“ In: (2014).

[98] J. Smagorinsky. „General circulation experiments with the primitive equations: I. The basic experiment.“ In: *Monthly weather review* 91.3 (1963), pp. 99–164.

[99] S. Stolz and N. A. Adams. „An approximate deconvolution procedure for large-eddy simulation.“ In: *Physics of Fluids* 11.7 (1999), pp. 1699–1701.

[100] S. Succi, G. Amati, and R. Benzi. „Challenges in lattice Boltzmann computing.“ In: *Journal of statistical physics* 81.1-2 (1995), pp. 5–16.

[101] S. Succi, H. Chen, C. Teixeira, G. Bella, A. De Maio, and K. Molvig. „An integer lattice realization of a Lax scheme for transport processes in multiple component fluid flows.“ In: *Journal of Computational Physics* 152.2 (1999), pp. 493–516.

[102] C. K. Tam, J. C. Webb, and Z. Dong. „A study of the short wave components in computational acoustics.“ In: *Journal of Computational Acoustics* 1.01 (1993), pp. 1–30.

[103] C. M. Teixeira. „Incorporating turbulence models into the lattice-Boltzmann method.“ In: *International Journal of Modern Physics C* 9.08 (1998), pp. 1159–1175.

[104] H. K. Versteeg and W. Malalasekera. *An introduction to computational fluid dynamics: the finite volume method*. Pearson education, 2007.

[105] T. Wang and R. Baker. „Coriolis flowmeters: a review of developments over the past 20 years, and an assessment of the state of the art and likely future directions.“ In: *Flow Measurement and Instrumentation* 40 (2014), pp. 99–123.

[106] M. Weickert, G. Teike, O. Schmidt, and M. Sommerfeld. „Investigation of the LES WALE turbulence model within the lattice Boltzmann framework.“ In: *Computers & Mathematics with Applications* 59.7 (2010), pp. 2200–2214.

[107] H. Werner and H. Wengle. „Large-eddy simulation of turbulent flow over and around a cube in a plate channel.“ In: *Turbulent Shear Flows 8*. 1993, pp. 155–168.

[108] T. Yasduda, T. Hashimoto, H. Minagawa, K. Morinishi, and N. Satofuka. „Efficient simulation for incompressible turbulent flow using lattice Boltzmann model.“ In: *Procedia Engineering* 61 (2013), pp. 173–178.

[109] P.-K. Yeung and S. B. Pope. „Lagrangian statistics from direct numerical simulations of isotropic turbulence.“ In: *Journal of Fluid Mechanics* 207 (1989), pp. 531–586.

[110] C.-S. Yih. „Dynamics of nonhomogeneous fluids(Book on mathematics and physics of fluid flows of variable density and entropy in gravitational field which is relevant to natural flows).“ In: *NEW YORK, MACMILLAN CO., 1965. 306 P* (1965).

[111] D. Yu, R. Mei, and W. Shyy. „A unified boundary treatment in lattice Boltzmann method.“ In: *41st Aerospace Sciences Meeting and Exhibit*. 2003, p. 953.

[112] G. Zhao-Li, Z. Chu-Guang, and S. Bao-Chang. „Non-equilibrium extrapolation method for velocity and pressure boundary conditions in the lattice Boltzmann method.“ In: *Chinese Physics* 11.4 (2002), p. 366.

Appendix

A List of Publications

Peer-Reviewed Journal Publications

- **M. Haussmann**, S. Simonis, H. Nirschl and M. J. Krause. Direct numerical simulation of decaying homogeneous isotropic turbulence – numerical experiments on stability, consistency and accuracy of distinct lattice Boltzmann methods. *International Journal of Modern Physics C (IJMPC)*, 30.09 (2019).

- **M. Haussmann**, A. Claro Barreto, G. Lipeme Kouyi, N. Rivière, H. Nirschl and M. J. Krause. Large-eddy simulation coupled with wall models for turbulent channel flows at high Reynolds numbers with a lattice Boltzmann method – Application to Coriolis mass flowmeter. *Computers & Mathematics with Applications*, 78.10 (2019).

- **M. Haussmann**, F. Ries, J. B. Jeppener-Haltenhoff, L. Yongxiang, M. Schmidt, C. Welch, L. Illmann, B. Böhm, H. Nirschl, M. J. Krause and Amsini Sadiki. Evaluation of a Near-Wall-Modeled Large Eddy Lattice Boltzmann Method for the Analysis of Complex Flows Relevant to IC Engines. *Computation*, 8.43 (2020).

- **M. Haussmann**, N. Hafen, F. Raichle, R. Trunk, H. Nirschl and M. J. Krause. Galilean Invariance Study on Different Lattice Boltzmann Fluid-Solid Interface Approaches for Vortex-Induced Vibrations. *Computers & Mathematics with Applications*, 80.5 (2020).

- P. Nathen, **M. Haussmann**, M. J. Krause and N. Adams. Adaptive filtering for the simulation of turbulent flows with lattice Boltzmann methods.*Computers & Fluids* 172 (2018).

- M. J. Krause, A. Kummerländer, S. Avis, H. Kusumaatmaja, D. Dapelo, F. Klemens, M. Gaedtke, N. Hafen, A. Mink, R. Trunk, J. Marquardt, M. Maier, **M. Haussmann** and S. Simonis. OpenLB—Open Source Lattice Boltzmann Code. *Computers & Mathematics with Applications*, Article in press (2020).

Preprints

- **M. Haussmann**, P. Reinshaus, S. Simonis, H. Nirschl and M. J. Krause. Fluid-Structure Interaction Simulation of a Coriolis Mass Flowmeter using a Lattice Boltzmann Method. *arXiv physics.comp-ph*, 2005.04070 (2020).

Talks

- **M. Haussmann**. Suspension Modelling in the Lattice Boltzmann Method. *Partnerships for International Research and Education (PIRE) Project Meeting*, New York City, USA (2018).

- **M. Haussmann**, A. Claro Barreto, G. Lipeme Kouyi, N. Rivière, H. Nirschl and M. J. Krause. Pressure Drop Calculation in a Coriolis Mass Flowmeter at High Reynolds Numbers. *27th International Conference on Discrete Simulation of Fluid Dynamics (DSFD)*, Worcester, USA (2018).

- **M. Haussmann**. Turbulence with the lattice Boltzmann method. *Spring School: Lattice Boltzmann Methods with OpenLB Software Lab*, Mannheim, Germany (2019).

- **M. Haussmann**, N. Hafen, F. Raichle, R. Trunk, H. Nirschl and M. J. Krause. Numerical Study on Different Lattice Boltzmann Fluid-Structure Interaction Approaches for Vortex-Induced Vibrations *16th International Conference for Mesoscopic Methods in Engineering and Science (ICMMES)*, Edinburgh, UK (2019).

- **M. Haussmann**. Turbulence with the lattice Boltzmann method. *Spring School: Lattice Boltzmann Methods with OpenLB Software Lab*, Berlin, Germany (2020).

Posters

- **M. Haussmann** , A. Claro Baretto and M. J. Krause. Large Eddy Simulationen mit Lattice Boltzmann Methoden und einer Wandfunktion für Coriolis Durchflussmesser. *Jahrestreffen der ProcessNet Fachgruppe Computational Fluid Dynamics*, Frankfurt, Germany (2018)

B List of OpenLB Test and Application Cases

The following table lists the presented test cases and the related commit hashes in the OpenLB git repository on the master branch.

Name	description	commit hash	case folder in `apps/marc/`
Taylor-Green vortex flow	Section 3.3	241a5a61	`tgv_cluster`
Bi-periodic turbulent channel flow	Section 4.3	237e2583	`tcf3d_scaled`
Coriolis mass flowmeter (NWM-LES)	Section 4.4	237e2583	`CoriolisWF`
In-cylinder fluid flow	Section 5.3	241a5a61	`PIV_setup`
Cylinder in a Couette flow	Section 6.3.1	e2235d05	`movingCylinder2d`
Cylinder in a free stream	Section 6.4.1	e2235d05	`inducedOscillatingCylinder`
Coriolis mass flowmeter (FSI)	Section 7.3	f0475218	`FSI_Giga_Full`